

Measurement of rock resistivity using inductive method in a cased well

Vasić, Darko

Doctoral thesis / Disertacija

2010

Degree Grantor / Ustanova koja je dodijelila akademski / stručni stupanj: **University of Zagreb, Faculty of Electrical Engineering and Computing / Sveučilište u Zagrebu, Fakultet elektrotehnike i računarstva**

Permanent link / Trajna poveznica: <https://urn.nsk.hr/urn:nbn:hr:168:516635>

Rights / Prava: [In copyright](#)/[Zaštićeno autorskim pravom.](#)

Download date / Datum preuzimanja: **2025-02-18**



Repository / Repozitorij:

[FER Repository - University of Zagreb Faculty of Electrical Engineering and Computing repository](#)



UNIVERSITY OF ZAGREB
FACULTY OF ELECTRICAL ENGINEERING AND COMPUTING
SVEUČILIŠTE U ZAGREBU
FAKULTET ELEKTROTEHNIKE I RAČUNARSTVA

Darko Vasić

**MEASUREMENT OF ROCK RESISTIVITY
USING INDUCTIVE METHOD
IN A CASED WELL**

**MJERENJE OTPORNOSTI STIJENA
INDUKTIVNOM METODOM U
ZACIJEVLJENOJ BUŠOTINI**

DOCTORAL THESIS
DOKTORSKA DISERTACIJA

Zagreb, 2010

This doctoral thesis has been done at the Department of Electronic Systems and Information Processing, Faculty of Electrical Engineering and Computing, University of Zagreb. The first experimental studies have been performed at the School of Electrical and Electronic Engineering, University of Manchester.

Supervisors:

Professor Vedran Bilas, Ph.D.

Faculty of Electrical Engineering and Computing, University of Zagreb

Professor Franjo Šumanovac, Ph.D.

Faculty of Mining, Geology and Petroleum Engineering, University of Zagreb

The doctoral thesis has *ix*, 162 pages.

Doctoral thesis number:

The dissertation evaluation committee:

1. Professor Ratko Magjarević, Ph.D.
Faculty of Electrical Engineering and Computing, University of Zagreb
2. Professor Vedran Bilas, Ph.D.
Faculty of Electrical Engineering and Computing, University of Zagreb
3. Professor Franjo Šumanovac, Ph.D.
Faculty of Mining, Geology and Petroleum Engineering, University of Zagreb
4. Professor Željko Štih, Ph.D.
Faculty of Electrical Engineering and Computing, University of Zagreb
5. Professor Anthony Peyton, Ph.D.
University of Manchester, UK

The dissertation defence committee:

1. Professor Ratko Magjarević, Ph.D.
Faculty of Electrical Engineering and Computing, University of Zagreb
2. Professor Vedran Bilas, Ph.D.
Faculty of Electrical Engineering and Computing, University of Zagreb
3. Professor Franjo Šumanovac, Ph.D.
Faculty of Mining, Geology and Petroleum Engineering, University of Zagreb
4. Professor Željko Štih, Ph.D.
Faculty of Electrical Engineering and Computing, University of Zagreb
5. Professor Anthony Peyton, Ph.D.
University of Manchester, UK

Date of dissertation defense: June 2, 2010

Teško je gledati kako se na meni ispunja zakon i mjera koja vrijedi za sve. I zašto mi je onda u sjenovitoj crkvi objavljeno da sam zvan za viša djela?

Ivo Andrić (1892–1975)

Nobel Prize Laureate for Literature, 1961,
from “*Nemir*,” 1920.

Perhaps the most valuable result of all education is the ability to make yourself do the thing you have to do, when it ought to be done, whether you like it or not; it is the first lesson that ought to be learned; and, however early a man's training begins, it is probably the last lesson that he learns thoroughly.

Thomas Henry Huxley (1825–1895)

English biologist, “Darwin's Bulldog,”
from “*Collected Essays III — Technical Education*,” 1877.

*Mojim roditeljima, Dariji, Sarah i Željki
za svu njihovu potporu, ljubav i smiješak.*

*To my parents, Darija, Sarah, and Željka
for all their support, love, and smile.*

Acknowledgements

This thesis would not have been possible without my mentor Professor Vedran Bilas, and his invaluable guidance at the beginning of my academic carrier and friendship through all these years.

I would like to thank to Professor Franjo Šumanovac for his help in the field of geophysics.

I am grateful to Mr. Marijan Kuri for his help in the experimental part of the research, to Professor Igor Krois for kindly providing and adjusting his amplifier, to Professor Hrvoje Džapo for introducing me with the Tarantola's book and MCMC methods, and to Professor Ratko Magjarevic and Professor Željko Štih for their comments.

I am in debt to Professor Anthony Peyton and his colleagues at the University of Manchester for their support and hospitality during my stay in the United Kingdom. Professor Peyton significantly affected my work with his comments and suggestions.

I thank to my friends, Mr. Zvonko Kostanjčar and Mr. Tomislav Petković for discussions about things related and unrelated to my dissertation during countless midday coffees and mint teas — I learn a lot from them.

I owe my deepest appreciation to all of my colleagues and friends from the Department of Electronic Systems and Information Processing for creating the stimulating and comfortable environment for the research and writing the thesis.

There are no words that can express my gratitude to my parents for their support and love, to Darija and Sarah for their care and joy, and to my Željka for her love, encouragement, help and smile.

Contents

1	Introduction	1
1.1	The background: Well logging	1
1.1.1	Definition and the basic principles	1
1.1.2	Resistivity measurement	2
1.2	The challenge: Through casing resistivity measurement	4
1.2.1	Cased borehole	4
1.2.2	Formation evaluation in cased boreholes	4
1.2.3	Cased-hole electrode measurement	6
1.2.4	Cased-hole inductive measurement	7
1.3	The contribution: This thesis	9
2	Forward problem	11
2.1	Modelled geometry and governing equations	11
2.1.1	Odd parity solution	14
2.1.2	Even parity solution	15
2.2	Boundary conditions	15
2.2.1	Cylindrical boundaries	16
2.2.2	Horizontal boundary	19
2.2.3	Interface equations in the matrix form	20
2.3	Solution to the eigenvalue equations	21
2.3.1	Odd-case eigenvalue equation	22
2.3.2	Even-case eigenvalue equation	27
2.3.3	Root-finding algorithm	28
2.4	Numerical implementation	32
2.5	Homogenous surrounding formation	35
2.5.1	Induced current density	37
3	Space-frequency analysis	38
3.1	Formation conductivity	38
3.1.1	Phase difference	38
3.1.2	Homogenous surrounding formation	40
3.1.3	Vertical spatial resolution	44
3.1.4	Radius of investigation	47
3.2	Casing properties	49
3.2.1	Spectrum of induced voltage	50

3.2.2	Wall thickness and electromagnetic properties	51
3.2.3	Casing factor and permeability-conductivity ratio	54
3.3	Correction for casing effect in case of known casing properties	56
4	Inverse problem	61
4.1	Sensitivity analysis and ill-conditioning	61
4.2	Theoretical considerations	66
4.2.1	Elements of probabilistic inverse problem theory	66
4.2.2	Gaussian theoretical and measurement uncertainties	68
4.2.3	Random and systematic uncertainties	69
4.3	Monte Carlo Markov chain methods	70
4.3.1	Metropolis-Hastings algorithm	70
4.3.2	MCMC output analysis	72
4.4	Formulation of the inverse problem	74
4.4.1	A priori information	75
4.4.2	Measurement data	76
4.4.3	Transition probability distribution	76
4.4.4	Metropolis-Hastings algorithm	77
4.5	Solution of the inverse problem	79
4.5.1	Introductory example	80
4.5.2	Maximal measurement uncertainty	85
4.5.3	Repeated experiments and systematic uncertainty	90
5	Experimental results	111
5.1	Scaled model	111
5.1.1	Scaling relations	111
5.1.2	Cased borehole model	113
5.1.3	Signal generation, acquisition and processing	115
5.1.4	Interference reduction	115
5.1.5	Results	119
5.1.6	Comparison with the analytical model	123
5.2	Single-coil method for inner radius	124
5.3	Remote-field technique	125
6	Electronic instrumentation	127
6.1	Influential factors	127
6.1.1	Coil decentralisation	127
6.1.2	Parasitic capacitances	128
6.1.3	Nonlinearity of casing material	128
6.1.4	Environmental temperature	129
6.2	Key system components	130
6.2.1	Transmitter coil	130
6.2.2	Receiver coil	132
6.2.3	Receiver amplifier	133
6.2.4	Mixed-signal and digital circuitry	134

CONTENTS

6.2.5	Digital phase-sensitive detection	134
6.3	Effects of noise and interferences	136
6.3.1	Scaled model vs. field system	136
6.3.2	Measurement channel	137
7	Conclusions	142
	Bibliography	147
	Summary	159
	About the author	160
	Sažetak	161
	Životopis	162

Chapter 1

Introduction

The last thing one knows in constructing a work is what to put first.

Blaise Pascal (1623–1662)

Pensées, no. 19, 1670

1.1 The background: Well logging

1.1.1 Definition and the basic principles

Well logging, originating from the French term *carottage électrique*, is the collection of methods and interpretation techniques used for evaluation of characteristics of rock formations, and measurements concerning completion evaluation, such as pipe and tubing corrosion, cement quality, pressure measurement and production logging services [1]. A well-logging measurement device (tool, sonde) is lowered into a well to record many physical quantities, which are presented in form of a log and used for the interpretation. Over fifty different logging tools are available today employing various physical principles [1].

Formation evaluation is concerned with answering the questions of existence, location, quantity and, ultimately, producibility of the hydrocarbons from a well. These questions are answered indirectly through the process of interpretation of rock properties measurements, including porosity, water and hydrocarbon (oil and gas) saturation, and permeability. Porosity, ϕ is a fraction of the volume of a rock that can be filled with fluids. The rock matrix material occupies the remaining fraction of the volume, $1 - \phi$. Water saturation, S_w is the fraction of the porosity ϕ that contains water. The fractional volume of the rock occupied by the water is $S_w\phi$. The remaining fraction of the porosity containing oil or gas is the hydrocarbon saturation, S_h . The fractional volume occupied by the hydrocarbons is $S_h\phi$ or $(1 - S_w)\phi$ [2]. Permeability (in geology) is a rock's ability to transmit fluids, e.g. fissured carbonates and sandstones. The later are very permeable and easily transmit fluids since they have many large, well-connected pores (sandstones are reservoir rocks for hy-

drocarbons) [3]. The most important formation evaluation methods, usually sensitive to either rock properties or pore-filling fluid, are measurements of the natural radiation (gamma ray), spontaneous potential and formation bulk density, neutron and acoustic measurements, and resistivity measurement [1].

The gamma ray and the spontaneous potential measurements are used to determine the zones with a low-volume fraction of shale (clean zones). The gamma ray logging is based on higher natural radioactivity of shale formations due to the presence of isotopes of potassium, thorium and uranium. In its simplest form it is also used for well to well correlation and depth control. The origin of spontaneous potential is in the diffusion of the dissolved ions in the fluids in the borehole and in the formation [1, 4]. The measured voltage is lower for the sand than for the shale zone, because the latter behaves as a cation selective membrane.

The hydrocarbons can exist in a rock only if it is porous. As the number of pores increases, the formation bulk density decreases. The density is determined from counting the scattered gamma rays by detectors placed at several distances from the gamma ray source [5]. The counting rate of a detector varies exponentially with the bulk density of the formation. The neutron logging tools are based on the fact that hydrogen, which is usually in the pores in form of water or hydrocarbons, is very efficient in the slowing-down of fast neutrons [6, 7]. The neutron logs are used with the density log, since they are very sensitive to environmental effects. The porosity increases the compressional wave slowness or interval transit time, measured by the acoustic tools [8]. The hydrogen presence can also be detected using nuclear magnetic resonance (NMR) tools [9].

1.1.2 Resistivity measurement

So far, this very brief overview of the formation evaluation measurement principles have shown how to locate clean and porous zones. Now remains the question whether the formation contains the hydrocarbons or not. Measurement of the formation electrical resistivity is the method of choice for answering the question. In short, the hydrocarbon bearing formation has very large resistivity, and if the formation contains brine the resistivity is low. The electrical resistivity measurement is the first logging method used in boreholes; the first electrical log was recorded in 1927 by the Schlumberger brothers and Henry Doll in the Pechelbronn field in Alsace-Lorraine [2].

In order to determine quantity of the hydrocarbons in the formation, one must determine the product of the formation porosity and water saturation, $S_w\phi$. The water saturation itself depends on the porosity. The relation is given in form of the Archie's law:

$$S_w^n = \frac{a\rho_w}{\phi^m\rho_t}, \quad (1.1)$$

where ρ_t is measured formation resistivity and ρ_w is the resistivity of the water in the undisturbed formation [10]. The constants a , m and n need to be

determined for investigated formation. There have been many attempts to find alternatives to the Archie's law, but it and its extensions still dominate [1]. Resistivity of some typical materials is shown in Table 1.1. The resistivity of formations of interest may range from $0.1 \Omega\text{m}$ to $10^3 \Omega\text{m}$, or 1 mS/m – 10 S/m .

Table 1.1: Resistivity values of typical materials. Adapted from [1], p. 47.

Material	Resistivity [Ωm]
Marble	$5 \cdot 10^7$ – 10^9
Quartz	10^{12} – $3 \cdot 10^{14}$
Petroleum	$2 \cdot 10^{14}$
Distilled water	$2 \cdot 10^{14}$
Saltwater (15 °C)	0.06–3.4
Formations	
Clay/shale	2–10
Saltwater sand	0.5–10
Oil sand	5 – 10^3
Limestone	10^3

The electrode type resistivity tools employ electrodes and low-frequency current sources, usually below 1000 Hz. The simplest and oldest version of such a tool uses only one voltage measurement electrode that measures the voltage drop across the formation caused by the current injected through an electrode 40.6 cm or 16" away from the measurement electrode ("short normal" device). Such a device measures the apparent resistivity which is different from the true resistivity due to the effects of mud, hole size and shoulder beds. To avoid these problems, the next generation of the electrode devices introduced two or six additional current electrodes. Such tools, known as laterologs, create almost horizontal (lateral) electric field that forces the main current deep into the adjacent horizontal layer of the formation. Dual laterologs rapidly change the role of various electrodes, what enables simultaneous measurement of deep and shallow formation regions. Sondes with three or four arms, each with an array of coils pressed against its section of the borehole wall, measure 3D orientation of strata intersecting the borehole. The modern imaging devices contain a few hundred electrodes mounted on six arms.

The induction type devices were originally designed as a replacement for the electrode devices in conditions of nonconductive mud or air-filled boreholes, but today they are widely used as complementary tools to the electrode ones. In its basic configuration, an induction tool uses a transmitter coil energised at frequencies on the order of 10 kHz and a receiver coil to measure the electromagnetic field affected by the presence of the conductive formation. Adding the receiver coils at different separations from the transmitter selec-

tively improves sensitivity to different layers and at different radial depth. As a result, these focused tools have increased vertical resolution. For a long time, so-called 6FF40 was standard configuration with three transmitters, three receivers (hence the number 6), fixed radial and vertical focusing (FF) and 40'' (about 1 m) separation between the main transmitter and receiver. The next generation, a multi-array induction tool, uses a set of coil arrays whose measurements are combined through advanced inverse problem algorithms in order to form outputs with desired vertical and radial response.

The induction tools are preferred when the resistivity near the borehole is high and the resistivity of the formation is low, whereas the opposite holds for the electrode devices. Detailed overview of the resistivity tools, including historical perspective and the modern trends, can be found in [1] and especially in [2]. Very thorough display of the theory of induction logging can be found in [11], whereas the best starting point is the seminal paper of Henry Doll [12].

1.2 The challenge: Through casing resistivity measurement

1.2.1 Cased borehole

The walls of a borehole are eventually lined with a casing, usually made of steel, Fig. 1.1. The casing fulfills following important tasks: keeps the hole from collapsing; serves as a high strength flow conduit; protects the freshwater-bearing formation from contamination; provides a stable support for the installation of tubing and pressure control devices; provides a safe passage for running well logging equipment; provides a selective communication with formations of interest (casing perforation) [13]. The casings are divided according to their primary task into conductor pipes, surface, intermediate and production casings, and liners. Production casings are separated from the borehole wall only with the cement, except in the production zones where the casing is perforated to allow fluid flow, Fig. 1.1.

The casing diameters and wall thickness are standardised according to [14]. Outside diameter of the production casings varies from $4\frac{1}{2}''$ to $9\frac{5}{8}''$, or approximately 114.3 mm – 244.5 mm with the tolerance of -0.75% . Wall thickness is in the range 5 mm – 23 mm with the minimal permissible thickness of 87.5% of the nominal value [13]. The casing steel is divided into the grades according to the yield and tensile strength and hardness. The conductivity of the steel is in the range 1 MS/m – 7 MS/m and relative incremental permeability is on the order of 100.

1.2.2 Formation evaluation in cased boreholes

Cased hole logging devices provide information on casing and well integrity, fluid flow during production and injection, and formation surrounding the cas-

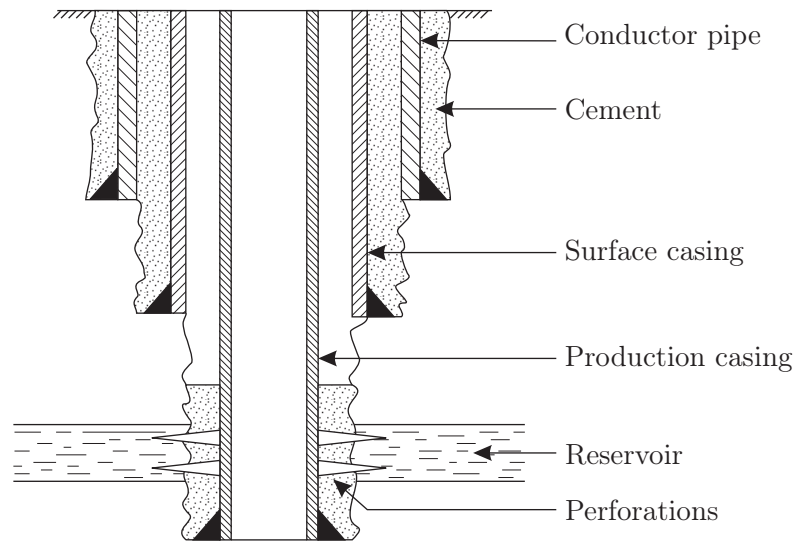


Figure 1.1: Typical cased hole (casing program) showing different casing sizes. Tubing is omitted. Adapted from [13].

ing, which is of primary interest herein. Methods for the formation evaluation through casing allow obtaining the essential well logs under any conditions (e.g. the holes that are cased immediately after drilling due to expected stability problems) [15]. A prominent application of these methods is finding and evaluating bypassed hydrocarbons in old wells. Bypassing hydrocarbon-bearing layers during the casing of the borehole can later in production result in recovering as low as 20% of estimated original oil in place [16–18]. Furthermore, one-time or time-lapse through-casing evaluation can assist in efficient reservoir management, e.g. movement monitoring of a reservoir or injected fluid [15, 19]. Using these methods, one can avoid drilling new wells for the sole purpose of data gathering, which is more cost effective and environment friendly. General overview of the cased-hole methods can be found in [20] and [21].

Cased-hole formation evaluation relies mainly on the radiation methods based on the gamma ray and neutron measurements, since these have a little or no interaction with the steel casing. The most valuable nuclear-based tool for such a purpose is a pulsed neutron device that can be run even from within the tubing [21]. Pulsed neutron devices employ a neutron source that emits 14 MeV neutrons periodically at about 1 ms intervals. Gamma ray emissions caused by the neutrons’ interaction with the borehole and formation are detected by usually two detectors, one near to the source (~ 30 cm) and the other far from the source (~ 60 cm). The rate of emitted gamma rays decays with time what reflects capturing (disappearing) of the neutrons, in turn connected with the thermal absorption properties of the borehole and formation (thermal neutron die-away or decay time logging) [1]. The gamma ray detected at the later time depends solely on the formation properties. In addition to the simple gamma ray counting, the next generation of the

pulsed neutron detectors employs gamma-ray spectroscopy for identification of neutron interactions with different elements in the formation. Pulsed neutron tools are used in the cased-hole formation evaluation for measurements of porosity, water saturation, shale content, gas detection, etc. [21]. However, their greatest drawback is depth of investigation of only ~ 50 cm.

The application of acoustic tools is similar to the open-hole evaluation [20]. They are used for porosity measurements and the log quality depends on the acoustic coupling of the casing and formation. Additional applications include measurement of formation fluid pressure, formation mechanical properties and fractures, permeability, and cement bond quality [1].

Similarly to the open-hole logging as briefly presented in Section 1.1, the responses of the cased-hole devices is interdependent regardless of their primary application, and one must always rely on their combination to obtain reliable information about the cased well. Considering the low investigation depth of the pulsed neutron tool, there is a need to round off the cased-hole formation evaluation process with through-casing resistivity measurement. That is not an easy task though, since it is clear from section 1.2.1 that the casing with its dimensions, weight and electromagnetic properties represents a formidable obstacle for the classical electromagnetic field.

1.2.3 Cased-hole electrode measurement

The first patent for a method of rock resistivity electrode measurement through the highly conductive casing was filed in the 1930s, but problems connected with the measurement of extremely small electrical potentials had held the development of these tools back until the late 1990s [22–25]. Prototyped by ParaMagnetic Logging in the USA, the tool was commercialised under the name Cased Hole Resistivity Tool (Schlumberger) [25–27].

The working principle of the tool is depicted in Fig. 1.2. The tool uses three voltage electrodes each 60 cm apart and pressed against the inner wall of the casing. In a “Measure” mode, one electrode of the current source is connected to the ground at the surface and the other is pressed against the casing. A very small amount ΔI of the total current I will leak to the formation behind the casing. This leak is visible as a voltage drop between the electrodes A and C. To cancel the effect of casing resistance R_C , difference $U_0 = U_2 - U_1$ is observed, which should depend solely on formation resistance R_f under the assumption that the casing resistances between electrodes A and B, and B and C are the same. However, since this is seldom true in the practice, “Calibrate” mode is required where both electrodes of the current source are connected to the casing. In that case $I = I_C$ and potential drops U_1 and U_2 are solely due to casing resistance R_C . By adjusting the gain for voltages U_1 and U_2 , it is possible to null the effects of the casing’s conductivity variations. If the calibration was made properly, any difference in voltages U_1 and U_2 can now be related to the changes in formation resistivity. Although the formation is typically nine orders of magnitude less conductive than the casing, it presents

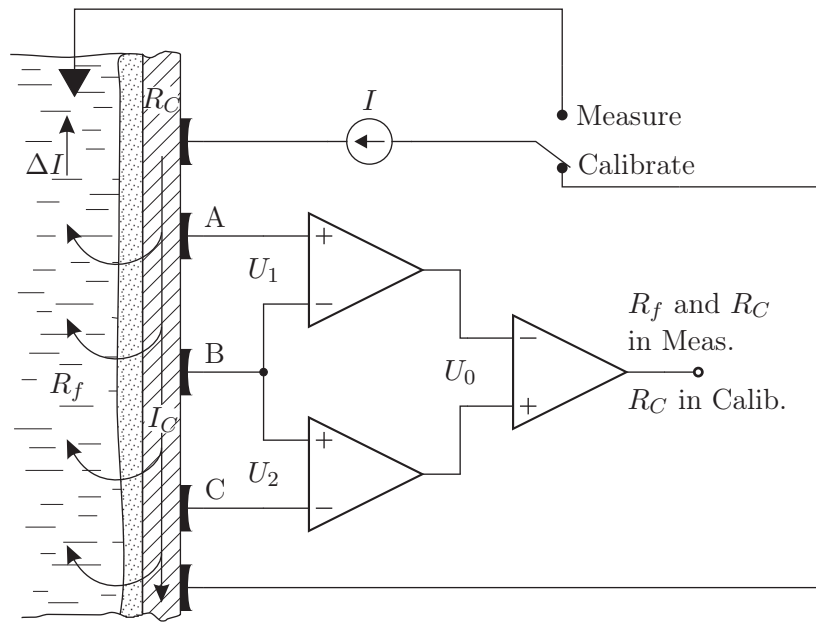


Figure 1.2: The basic principle of the electrode resistivity measurement through casing. Voltage difference U_0 is due to R_f and R_C in “Measure” mode, and R_C only in “Calibrate” mode. Adapted from [1].

a much larger mass and area, so that the ratio of the leakage current to the total current is around 10^{-4} [1].

The differential voltage U_0 is in nanovolts, and the measurement frequency is no more than a few hertz. The best measurement range is from $1 \Omega\text{m}$ to $100 \Omega\text{m}$ with vertical resolution of 1.22 m. The measurement is made while the tool is stationary, resulting in the effective logging speed of 73 m/h. Accuracy is specified as $\pm 10\%$ and depth of investigation is about 10 m [15]. There are two sizes of the tool, covering casing’s diameter range from $4\frac{1}{2}''$ to $9\frac{5}{8}''$ (production casings). Specified temperature rating is 150°C . The main disadvantages of the method are high requirements on accuracy and precision of the electronic instrumentation (measurements in the nanovolt range under harsh environment conditions), low measurement speed (stationary measurement), and large mechanical force required to establish a good contact between the electrodes and the casing. Such a force can damage or even rupture the casing of the older boreholes [28].

1.2.4 Cased-hole inductive measurement

Research on the inductive through casing resistivity measurement was focused from its start on the use of the transmitter coil outside the cased borehole, under the claim that the effects of the formation on the magnetic field, with the frequency low enough to penetrate the casing, would be otherwise practically undetectable [29]. In 1994, a consortium of academia (Lawrence Berkeley National Laboratory, Lawrence Livermore National Laboratory, and University of

California), industry and US Department of Energy began a research program with the aim to prototype a device for the through casing subsurface inductive measurement of formation resistivity [30, 31]. The chosen configuration was a very long transmitter positioned in one well with the receiver array in another remote well [32]. The corresponding patent was filed in 1999 and soon the others followed [33–35]. The result of the research was a commercial tool by Schlumberger, trade marked DeepLook-EM [36].

The tool uses a 9.88 m long transmitter coil and four receiver coils, each 22.5 m long. The transmitter coil and receiver array are placed in different wells. The tool is reported to work for the following combinations of the transmitter and receiver wells: open hole – open hole (1000 m max.), open hole – steel casing (450 m max.), open hole – chromium casing (500 m max.), and chromium casing – chromium casing (350 m max.). The excitation frequency is between 5 Hz and 1000 Hz. The tool operates in wells with maximum deviation of 20°. For each receiver station, the transmitter traverses the well with logging speed of 600 m/h to 1520 m/h. The process is repeated for a number of the array’s positions. From the measurement data, a tomographic image of the resistivity distribution between the wells can be obtained [37]. Successful applications of the tool to the waterflood monitoring and finding a bypassed pay have been reported [19, 38].

Evaluation of the casing effect is a crucial issue for the inductive measurement of the formation resistivity. The shielding effect of the thin-wall casing for a magnetic dipole was analysed by Wait and Hill [39, 40], whereas the complete analysis of the multilayered conductive and permeable structures can be found in the work of Dodd and Deeds [41, 42]. The casing behaves as a low-pass filter, which has small attenuation of the field at very low frequencies, and significant attenuation at high frequencies determined by the casing thickness and penetration depth. Augustin et al. noticed in [29] that the total magnetic field in surface-to-borehole inductive logging can be decomposed into the field of the formation in the absence of the casing and the field contributed by the casing. Similar conclusion is found to hold for the cross-well measurement [35, 43]. Augustin et al. in [29] also indicated the need for measurement of the casing properties (wall thickness, electrical conductivity and relative magnetic permeability) in order to compensate for their variations and calculate the casing contribution to the total field. They also proposed the use of the wireline casing inspection tools like the Schlumberger’s Multifrequency Electromagnetic Thickness Tool (METT) based on the remote field technique, [20, 44, 45]. However, the existing casing inspection tools are qualitative in nature and thus not suitable for the correction purposes [46, 47]. Proposals for model-based electromagnetic measurements of the casing properties using harmonic or pulsed excitation can be found in recent literature [46, 48–50].

The greatest advantage of the cross-well inductive measurement, high-power transmitter coil and tomographic imaging between the wells, is its disadvantage at the same time. The transmitter coil cannot be placed in a borehole cased with the usual casing steel; chromium casing has several times lower

conductivity than the casing steel and relative magnetic permeability equal to 1. The only situation where the steel casing is allowed is the one with the open transmitter and cased receiver wells. The high power transmitter placed in the steel casing would aggravate the problems arising due to the nonlinearity of the ferromagnetic steel. In order to overcome this limitation, there were some recent interesting proposals to use the casing as the AC source [51]. However, if one requires merely a cased hole counterpart to the traditional open-hole induction logging with depth of investigation of about 10 m, drilling a new well to place the transmitter for the cross-well measurement seems like an overkill. Hence, the single well inductive measurement of the formation resistivity would be a welcome addition to the through casing formation evaluation methods.

The challenge of placing both the transmitter and receiver in the same steel cased well in order to measure the resistivity of the surrounding formation was, to the best of this author's knowledge, first tackled by Kim and Lee in 2006 [52]. In their analysis, they used relatively "weak" casing with conductivity of only 1 MS/m, permeability of 6.25, inner radius of 100 mm and thickness of 10 mm. The excitation frequency was 100 Hz. They studied the effect of separation between transmitter and receiver up to 5 m and concluded that the phase difference between the measured magnetic field and the magnetic field calculated using the casing properties with the formation absent represents the best indication of the change in the surrounding formation conductivity. The phase difference was between 0.1° and 1° . The effects of the formation on the magnetic field amplitude were observable but negligible. The variations in the casing properties significantly affect the measurement. Assuming that these variations are localised, they proposed a simple low-pass space filtering of the phase log in order to remove the casing effect.

1.3 The contribution: This thesis

The objective of this thesis is to propose an inductive method and inversion procedure for simultaneous measurement of the formation resistivity and the casing properties from within a single steel-cased well.

We will derive and numerically implement an analytical model of the magnetic field distribution of a transmitter coil positioned inside a casing surrounded by a cylindrically layered low-conductive medium with one horizontal boundary. Using the model, we will show that the minimal tool configuration for achieving such a measurement requires one excitation frequency and three receiver coils. The modelled geometry will allow us to investigate vertical resolution, radius of investigation and the casing effect for the proposed configuration of the measurement.

We will adopt the stochastic formulation of the inverse problem of determination of the casing and formation properties. The stochastic formulation requires prior and results in posterior information on the properties in form of probability distributions. As a consequence, all properties are determined

simultaneously, and there is no need for independent measurement of the casing properties, or correction for their variations. Furthermore, the stochastic approach inherently allows use of a prior knowledge of the casing and formation obtained in previous time-lapse evaluations of the well using various well logging methods.

We will corroborate the measurement method on a laboratory scaled model of the cased borehole. Based on the results of Monte Carlo simulations and the scaled-model experiments, we will discuss the practical realisability of the electronic instrumentation capable for operation in the high-temperature environment of a well (~ 200 °C).

This thesis should be thought of as the first step towards realisation of the field system. It is to be expected that the field system will use more coils with more complex transmit and receive patterns, multi-frequency excitation and advanced stochastic inverse algorithms in order to achieve higher accuracy and vertical resolution required for useful geophysical interpretation of a reservoir. Even so, this thesis proves the basic concepts of such a tool.

To formally summarise, the contributions of this thesis to achieving the goal of the inductive measurement of the formation resistivity from within a single steel-cased well are as follows.

1. Development and validation of an inductive method for simultaneous measurement of the formation resistivity and casing properties from within a single cased well using one excitation frequency and three receiver coils.
2. Analytical modelling of the magnetic field distribution, and space-frequency sensitivity analysis of the directly measured quantities (field and induced voltage) on the formation and casing properties.
3. Stochastic approach to the inverse problem of determination of the formation and casing properties with possibility to include existing knowledge.
4. Experimental confirmation of the proposed method on a scaled model of the cased borehole.
5. Analysis of realisability of the electronic instrumentation based on the modelling and experimental results.

The model is derived in Chapter 2. The results of the space-frequency sensitivity analysis, and discussions on the radius of investigation, vertical resolution and the casing effect are given in Chapter 3. Chapter 4 contains the stochastic formulation of the inverse problem and results of Monte Carlo simulations for the analysis of the total measurement uncertainty. The experiments on the scaled borehole model are described in Chapter 5. Chapter 6 brings discussion about the influential factors, and requirements and realisability of the electronic instrumentation. Chapter 7 contains the final concluding remarks.

Chapter 2

Forward problem

In mathematics you don't understand things. You just get used to them.

John von Neumann (1903–1957)

In reply to a young man as quoted in Gary Zukav,
"The Dancing Wu Li Masters," p. 208, 1984

In this chapter we derive an analytical model of a single-turn coil positioned inside the highly conductive, magnetic tube surrounded with a low conductive, cylindrically layered medium with one horizontal boundary. The model is based on the quasi-static approximation of the Maxwell's equations and the truncated region method with eigenvalue expansion of the vector magnetic potential [42, 53]. A special care is taken to represent the model equations in a form suitable for a numerical implementation.

2.1 Modelled geometry and governing equations

The geometry of the problem is given in Fig. 2.1. Because of the axial symmetry of the problem domain, it is convenient to employ the cylindrical coordinate system with unit vectors $(\hat{\mathbf{r}}, \hat{\mathbf{z}}, \hat{\boldsymbol{\varphi}})$. We shall consider a single-turn coil with radius r_0 positioned at height z_0 . This is the most basic configuration, and solutions for the multi-turn (one-layer and multi-layer) coils follow from this case by the principle of superposition [41]. The coil is driven with a sinusoidal current i of constant amplitude I and frequency f , i.e. $\omega = 2\pi f$. The casing has inner radius r_1 , outer radius r_2 and wall thickness $c = r_2 - r_1$. The tube material is assumed to be linear, isotropic and homogenous with electrical conductivity σ_t and relative magnetic permeability μ_r . The formation surrounding the casing consists of three regions with different electrical conductivities, Fig. 2.1. We shall assume that it is possible to model effects of the casing's cement and the invaded part of the formation using the lump conductivity σ_l of region 4 (lump zone). Regions 5 and 6 (layers A and B) represent a two-layer uninvaded formation with their respective electrical conductivities

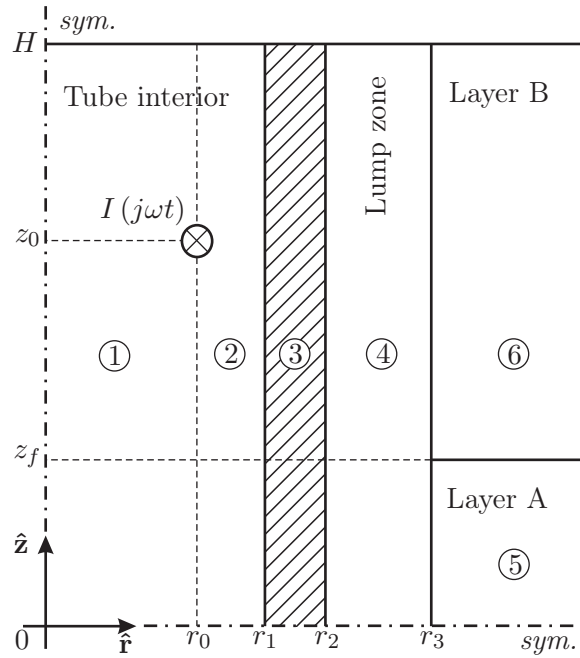


Figure 2.1: Geometry of the analysed problem

σ_a and σ_b . Both regions border region 4 at $r = r_3$ and extend to infinity in the radial direction. In the axial direction, region 5 extends between $-z_f$ and z_f and the whole problem domain is truncated at $z = -H$ and $z = H$ [53].

We can neglect the displacement current and use the diffusion equation for the vector magnetic potential:

$$\nabla^2 \mathbf{A} - \mu_0 \mu_r \sigma \frac{\partial \mathbf{A}}{\partial t} = 0.$$

In the frequency domain the potential satisfies the Helmholtz equation:

$$\nabla^2 \mathbf{A} - j\omega \mu_0 \mu_r \sigma \mathbf{A} = 0.$$

The excitation current i has the φ -component only, and so does the vector magnetic potential \mathbf{A} , too. Because of the axial symmetry, the φ -component of the potential depends on coordinates r and z , and not on coordinate φ . Taking into account the form of the Laplacian operator in a cylindrical coordinate system, we can write the governing equation for the φ -component of the potential in the case of the axial symmetry:

$$\frac{\partial^2 A}{\partial r^2} + \frac{1}{r} \frac{\partial A}{\partial r} + \frac{\partial^2 A}{\partial z^2} - \frac{A}{r^2} - j\omega \mu_0 \mu_r \sigma A = 0, \quad (2.1)$$

where the last summand is zero in the case of nonconductive materials.

The governing equation needs to be solved for each region. We shall assume that solutions can be obtained by linear combinations of members of the set of solutions that are separable into factors, each dependent on only one coordinate:

$$A(r, z) = R(r)Z(z). \quad (2.2)$$

Inserting (2.2) into (2.1) and dividing by $R(r)Z(z)$ results in:

$$\frac{1}{R} \frac{d^2 R}{dr^2} + \frac{1}{rR} \frac{dR}{dr} - \frac{1}{r^2} + \frac{1}{Z} \frac{d^2 Z}{dz^2} = j\omega\mu_0\mu_r\sigma. \quad (2.3)$$

We will separate (2.3) in two different ways. For regions 1 through 4, we will leave $j\omega\mu_0\mu_r\sigma$ with the r -dependent part of the equation:

$$\frac{1}{R} \frac{d^2 R}{dr^2} + \frac{1}{rR} \frac{dR}{dr} - \frac{1}{r^2} - j\omega\mu_0\mu_r\sigma = \alpha^2, \quad (2.4)$$

$$-\frac{1}{Z} \frac{d^2 Z}{dz^2} = \alpha^2, \quad (2.5)$$

whereas for regions 5 and 6 we will leave it with the z -dependent part, because the regions' properties vary in the z direction:

$$\frac{1}{R} \frac{d^2 R}{dr^2} + \frac{1}{rR} \frac{dR}{dr} - \frac{1}{r^2} = \kappa^2, \quad (2.6)$$

$$-\frac{1}{Z} \frac{d^2 Z}{dz^2} + j\omega\mu_0\mu_r\sigma = \kappa^2. \quad (2.7)$$

Solutions to equations (2.4) and (2.6) are in terms of modified Bessel functions of the first and second kind:

$$R(r) = c_I I_1(ar) + c_K K_1(ar),$$

where c_I and c_K are constants, $a = \sqrt{\alpha^2 + j\omega\mu_0\mu_r\sigma}$ for (2.4) and $a = \kappa$ for (2.6). Equations (2.5) and (2.7) are ordinary second-order differential equations whose solutions can be written as linear combinations of sine and cosine terms.

To simplify the problem, we shall separate the solution to its odd and even parts with respect to z . This means that we can consider only one half of the problem domain ($0 \leq z \leq H$). Physically, the odd parity solution is for the case of two single-turn coils at positions $z = z_0$ and $z = -z_0$ carrying current in opposite directions [54]. The even parity solution is for two coils carrying current in the same direction. Superposition of these two physical situations leaves us with only one coil in the upper half of the domain. If the excitation currents in the odd and even cases have the same amplitudes as in the real case, then the final solution is:

$$A(r, z) = \frac{A_{odd}(r, z) + A_{evn}(r, z)}{2}.$$

Because of the axial symmetry, the magnetic induction \mathbf{B} has only r and z components:

$$\mathbf{B} = \nabla \times \mathbf{A} = -\frac{\partial A}{\partial z} \hat{\mathbf{r}} + \frac{1}{r} \frac{\partial (rA)}{\partial r} \hat{\mathbf{z}}.$$

2.1.1 Odd parity solution

The magnetic vector potential A for each region must satisfy the homogenous Dirichlet condition:

$$A(r, \pm H) = 0. \quad (2.8)$$

Also, for the odd parity solution:

$$A(r, 0) = 0.$$

As a result of these boundary conditions at $z = H$ and $z = 0$ and required parity, we can write the odd parity solution for each region in terms of a series of appropriate discrete eigenvalues:

$$A_{odd,1} = \sum_i \sin(\alpha_i z) I_1(\alpha_i r) C_{1,i}, \quad (2.9)$$

$$A_{odd,2} = \sum_i \sin(\alpha_i z) [I_1(\alpha_i r) C_{2,i} + K_1(\alpha_i r) D_{2,i}], \quad (2.10)$$

$$A_{odd,3} = \sum_i \sin(\alpha_i z) [I_1(\beta_i r) C_{3,i} + K_1(\beta_i r) D_{3,i}], \quad (2.11)$$

$$A_{odd,4} = \sum_i \sin(\alpha_i z) [I_1(\gamma_i r) C_{4,i} + K_1(\gamma_i r) D_{4,i}], \quad (2.12)$$

$$A_{odd,5} = \sum_i \sin(p_i z) K_1(\kappa_i r) D_{5,i}, \quad (2.13)$$

$$A_{odd,6} = \sum_i k_i \sin(q_i (H - z)) K_1(\kappa_i r) D_{5,i}. \quad (2.14)$$

Because of (2.8), the eigenvalues α_i are given with:

$$\alpha_i = \frac{i\pi}{H}, \quad i \in \mathbb{N}.$$

Writing equations (2.4)–(2.7) for each region, we end up with the following:

$$\beta_i = \sqrt{\alpha_i^2 + j\omega\mu_0\mu_r\sigma_t}, \quad (2.15)$$

$$\gamma_i = \sqrt{\alpha_i^2 + j\omega\mu_0\sigma_l}, \quad (2.16)$$

$$p_i = \sqrt{\kappa_i^2 - j\omega\mu_0\sigma_a}, \quad (2.17)$$

$$q_i = \sqrt{\kappa_i^2 - j\omega\mu_0\sigma_b}. \quad (2.18)$$

Term $K_1(\alpha_i r) D_{1,i}$ is omitted in (2.9) because $D_{1,i} = 0, \forall i$ due to the divergence of $K_1(\alpha_i r)$ at $r = 0$. Similarly, term $I_1(\kappa_i r) C_{5,i}$ is not present in (2.13) and (2.14) because $C_{5,i} = 0, \forall i$ due to the divergence of $I_1(\kappa_i r)$ as r goes to infinity.

Solutions for regions 5 and 6 have the same r -dependent parts because of the joint boundary in the axial direction. However, they have different conductivities and that results in different values of p_i and q_i . Term k_i in (2.14) is required in order to satisfy continuity equations between regions 5 and 6. Since q_i is complex in general, the argument $q_i (H - z)$ ensures the zero value of the sine term required by the Dirichlet condition at $z = H$.

2.1.2 Even parity solution

In order to obtain the even parity part, we will follow a procedure similar to the one in 2.1.1. The even parity part of the solution also needs to satisfy the homogenous Dirichlet condition at $z = H$ and $z = -H$. As a consequence, the even parity solution should be of the following form, depending on the region:

$$A_{evn,1} = \sum_i \cos(\alpha_i z) I_1(\alpha_i r) C_{1,i}, \quad (2.19)$$

$$A_{evn,2} = \sum_i \cos(\alpha_i z) [I_1(\alpha_i r) C_{2,i} + K_1(\alpha_i r) D_{2,i}], \quad (2.20)$$

$$A_{evn,3} = \sum_i \cos(\alpha_i z) [I_1(\beta_i r) C_{3,i} + K_1(\beta_i r) D_{3,i}], \quad (2.21)$$

$$A_{evn,4} = \sum_i \cos(\alpha_i z) [I_1(\gamma_i r) C_{4,i} + K_1(\gamma_i r) D_{4,i}], \quad (2.22)$$

$$A_{evn,5} = \sum_i \cos(p_i z) K_1(\kappa_i r) D_{5,i}, \quad (2.23)$$

$$A_{evn,6} = \sum_i k_i \sin(q_i (H - z)) K_1(\kappa_i r) D_{5,i}. \quad (2.24)$$

The eigenvalues α_i are determined from the Dirichlet condition:

$$\alpha_i = \frac{(2i - 1)\pi}{2H}, \quad i \in \mathbb{N}.$$

Equations (2.15)–(2.18) for β_i , γ_i , p_i and q_i and notes on the form of the solutions for regions 5 and 6 in 2.1.1 are also valid for the even parity case.

In the following text, we keep the same notation for eigenvalues because the majority of the equations are the same for the odd and even parity cases. However, one should always bear in mind that although the notation is the same, actual values of e.g. $C_{1,i}$, α_i or κ_i are completely different. It will be explicitly stated if an equation or eigenvalue is valid only for one particular case (odd or even).

2.2 Boundary conditions

We will determine values of $C_{1,i}$, $C_{2,i}$, $D_{2,i}, \dots, D_{5,i}$ from the boundary conditions. In general, the boundary conditions for the tangential and normal components of a magnetic field of strength H and magnetic induction B , which should be satisfied at the surface between two homogeneous, linear and isotropic materials, are:

$$\begin{aligned} \hat{\mathbf{n}} \times (\mathbf{H}_{n+1} - \mathbf{H}_n) &= \mathbf{J}_s, \\ \hat{\mathbf{n}} \cdot (\mathbf{B}_{n+1} - \mathbf{B}_n) &= 0, \end{aligned}$$

2.2 Boundary conditions

In these equations, \mathbf{J}_s is the linear density of any free current flowing in an infinitesimally thin sheet at the surface, n and $n + 1$ are the indices of the neighbouring regions, and $\hat{\mathbf{n}}$ is the unit vector normal to the surface boundary between the regions, pointing into the region $n + 1$.

For all cylindrical boundaries the unit vector normal is $\hat{\mathbf{n}} = \hat{\mathbf{r}}$. Taking into account that magnetic potential has only φ -component and applying some elementary rules of vector analysis, we find boundary conditions for cylindrical boundaries:

$$\frac{1}{\mu_{n+1}} \left(\frac{\partial A_{n+1}}{\partial r} + \frac{A_{n+1}}{r} \right) = \frac{1}{\mu_n} \left(\frac{\partial A_n}{\partial r} + \frac{A_n}{r} \right) + J_s, \quad (2.25)$$

$$\frac{\partial A_{n+1}}{\partial z} = \frac{\partial A_n}{\partial z}, \quad (2.26)$$

where J_s is φ -component of the current linear density. For all boundaries $J_s = 0$ except for boundary $r = r_0$ between regions 1 and 2 where $J_s = J \delta(r - r_0) \delta(z - z_0)$. The delta functions δ describe a single-turn coil of radius $r = r_0$ at height $z = z_0$. For the horizontal boundary between regions 5 and 6, $\hat{\mathbf{n}} = \hat{\mathbf{z}}$ and $J_s = 0$. This results in following boundary conditions:

$$\frac{1}{\mu_{n+1}} \frac{\partial A_{n+1}}{\partial z} = \frac{1}{\mu_n} \frac{\partial A_n}{\partial z}, \quad (2.27)$$

$$\frac{\partial A_{n+1}}{\partial r} + \frac{A_{n+1}}{r} = \frac{\partial A_n}{\partial r} + \frac{A_n}{r}. \quad (2.28)$$

Since the solutions for regions 1 through 4 have equal z -dependent parts and the solutions for regions 5 and 6 have equal r -dependent parts and permeability, conditions (2.26) and (2.27) can take simpler form (condition of continuity):

$$A_{n+1} = A_n. \quad (2.29)$$

2.2.1 Cylindrical boundaries

Condition (2.29) for the odd parity case and boundary $r = r_2$ between regions 3 and 4 results in:

$$\sum_i \sin(\alpha_i z) [I_1(\gamma_i r_2) C_{4,i} + K_1(\gamma_i r_2) D_{4,i}] = \sum_i \sin(\alpha_i z) [I_1(\beta_i r_2) C_{3,i} + K_1(\beta_i r_2) D_{3,i}]. \quad (2.30)$$

If truncated to N terms, the above expression can be transformed into a linear system of N equations using the orthogonality of the sine function:

$$\int_0^H \sin(\alpha_i z) \sin(\alpha_j z) dz = \begin{cases} \frac{H}{2} & \text{if } \alpha_i = \alpha_j, \\ 0 & \text{if } \alpha_i \neq \alpha_j. \end{cases}$$

The system obtained multiplying (2.30) by $\sin(\alpha_j z)$, $\forall j = 1, \dots, N$ and integrating over z from 0 to H is:

$$\begin{aligned} I_1(\gamma_i r_2) C_{4,i} + K_1(\gamma_i r_2) D_{4,i} &= \\ &= I_1(\beta_i r_2) C_{3,i} + K_1(\beta_i r_2) D_{3,i} \quad \forall i = 1, \dots, N, \end{aligned}$$

where we replaced j with i since $i = j$. Similarly, condition (2.25) results in:

$$\begin{aligned} \mu_r \gamma_i I_0(\gamma_i r_2) C_{4,i} - \mu_r \gamma_i K_0(\gamma_i r_2) D_{4,i} &= \\ &= \beta_i I_0(\beta_i r_2) C_{3,i} - \beta_i K_0(\beta_i r_2) D_{3,i} \quad \forall i = 1, \dots, N, \end{aligned}$$

where we used the property of the Bessel functions:

$$I_\nu(x) K_{\nu+1}(x) + I_{\nu+1}(x) K_\nu(x) = \frac{1}{x}.$$

Conditions (2.25) and (2.29) give rise to the same equations in the even case. The only difference is that we start from the orthogonality of the cosine function:

$$\int_0^H \cos(\alpha_i z) \cos(\alpha_j z) dz = \begin{cases} \frac{H}{2} & \text{if } \alpha_i = \alpha_j, \\ 0 & \text{if } \alpha_i \neq \alpha_j. \end{cases}$$

Equations for the boundary at $r = r_1$ between regions 2 and 3 are obtained using the same procedure as before:

$$\begin{aligned} I_1(\beta_i r_1) C_{3,i} + K_1(\beta_i r_1) D_{3,i} &= \\ &= I_1(\alpha_i r_1) C_{2,i} + K_1(\alpha_i r_1) D_{2,i} \quad \forall i = 1, \dots, N, \\ \beta_i I_0(\beta_i r_1) C_{3,i} - \beta_i K_0(\beta_i r_1) D_{3,i} &= \\ &= \mu_r \alpha_i I_0(\alpha_i r_1) C_{2,i} - \mu_r \alpha_i K_0(\alpha_i r_1) D_{2,i} \quad \forall i = 1, \dots, N. \end{aligned}$$

Applied to the boundary $r = r_0$ between regions 1 and 2, (2.29) results in:

$$I_1(\alpha_i r_0) C_{2,i} + K_1(\alpha_i r_0) D_{2,i} = I_1(\alpha_i r_0) C_{1,i} \quad \forall i = 1, \dots, N.$$

Since the single-turn coil is located at the boundary between regions 1 and 2, the result of (2.25) for $r = r_0$ looks somewhat different than for the other regions. We introduce:

$$\text{exc}(x) = \begin{cases} \sin(x), & \text{for the odd parity,} \\ \cos(x), & \text{for the even parity.} \end{cases} \quad (2.31)$$

With the help of (2.31) we can write:

$$\int_{r=r_0}^H J \delta(r - r_0) \delta(z - z_0) \text{exc}(\alpha_j z) dz = J \text{exc}(\alpha_i z_0), \quad i = j,$$

Finally,

$$\begin{aligned} \alpha_i I_0(\alpha_i r_0) C_{2,i} - \alpha_i K_0(\alpha_i r_0) D_{2,i} + \frac{2\mu_0}{H} J \text{exc}(\alpha_i z_0) &= \\ &= \alpha_i I_0(\alpha_i r_0) C_{1,i} \quad \forall i = 1, \dots, N. \end{aligned}$$

Cylindrical boundary at $r = r_3$

Because of the different separation of the r - and z -dependent parts, the interface equations between region 4 on one and regions 5 and 6 on the other side will have more complicated form than for the boundaries between regions 1–4. Condition (2.29) for the odd-parity case results in:

$$\begin{aligned} \sum_i \left\{ \begin{array}{c} \sin(p_i z) \\ k_i \sin(q_i(H-z)) \end{array} \right\} K_1(\kappa_i r_3) D_{5,i} = \\ = \sum_i \sin(\alpha_i z) [I_1(\gamma_i r) C_{4,i} + K_1(\gamma_i r) D_{4,i}]. \end{aligned} \quad (2.32)$$

The system obtained multiplying (2.32) by $\sin(\alpha_j z)$, $\forall j = 1, \dots, N$ and taking the integral of z from 0 to H is:

$$\begin{aligned} \sum_{i=1}^N P_{ji} K_1(\kappa_i r_3) D_{5,i} = \\ \frac{H}{2} [I_1(\gamma_j r_3) C_{4,j} + K_1(\gamma_j r_3) D_{4,j}], \quad \forall j = 1, \dots, N, \end{aligned} \quad (2.33)$$

where:

$$\begin{aligned} P_{ji} = \int_0^{z_f} \sin(p_i z) \sin(\alpha_j z) dz + \int_{z_f}^H k_i \sin(q_i(H-z)) \sin(\alpha_j z) dz, \\ \forall i = 1, \dots, N \wedge j = 1, \dots, N, \end{aligned}$$

or, after integration:

$$\begin{aligned} P_{ji} = \frac{p_i \cos(p_i z_f) \sin(\alpha_j z_f) - \alpha_j \cos(\alpha_j z_f) \sin(p_i z_f)}{\alpha_j^2 - p_i^2} + \\ + k_i \frac{q_i \cos(q_i(H-z_f)) \sin(\alpha_j z_f) + \alpha_j \cos(\alpha_j z_f) \sin(q_i(H-z_f))}{\alpha_j^2 - q_i^2}, \\ \forall i = 1, \dots, N \wedge j = 1, \dots, N. \end{aligned} \quad (2.34)$$

The second equation based on (2.25) is:

$$\begin{aligned} \sum_i \left\{ \begin{array}{c} -\sin(p_i z) \\ -k_i \sin(q_i(H-z)) \end{array} \right\} \kappa_i K_0(\kappa_i r_3) D_{5,i} = \\ = \sum_i \sin(\alpha_i z) [\gamma_i I_0(\gamma_i r) C_{4,i} - \gamma_i K_0(\gamma_i r) D_{4,i}]. \end{aligned}$$

Applying the same procedure as for (2.32) we get:

$$\begin{aligned} \sum_{i=1}^N P_{ji} \kappa_i K_0(\kappa_i r_3) D_{5,i} = \\ \frac{H}{2} \gamma_j I_0(\gamma_j r_3) C_{4,j} - \frac{H}{2} \gamma_j K_0(\gamma_j r_3) D_{4,j}, \quad \forall j = 1, \dots, N. \end{aligned} \quad (2.35)$$

Equations (2.33) and (2.35) are valid for the even case, too. We just need to redefine P_{ji} in the following way:

$$P_{ji} = \int_0^{z_f} \cos(p_i z) \cos(\alpha_j z) dz + \int_{z_f}^H k_i \sin(q_i(H-z)) \cos(\alpha_j z) dz,$$

$$\forall i = 1, \dots, N \wedge j = 1, \dots, N,$$

which is, after integration, equal to:

$$P_{ji} = \frac{\alpha_j \cos(p_i z_f) \sin(\alpha_j z_f) - p_i \cos(\alpha_j z_f) \sin(p_i z_f)}{\alpha_j^2 - p_i^2} +$$

$$+ k_i \frac{q_i \cos(q_i(H-z_f)) \cos(\alpha_j z_f) - \alpha_j \sin(\alpha_j z_f) \sin(q_i(H-z_f))}{\alpha_j^2 - q_i^2},$$

$$\forall i = 1, \dots, N \wedge j = 1, \dots, N. \quad (2.36)$$

2.2.2 Horizontal boundary

Since solutions for regions 5 and 6 have the same r -dependent part, conditions (2.28) and (2.29) can be satisfied if the z -dependent parts are matched on a term-by-term basis. For the odd parity case, this results in:

$$\sin(p_i z_f) = k_i \sin(q_i(H-z_f)), \quad (2.37)$$

$$p_i \cos(p_i z_f) = -k_i q_i \cos(q_i(H-z_f)). \quad (2.38)$$

From (2.38) follows the expression for k_i :

$$k_i = -\frac{p_i \cos(p_i z_f)}{q_i \cos(q_i(H-z_f))}.$$

Dividing (2.37) by (2.38) we get:

$$p_i \tan(q_i(H-z_f)) + q_i \tan(p_i z_f) = 0, \quad (2.39)$$

where $\forall i p_i \neq 0 \wedge q_i \neq 0$.

For the even parity case we get:

$$\cos(p_i z_f) = k_i \sin(q_i(H-z_f)), \quad (2.40)$$

$$p_i \sin(p_i z_f) = k_i q_i \cos(q_i(H-z_f)). \quad (2.41)$$

From (2.41):

$$k_i = \frac{p_i \sin(p_i z_f)}{q_i \cos(q_i(H-z_f))}.$$

Dividing (2.40) by (2.41) we get:

$$q_i \frac{1}{\tan(p_i z_f)} - p_i \tan(q_i(H-z_f)) = 0, \quad (2.42)$$

where $\forall i p_i \neq 0 \wedge q_i \neq 0$.

Equations (2.39) and (2.42) are eigenvalue equations for the odd and even parity cases, respectively. Since p_i and q_i are functions of κ_i , (2.39) and (2.42) are transcendental equations with one unknown $\kappa_i \in \mathbb{C}$. If we want to reduce the sums in (2.9)–(2.14) and (2.19)–(2.24) to N terms, we need to find N zeros (roots) of (2.39) and (2.42). Omitting or skipping only one of the zeros would introduce significant modelling errors. More detailed analysis of the eigenvalue equations and the root-finding algorithm is given in 2.3.

2.2.3 Interface equations in the matrix form

Let values of $\alpha_i, \beta_i, \gamma_i, \kappa_i, p_i$ and q_i be N components of column vectors $\boldsymbol{\alpha}, \boldsymbol{\beta}, \boldsymbol{\gamma}, \boldsymbol{\kappa}, \mathbf{p}$ and \mathbf{q} , respectively. Furthermore, let values of $C_{1,i}, C_{2,i}, D_{2,i}, \dots, D_{5,i}$ be components of column vectors $\mathbf{C}_1, \mathbf{C}_2, \mathbf{D}_2, \dots, \mathbf{D}_5$, respectively. We shall adopt the notation $\mathbf{x}^D = \text{diag}(\mathbf{x})$, where \mathbf{x}^D is a diagonal matrix whose diagonal elements are the elements of a column vector \mathbf{x} . We introduce the following matrices:

$$\mathbf{P} = (P_{ji}), \quad (2.43)$$

$$\mathbf{I}_1(\boldsymbol{\alpha}r) = \begin{cases} I_1(\alpha_i r), & \text{if } i = j \\ 0 & \text{otherwise} \end{cases}, \quad (2.44)$$

for $i = 1, \dots, N$ and $j = 1, \dots, N$. Other matrices denoted with $\mathbf{I}_\nu(\cdot)$ and $\mathbf{K}_\nu(\cdot)$, defined analogously to (2.44), are diagonal with the main diagonals containing N values of $I_\nu(\cdot)$ and $K_\nu(\cdot)$.

We are now ready to rewrite the cylindrical interface equations in the matrix form for all regions:

$$\mathbf{M}_{11}\mathbf{D}_5 = \mathbf{M}_{12}\mathbf{C}_4 + \mathbf{M}_{13}\mathbf{D}_4, \quad (2.45)$$

$$\mathbf{M}_{21}\mathbf{D}_5 = \mathbf{M}_{22}\mathbf{C}_4 + \mathbf{M}_{23}\mathbf{D}_4, \quad (2.46)$$

$$\mathbf{M}_{31}\mathbf{C}_3 + \mathbf{M}_{32}\mathbf{D}_3 = \mathbf{M}_{33}\mathbf{C}_4 + \mathbf{M}_{34}\mathbf{D}_4, \quad (2.47)$$

$$\mathbf{M}_{41}\mathbf{C}_3 + \mathbf{M}_{42}\mathbf{D}_3 = \mathbf{M}_{43}\mathbf{C}_4 + \mathbf{M}_{44}\mathbf{D}_4, \quad (2.48)$$

$$\mathbf{M}_{51}\mathbf{C}_2 + \mathbf{M}_{52}\mathbf{D}_2 = \mathbf{M}_{53}\mathbf{C}_3 + \mathbf{M}_{54}\mathbf{D}_3, \quad (2.49)$$

$$\mathbf{M}_{61}\mathbf{C}_2 + \mathbf{M}_{62}\mathbf{D}_2 = \mathbf{M}_{63}\mathbf{C}_3 + \mathbf{M}_{64}\mathbf{D}_3, \quad (2.50)$$

$$\mathbf{M}_{71}\mathbf{C}_1 = \mathbf{M}_{72}\mathbf{C}_2 + \mathbf{M}_{73}\mathbf{D}_2, \quad (2.51)$$

$$\mathbf{M}_{81}\mathbf{C}_1 = \mathbf{M}_{82}\mathbf{C}_2 + \mathbf{M}_{83}\mathbf{D}_2 + \frac{2\mu_0}{H} J_{\text{exc}}(\boldsymbol{\alpha}z_0), \quad (2.52)$$

where \mathbf{M} matrices are given with:

$$\begin{aligned}
 \mathbf{M}_{11} &= \mathbf{P}\mathbf{K}_1(\boldsymbol{\kappa}r_3) & \mathbf{M}_{12} &= \frac{H}{2}\mathbf{I}_1(\boldsymbol{\gamma}r_3) \\
 \mathbf{M}_{13} &= \frac{H}{2}\mathbf{K}_1(\boldsymbol{\gamma}r_3) & \mathbf{M}_{21} &= -\mathbf{P}\boldsymbol{\kappa}^D\mathbf{K}_0(\boldsymbol{\kappa}r_3) \\
 \mathbf{M}_{22} &= \frac{H}{2}\boldsymbol{\gamma}^D\mathbf{I}_0(\boldsymbol{\gamma}r_3) & \mathbf{M}_{23} &= -\frac{H}{2}\boldsymbol{\gamma}^D\mathbf{K}_0(\boldsymbol{\gamma}r_3) \\
 \mathbf{M}_{31} &= \mathbf{I}_1(\boldsymbol{\beta}r_2) & \mathbf{M}_{32} &= \mathbf{K}_1(\boldsymbol{\beta}r_2) \\
 \mathbf{M}_{33} &= \mathbf{I}_1(\boldsymbol{\gamma}r_2) & \mathbf{M}_{34} &= \mathbf{K}_1(\boldsymbol{\gamma}r_2) \\
 \mathbf{M}_{41} &= \boldsymbol{\beta}^D\mathbf{I}_0(\boldsymbol{\beta}r_2) & \mathbf{M}_{42} &= -\boldsymbol{\beta}^D\mathbf{K}_0(\boldsymbol{\beta}r_2) \\
 \mathbf{M}_{43} &= \mu_r\boldsymbol{\gamma}^D\mathbf{I}_0(\boldsymbol{\gamma}r_2) & \mathbf{M}_{44} &= -\mu_r\boldsymbol{\gamma}^D\mathbf{K}_0(\boldsymbol{\gamma}r_2) \\
 \mathbf{M}_{51} &= \mathbf{I}_1(\boldsymbol{\alpha}r_1) & \mathbf{M}_{52} &= \mathbf{K}_1(\boldsymbol{\alpha}r_1) \\
 \mathbf{M}_{53} &= \mathbf{I}_1(\boldsymbol{\beta}r_1) & \mathbf{M}_{54} &= \mathbf{K}_1(\boldsymbol{\beta}r_1) \\
 \mathbf{M}_{61} &= \mu_r\boldsymbol{\alpha}^D\mathbf{I}_0(\boldsymbol{\alpha}r_1) & \mathbf{M}_{62} &= -\mu_r\boldsymbol{\alpha}^D\mathbf{K}_0(\boldsymbol{\alpha}r_1) \\
 \mathbf{M}_{63} &= \boldsymbol{\beta}^D\mathbf{I}_0(\boldsymbol{\beta}r_1) & \mathbf{M}_{64} &= -\boldsymbol{\beta}^D\mathbf{K}_0(\boldsymbol{\beta}r_1) \\
 \mathbf{M}_{71} &= \mathbf{I}_1(\boldsymbol{\alpha}r_0) & \mathbf{M}_{72} &= \mathbf{I}_1(\boldsymbol{\alpha}r_0) \\
 \mathbf{M}_{73} &= \mathbf{K}_1(\boldsymbol{\alpha}r_0) & \mathbf{M}_{81} &= \boldsymbol{\alpha}^D\mathbf{I}_0(\boldsymbol{\alpha}r_0) \\
 \mathbf{M}_{82} &= \boldsymbol{\alpha}^D\mathbf{I}_0(\boldsymbol{\alpha}r_0) & \mathbf{M}_{83} &= -\boldsymbol{\alpha}^D\mathbf{K}_0(\boldsymbol{\alpha}r_0).
 \end{aligned} \tag{2.53}$$

System (2.45)–(2.52) contains total of eight unknown vectors, each having N components. Since matrix \mathbf{P} is not diagonal, we cannot solve the system separately, i.e. considering only the i -th components ($i = 1, \dots, N$) of the vectors. In the scalar notation, system (2.45)–(2.52) has $8N$ equations with $8N$ unknowns. Well-posedness of this system is of the utmost concern for the stability of the numerical implementation of the model and we will discuss it in 2.4.

2.3 Solution to the eigenvalue equations

For clarity, we shall omit indices i from our notation in this section and introduce indices re and im to denote the real and imaginary parts of κ , p and q . It is more suitable for the following discussion to rewrite (2.39) and (2.42) as functions of κ . Since:

$$p = \sqrt{\kappa^2 - j\omega\mu_0\sigma_a}, \tag{2.17}$$

$$q = \sqrt{\kappa^2 - j\omega\mu_0\sigma_b}, \tag{2.18}$$

we can write:

$$g_{odd}(\kappa) = p \tan(q(H - z_f)) + q \tan(pz_f), \tag{2.54}$$

$$g_{evn}(\kappa) = \frac{q}{\tan(pz_f)} - p \tan(q(H - z_f)). \tag{2.55}$$

In what follows, we will analyse both functions in order to locate their poles and isolate their zeros. As a result of the analysis, we will construct an algorithm for locating the zeros of (2.54) and (2.55).

We will take that the argument of a complex number is in $(-\pi, \pi]$ so that the argument of the square root of the complex number is in $(-\frac{\pi}{2}, \frac{\pi}{2}]$. As a consequence, we can limit the analysis in p - and q -planes to their right halves, i.e. $p_{re} \geq 0$ and $q_{re} \geq 0$. Furthermore, it is sufficient to analyse only right half of κ -plane ($\kappa_{re} \geq 0$) because of κ^2 in (2.17) and (2.18). If we square (2.17) and separate real and imaginary parts, we get:

$$p_{re}^2 - p_{im}^2 = \kappa_{re}^2 - \kappa_{im}^2, \quad (2.56)$$

$$p_{re}p_{im} = \kappa_{re}\kappa_{im} - \frac{\omega\mu_0\sigma_a}{2}. \quad (2.57)$$

Following conclusions can be drawn from (2.56) and (2.57) for $\kappa_{re} \geq 0$:

$$p = 0 \Rightarrow (p_{re} = 0) \wedge (p_{im} = 0) \Rightarrow \kappa_{re} = \kappa_{im} = \sqrt{\frac{\omega\mu_0\sigma_a}{2}}, \quad (2.58)$$

$$(p_{re} = 0) \wedge (|p_{im}| > 0) \Rightarrow (\kappa_{re} < \kappa_{im}) \wedge \left(\kappa_{re}\kappa_{im} = \frac{\omega\mu_0\sigma_a}{2} \right), \quad (2.59)$$

$$(p_{re} > 0) \wedge (p_{im} = 0) \Rightarrow (\kappa_{re} > \kappa_{im}) \wedge \left(\kappa_{re}\kappa_{im} = \frac{\omega\mu_0\sigma_a}{2} \right). \quad (2.60)$$

Mapping from p right half-plane to κ right half-plane is depicted in Fig. 2.2. Analogous results follow from (2.18):

$$q = 0 \Rightarrow (q_{re} = 0) \wedge (q_{im} = 0) \Rightarrow \kappa_{re} = \kappa_{im} = \sqrt{\frac{\omega\mu_0\sigma_b}{2}},$$

$$(q_{re} = 0) \wedge (|q_{im}| > 0) \Rightarrow (\kappa_{re} < \kappa_{im}) \wedge \left(\kappa_{re}\kappa_{im} = \frac{\omega\mu_0\sigma_b}{2} \right),$$

$$(q_{re} > 0) \wedge (q_{im} = 0) \Rightarrow (\kappa_{re} > \kappa_{im}) \wedge \left(\kappa_{re}\kappa_{im} = \frac{\omega\mu_0\sigma_b}{2} \right).$$

2.3.1 Odd-case eigenvalue equation

Since $p \neq 0$ and $q \neq 0$, g_{odd} has the same zeros and poles as:

$$g_{odd}^*(\kappa) = \frac{\tan(pz_f)}{p} + \frac{\tan(q(H - z_f))}{q}.$$

We shall introduce the following:

$$\begin{aligned} E_1 &= \frac{\tan(pz_f)}{p}, \\ E_2 &= \frac{\tan(q(H - z_f))}{q}, \\ p' &= 2z_f p, \\ q' &= 2(H - z_f) q. \end{aligned} \quad (2.61)$$

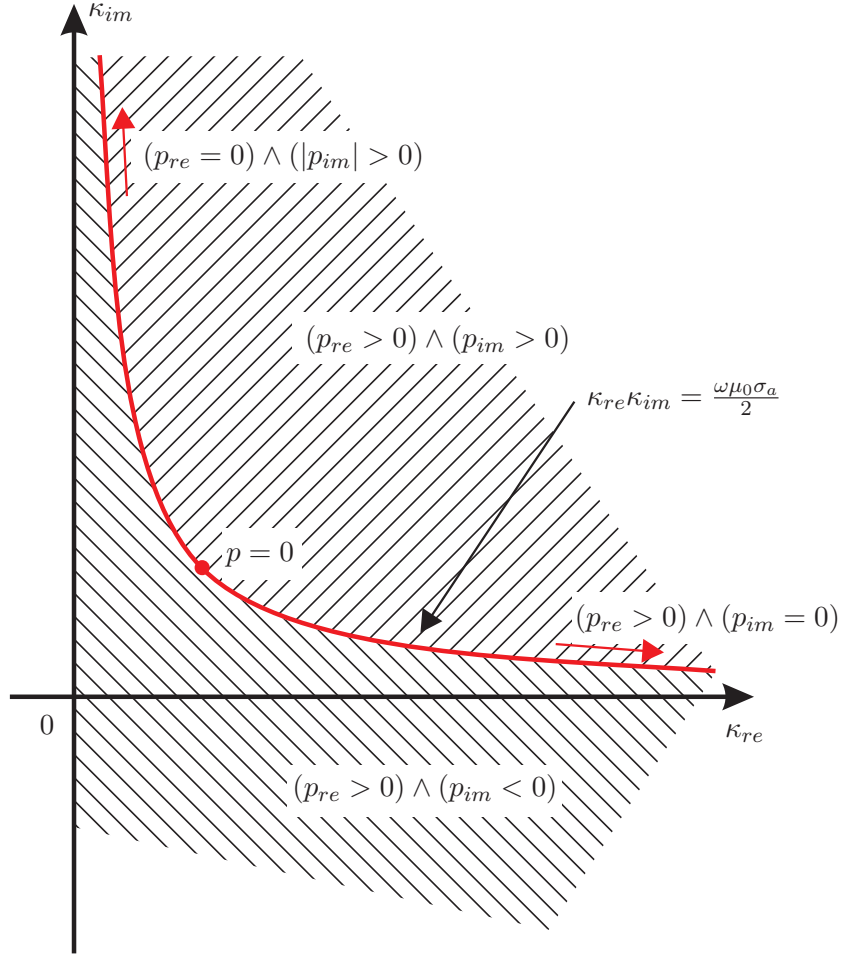


Figure 2.2: Mapping of the first and second quadrants of p -plane into κ -plane.

Imaginary parts of E_1 and E_2 are:

$$\Im(E_1) = 2z_f \frac{p'_{re} \sinh p'_{im} - p'_{im} \sin p'_{re}}{(p'^2_{re} + p'^2_{im})(\cos p'_{re} + \cosh p'_{im})},$$

$$\Im(E_2) = 2(H - z_f) \frac{q'_{re} \sinh q'_{im} - q'_{im} \sin q'_{re}}{(q'^2_{re} + q'^2_{im})(\cos q'_{re} + \cosh q'_{im})}.$$

For the denominator of $\Im(E_1)$ following holds:

$$(\cos p'_{re} + \cosh p'_{im}) \begin{cases} = 0 & \text{if } (p'_{im} = 0) \wedge (p'_{re} = (2n + 1)\pi), \forall n \in \mathbb{N}_0, \\ > 0 & \text{otherwise.} \end{cases} \quad (2.62)$$

Since $\sinh p'_{im} > p'_{im}$ and $p'_{re} > \sin p'_{re}$, we have for the numerator of $\Im(E_1)$ in p right half-plane:

$$(p'_{re} \sinh p'_{im} - p'_{im} \sin p'_{re}) \begin{cases} > 0 & \text{if } p'_{im} > 0, \\ = 0 & \text{if } (p'_{im} = 0) \vee (p'_{re} = 0) \\ < 0 & \text{if } p'_{im} < 0. \end{cases} \quad (2.63)$$

2.3 Solution to the eigenvalue equations

It is clear from (2.58)–(2.60) and (2.62)–(2.63) that $\Im(E_1)$ is positive for $p'_{im} > 0$, negative for $p'_{im} < 0$ and zero at $\kappa_{re}\kappa_{im} = \frac{\omega\mu_0\sigma_a}{2}$ except for the singular points. Let set S_{odd}^p contain the singular points of E_1 for the odd parity case in κ plane:

$$S_{odd}^p = \{\kappa \mid (p'_{re} = (2n + 1)\pi) \wedge (p'_{im} = 0), \forall n \in \mathbb{N}\}.$$

Finally, we can conclude that:

$$\Im(E_1) \begin{cases} \text{sing.} & \text{for } \kappa \in S_{odd}^p, \\ 0 & \text{if } (\kappa \notin S_{odd}^p) \wedge (\kappa_{re}\kappa_{im} = \frac{\omega\mu_0\sigma_a}{2}), \\ > 0 & \text{if } \kappa_{re}\kappa_{im} > \frac{\omega\mu_0\sigma_a}{2}, \\ < 0 & \text{if } \kappa_{re}\kappa_{im} < \frac{\omega\mu_0\sigma_a}{2}. \end{cases}$$

From the similar analysis of $\Im(E_2)$ it follows that:

$$\Im(E_2) \begin{cases} \text{sing.} & \text{for } \kappa \in S_{odd}^q, \\ 0 & \text{if } (\kappa \notin S_{odd}^q) \wedge (\kappa_{re}\kappa_{im} = \frac{\omega\mu_0\sigma_b}{2}), \\ > 0 & \text{if } \kappa_{re}\kappa_{im} > \frac{\omega\mu_0\sigma_b}{2}, \\ < 0 & \text{if } \kappa_{re}\kappa_{im} < \frac{\omega\mu_0\sigma_b}{2}, \end{cases}$$

where S_{odd}^q contains the singular points of E_2 for the odd parity case in κ plane:

$$S_{odd}^q = \{\kappa \mid (q'_{re} = (2n + 1)\pi) \wedge (q'_{im} = 0), \forall n \in \mathbb{N}\}.$$

In general, $\sigma_a \neq \sigma_b$, because there would be no need for the horizontal boundary at $z = z_f$ if $\sigma_a = \sigma_b$. Without loss of generality and for the sake of simplicity, we shall assume that $\sigma_a > \sigma_b$. Hyperbolas $\kappa_{re}\kappa_{im} = \frac{\omega\mu_0\sigma_a}{2}$ and $\kappa_{re}\kappa_{im} = \frac{\omega\mu_0\sigma_b}{2}$ bound the area in which $\Im(E_1)$ and $\Im(E_2)$ have different signs. As a consequence, curve $\Im(E_1 + E_2) = 0$ must be bounded by the hyperbolas. Since $E_1 + E_2 = 0$ is equivalent to $(\Re(E_1 + E_2) = 0) \wedge (\Im(E_1 + E_2) = 0)$, the zeros must also be located within the area bounded by the hyperbolas, Fig. 2.3.

The limits of functions $\Im(E_1)$ and $\Im(E_2)$ as p and q tend to their corresponding singular points depend on the approach trajectories. We will illustrate this for the limit of $\Im(E_1)$ as p approaches to singular point $p' = (\pi, 0)$ with trajectory $p'_{im}(p'_{re}) = \frac{k\pi}{2}(p'_{re} - \pi)^2$ where $k \in \mathbb{C}$ [55]:

$$\lim_{\substack{p'_{re} \rightarrow \pi \\ p'_{im} = p'_{im}(p'_{re})}} \Im(E_1) = 2z_f k.$$

Since the limit value depends on the direction that is fixed with k , singular point $(\pi, 0)$ is an essential singularity of $\Im(E_1)$ [56]. This can be shown for all elements of S_{odd}^p and S_{odd}^q for $\Im(E_1)$ and $\Im(E_2)$, respectively. According to the Picard theorem from the complex analysis, the functions will take all possible values infinitely often on any open set containing the singular point [56].

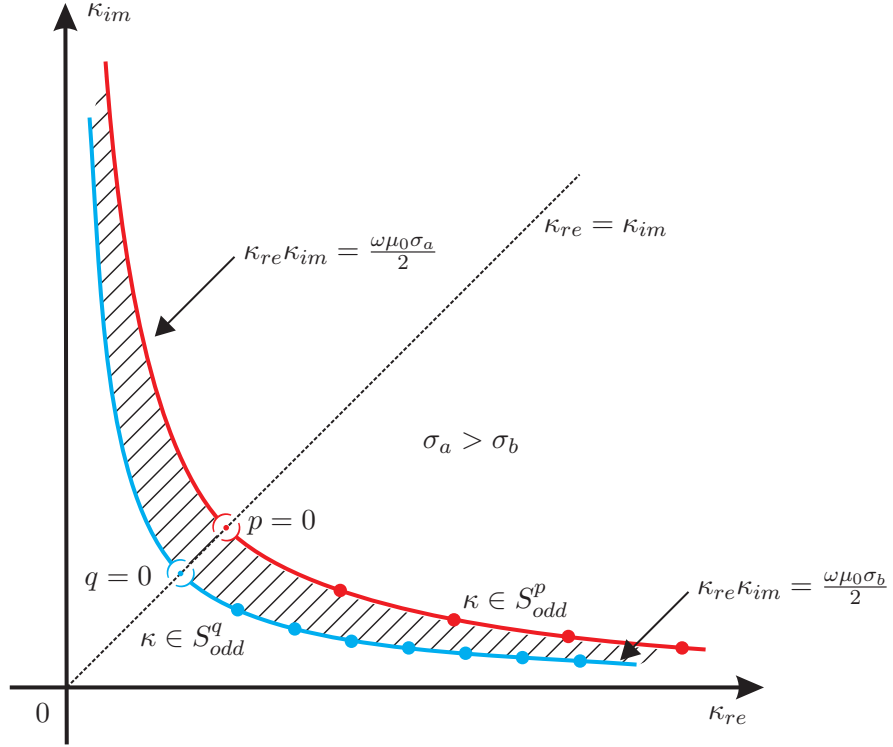


Figure 2.3: Two depicted hyperbolas bound all zeros of the odd-case eigenvalue equation for case $\sigma_a > \sigma_b$. Singular points $\kappa \in S_{odd}^p \cup S_{odd}^q$ lie on the hyperbolas.

Practically, this means that there is a trajectory passing through a singular point of $\Im(E_1)$ for which $\Im(E_1) = -\Im(E_2)$ and vice versa for singularities of $\Im(E_2)$. Finally, we can conclude that curve $\Im(E_1 + E_2) = 0$ certainly passes through any, arbitrarily small region around any $\kappa \in S_{odd}^p \cup S_{odd}^q$.

Real parts of E_1 and E_2 :

$$\Re(E_1) = 2z_f \frac{p'_{re} \sin p'_{re} + p'_{im} \sinh p'_{im}}{(p'^2_{re} + p'^2_{im})(\cos p'_{re} + \cosh p'_{im})},$$

and:

$$\Re(E_2) = 2(H - z_f) \frac{q'_{re} \sin q'_{re} + q'_{im} \sinh q'_{im}}{(q'^2_{re} + q'^2_{im})(\cos q'_{re} + \cosh q'_{im})},$$

have the same singular points as $\Im(E_1)$ and $\Im(E_2)$, respectively. These points are essential singularities of $\Re(E_1)$ and $\Re(E_2)$, too. For example, the limit of $\Re(E_1)$ as p approaches to singular point $p' = (\pi, 0)$ with trajectory $p'_{im}(p'_{re}) = \left(\frac{2}{k\pi}\right)^{1/2} (p'_{re} - \pi)^{1/2}$ where $k \in \mathbb{C}$ is [55]:

$$\lim_{\substack{p'_{re} \rightarrow \pi \\ p'_{im} = p'_{im}(p'_{re})}} \Re(E_1) = 2z_f \left(-k + \frac{2}{\pi^2} \right).$$

2.3 Solution to the eigenvalue equations

Since the limit value depends on the path, the singular point is an essential singularity. Following the arguments made for $\Im(E_1 + E_2) = 0$, we can conclude that curve $\Re(E_1 + E_2) = 0$ also approaches arbitrarily close to any point $\kappa \in S_{odd}^p \cup S_{odd}^q$.

Further numerical analysis of curves $\Re(E_1 + E_2) = 0$ and $\Im(E_1 + E_2) = 0$ corroborates following statements:

1. Two consecutive singular points are said to be spaced if relation $\Im(E_1 + E_2) = 0$ between the singular points is an implicit function $\kappa_{im}(\kappa_{re})$, i.e. for each κ_{re} there is only one κ_{im} that satisfies $\Im(E_1 + E_2) = 0$.
2. There is only one crossing of $\Re(E_1 + E_2) = 0$ and $\Im(E_1 + E_2) = 0$ between two singular points (not necessarily spaced), i.e. we can pair each singular point with a corresponding zero.

Fig. 2.4 depicts an illustration of these statements for $H = 5$ m, $z_f = 2$ m, $f = 60$ Hz, $\sigma_a = 10$ S/m and $\sigma_b = 1$ S/m. It shows first three zeros of g_{odd}^* that are enclosed between $\kappa_{re}\kappa_{im} = \frac{\omega\mu_0\sigma_a}{2}$ and $\kappa_{re}\kappa_{im} = \frac{\omega\mu_0\sigma_b}{2}$. Essential singularities of $\Im(E_1 + E_2) = 0$ and $\Re(E_1 + E_2) = 0$ are located at the hyperbolas. Fig. 2.5 shows the similar example with exception of $H = 12$ m. For this case, two consecutive singularities have the same real parts, i.e. they are not spaced. As a result, for a given κ_{re} there are more than one κ_{im} that satisfies $\Im(E_1 + E_2) = 0$. However, there is still only one zero between two consecutive singularities.

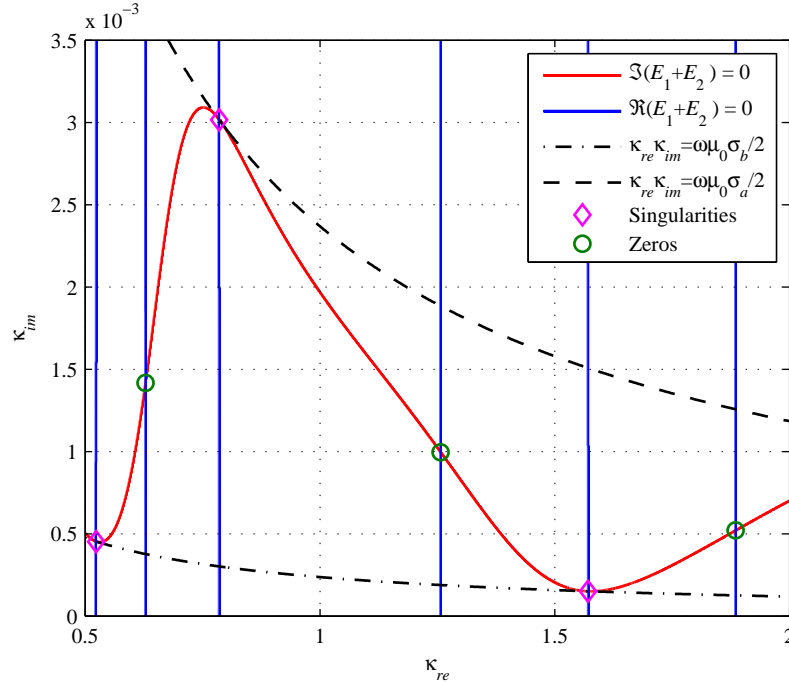


Figure 2.4: Zero contour lines of real and imaginary parts of g_{odd}^* and its singularities and zeros bounded with two hyperbolas.

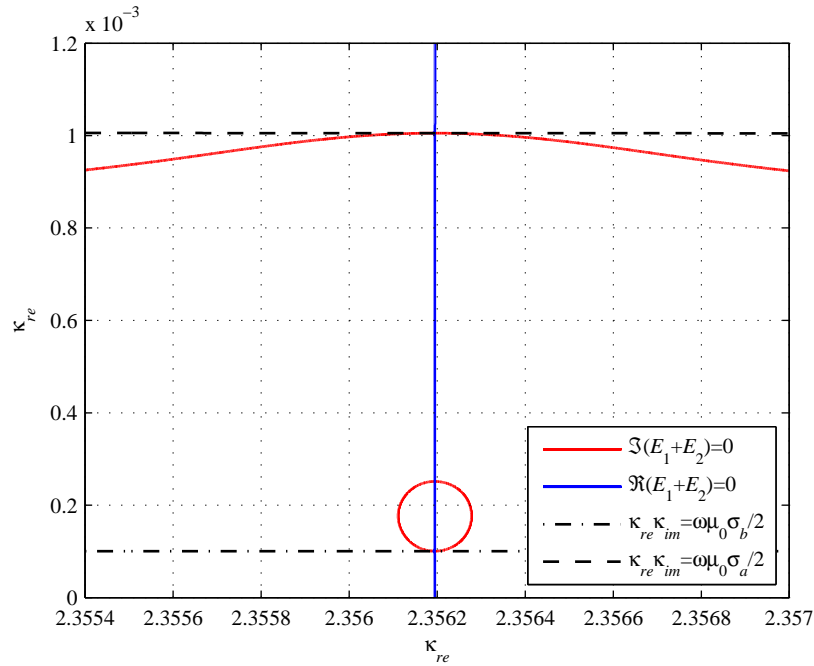


Figure 2.5: Zero contour lines of real and imaginary parts of g_{odd}^* for the case of two singularities having the same real parts.

Singular points $\kappa_p \in S_{odd}^p$, in contrast to being essential singularities of $\Im(E_1)$ and $\Re(E_1)$, are poles of function $E_1(\kappa)$. This can be confirmed by observing that [56]:

$$\lim_{\substack{\kappa \rightarrow \kappa_p \\ \kappa_p \in S_{odd}^p}} |E_1(\kappa)| = \infty.$$

The poles are of order 1 since function $(\kappa - \kappa_p) E_1(\kappa)$ has a removable singularity at κ_p [57]. By complete analogy, singularities $\kappa_q \in S_{odd}^q$ are poles of order 1 for function $E_2(\kappa)$.

2.3.2 Even-case eigenvalue equation

Since $p \neq 0$ and $q \neq 0$, g_{evn} has the same zeros and poles as:

$$g_{evn}^*(\kappa) = \frac{\cot(pz_f)}{p} - \frac{\tan(q(H - z_f))}{q}.$$

If $p' = 2z_f p$, $q' = 2(H - z_f) q$ and:

$$E_3 = \frac{\cot(pz_f)}{p},$$

we can write $g_{evn}^* = E_3 - E_2$, where E_2 is given by (2.61).

2.3 Solution to the eigenvalue equations

We will proceed with the analysis of E_3 only, since we have already analysed function E_2 in the previous section. Real and imaginary parts of E_3 are:

$$\begin{aligned}\Re(E_3) &= 2z_f \frac{-p'_{re} \sin p'_{im} + p'_{im} \sinh p'_{im}}{(p'^2_{re} + p'^2_{im})(\cos p'_{re} - \cosh p'_{im})}, \\ \Im(E_3) &= 2z_f \frac{p'_{re} \sinh p'_{im} + p'_{im} \sin p'_{re}}{(p'^2_{re} + p'^2_{im})(\cos p'_{re} - \cosh p'_{im})}.\end{aligned}$$

For the denominator of $\Re(E_3)$ and $\Im(E_3)$ the following holds:

$$(\cos p'_{re} - \cosh p'_{im}) \begin{cases} = 0 & \forall p | \kappa \in S^p_{evn}, \\ < 0 & \text{otherwise,} \end{cases}$$

where set S^p_{evn} contains singular points of $\Re(E_3)$ and $\Im(E_3)$ in κ plane:

$$S^p_{evn} = \{\kappa | (p'_{re} = 2n\pi) \wedge (p'_{im} = 0), \forall n \in \mathbb{N}\}.$$

Sign of the numerator of $\Im(E_3)$ in the p right half-plane is:

$$p'_{re} \sinh p'_{im} + p'_{im} \sin p'_{re} \begin{cases} > 0 & \text{if } p'_{im} > 0, \\ = 0 & \text{if } (p'_{im} = 0) \vee (p'_{re} = 0), \\ < 0 & \text{if } p'_{im} < 0. \end{cases}$$

Function $\Im(E_3)$ is:

$$\Im(E_3) \begin{cases} \text{sing.} & \text{for } \kappa \in S^p_{evn}, \\ 0 & \text{if } (\kappa \in S^p_{evn}) \wedge (\kappa_{re} \kappa_{im} = \frac{\omega \mu_0 \sigma_a}{2}), \\ < 0 & \text{if } \kappa_{re} \kappa_{im} > \frac{\omega \mu_0 \sigma_a}{2}, \\ > 0 & \text{if } \kappa_{re} \kappa_{im} < \frac{\omega \mu_0 \sigma_a}{2}. \end{cases}$$

Similarly to the odd parity case, hyperbolas $\kappa_{re} \kappa_{im} = \frac{\omega \mu_0 \sigma_a}{2}$ and $\kappa_{re} \kappa_{im} = \frac{\omega \mu_0 \sigma_b}{2}$ bound the area in which $\Im(E_3)$ and $-\Im(E_3)$ have different signs. Hence, the zeros of the even-case equation are confined in the same region as for the odd parity case. We will skip analysis of the singular points because it is completely analogous to one in the previous section. We will only state that singular points $\kappa_p \in S^p_{evn}$ are essential singularities of $\Re(E_3)$ and $\Im(E_3)$, and poles of order 1 for $E_3(\kappa)$.

2.3.3 Root-finding algorithm

In this section, we will describe the main features of the proposed algorithm for isolation and finding zeros (or roots) of eigenvalue functions $g_{odd}(\kappa)$ and $g_{evn}(\kappa)$. This task is equivalent to the task of finding the zeros of $g^*_{odd}(\kappa)$ and $g^*_{evn}(\kappa)$ if $p \neq 0$ and $q \neq 0$. We will assume that we have already determined sets S^p_{odd} , S^q_{odd} , S^p_{evn} , and S^q_{evn} based on the analyses from the previous sections.

Also, we will assume that we know how many zeros (i.e. eigenvalues) we must find to ensure convergence of the series in (2.9)–(2.14) and (2.19)–(2.24).

There are two groups of root-finding algorithms for this kind of eigenvalue equations. The first one is a modification of the Newton-Raphson iteration technique [58, 59]. The first step of the method as proposed in [59] and applied to model geometry in Fig. 2.1 would be to find two initial sets of zeros for the cases of $z_f = 0$ and $z_f = H$. In the subsequent steps, the boundary is increased in the first case and decreased in the second case by a small step Δz . Two new sets of zeros are calculated using the zeros from the previous steps as the initial values for the Newton-Raphson solver. The procedure is repeated until the boundaries in both cases reach the target value of z_f . The final set of zeros is a union of the two sets from the last step. The authors in [54] propose the `FindRoot` function in Mathematica for a core iteration solver [55].

However, it is a difficult task to attempt to obtain all the zeros of an eigenvalue equation within a given finite region using the iteration methods proposed in [58] and [59]. The biggest concern is that there is no evidence why the iterations should end in different zeros if they are started at different initial guesses taken from the initial set of zeros. In implementing the iteration algorithm, we observed that it was difficult to stop the procedures to converge to the same zero. Also, for a significant number of zeros, the basic iteration algorithm results in a nonconvergent cycle, thus raising the need for more advanced iteration algorithms, e.g. backtracking modifications and Brent's method. The function `FindRoot` can handle such situations, but being the part of a closed commercial package, it is hard to use it in a stand-alone, proprietary codes or libraries.

The second group of algorithms, based on the explicit use of the Cauchy's theorem (zero-counting), is much more reliable, although potentially somewhat slower [56]. Such algorithms can be found in [60–62]. The argument principle, based on the Cauchy's theorem, states the following: If a function f is a meromorphic in a simple connected region G with poles $\kappa_{p,1}, \dots, \kappa_{p,m}$ and zeros $\kappa_{z,1}, \dots, \kappa_{z,n}$ closed inside some positively oriented Jordan curve γ in G and counted according to their order (multiplicity), then:

$$\frac{1}{2\pi j} \oint_{\gamma} \frac{f'(\kappa)}{f(\kappa)} d\kappa = \sum_{k=1}^n n(\gamma, \kappa_{z,k}) - \sum_{k=1}^m n(\gamma, \kappa_{p,k}), \quad (2.64)$$

where $n(\gamma, \kappa_{z,k})$ and $n(\gamma, \kappa_{p,k})$ are the order of zero $\kappa_{z,k}$ and the multiplicity of pole $\kappa_{p,k}$ within γ , respectively. Our knowledge of locations of the poles and bounded regions where zeros can exist for both eigenvalue equations enables us to count and isolate the zeros in the observed region using the argument principle as a criteria. The integral in (2.64) can be approximated with:

$$\frac{1}{2\pi j} \oint_{\gamma} \frac{f'(\kappa)}{f(\kappa)} d\kappa \approx \frac{1}{2\pi j} \sum_{l=1}^L \ln \frac{f(\kappa_l)}{f(\kappa_{l-1})}, \quad (2.65)$$

where $\kappa_0, \dots, \kappa_L$ are the points on γ sorted in the positive direction (counter-clockwise).

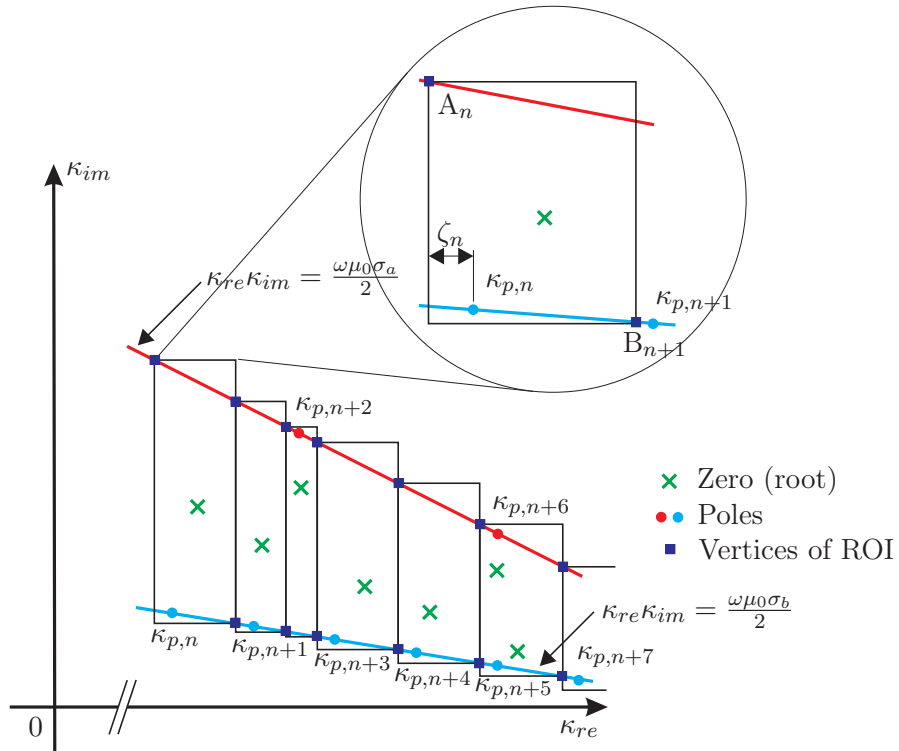


Figure 2.6: Definition of regions of interest (ROI), see Algorithm 1.

Fig. 2.6 depicts the main idea of the root-finding algorithm that we propose here. Since we know that the zeros are located between the two hyperbolas, we will define regions of interest (ROI) in form of rectangles. For pole $\kappa_{p,n}$ two defining vertices of the corresponding ROI are given with:

$$A_n \dots \left(\Re(\kappa_{p,n}) - \zeta_n, \frac{\omega \mu_0 \sigma_a}{2 (\Re(\kappa_{p,n}) - \zeta_n)} \right),$$

$$B_{n+1} \dots \left(\Re(\kappa_{p,n+1}) - \zeta_{n+1}, \frac{\omega \mu_0 \sigma_b}{2 (\Re(\kappa_{p,n+1}) - \zeta_{n+1})} \right),$$

where ζ_n and ζ_{n+1} are real positive numbers much smaller than the distance between the neighboring poles. Defined in such a way, the ROI has exactly one pole. If two consecutive poles have the same real parts, pole κ_{n+1} is skipped, point B is determined using pole κ_{n+2} and, as a consequence, the ROI has two poles and two zeros instead of one. Using the iterative procedure of successive division of the ROI and criteria based on (2.65) all of the zeros in ROI can be found. Thus, the problem of finding unknown number of the zeros in a single vast region is separated into a number (defined by the model convergence) of much simpler problems of finding the zeros in a smaller finite region with known poles. More details on the implementation of the root-finding algorithm are given in a pseudocode form in Algorithm 1.

Algorithm 1 Locating the zeros using the argument principle

Require: $H, z_f, \omega, \sigma_a, \sigma_b, \kappa_{re,max}$, parity: odd or even**Ensure:** Set S_{zero} of all zeros κ_z for which $\Re(\kappa_z) \leq \kappa_{re,max}$

```
1: if odd case then
2:   Calculate  $S_{odd}^p$  and  $S_{odd}^q$ 
3:    $S \leftarrow S_{odd}^p \cup S_{odd}^q$ 
4: else
5:   Calculate  $S_{evn}^p$  and  $S_{evn}^q$ 
6:    $S \leftarrow S_{evn}^p \cup S_{evn}^q$ 
7: end if
8: Sort the elements of  $S$  by their real part in ascending order
9:  $N \leftarrow$  number of elements in  $S = \{\kappa_{p,1}, \dots, \kappa_{p,N}\}$ 
10:  $m \leftarrow 0$ 
11: for  $n = 1$  to  $N - 1$  do
12:    $m \leftarrow m + 1$  // increase the ROI counter
13:   Calculate vertex  $A_n$  // See Fig. 2.6
14:   if  $\Re(\kappa_{p,n}) < \Re(\kappa_{p,n+1})$  then
15:     Calculate vertex  $B_{n+1}$ 
16:     Define ROI( $m$ ) as a rectangle between  $A_n$  and  $B_{n+1}$ 
17:     ROI( $m$ ).poles  $\leftarrow 1$  // One pole!
18:   end if
19:   if  $\Re(\kappa_{p,n}) = \Re(\kappa_{p,n+1})$  then
20:     Calculate vertex  $B_{n+2}$  // e.g.  $\kappa_{p,n+5}$  and  $\kappa_{p,n+6}$  in Fig. 2.6
21:     Define ROI( $m$ ) as a rectangle between  $A_n$  and  $B_{n+2}$ 
22:     ROI( $m$ ).poles  $\leftarrow 2$  // Two poles!
23:      $n \leftarrow n + 1$  // skip the next pole in FOR loop
24:   end if
25: end for
26:  $M \leftarrow$  total number of ROI
27:  $S_{zero} = \emptyset$ 
28: for  $m = 1$  to  $M$  do
29:    $a \leftarrow$  result of (2.65)
30:   ROI( $m$ ).zeros  $\leftarrow a +$  ROI( $m$ ).poles // Number of zeros in ROI
31:   repeat
32:     Divide ROI( $m$ ) into subregions
33:   until Number of subregions with one zero is ROI( $m$ ).zeros
34:   for  $k = 1$  to ROI( $m$ ).zeros do
35:     repeat
36:       Successive division of the subregion corresponding to  $k$ -th
       zero of ROI( $m$ ) using (2.65) as criteria
37:     until convergence criteria is met
38:      $S_{zero} = S_{zero} \cup \{k\text{-th zero of ROI}(m)\}$ 
39:   end for
40: end for
```

2.4 Numerical implementation

As we will see in the next chapter, we require knowledge of the magnetic field in the interior of the tube only. Since we expect that distances from the excitation coil required for successful measurement of the casing properties and formation conductivity are several times larger than the casing diameter, we can assume that z -component of the magnetic field at such large distances does not vary significantly with r [48, 63]. Hence, we can concentrate here on obtaining the components of vector \mathbf{C}_1 only.

The matrices given in (2.53) are diagonal except matrices \mathbf{M}_{11} and \mathbf{M}_{21} . This means that equations (2.47)–(2.52) can be written independently for each component. We shall denote with m_{xy} an element on the main diagonal of the corresponding matrix \mathbf{M}_{xy} , where we left out index i of the element's row. Similarly, we will shorten $C_{1,i}$ into C_1 (a component of \mathbf{C}_1).

We need to normalise the coefficients and unknowns of the linear system because their orders of magnitude can differ for more than 40 times, if left as in (2.53). We will denote normalised coefficients and unknowns with the asterisk (*). The normalised components of the unknown vectors are:

$$\begin{aligned}
 C_1 &= \frac{C_1^*}{m_{81}}, \\
 C_2 &= \frac{C_2^*}{m_{61}}, & D_2 &= \frac{D_2^*}{m_{62}}, \\
 C_3 &= \frac{C_3^*}{m_{41}}, & D_3 &= \frac{D_3^*}{m_{42}}, \\
 C_4 &= \frac{C_4^*}{m_{43}}, & D_4 &= \frac{D_4^*}{m_{44}}, \\
 D_5 &= \frac{D_5^*}{\kappa K_0(\kappa r_3)}.
 \end{aligned} \tag{2.66}$$

From that and (2.45)–(2.52) we yield the normalised coefficients:

$$\begin{aligned}
 m_{12}^* &= \frac{m_{12}}{m_{43}}, & m_{13}^* &= \frac{m_{13}}{m_{44}}, \\
 m_{22}^* &= \frac{m_{22}}{m_{43}}, & m_{23}^* &= \frac{m_{23}}{m_{44}}, \\
 m_{63}^* &= \frac{m_{63}}{m_{41}}, & m_{64}^* &= \frac{m_{64}}{m_{42}}, \\
 m_{82}^* &= \frac{m_{82}}{m_{61}}, & m_{83}^* &= \frac{m_{83}}{m_{62}}, \\
 m_{71}^* &= \frac{m_{71}}{m_{81}}, & m_{72}^* &= \frac{m_{72}}{m_{61}}, & m_{73}^* &= \frac{m_{73}}{m_{62}}, \\
 m_{41}^* &= m_{42}^* = m_{43}^* = m_{44}^* = m_{61}^* = m_{62}^* = m_{81}^* = 1, \\
 m_{31}^* &= \frac{m_{31}}{m_{41}}, & m_{32}^* &= \frac{m_{32}}{m_{42}}, & m_{33}^* &= \frac{m_{33}}{m_{43}}, & m_{34}^* &= \frac{m_{34}}{m_{44}}, \\
 m_{51}^* &= \frac{m_{51}}{m_{61}}, & m_{52}^* &= \frac{m_{52}}{m_{62}}, & m_{53}^* &= \frac{m_{53}}{m_{41}}, & m_{54}^* &= \frac{m_{54}}{m_{42}}.
 \end{aligned} \tag{2.67}$$

Normalisation of the elements of \mathbf{M}_{11} and \mathbf{M}_{21} is somewhat more difficult because of the full matrix \mathbf{P} . We have for normalised matrices \mathbf{M}_{11}^* and \mathbf{M}_{21}^* :

$$\begin{aligned}\mathbf{M}_{11}^* &= \mathbf{P}\mathbf{K}_1(\kappa r_3) [\kappa^D \mathbf{K}_0(\kappa r_3)]^{-1}, \\ \mathbf{M}_{21}^* &= -\mathbf{P},\end{aligned}$$

where the inverse of $\kappa^D \mathbf{K}_0(\kappa r_3)$ is easy to obtain since both factors are diagonal matrices.

We will first find the relation between C_1 , C_4 and D_4 using equations (2.47)–(2.52) and then eliminate D_5 combining (2.45) and (2.46). If we introduce:

$$\begin{aligned}\mathbf{V}_1 &= \begin{bmatrix} m_{72}^* & m_{73}^* \\ m_{82}^* & m_{83}^* \end{bmatrix}, & \mathbf{V}_2^{-1} &= \frac{1}{m_{51}^* - m_{52}^*} \begin{bmatrix} 1 & -m_{52}^* \\ -1 & m_{51}^* \end{bmatrix}, \\ \mathbf{V}_3 &= \begin{bmatrix} m_{53}^* & m_{54}^* \\ m_{63}^* & m_{64}^* \end{bmatrix}, & \mathbf{V}_4^{-1} &= \frac{1}{m_{31}^* - m_{32}^*} \begin{bmatrix} 1 & -m_{32}^* \\ -1 & m_{31}^* \end{bmatrix}, \\ & & \mathbf{V}_5 &= \begin{bmatrix} m_{33}^* & m_{34}^* \\ 1 & 1 \end{bmatrix},\end{aligned}$$

$$\mathbf{V} = \begin{bmatrix} V_{11} & V_{12} \\ V_{21} & V_{22} \end{bmatrix} = \mathbf{V}_1 \mathbf{V}_2^{-1} \mathbf{V}_3 \mathbf{V}_4^{-1} \mathbf{V}_5,$$

then $\forall i = 1, \dots, N$:

$$\begin{bmatrix} m_{71}^* \\ 1 \end{bmatrix} C_1^* = \mathbf{V} \begin{bmatrix} C_4^* \\ D_4^* \end{bmatrix} + \begin{bmatrix} 0 \\ \frac{2\mu_0 J}{H} \operatorname{exc}(\alpha z_0) \end{bmatrix}. \quad (2.68)$$

Calculation of \mathbf{V} and $\det \mathbf{V}$ is crucial for overall stability of the numerical implementation. In order to avoid loss of significance in floating-point arithmetics, we need to limit dynamics of operands involving Bessel's functions during calculation of \mathbf{V} by carefully rearranging the expressions. The following expressions have proved to be stable if one first calculates ratios of the Bessel's functions and than their products:

$$\begin{aligned}\mathbf{V}_1 \mathbf{V}_2^{-1} &= \alpha r_1 I_0(\alpha r_1) K_1(\alpha r_0) \cdot \\ &\cdot \begin{bmatrix} \frac{I_1(\alpha r_0) K_0(\alpha r_1)}{I_0(\alpha r_1) K_1(\alpha r_0)} + 1 & \frac{1}{\alpha \mu_r} \left(\frac{I_1(\alpha r_0) K_1(\alpha r_1)}{I_0(\alpha r_1) K_1(\alpha r_0)} - \frac{I_1(\alpha r_1)}{I_0(\alpha r_1)} \right) \\ \alpha \left(\frac{I_0(\alpha r_0) K_0(\alpha r_1)}{I_0(\alpha r_1) K_1(\alpha r_0)} - \frac{K_0(\alpha r_0)}{K_1(\alpha r_0)} \right) & \frac{1}{\mu_r} \left(\frac{I_0(\alpha r_0) K_1(\alpha r_1)}{I_0(\alpha r_1) K_1(\alpha r_0)} + \frac{I_1(\alpha r_1) K_0(\alpha r_0)}{I_0(\alpha r_1) K_1(\alpha r_0)} \right) \end{bmatrix},\end{aligned}$$

$$\begin{aligned}\mathbf{V}_3 \mathbf{V}_4^{-1} &= \beta r_2 I_0(\beta r_2) K_1(\beta r_1) \cdot \\ &\cdot \begin{bmatrix} \frac{I_1(\beta r_1) K_0(\beta r_2)}{I_0(\beta r_2) K_1(\beta r_1)} + 1 & \frac{1}{\beta} \left(\frac{I_1(\beta r_1) K_1(\beta r_2)}{I_0(\beta r_2) K_1(\beta r_1)} - \frac{I_1(\beta r_2)}{I_0(\beta r_2)} \right) \\ \beta \left(\frac{I_0(\beta r_1) K_0(\beta r_2)}{I_0(\beta r_2) K_1(\beta r_1)} - \frac{K_0(\beta r_1)}{K_1(\beta r_1)} \right) & \frac{I_0(\beta r_1) K_1(\beta r_2)}{I_0(\beta r_2) K_1(\beta r_1)} + \frac{I_1(\beta r_2) K_0(\beta r_1)}{I_0(\beta r_2) K_1(\beta r_1)} \end{bmatrix}.\end{aligned}$$

2.4 Numerical implementation

Matrix \mathbf{V} is then calculated as $\mathbf{V} = (\mathbf{V}_1 \mathbf{V}_2^{-1}) (\mathbf{V}_3 \mathbf{V}_4^{-1}) \mathbf{V}_5$. Using the multiplicativity of the determinants, it can be shown that:

$$\det \mathbf{V} = \frac{1}{\mu_r^2 \gamma^2 r_0 I_0(\gamma r_2) K_0(\gamma r_2)}.$$

Equations (2.45) and (2.46) yield for j -th rows $\mathbf{m}_{11,j}^*$ and $\mathbf{m}_{21,j}^*$ of matrices \mathbf{M}_{11}^* and \mathbf{M}_{21}^* , respectively:

$$\mathbf{m}_{11,j}^* \mathbf{D}_5^* = [m_{12}^* \quad m_{13}^*] \begin{bmatrix} C_4^* \\ D_4^* \end{bmatrix}, \quad (2.69)$$

$$\mathbf{m}_{21,j}^* \mathbf{D}_5^* = [m_{22}^* \quad m_{23}^*] \begin{bmatrix} C_4^* \\ D_4^* \end{bmatrix}. \quad (2.70)$$

Let us introduce:

$$l_1 = (m_{12}^* m_{71}^* V_{22} - m_{12}^* V_{12} - m_{13}^* m_{71}^* V_{21} + m_{13}^* V_{11}), \quad (2.71)$$

$$l_2 = (m_{22}^* m_{71}^* V_{22} - m_{22}^* V_{12} - m_{23}^* m_{71}^* V_{21} + m_{23}^* V_{11}), \quad (2.72)$$

$$l_3 = \frac{2\mu_0 J}{H} (m_{22}^* V_{12} - m_{23}^* V_{11}) \operatorname{exc}(\alpha z_0). \quad (2.73)$$

Combining equations (2.68)–(2.73) we obtain:

$$\mathbf{S} \mathbf{D}_5^* = \mathbf{x}, \quad (2.74)$$

$$C_1^* = \frac{\det \mathbf{V}}{l_2} \mathbf{m}_{21,j}^* \mathbf{D}_5^* - \frac{l_3}{l_2}, \quad (2.75)$$

where j -th row vector \mathbf{s}_j of matrix \mathbf{S} and the corresponding element x of vector \mathbf{x} are:

$$\mathbf{s}_j = \mathbf{m}_{11,j}^* - \frac{l_1}{l_2} \mathbf{m}_{21,j}^*, \quad (2.76)$$

$$x = \frac{\mu_0 J H}{2} \frac{r_0 m_{71}^*}{r_3 l_2} \det \mathbf{V} \operatorname{exc}(\alpha z_0). \quad (2.77)$$

It is worth to repeat that matrix \mathbf{V} , l_1 , l_2 and l_3 must be calculated for each of the N equations of system 2.74.

The component of the magnetic induction \mathbf{B} in z direction is given by:

$$B_{z,odd}(r, z) = \sum_{i=1}^N \sin(\alpha_i^{odd} z) I_0(\alpha_i^{odd} r) \frac{C_{1,i}^{*odd}}{I_0(\alpha_i^{odd} r_0)},$$

$$B_{z,even}(r, z) = \sum_{i=1}^N \cos(\alpha_i^{even} z) I_0(\alpha_i^{even} r) \frac{C_{1,i}^{*even}}{I_0(\alpha_i^{even} r_0)},$$

$$B(r, z) = \frac{B_{z,odd}(r, z) + B_{z,even}(r, z)}{2}.$$

The magnetic field of the transmitter coil can be represented as a sum of the magnetic field of the coil in the air and the contribution of the surrounding conductive medium. Starting from (2.51) and (2.52) and after the normalisation we get:

$$\begin{aligned} C_1^* &= C_{1,air}^* + C_{1,mdm}^*, \\ C_{1,air}^* &= \frac{2\mu_0 J}{H} \alpha r_0 I_0(\alpha r_0) K_1(\alpha r_0), \\ C_{1,mdm}^* &= \frac{I_0(\alpha r_0)}{\mu_r I_0(\alpha r_1)} C_2^*, \end{aligned}$$

where $C_{1,air}^*$ would be the elements of the coefficient vector \mathbf{C}_1^* in the case without surrounding medium (only air) and $C_{1,mdm}^*$ is the contribution of the surrounding medium. The elements of \mathbf{C}_2^* can be calculated using following expressions:

$$\begin{aligned} \mathbf{U} &= \begin{bmatrix} U_{11} & U_{12} \\ U_{21} & U_{22} \end{bmatrix} = \mathbf{V}_2^{-1} \mathbf{V}_3 \mathbf{V}_4^{-1} \mathbf{V}_5, \\ \det \mathbf{U} &= \frac{\alpha^2 I_0(\alpha r_1) K_0(\alpha r_1)}{\gamma^2 I_0(\gamma r_2) K_0(\gamma r_2)}, \\ t_1 &= m_{12}^* U_{22} - m_{13}^* U_{21}, \\ t_2 &= m_{22}^* U_{22} - m_{23}^* U_{21}, \\ t_3 &= \frac{2\mu_0 J}{H} \mu_r \alpha r_0 I_1(\alpha r_0) K_0(\alpha r_1) (m_{22}^* U_{12} - m_{23}^* U_{11}) \text{exc}(\alpha z_0), \\ \mathbf{s}'_j &= \mathbf{m}_{11,j}^* - \frac{t_1}{t_2} \mathbf{m}_{21,j}^*, \\ x' &= \frac{\mu_0 H J}{2} \frac{r_0}{\mu_r r_3 t_2} \frac{\alpha I_1(\alpha r_0) K_0(\alpha r_1)}{\gamma^2 I_0(\gamma r_2) K_0(\gamma r_2)} \text{exc}(\alpha z_0), \\ \mathbf{S}' \mathbf{D}_5^* &= \mathbf{x}', \\ C_2^* &= \frac{\det \mathbf{U}}{t_2} \mathbf{m}_{21,j}^* \mathbf{D}_5^* - \frac{t_3}{t_2}. \end{aligned}$$

The elements of \mathbf{S} are complex numbers in double precision and since N can easily grow to several thousands, one must use iterative procedures for obtaining the solution to the linear system (2.74). Minimum residual methods and biconjugate gradients methods as implemented in Matlab provided reliable solutions [64]. The usage of the expressions given above is summarised in a pseudocode form in Algorithm 2.

2.5 Homogenous surrounding formation

The case of homogeneously conductive surrounding formation will be of interest in the sensitivity analysis for evaluation of the casing effect, minimal measurable contrast in conductivities of horizontal layers in the formation and

Algorithm 2 Numerical implementation of the TREE model - vector \mathbf{C}_1^*

Require: $H, z_f, r_0, r_1, r_2, r_3, \omega, \sigma_a, \sigma_b, N, S_{zero}^{odd}, S_{zero}^{evn}$

Ensure: N elements of vectors \mathbf{C}_1^* for the odd and even parity cases

- 1: **for** odd-parity and even-parity case **do**
 - 2: Calculate $N \times N$ matrix \mathbf{P} — use (2.34) for odd-parity case and (2.36) for even-parity case.
 - 3: Calculate \mathbf{M}_{xy} using (2.53)
 - 4: Normalise \mathbf{M}_{xy} and obtain \mathbf{M}_{xy}^*
 - 5: **for** $i = 1$ to N **do**
 - 6: Calculate \mathbf{V} ,
 - 7: Calculate l_1, l_2 and l_3 using (2.71)–(2.73)
 - 8: **end for**
 - 9: Form \mathbf{S} using (2.76)
 - 10: Form \mathbf{x} using (2.77)
 - 11: Numerically solve the system (2.74) for \mathbf{D}_5^*
 - 12: Calculate N elements of \mathbf{C}_1^* using (2.75)
 - 13: **end for**
-

maximum radial depth of formation conductivity measurement. Because of the formation homogeneity, there is no need to solve the eigenvalue equations and all matrices from the previous sections in this chapter are diagonal. As a result, this case is a much lighter computational burden than the case of two-layered formation.

We will take that layer B in Fig. 2.1 has the same conductivity as layer A, i.e. $\sigma_b = \sigma_a$, what is equivalent to letting $z_f = H$. Although only even part of the solution would suffice to completely describe the magnetic potential in this case, we shall calculate both even and odd case in order to be able to distinguish between different positions of the transmitter coil with respect to the boundaries $z = \pm H$. Also, this opens the possibility of comparison of coefficients C_1^{odd} and C_1^{evn} between homogenous and two-layered formation.

Eigenvalues α_i remain the same: $\alpha_i = \frac{i\pi}{H}$ for the odd parity solution and $\alpha_i = \frac{(2i-1)\pi}{2H}$ for the even parity solution. This difference in the eigenvalues is the only difference between the odd and even parity case. The rest of the equations is the same for both cases. Since $\sigma_b = \sigma_a$, we have $p_i = q_i = a_i$ and thus:

$$\begin{aligned}\beta_i &= \sqrt{\alpha_i^2 + j\omega\mu_0\mu_r\sigma_t}, \\ \gamma_i &= \sqrt{\alpha_i^2 + j\omega\mu_0\sigma_l}, \\ \kappa_i &= \sqrt{\alpha_i^2 + j\omega\mu_0\sigma_a}.\end{aligned}$$

In the homogenous case, matrix \mathbf{P} is identity matrix of size N and we are allowed to reshape diagonals of matrices \mathbf{M}_{xy} given in (2.53) into corresponding column vectors \mathbf{m}_{xy} . Normalisation relations (2.66) and (2.67) as well as

definitions of \mathbf{V} , l_1 , l_2 , l_3 and \mathbf{x} from section 2.4 are the same for the case of homogeneous formation. Matrix \mathbf{S} in the two-layered case is now a column vector \mathbf{s} whose i -th element s (we omitted index i as in 2.4) is:

$$s = m_{11}^* - \frac{l_1}{l_2} m_{21}^*.$$

Instead of time-consuming iterative methods for solving (2.74), column vector of coefficients \mathbf{D}_5^* is in this case simply obtained using:

$$\mathbf{D}_5^* = \frac{[\mathbf{x}]}{[\mathbf{s}]},$$

where the right side notation is element-wise (Hadamard) division of two vectors or matrices (with the same number of rows and columns). An element C_1^* of vector \mathbf{C}_1^* is:

$$C_1^* = \frac{\det \mathbf{V}}{l_2} m_{21}^* D_5^* - \frac{l_3}{l_2}.$$

2.5.1 Induced current density

According to the Maxwell-Faraday equation:

$$\nabla \times \mathbf{E} = -\frac{\partial \mathbf{B}}{\partial t},$$

electric field \mathbf{E} has only the φ component if the problem geometry is axially symmetric and the magnetic field has only r and z components. The electric field is related to the potentials via:

$$\mathbf{E} = -\nabla\phi - \frac{\partial \mathbf{A}}{\partial t}.$$

The gradient of the scalar potential ϕ vanishes because of the axial symmetry, leaving in the frequency domain:

$$E_\varphi = -j\omega A.$$

Using the Ohm's law $\mathbf{J} = \sigma\mathbf{E}$ we can write for the induced currents in the casing and surrounding medium:

$$J_n = -j\omega\sigma_n A_n, \tag{2.78}$$

where index n denotes a region. The induced currents in the case of the axial symmetry as in Fig. 2.1 have only the φ component.

Chapter 3

Space-frequency analysis

You know my methods. Apply them!

Sherlock Holmes

Sir Arthur Conan Doyle,
“The Sign of Four,” Ch. 6, p. 112, 1890

In this chapter we use the model developed in Chapter 2 to analyse the sensitivity of the outputs, i.e. measured electrical quantities (magnetic field, induced voltage and coil impedance), to the changes of the inputs (tube and formation properties). We are concerned with the questions of how far from the transmitter coil we should position the receiver coils and what excitation frequency we should use in order to selectively maximise sensitivity to a certain tube or formation property; hence the name space-frequency sensitivity analysis. As the final result of the analysis, we will be able to propose proper sensor configurations, i.e. number of the coils, their characteristics and mutual positions. Requirements for the sensor interface (transmitting and data-acquisition circuitry) will be discussed in Chapter 6.

Fig. 3.1 is a good illustration of the fundamental reason why the coil separation and excitation frequency need to be chosen carefully. It shows attenuation of the magnetic field of a transmitter loop caused by the presence of a ferromagnetic casing. In the interesting ranges of the frequency and separation, one can expect attenuation of more than 200 dB and magnetic fields as small as 10 pT.

3.1 Formation conductivity

3.1.1 Phase difference

Following [52], we shall analyse effects of variations in the formation conductivity mainly observing a phase difference between voltages U_R induced in the receiver for two different surrounding media. For brevity, we will use $\Delta\varphi_{hom}(\sigma_1; \sigma_2)$ to denote the phase difference between the induced voltages for

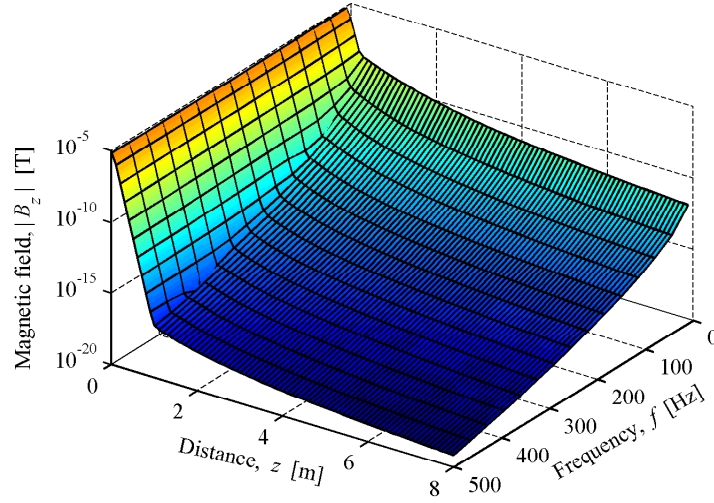


Figure 3.1: Amplitude of the magnetic field B_z as a function of distance z from the transmitter coil and excitation frequency f . For the simulation details see section 3.1.2.

two homogenous media with conductivities σ_1 and σ_2 , i.e.:

$$\Delta\varphi_{hom}(\sigma_1; \sigma_2) = \arg U_R(\sigma_1) - \arg U_R(\sigma_2),$$

where both $\arg U_R(\sigma_1)$ and $\arg U_R(\sigma_2)$ are measured or calculated with the same casing, coil, and excitation properties. If the second medium is air ($\sigma_2 = 0$ S/m), we will write only $\Delta\varphi_{hom}(\sigma_1)$. In the model from Chapter 2, a homogenous medium can be achieved by setting $\sigma_l = \sigma_a = \sigma_b$, Fig. 2.1.

The phase difference for the formation consisting of two layers with conductivities σ_a and σ_b with respect to the case of a homogenous medium with conductivity σ_2 is:

$$\Delta\varphi(\sigma_a, \sigma_b; \sigma_2) = \arg U_R(\sigma_a, \sigma_b) - \arg U_R(\sigma_2).$$

We assume that $\sigma_b = \sigma_2$ if we denote the phase difference as $\Delta\varphi(\sigma_a; \sigma_b)$. In contrast to $\Delta\varphi_{hom}$, $\Delta\varphi$ depends on the sonde position.

For the sake of clarity, we will introduce a shorthand description of the casing and surrounding media.

- $C(r_1, c, \sigma_t, \mu_r)$ describes the casing with the listed properties.
- $M_{hom}(\sigma_{form})$ describes the homogeneously conductive surrounding medium, $\sigma_{form} = \sigma_l = \sigma_a = \sigma_b$.
- $M_{cyl}(r_3, \sigma_l, \sigma_{form})$ describes the cylindrical two-layered formation (layers A and B are assumed equally conductive, $\sigma_{form} = \sigma_a = \sigma_b$), Fig. 2.1.
- $M(2z_f, \sigma_a, \sigma_b)$ describes the two-layered formation with the specified thickness of layer A is $2z_f$, Fig. 3.8.

3.1.2 Homogenous surrounding formation

In order to answer the question of the choice of the excitation frequency and transmitter-receiver distance required for the measurement of rock conductivity, we can without any loss of generality assume homogenous surrounding formation. Phase difference $\Delta\varphi_{hom}$ (1 S/m) and induced voltage U_R (1 S/m) are depicted in Figs 3.2 and 3.3, respectively, as functions of excitation frequency f and distance z from the transmitter coil for $C(100 \text{ mm}, 10 \text{ mm}, 4.6 \text{ MS/m}, 100)$. The phase difference is larger for higher excitation frequencies and larger coil separations, whereas the induced voltage rapidly decreases with the frequency and distance.

Accurate phase measurement, sensitive to changes in the formation conductivity, requires larger phase difference and amplitude of the induced voltage, what is contradictory. Furthermore, increasing coil separation decreases the vertical resolution, section 3.1.3. For the shaded area in Fig. 3.4, obtained combining Figs. 3.2 and 3.3, amplitude of induced voltage U_R is larger than $10 \mu\text{V}$ and absolute value of phase difference $|\Delta\varphi_{hom} (1 \text{ S/m})|$ is larger than 0.1° . This effectively establishes minimum requirements for the sensor interfacing circuitry, which we discuss in greater detail in Chapter 6.

Within the bounds of the analysis presented here, the primary criteria for selecting the excitation frequency and coil separation is one presented as the shaded area of Fig. 3.4. Fig. 3.5 shows the induced voltage and phase difference as functions of the excitation frequency at the distance $z = 5 \text{ m}$. For the excitation frequency of 60 Hz, we can expect the induced voltage around $100 \mu\text{V}$ and phase difference of approximately -0.35° .

Space-frequency dependence of induced voltage U_R for $C(50 \text{ mm}, 10 \text{ mm}, 4.6 \text{ MS/m}, 100)$ is depicted in Fig. 3.6. In comparison to Fig. 3.3, one can immediately notice attenuation of the amplitude for the factor of 10. However, the choice (5 m, 60 Hz) still meets the criteria mentioned above.

Fig. 3.7 shows the dependence of induced voltage U_R on casing inner radius r_1 for the transmitter coils of different radii (K1 being the smallest) and magnetic moments. The design and properties of the transmitter coils are described in Chapter 6. For now, we give the most important properties in Table 3.1. It can be concluded that the measurement of formation conductivity is expected to be easier in casings with larger radius primarily because of a larger achievable magnetic moment of the transmitter.

Table 3.1: Some properties of the transmitter coils, see Chapter 6.

Designation	Mean radius	Number of turns	Magnetic moment (air)
K1	32.5 mm	2344	41 Am ²
K2	47.5 mm	2344	81 Am ²
K3	62.5 mm	2344	122 Am ²
K4	80.0 mm	1875	158 Am ²

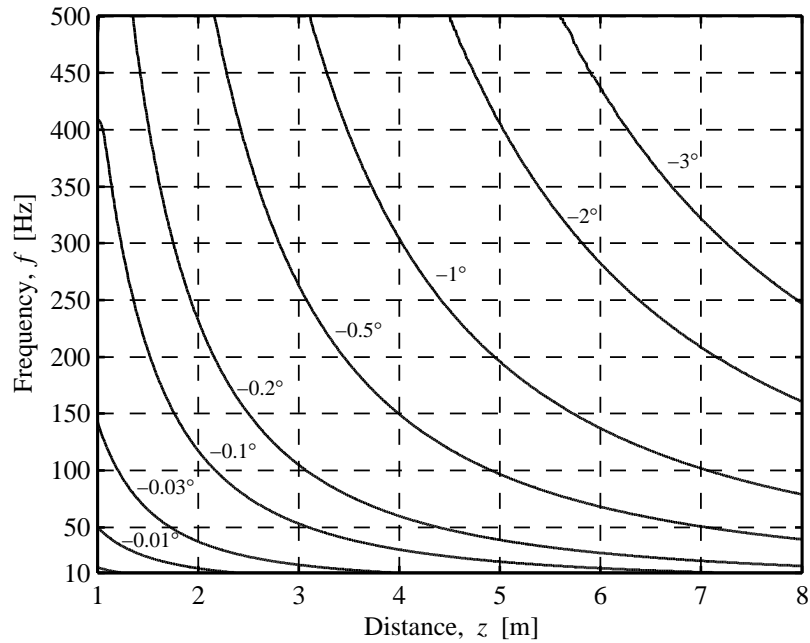


Figure 3.2: Phase difference $\Delta\varphi_{hom}$ (1 S/m) as a function of distance z from the transmitter coil and excitation frequency f .

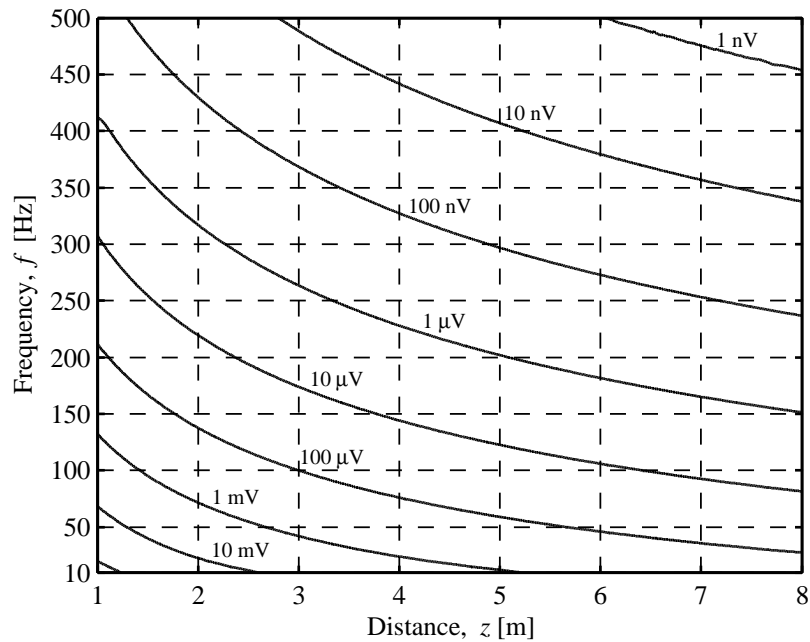


Figure 3.3: Amplitude of the induced voltage U_R as a function of distance z from the transmitter coil and excitation frequency f (casing inner radius 100 mm).

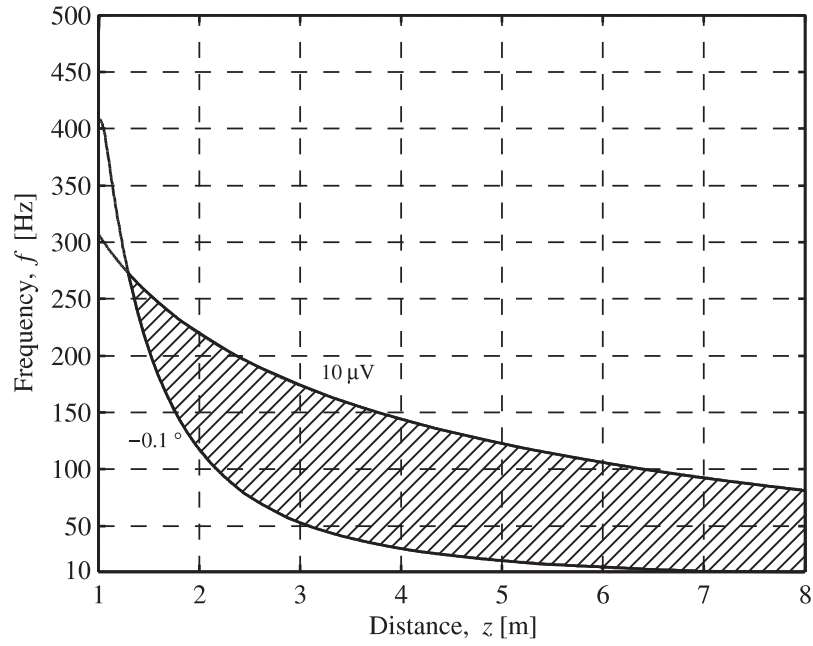


Figure 3.4: Shaded area contains all pairs (z, f) for which $|U_R| \geq 10 \mu\text{V}$ and $|\Delta\varphi_{hom}(1 \text{ S/m})| \geq 0.1^\circ$. See Figs. 3.2 and 3.3.

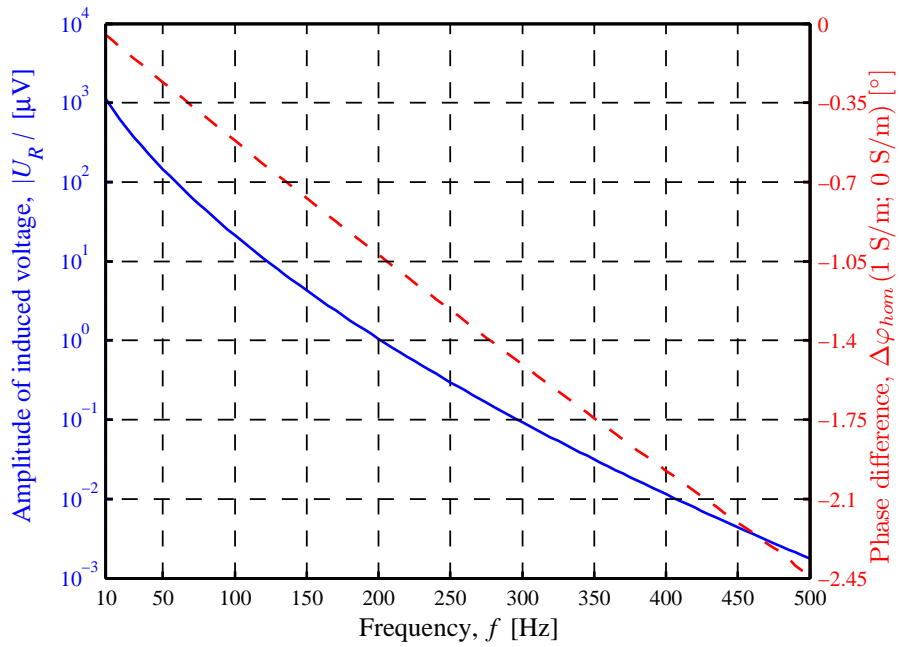


Figure 3.5: Amplitude of the induced voltage U_R (the blue solid line) and phase difference $\Delta\varphi_{hom}(1 \text{ S/m})$ (the red dashed line) as functions of frequency f at $z = 5 \text{ m}$.

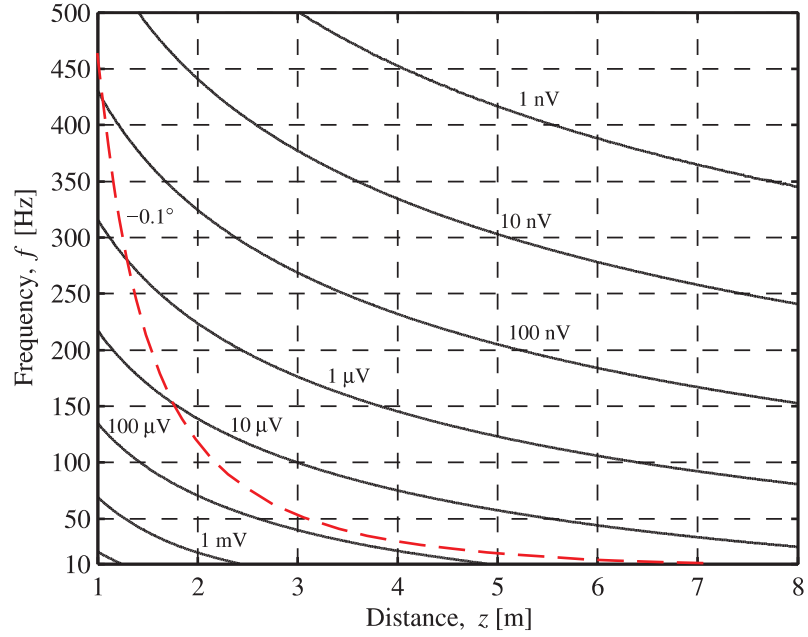


Figure 3.6: Amplitude of the induced voltage U_R as a function of distance z from the transmitter coil and excitation frequency f (casing inner radius 50 mm). For the red dashed line, $\Delta\varphi_{hom}(1 \text{ S/m}) = -0.1^\circ$.

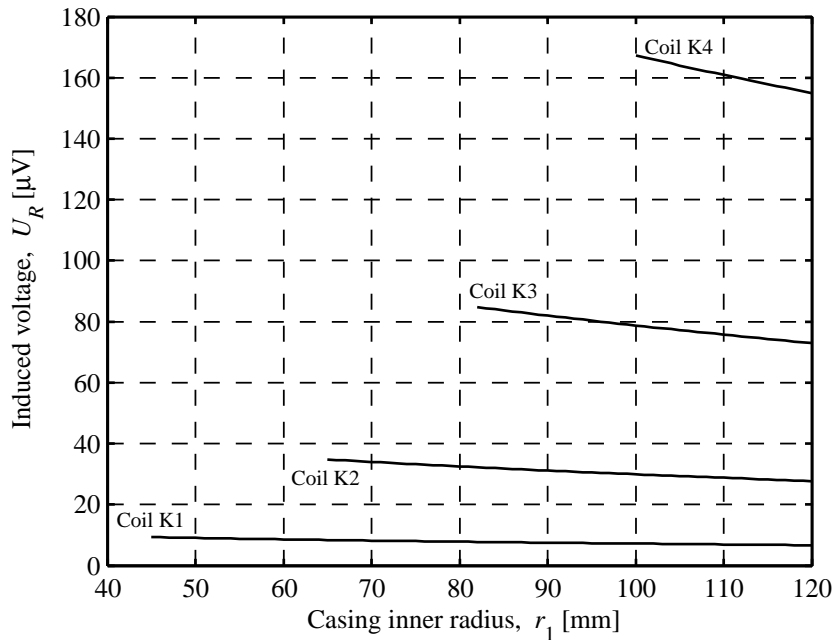


Figure 3.7: Amplitude of the induced voltage U_R as a function of casing inner radius r_1 for distance $z = 5$ m and excitation frequency $f = 60$ Hz. Properties of the coils are given in Table 3.1.

3.1.3 Vertical spatial resolution

Response of the two-coil sonde in a layered surrounding medium, Figs. 2.1 and 3.8, to the change in conductivity of a layer (σ_a) is a function of the layer thickness ($2z_f$), conductivities of the adjacent layers (σ_b), position of the middle of the sonde with respect to the middle of the layer (z_s) and transmitter-receiver separation (sonde length, D_s) [11]. Instead of the true layer conductivity, the sonde response represents the apparent conductivity, i.e. the conductivity of a homogenous medium that would produce the same signal response as the present layered medium [12, 65].

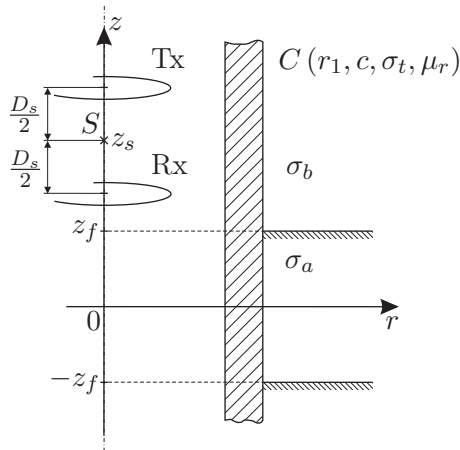


Figure 3.8: Coordinate system and sonde position, see Fig. 2.1.

Fig. 3.9 depicts results obtained using our model and the geometry in Fig. 3.8 with the same properties of the coils, casing and surrounding medium as in [52]: the casing $C(100 \text{ mm}, 10 \text{ mm}, 1 \text{ MS/m}, 6.25)$, the medium $M(5 \text{ m}, 2 \text{ S/m}, 0.2 \text{ S/m})$, and the excitation frequency 100 Hz . The results quantitatively agree with the ones in [52], what supports validity of the model. Maximum of the phase difference occurs when the middle of the sonde (point S in Fig. 3.8) coincides with the middle of layer A, i.e. when $z_s = 0$. As expected, the phase difference increases with the coil separation, but the vertical resolution decreases. The phase differences for two different casings $C(100 \text{ mm}, 10 \text{ mm}, 1 \text{ MS/m}, 6.25)$ and $C(100 \text{ mm}, 10 \text{ mm}, 4.6 \text{ MS/m}, 100)$ are shown in Fig. 3.10. Although the penetration depth for the latter casing is smaller for more than 8 times, the phase logs overlap. This feature is of the utmost interest and will be discussed in more details in section 3.3. Figs. 3.11 and 3.12 show the phase logs at $f = 60 \text{ Hz}$ for thicknesses of layer A 3 m and 20 m , respectively. Although the conductivity of layer A in both figures is $\sigma_a = 1 \text{ S/m}$, maximum absolute value of $\Delta\varphi(1 \text{ S/m}; 0 \text{ S/m})$ is larger for the thickness of 20 m . This is clearly shown in Fig. 3.13. Extreme value of $\Delta\varphi(1 \text{ S/m}; 0 \text{ S/m})$ for a given coil separation D_s approaches its homogenous limit $\Delta\varphi_{hom}(1 \text{ S/m})$ as the layer thickness increases. For the coil separation of 1 m the homogenous limit is achieved for layers thicker than 3 m , whereas for the coil separation of 5 m , the limit is not achieved even for layers thicker than 20 m .

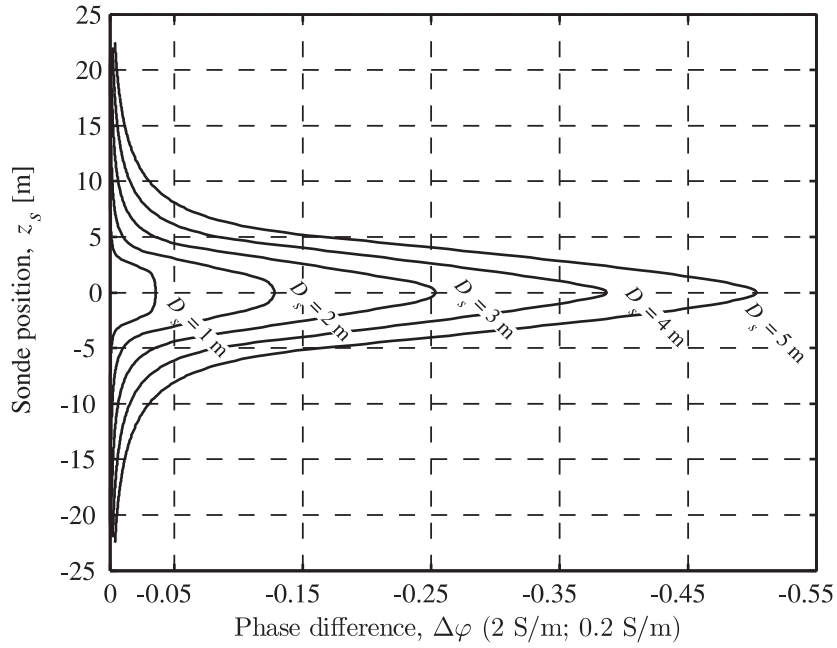


Figure 3.9: Relationships of phase differences $\Delta\varphi$ (2 S/m; 0.2 S/m) and sonde position z_s for five transmitter-receiver separations D_s . Casing and excitation frequency are chosen according to [52]: C (100 mm, 10 mm, 1 MS/m, 6.25) and $f = 100$ Hz.

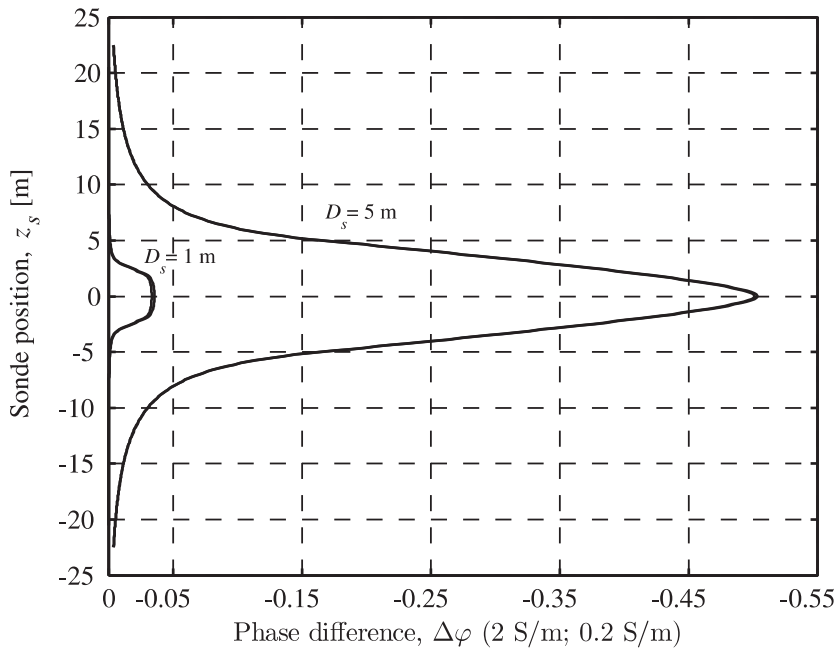


Figure 3.10: Comparison of phase differences $\Delta\varphi$ (2 S/m; 0.2 S/m) for two casings: C (100 mm, 10 mm, 1 MS/m, 6.25) and C (100 mm, 10 mm, 4.6 MS/m, 100). There is no significant difference between the curves. For other settings see Fig. 3.9.

3.1 Formation conductivity

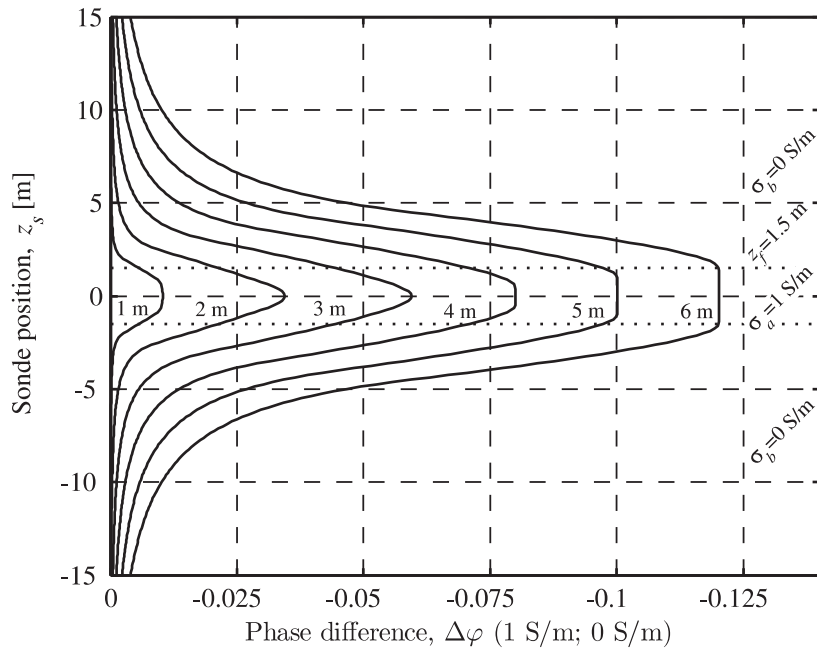


Figure 3.11: Phase differences $\Delta\varphi$ (1 S/m; 0 S/m) for the range of coil separation D_s from 1 m to 6 m. Dotted lines bound layer A. The casing parameters are C (100 mm, 10 mm, 4.6 MS/m, 100), and the medium is M (3 m, 1 S/m, 0 S/m).

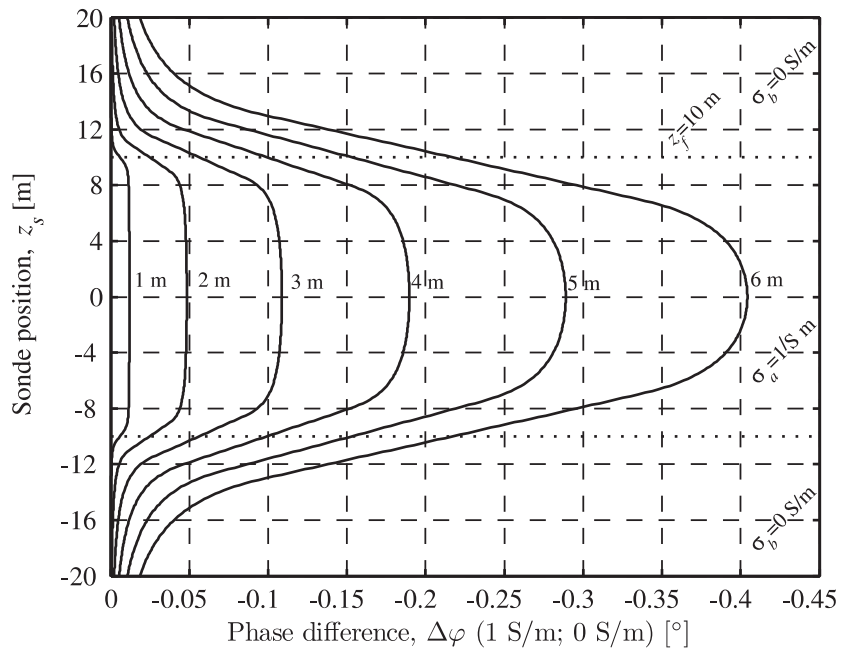


Figure 3.12: Phase differences $\Delta\varphi$ (1 S/m; 0 S/m) for the range of coil separation D_s from 1 m to 6 m. Dotted lines bound layer A. The casing parameters are C (100 mm, 10 mm, 4.6 MS/m, 100), and the medium is M (20 m, 1 S/m, 0 S/m).

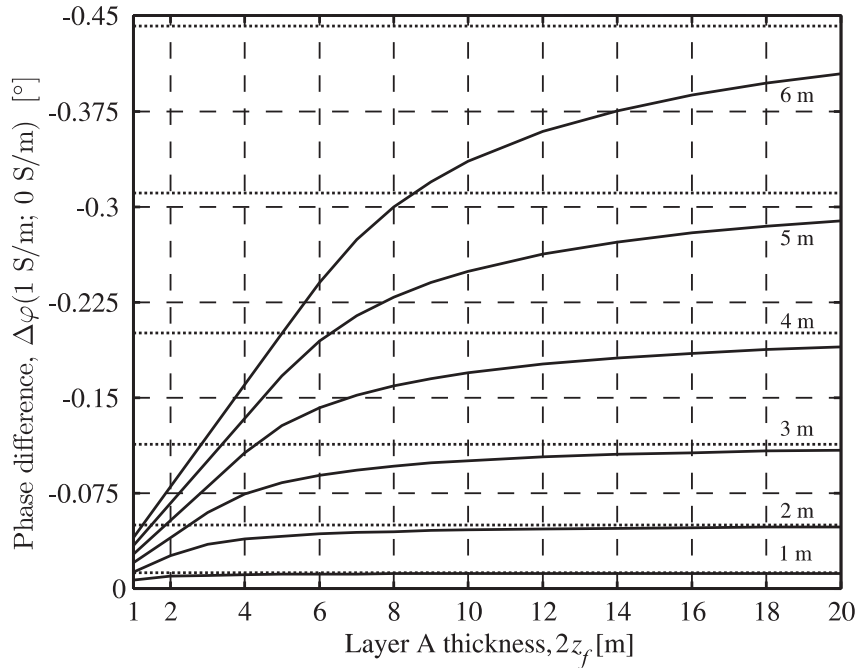


Figure 3.13: Maximum of $\Delta\varphi(1 \text{ S/m}; 0 \text{ S/m})$ (at $z_s = 0 \text{ m}$) as a function of the thickness of layer A for several coil separations. All curves approach homogenous limit $\Delta\varphi_{hom}(1 \text{ S/m})$ (dotted lines) as the layer thickness increases.

Based on this analysis, we can conclude that the simplest two-coil sonde for the cased-hole measurement shows the same limitations of the vertical resolution as for the open-hole case [12, 65]. The problem is even more severe considering that a typical open-hole sonde has several times smaller transmitter-receiver separation (about 1 m or 40") than it can be expected for the cased-hole sonde (about 5 m). In open-hole induction logging, the vertical resolution was improved using focused tools which were replaced by multi-array and tri-axial induction tools in the early 1990s [1]. Because of the similarities between the responses of probes to the properties of surrounding rocks in the cased and open-hole situations, we expect that the vertical resolution of cased-hole probes can be ameliorated using similar techniques as in open-hole induction tools, namely multi-receiver tools and inverse problem solving techniques [1].

3.1.4 Radius of investigation

Radius of investigation is a radial distance from the axis of a borehole that describes how far into the formation a tool can measure its properties [3, 66]. The term is more appropriate than "depth of investigation" for axially symmetric measurements [66]. For resistivity measurements, the radius of investigation can vary considerably depending on formation homogeneity and electrical conductivity. Thus, one should always specify the conditions for which the stated radius of investigation is valid.

3.1 Formation conductivity

We will investigate the radius of investigation using the geometry depicted in Fig. 3.14. The formation consist of two cylindrical layers: the inner layer with conductivity 0 S/m, and the outer layer with conductivity 1 S/m. The boundary between the layers is at $r = r_3$. By varying r_3 , we can determine at what distance from the borehole axis the effect of formation on the phase difference becomes negligible.

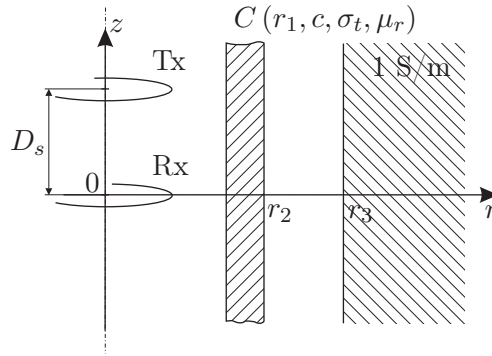


Figure 3.14: Definition of the radius of investigation. Medium surrounding the casing consists of two cylindrical layers with boundary at $r = r_3$. The inner layer has conductivity of 0 S/m and the outer layer 1 S/m. See Fig. 2.1.

Phase difference $\Delta\varphi_{roi}$ in the case of geometry from Fig. 3.14 is a function of r_3 , and, as usual, we define it with respect to the phase at the same position in the case of the same casing surrounded by the nonconductive medium (air). The phase difference $\Delta\varphi_{roi}$ is maximal for $r_3 = r_2$, i.e. $\Delta\varphi_{roi}(r_3 = r_2) = \Delta\varphi_{hom}(1 \text{ S/m})$. Since we are interested in the relative decrease of the phase difference as r_3 increases, we will define the normalised phase difference:

$$\Delta\varphi_{norm} = \frac{\Delta\varphi_{roi}(r_3)}{\Delta\varphi_{roi}(r_3 = r_2)} = \frac{\Delta\varphi_{roi}(r_3)}{\Delta\varphi_{hom}(1 \text{ S/m})}. \quad (3.1)$$

Fig. 3.15 depicts $\Delta\varphi_{norm}$ for three values of coil separation $D_s = 1 \text{ m}$, 5 m and 10 m . As expected, $\Delta\varphi_{norm}$ decreases as r_3 increases, but more slowly for the larger coil separation. This confirms the fact, well-known in the open-hole logging, that with increase of the coil separation, the influence of more remote parts of the formation increases [11]. The formation parts beyond $r_3 > D_s$ contribute less than 40% to 50% of the total phase difference, and around 20% for $r_3 > 2D_s$. If we accept 20% as the limit, we can establish a rule of thumb for assessment of the radius of investigation: for coil separation D_s the radius of investigation is around $2D_s$.

Radial dependence of the modulus (normalised to 1) of the current density in the formation is shown in Fig. 3.16 for $z = 2 \text{ m}$, 5 m and 10 m . We calculated the current density using (2.78). Again, it is clear that the more distant receiver means larger radius of investigation. Furthermore, we can see that there is a radial distance for every z at which the current density is maximal. The parts of the medium with higher current density build up

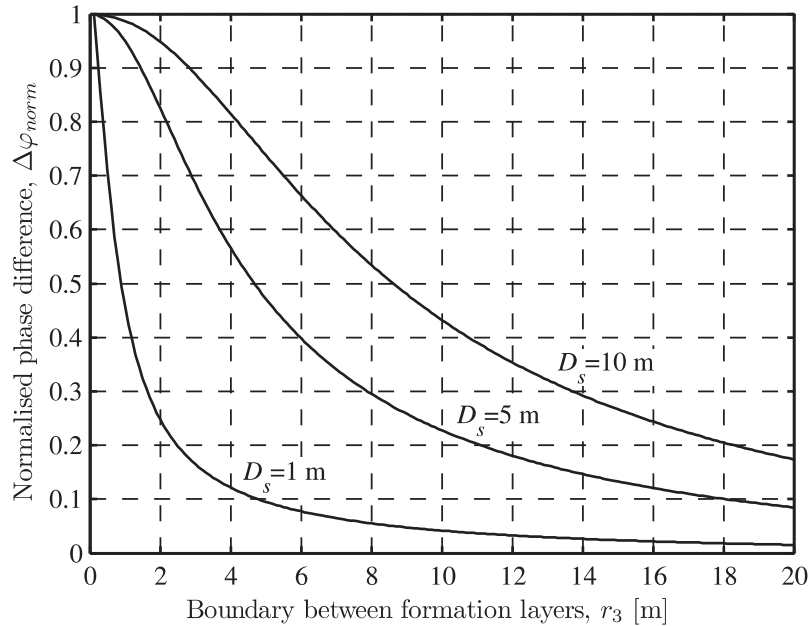


Figure 3.15: Relationship of normalised phase difference $\Delta\varphi_{norm}$, see (3.1), and radial boundary r_3 from Fig. 3.14 for three values of coil separation D_s .

the greatest part of the formation contribution to the receiver signal. This means that by choosing the coil separation, we choose a radial interval of the formation to which our sonde will have the greatest sensitivity or resolution.

The radial resolution is closely connected to the radius of investigation [66]. The change in the remote part ($r_3 = 18$ m) of formation from 0 S/m to 1 S/m results in the phase difference that is 10% of the maximum phase difference in the homogenous case, Fig. 3.15.

3.2 Casing properties

Inductive measurement of the oil-well casing properties is discussed by a number of authors [44, 46, 48, 49, 63, 67–70]. The main principle of the inductive measurements of the casing’s properties is based on a careful selection of the coil separation and excitation frequency. For the measurement of the inner radius one should use transmitter and receiver coils (known as calliper coils) placed next to each other or a single-coil method based on the impedance measurement [68, 71]. In both cases, excitation frequency is on the order of 10 kHz. For measurement of the wall thickness one uses so-called remote-field technique, where the coil separation is 2 to 5 times larger than the casing inner diameter and excitation frequency is on the order of 10 Hz [48, 67]. The casing electromagnetic properties are measured using a transmitter-receiver pair at mutual distance “somewhere” in between distances used for the calliper coils and thickness coils [20]. The choice of the excitation frequency is such that

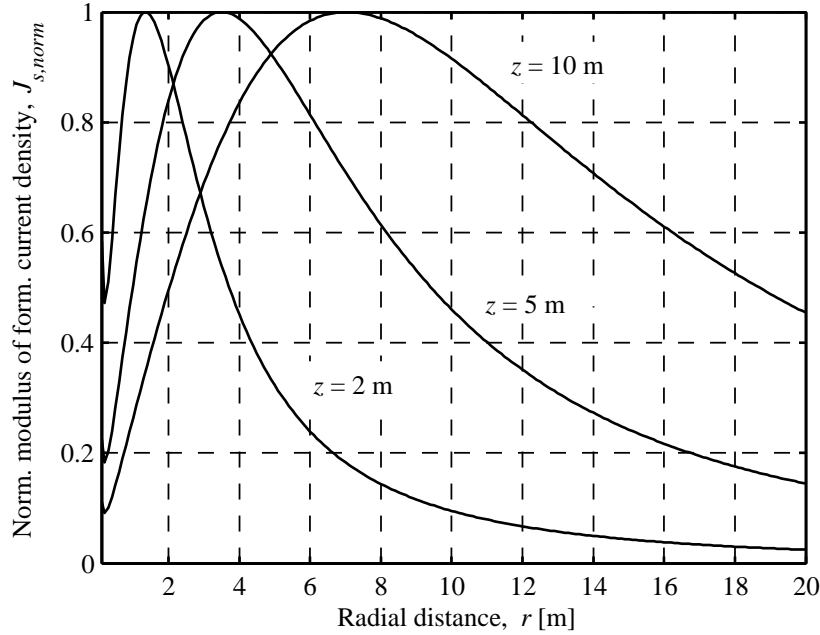


Figure 3.16: Radial dependence of the normalised modulus of current density in surrounding medium at three heights z from the transmitter.

the measurement is unaffected by the casing wall thickness.

In summary, the casing properties are measured using three transmitter-receiver pairs and at least three excitation frequencies. Firstly, the inner radius is measured. Then, the measurement of the electromagnetic properties are corrected for variations in the inner radius. Finally, the wall thickness is obtained, corrected for variations in the electromagnetic properties [20].

In the rest of this section we will analyse the choice of separations and frequencies using the analytical derivatives of the magnetic field with respect to the casing properties. Without such an analysis, and based on simplified models or empirical results only, one has difficulties to justify chosen spacings and frequencies or to find the optimal choice [44].

3.2.1 Spectrum of induced voltage

Figs. 3.17 show amplitude spectra of the field-frequency product $B_z f$ (proportional to the voltage picked-up by the receiver) depending on wall thinning (inner or outer) for three coil separations $D_s = 0.8 \text{ m} = 4 \text{ ID}$, $D_s = 0.45 \text{ m} = 2.25 \text{ ID}$ and $D_s = 0.2 \text{ m} = 1 \text{ ID}$, where ID denotes casing's inner diameter. The energy of the spectrum has distinctive low and high frequency bands as discussed in our papers [48, 63]. For larger coil separations as in Fig. 3.17(a), the energy is concentrated at low frequencies, while at locations closer to the transmitter the energy of the higher band dominates, Fig. 3.17(c). At intermediate distances from the transmitter, both bands are visible, Fig. 3.17(b).

In Figs. 3.17, casings 2 and 3 have the same wall thickness, which is smaller than thickness of casing 1. Casings 1 and 2 have the same inner radii, whereas casings 1 and 3 have the same outer radii. Casings with the same wall thickness have similar low-frequency bands regardless of the actual values of their radii, Fig. 3.17(a). Casings with the same inner radius have the same high-frequency band regardless of their wall thickness, Fig. 3.17(c). In Fig. 3.17(b), one can observe a boundary frequency that divides the spectra into low and high bands related to wall thickness variations and inner radius variations, respectively. It is customary to say that a receiver is in a direct zone if the choice of the separation and frequency is such that the sensitivity to the inner radius is high. Similarly, the receiver is said to be in a remote zone if the chosen separation and frequency result in the high thickness sensitivity [48, 67].

The separation of the spectrum into two bands and their commensurability at intermediate distances can be exploited for simultaneous measurement of inner radius and thickness with only one transmitter-receiver pair. This is achieved using a pulsed excitation for which the induced voltage has radius- and thickness-dependent parts “separated in time”, as discussed in our paper [48].

3.2.2 Wall thickness and electromagnetic properties

In addition to being complex, the derivatives of B_z over casing properties are incommensurable because the thickness, permeability and conductivity have values on the scale from 10^{-2} to 10^6 . In order to have comparable measures of sensitivity, we will define the relative sensitivity of the magnetic field with respect to a casing property x (thickness c , conductivity σ_t or relative permeability μ_r) as:

$$S_x = \left| \frac{x}{B_z} \frac{\partial B_z}{\partial x} \right|.$$

S_x is an absolute value of the ratio of the relative change of the magnetic field and the relative change of a casing property. Since the induced voltage is proportional to the field, S_x also represents the relative sensitivity of the voltage.

Figs. 3.18 and 3.19 depict spatial dependencies of relative sensitivities S_c , S_σ and S_μ for excitation frequencies 60 Hz and 200 Hz, respectively. For both frequencies and at large distances from the transmitter, all three casing parameters have a significant effect on the magnetic field. As the coil separation decreases, S_c decreases more rapidly than S_σ and S_μ . This is especially noticeable in Fig. 3.19 for 200 Hz, where S_c is smaller than S_σ and S_μ as far as $z = 0.5$ m. In the transmitter’s vicinity S_c is smaller for almost four orders of magnitude. This illustrates the aforesaid principle of the measurement of the electromagnetic properties.

3.2 Casing properties

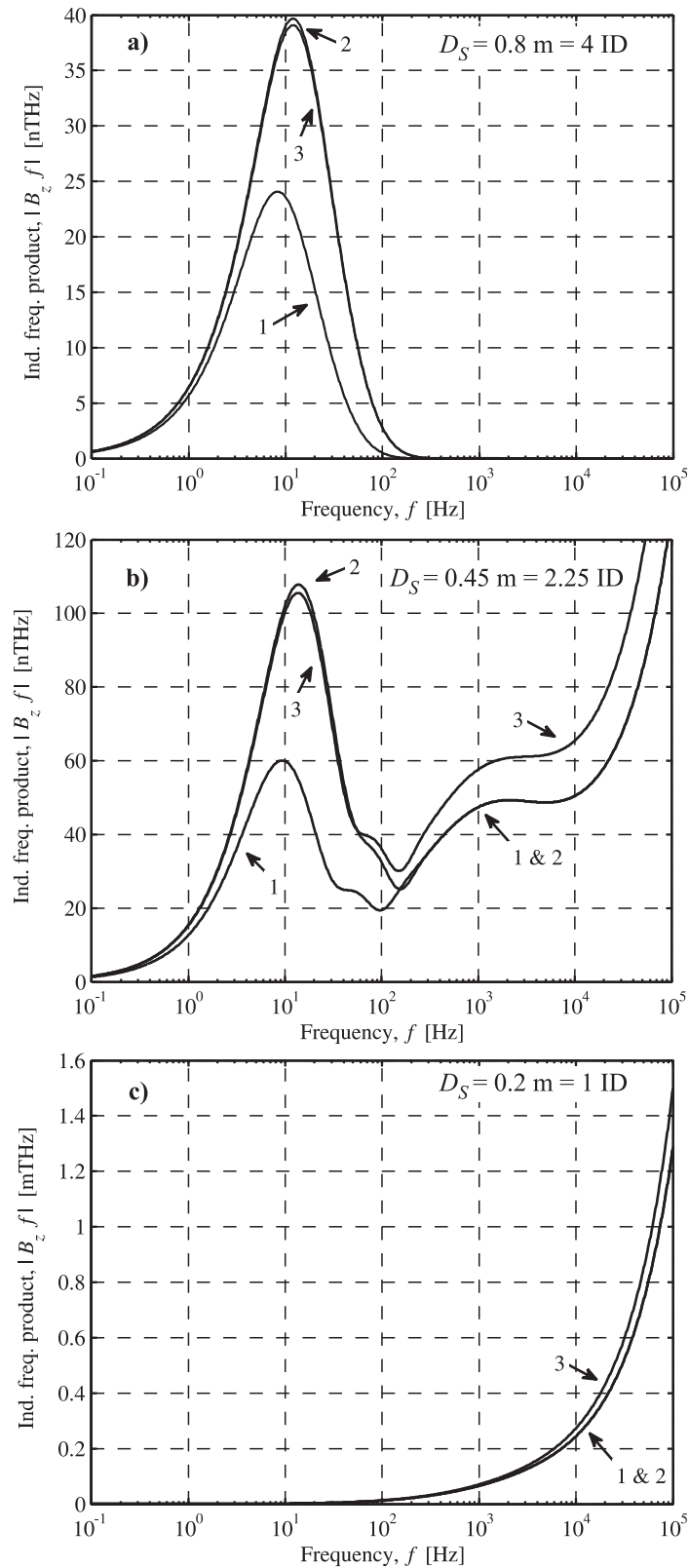


Figure 3.17: Amplitude spectra of $B_z f$ for three values of coil separation D_s and casings: 1— $C(100 \text{ mm}, 10 \text{ mm}, 4.6 \text{ MS/m}, 100)$; 2— $C(100 \text{ mm}, 8 \text{ mm}, 4.6 \text{ MS/m}, 100)$, outer thinning with respect to case 1; and 3— $C(102 \text{ mm}, 8 \text{ mm}, 4.6 \text{ MS/m}, 100)$, inner thinning with respect to case 1. ID denotes casing's inner diameter.

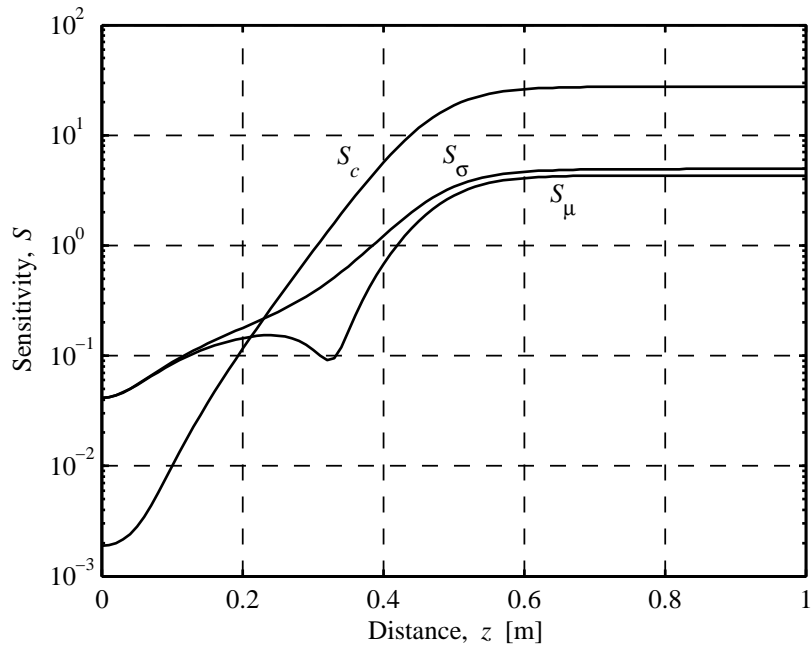


Figure 3.18: Relative sensitivities of the magnetic field to the casing properties at 60 Hz.

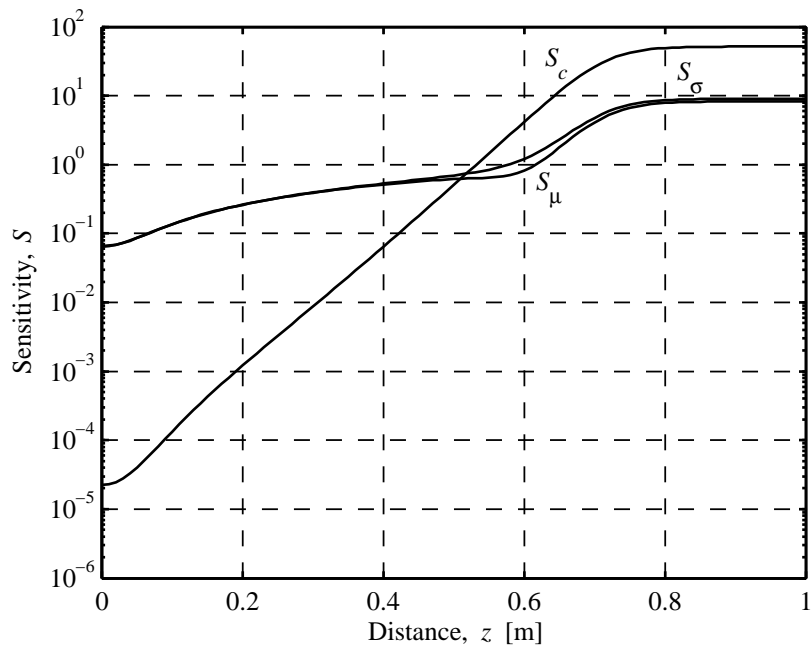


Figure 3.19: Relative sensitivities of the magnetic field to the casing properties at 200 Hz.

3.2.3 Casing factor and permeability-conductivity ratio

As we will see in Chapter 4, for the inverse problem of determination of the casing properties from the measured magnetic field, it is of interest to know a levelset $L_C = \{(c, \sigma_t, \mu_r) | B_z(c, \sigma_t, \mu_r) = B_z(c_0, \sigma_{t0}, \mu_{r0})\}$ for a given triple $(c_0, \sigma_{t0}, \mu_{r0})$. For now, we will focus ourselves to finding the approximate shape of such a levelset.

Magnetic field B_z can be written as a function of logarithmic values of the casing properties, namely $\ln c$, $\ln \sigma_t$ and $\ln \mu_r$. If we consider these logarithmic values as Cartesian coordinates, the gradient of B_z in a point with coordinates $(\ln c_0, \ln \sigma_{t0}, \ln \mu_{r0})$ is a vector normal to the tangential plane containing the point [72]. The plane is a very good approximation of the levelset even in a larger area around the point. We confirmed this by extensive numerical simulations, which we skip here for the sake of shortness.

The components of the gradient of B_z are:

$$\begin{aligned} C_c &= \frac{\partial B_z}{\partial \ln c} = c \frac{\partial B_z}{\partial c}, \\ C_\sigma &= \frac{\partial B_z}{\partial \ln \sigma_t} = \sigma_t \frac{\partial B_z}{\partial \sigma_t}, \\ C_\mu &= \frac{\partial B_z}{\partial \ln \mu_r} = \mu_r \frac{\partial B_z}{\partial \mu_r}. \end{aligned}$$

If we define the normal vector $\mathbf{n} = [1 \ C_\mu/C_\sigma \ C_c/C_\sigma]^T$ and radius vectors $\mathbf{t} = [\ln \sigma_t \ \ln \mu_r \ \ln c]$ and $\mathbf{t}_0 = [\ln \sigma_{t0} \ \ln \mu_{r0} \ \ln c_0]$, we can write for the tangential plane:

$$\mathbf{n} \cdot (\mathbf{t} - \mathbf{t}_0) = 0.$$

The thickness-related component of vector \mathbf{n} , ratio C_c/C_σ is zero in a region close to the transmitter, Fig. 3.20. This region of insensitivity to the thickness is wider for higher frequencies, as already discussed in section 3.2.2. After a transition zone in which both parts are commensurable, imaginary part of the ratio becomes zero again, whereas the real part levels at a constant value between 1.85 and 2 depending on the frequency. The permeability-related component of the normal vector, ratio C_μ/C_σ has similar spatial dependence of the imaginary part as C_c/C_σ , Fig. 3.21. In the vicinity of the transmitter the imaginary part is zero and the real part is -1 . Far from the transmitter and after the transition zone, the imaginary part is zero again and the real part is a constant value between 0.85 and 0.92, depending on the frequency. Because the imaginary parts of the ratios vanish in the vicinity of the transmitter and in the remote zone, the real and imaginary parts of B_z have the same levelsets in these regions, thus containing the same information about the casing properties.

The levelset can be written as:

$$L_C = c^{\nu_c} \mu_r^{\nu_\mu} \sigma_t = c_0^{\nu_c} \mu_{r0}^{\nu_\mu} \sigma_{t0} = \text{const.}, \quad (3.2)$$

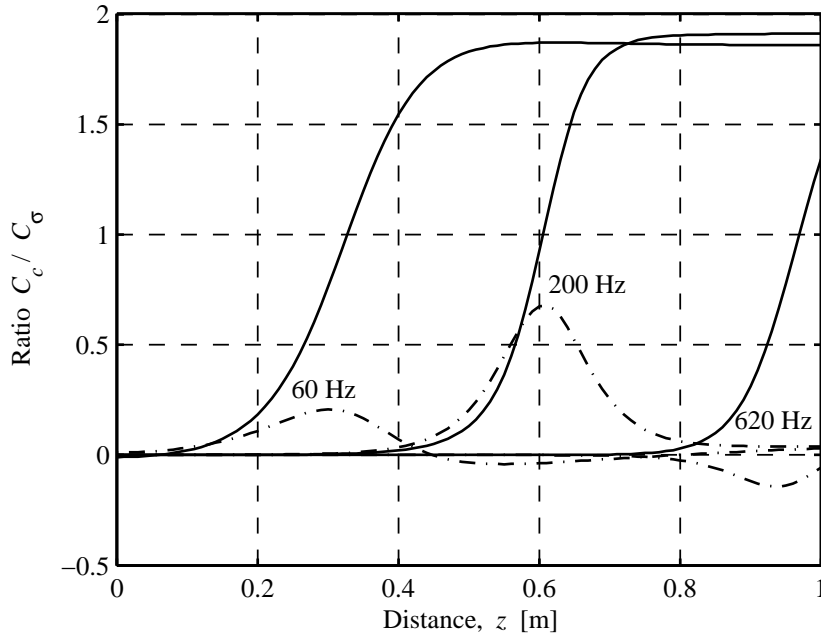


Figure 3.20: Real (full lines) and imaginary (dash-dot lines) parts of ratio C_c/C_σ against distance from the transmitter for three excitation frequencies.

where $\nu_c = C_c/C_\sigma$ and $\nu_\mu = C_\mu/C_\sigma$. For small coil separations and high excitation frequencies, $\nu_c = 0$, $\nu_\mu = -1$ and, from (3.2), the levelset is the permeability-to-conductivity ratio PCR ,

$$L_C = \frac{\sigma_t}{\mu_r} = \frac{1}{PCR}.$$

For larger coil separations and lower frequencies, ν_c is close to 2 and ν_μ is close to 1, so the sought levelset is approximately equal to the square value of a casing factor:

$$L_C \approx C_f^2 = c^2 \mu_r \sigma_t. \quad (3.3)$$

L_C with its spatially and frequency dependent exponents ν_c and ν_μ consolidates the notion of PCR and C_f as values that can be successfully resolved from the measured impedance or voltage, even in the case of degraded accuracy [49, 73]. While PCR is a good representation of L_C in the vicinity of the transmitter, casing factor C_f as defined in (3.3) is only the first approximation of L_C in the remote zone and one must use it with a caution.

Although we made this analysis for a particular casing, its validity can be corroborated by the model laid out in Chapter 2. Under the assumption of large values of βr_1 and βr_2 , Bessel's functions involving these arguments can be replaced by their asymptotic exponential form [72]. After straightforward but laborious algebraic manipulations, it becomes evident that the casing properties are involved only through βc and μ_r/β . For small values of α , arguments βc and μ_r/β are proportional to C_f and \sqrt{PCR} , respectively. Interaction of

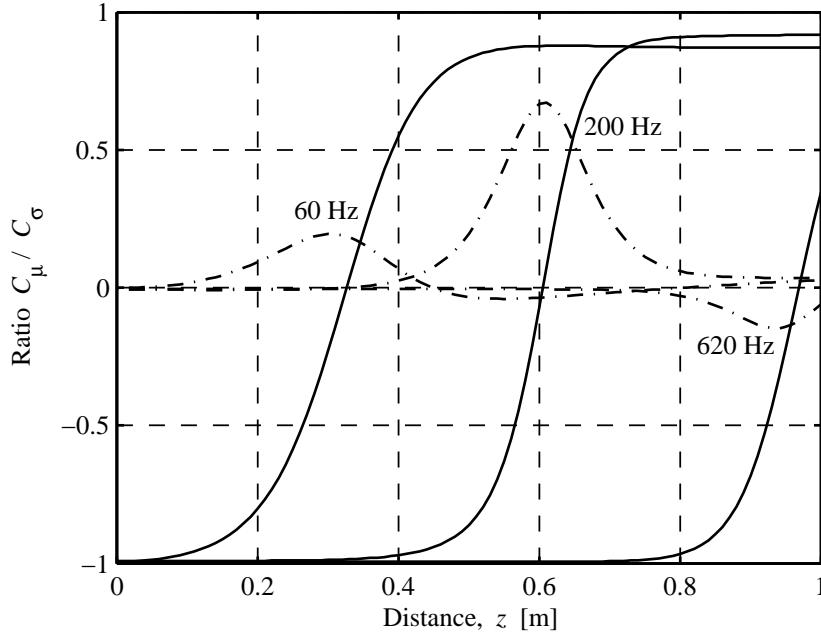


Figure 3.21: Real (full lines) and imaginary (dash-dot lines) parts of ratio C_μ/C_σ against distance from the transmitter for three excitation frequencies.

expressions involving βc and μ_r/β results in the space-frequency dependence of L_C as we discussed previously.

3.3 Correction for casing effect in case of known casing properties

At a large distance from the transmitter loop its vector potential can be approximated with the potential due to a magnetic dipole of moment $m = I_t \pi r_0^2$. The axial component of the magnetic field of the transmitter in air along z axis is given with:

$$B_{z,air}(r=0, z) = \mu_0 \frac{m}{2\pi|z|^3}, \quad (3.4)$$

for $z \gg r_0$. Comparison of the transmitter field calculated using the model and the dipole approximation (3.4) is depicted in Fig. 3.22. For distances larger than 1 m (10 casing's radii) the difference between the two models is indistinguishable.

If the transmitter loop is positioned inside the casing, the magnetic field at distances $z \gg r_0$ will be severely attenuated but its magnitude will still be proportional to the factor $r_0^2|z|^{-3}$. Because of that proportionality, the field of the dipole with moment m inside the casing can be related to a dipole with

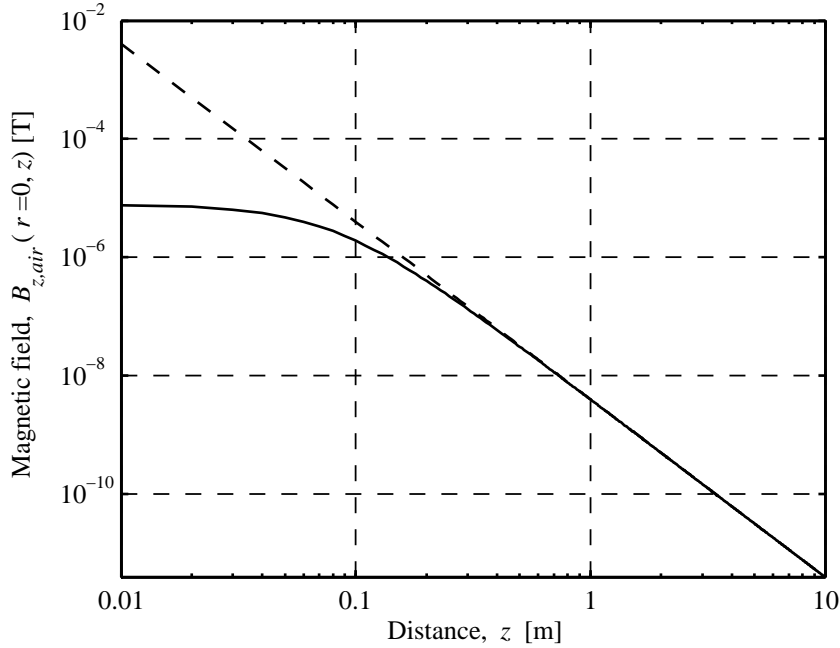


Figure 3.22: Axial component of the magnetic field of a transmitter loop along z axis: the model prediction (full line), dipole approximation (dashed line).

effective magnetic moment $m_c = k_c m$:

$$B_{z,c}(r=0, z) = \mu_0 \frac{m_c}{2\pi|z|^3} = \mu_0 \frac{k_c m}{2\pi|z|^3} = k_c B_{z,air}(r=0, z),$$

where complex function k_c is a casing attenuation factor, which depends on the casing properties and excitation frequency. The axial dependence of the modulus and phase of k_c for casing $C(100 \text{ mm}, 10 \text{ mm}, 4.6 \text{ MS/m}, 100)$ is shown in Fig. 3.23. It can be seen that $|k_c|$ does not depend significantly on z for distances larger than 1 m, thus confirming the dipole character of $B_{z,c}$. However, the phase of k_c depends on the distance for the entire range of interest (up to 10 m).

If a magnetic dipole is placed in an open borehole in homogeneously conductive medium, the magnetic field along z axis also shows $r_0^2|z|^{-3}$ dependence. Similarly to the previous situation with casing alone, we can write for an effective moment of the dipole in the open borehole $m_f = k_f m$. The formation factor k_f depends on the formation conductivity, excitation frequency and borehole radius. A closed-form solution can be found for borehole radius $r_1 = 0$ m (i.e. a dipole embedded in a homogenous conductive medium) [65, 74]:

$$B_{z,f} = \mu_0 \frac{m_f}{2\pi|z|^3} = \mu_0 \frac{k_f m}{2\pi|z|^3},$$

3.3 Correction for casing effect in case of known casing properties

where

$$k_f = (1 + j\kappa_f z) \exp(-j\kappa_f z), \quad (3.5)$$

$$\kappa_f^2 = -j\omega\mu_0\sigma_f. \quad (3.6)$$

It can be expected that k_f shows similar dependence for a borehole of finite radius.

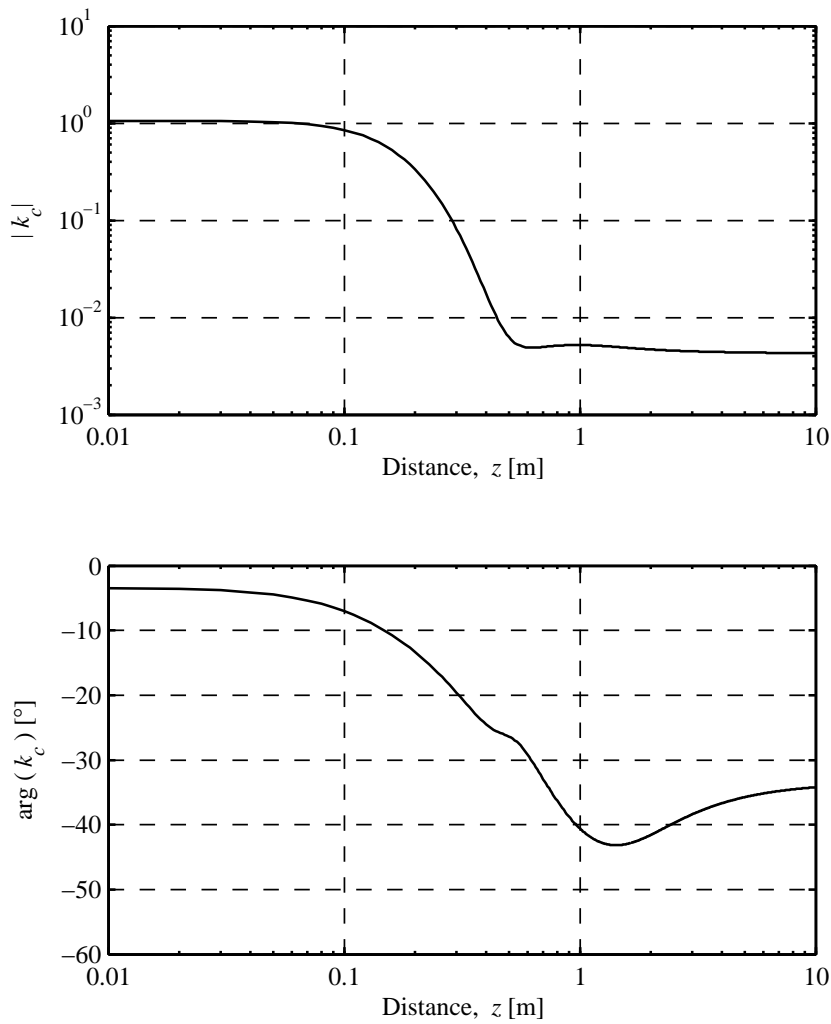


Figure 3.23: Modulus and argument of the casing attenuation factor along z axis for $C(100 \text{ mm}, 10 \text{ mm}, 4.6 \text{ MS/m}, 100)$

We can assume that the surrounding medium changes the far field of a dipole inside the casing in the same way as it changes the field of a dipole in the open borehole. This can be justified by the dipole nature of the magnetic field of a current loop inside the casing at large distances and by the fact that the casing is uncoupled from the surrounding medium, meaning that the

induced current flowing in the medium has no effect on the current distribution within the casing. Similar conclusions were corroborated by numerical and scaled experimental studies for other configurations, e.g. surface-to-borehole measurements in [29]. Thus, when the casing and formation are present:

$$B_{z,c+f} = k_f B_{z,c} = k_f k_c B_{z,air}. \quad (3.7)$$

Importance of (3.7) lies in a simple correction of the formation conductivity measurement for variations in the casing properties. The casing attenuation can be calculated and compensated if one measures the casing properties. In other words, the casing acts as a filter for which the inverse of its transfer function can be calculated for known casing properties [30].

The homogenous phase difference for two surrounding media of conductivities σ_1 and σ_2 , defined in section 3.1.1 can be calculated using the magnetic field instead of the induced voltage:

$$\Delta\varphi_{hom}(\sigma_1; \sigma_2) = \arg B_{z,c+f}(\sigma_1) - \arg B_{z,c+f}(\sigma_2), \quad (3.8)$$

where the casing for both fields is the same. It follows from (3.7) that:

$$B_{z,c+f} = |k_f| |k_c| B_{z,air} \exp(j(\arg k_f + \arg k_c)), \quad (3.9)$$

where we took into account that $B_{z,air}$ is real-valued. Combining (3.8) and (3.9) we get:

$$\Delta\varphi_{hom}(\sigma_1; \sigma_2) = \arg k_f(\sigma_1) - \arg k_f(\sigma_2). \quad (3.10)$$

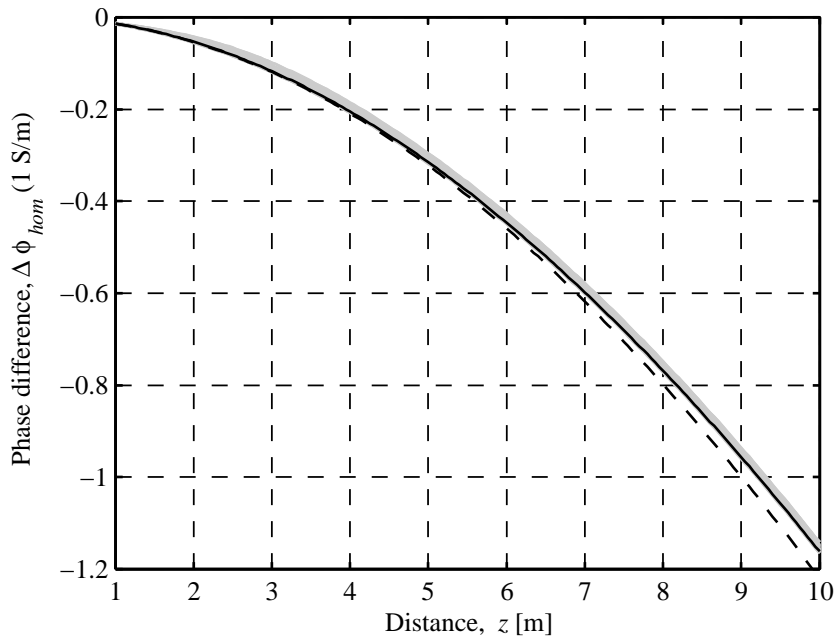


Figure 3.24: Phase difference $\Delta\varphi_{hom}$ (1 S/m) calculated for 36 different casings (overlapped gray lines, see text for properties), open borehole (black, full line) and using closed form solution for borehole radius 0 m (black, dashed line).

The casing attenuation factor k_c is cancelled out in (3.10), leaving the phase difference independent of the casing properties.

Fig. 3.24 illustrates the cancellation of the casing effect. We calculated the phase difference $\Delta\varphi$ (1 S/m) for 36 different casings. Each casing is a combination taken from the set of all possible combinations of four values of the permeability (1, 50, 100 and 200), three values of the conductivity (1 MS/m, 4.6 MS/m and 10 MS/m) and three values of the thickness (2 mm, 10 mm and 20 mm) for the inner radius of 100 mm. In spite of these very different casings and, consequently, values of k_c , the curves of the phase difference overlap. Furthermore, they deviate on average only 0.005° from the phase difference at $z = 5$ m in the situation without the casing. The phase difference using closed-form solution (3.5) for borehole radius 0 m is also in a good agreement with the rest of the curves, indicating the correctness of our assumption that, at such large distances, the contribution of the borehole can be neglected in the first approximation. The insensitivity of the phase difference to the casing properties is also evident in the case of inhomogeneous surrounding medium, as already shown in Fig. 3.10.

Chapter 4

Inverse problem

We must take care not to admit as true anything, which is only probable.

Benedictus de Spinoza (1632–1677)

Letter 56(60), to Hugo Boxel, 1674

In this chapter we develop a stochastic formulation of the inverse problem of determination of the casing properties and conductivity of the surrounding homogenous medium from the magnetic field measured at multiple distances from the single transmitter. The inversion procedure is based on the Monte Carlo Markov chain (MCMC) method and the analytical model presented in previous chapters.

4.1 Sensitivity analysis and ill-conditioning

The most important requirement for the successful correction procedure from section 3.3 is the ability to estimate the magnetic field in the case of the nonconductive surrounding medium. In a practical realisation, the estimation is based on the field values measured at two or more positions closer to the transmitter. This immediately raises the question of a relationship between the uncertainties of the estimated and measured values of the magnetic field. For a successful correction, small uncertainties of the measured values should result in small uncertainty of the estimated magnetic field. We examine this issue using the Jacobian of the magnetic field.

Let the real and imaginary parts of the magnetic field be B_{re} and B_{im} , respectively. We can order the real and imaginary parts of the magnetic field measured at locations z_1, z_2, \dots, z_n (in the region insensitive to the formation of the surrounding medium) into a vector $\mathbf{B}_C = [B_{re,1} \ B_{im,1} \ \dots \ B_{re,n} \ B_{im,n}]^T$.

The Jacobian matrix of \mathbf{B}_C is:

$$\mathbf{J}_C(\mu_r, \sigma_t, c) = \begin{bmatrix} \frac{\partial B_{re,1}}{\partial \mu_r} & \frac{\partial B_{re,1}}{\partial \sigma_t} & \frac{\partial B_{re,1}}{\partial c} \\ \frac{\partial B_{im,1}}{\partial \mu_r} & \frac{\partial B_{im,1}}{\partial \sigma_t} & \frac{\partial B_{im,1}}{\partial c} \\ \vdots & \vdots & \vdots \\ \frac{\partial B_{re,n}}{\partial \mu_r} & \frac{\partial B_{re,n}}{\partial \sigma_t} & \frac{\partial B_{re,n}}{\partial c} \\ \frac{\partial B_{im,n}}{\partial \mu_r} & \frac{\partial B_{im,n}}{\partial \sigma_t} & \frac{\partial B_{im,n}}{\partial c} \end{bmatrix}.$$

The first-order approximation of the relationship between changes of the casing properties and magnetic field is:

$$\Delta \mathbf{B}_C = \mathbf{J}_C \begin{bmatrix} \Delta \mu_r \\ \Delta \sigma_t \\ \Delta c \end{bmatrix}. \quad (4.1)$$

A component of $\Delta \mathbf{B}_C$ can be viewed as an uncertainty of the measurement of the corresponding real or imaginary part of the magnetic field. We can assume that these uncertainties are proportional to the magnitude of the field and not to the real or imaginary part in question, see section 4.5. Thus:

$$\Delta \mathbf{B}_C = \begin{bmatrix} |B_1| & 0 & \cdots & 0 & 0 \\ 0 & |B_1| & \cdots & 0 & 0 \\ \vdots & & \ddots & & \vdots \\ 0 & 0 & \cdots & |B_n| & 0 \\ 0 & 0 & \cdots & 0 & |B_n| \end{bmatrix} \begin{bmatrix} p_{B1} \\ p_{B1} \\ \vdots \\ p_{Bn} \\ p_{Bn} \end{bmatrix}. \quad (4.2)$$

In terms of the relative changes, we have:

$$\Delta \mathbf{B}_C = \mathbf{J}_C \begin{bmatrix} \mu_r & 0 & 0 \\ 0 & \sigma_t & 0 \\ 0 & 0 & c \end{bmatrix} \begin{bmatrix} \Delta \mu_r / \mu_r \\ \Delta \sigma_t / \sigma_t \\ \Delta c / c \end{bmatrix}. \quad (4.3)$$

If we introduce:

$$p_B = \begin{bmatrix} \|p_{B1}\| \\ p_{B1} \\ \vdots \\ p_{Bn} \\ \|p_{Bn}\| \end{bmatrix}, \quad (4.4)$$

$$p_{em} = \begin{bmatrix} \|\Delta \mu_r / \mu_r\| \\ \|\Delta \sigma_t / \sigma_t\| \\ \|\Delta c / c\| \end{bmatrix}, \quad (4.5)$$

$$\mathbf{S}_{em} = \begin{bmatrix} 1/|B_1| & 0 & \cdots & 0 & 0 \\ 0 & 1/|B_1| & \cdots & 0 & 0 \\ \vdots & & \ddots & & \vdots \\ 0 & 0 & \cdots & 1/|B_n| & 0 \\ 0 & 0 & \cdots & 0 & 1/|B_n| \end{bmatrix} \mathbf{J}_C \begin{bmatrix} \mu_r & 0 & 0 \\ 0 & \sigma_t & 0 \\ 0 & 0 & c \end{bmatrix}, \quad (4.6)$$

we obtain a measure of stability of the electromagnetic properties with respect to the small variations in the measured magnetic field. From (4.1)–(4.6) we have:

$$p_{em} \leq \| \mathbf{S}_{em}^\dagger \| p_B,$$

where \mathbf{S}_{em}^\dagger is the Moore-Penrose pseudoinverse of \mathbf{S}_{em} what guarantees the minimal value of p_{em} [75]. The norm $\| \mathbf{S}_{em}^\dagger \|$ represents the sought measure of stability which we will call an error ratio for the casing properties. Its exact value is determined by our choice of the Euclidian matrix norm. If the error ratio is large, one can expect large relative errors in the determination of the electromagnetic properties.

Similarly, we can derive an error ratio for the casing's lump parameters — casing factor $C_f = c\sqrt{\mu_r\sigma_t}$ and permeability-to-conductivity ratio PCR = μ_r/σ_t . The Jacobian matrix \mathbf{J}_L of the lump parameters with respect to the casing properties is:

$$\mathbf{J}_L = \begin{bmatrix} \frac{\partial C_f}{\partial \mu_r} & \frac{\partial C_f}{\partial \sigma_t} & \frac{\partial C_f}{\partial c} \\ \frac{\partial \text{PCR}}{\partial \mu_r} & \frac{\partial \text{PCR}}{\partial \sigma_t} & \frac{\partial \text{PCR}}{\partial c} \end{bmatrix} = \begin{bmatrix} \frac{C_f}{2\mu_r} & \frac{C_f}{2\sigma_t} & \frac{C_f}{c} \\ \frac{1}{\sigma_t} & -\frac{\text{PCR}}{\sigma_t} & 0 \end{bmatrix}.$$

Using:

$$p_L = \left\| \begin{bmatrix} \Delta C_f/C_f \\ \Delta \text{PCR}/\text{PCR} \end{bmatrix} \right\|,$$

and:

$$\mathbf{S}_L = \begin{bmatrix} 1/|B_1| & 0 & \cdots & 0 & 0 \\ 0 & 1/|B_1| & \cdots & 0 & 0 \\ \vdots & & \ddots & & \vdots \\ 0 & 0 & \cdots & 1/|B_n| & 0 \\ 0 & 0 & \cdots & 0 & 1/|B_n| \end{bmatrix} \mathbf{J}_C \mathbf{J}_L^\dagger \begin{bmatrix} C_f & 0 \\ 0 & \text{PCR} \end{bmatrix}, \quad (4.7)$$

the measure of stability of the casing's lump parameters is:

$$p_L \leq \| \mathbf{S}_L^\dagger \| p_B. \quad (4.8)$$

Let B'_{n+1} be the estimated field at location z_{n+1} in the case of the non-conductive surrounding medium. The measured magnetic field B_{n+1} depends on the conductivity of the surrounding medium. As discussed in section 3.3, the phase difference between B_{n+1} and B'_{n+1} is independent of variations in the casing properties. Uncertainty of the estimation $\Delta B'_{n+1}$ depends on the uncertainty of the casing properties:

$$\begin{bmatrix} \Delta B'_{re,n+1} \\ \Delta B'_{im,n+1} \end{bmatrix} = \mathbf{J}_{C,n+1} \mathbf{J}_L^\dagger \begin{bmatrix} C_f & 0 \\ 0 & \text{PCR} \end{bmatrix} \begin{bmatrix} \Delta C_f/C_f \\ \Delta \text{PCR}/\text{PCR} \end{bmatrix}, \quad (4.9)$$

where $\mathbf{J}_{C,n+1}$ is the Jacobian matrix of the real and imaginary parts of B'_{n+1} . Using (4.7)–(4.9), $p'_B = [\Delta B'_{re,n+1}/|B'_{n+1}| \ \Delta B'_{im,n+1}/|B'_{n+1}|]^T$, and error ratio

4.1 Sensitivity analysis and ill-conditioning

for the magnetic field $\|\mathbf{S}_B\|$, we can link measurement uncertainty p_B and estimation uncertainty p'_B as:

$$p'_B \leq \|\mathbf{S}_B\| p_B,$$

where matrix \mathbf{S}_B is given as:

$$\mathbf{S}_B = \frac{1}{|B'_{n+1}|} \mathbf{J}_{C,n+1} \mathbf{J}_C^\dagger \begin{bmatrix} C_f & 0 \\ 0 & \text{PCR} \end{bmatrix} \mathbf{S}_L^\dagger.$$

Fig. 4.1 depicts a frequency dependence of error ratio $\|\mathbf{S}_B\|$ for casing $C(100 \text{ mm}, 10 \text{ mm}, 4.6 \text{ MS/m}, 100)$. The field is measured at locations $z_1 = 0.15 \text{ m}$ and $z_2 = 0.9 \text{ m}$, and estimated for location $z_3 = 5 \text{ m}$. Since the error ratio is over 1, the uncertainty of the estimation is greater than the measurement uncertainty. However, the fact that the error ratio is lower than 2 indicates that the procedure for estimation of the magnetic field at a large distance from the two values measured closer to the transmitter is well conditioned. For the excitation frequency of 60 Hz, the error ratio is about 1.45. This means that the magnetic field measured at two locations with e.g. 100 ppm uncertainty allow us to estimate the far field with uncertainty better than 145 ppm at 60 Hz.

The fact that the error ratio depends on the receivers' positions z_1 and z_2 can be used for minimisation of the estimation uncertainty. In a practical

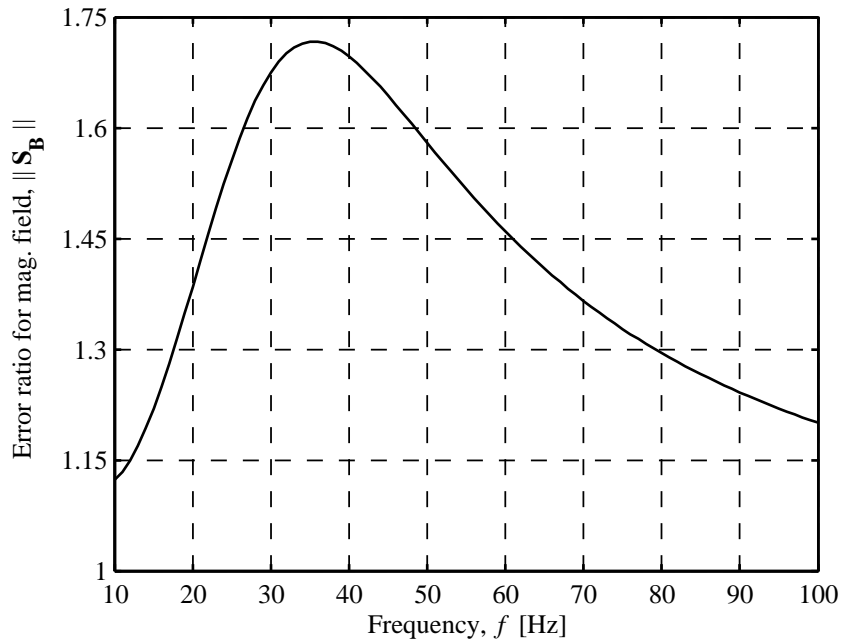


Figure 4.1: Ratio of the relative uncertainty of the estimated field at location $z_3 = 5 \text{ m}$ and relative uncertainties of the field measured at locations $z_1 = 0.15 \text{ m}$ and $z_2 = 0.9 \text{ m}$. Casing is $C(100 \text{ mm}, 10 \text{ mm}, 4.6 \text{ MS/m}, 100)$.

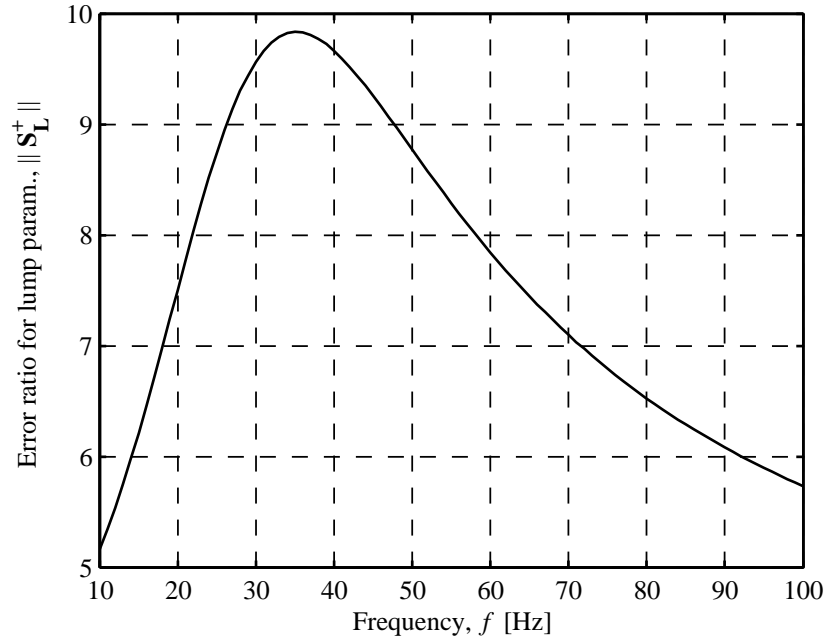


Figure 4.2: Ratio of the relative uncertainty of the casing lump parameters and relative uncertainties of the field measured at locations $z_1 = 0.15$ m and $z_2 = 0.9$ m. Casing is $C(100$ mm, 10 mm, 4.6 MS/m, 100).

realisation, it is much easier to vary the excitation frequency for the same purpose. We are, off course, limited by the lowest detectable voltage as discussed in section 3.1.2. It is interesting to note that there is a frequency for which the error ratio is the highest, i.e. the estimation uncertainty is the worst. In case of Fig. 4.1, that frequency is about 35 Hz.

Frequency dependence of the error ratio of the casing lump parameters $\|\mathbf{S}_L^+\|$ is depicted in Fig. 4.2 for casing $C(100$ mm, 10 mm, 4.6 MS/m, 100) and measurement locations $z_1 = 0.15$ m and $z_2 = 0.9$ m. The error ratio is between 5 and 10 what indicates that the uncertainty of determination of the casing lump parameters is the order of magnitude larger than the uncertainty of the magnetic field measurement. Similarly to Fig. 4.1, maximum of the error ratio is at 35 Hz.

The error ratio for the casing properties $\|\mathbf{S}_{em}^+\|$ is very high indicating that the determination of the casing properties μ_r , σ_t and c is ill-conditioned. For example, $\|\mathbf{S}_{em}^+\|$ is 121 at 60 Hz for casing $C(100$ mm, 10 mm, 4.6 MS/m, 100) and measurement locations $z_1 = 0.15$ m and $z_2 = 0.9$ m. The situation does not improve even if we introduce multiple receivers.

4.2 Theoretical considerations

4.2.1 Elements of probabilistic inverse problem theory

Let \mathfrak{M} be a space of all conceivable states of a system. We need to choose a particular parametrisation, i.e. a coordinate system over \mathfrak{M} that joins a set of numerical values $\{m_1, \dots, m_n\}$ to each point in \mathfrak{M} . We will use a shorthand notation $\mathbf{m} = \{m_1, \dots, m_n\}$. Only in a case that \mathfrak{M} is a linear space, \mathbf{m} can be called a vector. Similarly, let \mathfrak{D} be a space of all conceivable measurement results (observable data) and let \mathbf{d} be a set of numerical values describing a measurement result from \mathfrak{D} . We will call \mathfrak{M} a model space and \mathfrak{D} a data space. Points \mathbf{m} and \mathbf{d} are realisations of random variables \mathbf{M} and \mathbf{D} , respectively.

We assume that our knowledge on the random variables \mathbf{M} and \mathbf{D} can be represented using probability densities. Our *a priori* information on the model parameters \mathbf{M} and measurement result \mathbf{D} is described with a joint prior probability density function $\pi(\mathbf{d}, \mathbf{m})$.

Situations where we have an exact theoretical relation between model parameters and measured quantities are rare. Instead of an exact relation:

$$\mathbf{d} = \Gamma(\mathbf{m}), \quad (4.10)$$

where $\Gamma(\cdot)$ is a mathematical model of the physical system, we have to write:

$$\mathbf{d} \approx \Gamma(\mathbf{m}). \quad (4.11)$$

In the probabilistic approach, (4.11) can be described by a theoretical joint probability density function $\theta(\mathbf{d}, \mathbf{m})$. Besides being useful for representation of approximate theoretical relations, $\theta(\mathbf{d}, \mathbf{m})$ arises naturally in empirical relations between \mathbf{m} and \mathbf{d} based on the accumulation of observations.

Noninformative prior probability distributions (or just “priors”) are used in Bayesian analysis in situations when no or minimal prior knowledge about parameters is available [76]. The first obvious choice is to assign equal likelihood to each value of a parameter. This is called Laplace’s prior or “principle of insufficient reason” [77]. The main criticism of Laplace’s prior is that it depends on parametrisation of the model space. The most widely used noninformative priors, Jeffreys priors are proportional to square root of the determinant of the Fisher information matrix that is invariant under reparametrisation [76, 77]. Detail accounts on the Jeffreys rule can be found in [78] and references therein. Geometric explanation of the Jeffreys approach is based on the key idea that natural volume elements generate homogenous measures in the sense that equal probability is assigned to regions having equal volumes [79]. Similar approach, given in [80] by Tarantola and adopted here, is based on the notion of a distance between parameters from which a volume element is deduced. In contrast to the Bayesian literature, Tarantola in [80] uses the name homogeneous distribution instead of noninformative distribution mainly to stress its relation to volume elements and the fact that it carries minimal, but existing information on the parameters.

Let $dV(\mathbf{x}) = v(\mathbf{x}) d\mathbf{x}$ be volume element of manifold \mathfrak{X} , where $\mathbf{x} \in \mathfrak{X}$. If $\mathcal{A} \subseteq \mathfrak{X}$ then volume of \mathcal{A} is:

$$V(\mathcal{A}) = \int_{\mathcal{A}} v(\mathbf{x}) d\mathbf{x}.$$

If \mathfrak{X} has a finite volume V then the homogeneous probability density function is $\nu(\mathbf{x}) = v(\mathbf{x})/V$. It assigns equal probability to $\mathcal{A} \subseteq \mathfrak{X}$ and $\mathcal{B} \subseteq \mathfrak{X}$ if they have the same volume, $V(\mathcal{A}) = V(\mathcal{B})$. If \mathfrak{X} has an infinite volume, the homogeneous probability density function is improper (it cannot be normalised). In that case one can simply take $\nu(\mathbf{x}) \propto v(\mathbf{x})$ as this generally causes no problems as long as one ensures that the posterior density functions are proper [76, 80]. The consequence of this definition is that the homogeneous probability density function does not need to be constant (take for example a volume element of the spherical coordinate system, $dV = r^2 \sin \theta dr d\theta d\varphi$).

A *posteriori* information in form of a posterior joint probability density function $\pi'(\mathbf{d}, \mathbf{m})$ can be obtained as:

$$\pi'(\mathbf{d}, \mathbf{m}) = k \frac{\pi(\mathbf{d}, \mathbf{m}) \theta(\mathbf{d}, \mathbf{m})}{\nu(\mathbf{d}, \mathbf{m})}. \quad (4.12)$$

Equation (4.12) is based on a notion of the conjunction of states of information (given as probability density functions), which bears intuitive resemblance to the “and” operation as described in [81]. It is quite general and first we will introduce some simplifications that are readily met in practical inverse problems.

The *a priori* information on model parameters is independent of observations. This is valid for both distributions, the prior and homogeneous, and we can write $\pi(\mathbf{d}, \mathbf{m}) = \pi(\mathbf{d}) \pi(\mathbf{m})$ and $\nu(\mathbf{d}, \mathbf{m}) = \nu(\mathbf{d}) \nu(\mathbf{m})$. The theoretical joint density function $\theta(\mathbf{d}, \mathbf{m})$ can be written as:

$$\theta(\mathbf{d}, \mathbf{m}) = \theta(\mathbf{d}|\mathbf{m}) \nu(\mathbf{m}).$$

Taking the above into the account, for the solution of the inverse problem, we have:

$$\pi'(\mathbf{d}, \mathbf{m}) = k \frac{\pi(\mathbf{d}) \pi(\mathbf{m}) \theta(\mathbf{d}|\mathbf{m})}{\nu(\mathbf{d})}. \quad (4.13)$$

We will assume that the wanted solution of the inverse problem is the marginal posterior probability density function for model parameters:

$$\pi'(\mathbf{m}) = \int_{\mathfrak{D}} \pi'(\mathbf{d}, \mathbf{m}) d\mathbf{d}. \quad (4.14)$$

Combining (4.13) and (4.14), we obtain a practicable version of (4.12) as:

$$\pi'(\mathbf{m}) = k \pi(\mathbf{m}) \int_{\mathfrak{D}} \frac{\pi(\mathbf{d}) \theta(\mathbf{d}|\mathbf{m})}{\nu(\mathbf{d})} d\mathbf{d} = k \pi(\mathbf{m}) L(\mathbf{m}), \quad (4.15)$$

where $L(\mathbf{m})$ is the likelihood function:

$$L(\mathbf{m}) = \int_{\mathfrak{D}} \frac{\pi(\mathbf{d})\theta(\mathbf{d}|\mathbf{m})}{\nu(\mathbf{d})} d\mathbf{d}. \quad (4.16)$$

Solution of the inverse problem can be given in a more familiar version of the Bayes theorem [82]. If we take that:

$$\pi'(\mathbf{m}|\mathbf{d}) = \frac{\pi'(\mathbf{d}, \mathbf{m})}{\pi(\mathbf{d})},$$

where we assumed equal marginal posterior and prior probability densities of the measurement data, we arrive to:

$$\pi'(\mathbf{m}|\mathbf{d}) \propto \pi(\mathbf{m})\theta(\mathbf{d}|\mathbf{m}),$$

which corresponds to the Bayes theorem for inverse problems [82]. More formal procedure for obtaining the Bayes theorem from (4.12) can be found in [81].

Conditional probability density functions are not invariant under coordinate transformations, as illustrated by the Borel-Kolmogorov paradox [83]. In order to avoid the problems arising in calculation of the conditioning limit as in [83], Tarantola et al. proposed (4.12) or its simplified version with the marginal probability density (4.15) [81, 84].

4.2.2 Gaussian theoretical and measurement uncertainties

An important case for application of (4.15) is when theoretical and measurement results are distributed normally. Instead of the exact theoretical relation $\mathbf{d} = \Gamma(\mathbf{m})$ we have the theoretical probability density function:

$$\theta(\mathbf{d}|\mathbf{m}) \propto \exp\left(-\frac{1}{2}(\mathbf{d} - \Gamma(\mathbf{m}))^T \mathbf{C}_T^{-1}(\mathbf{d} - \Gamma(\mathbf{m}))\right), \quad (4.17)$$

where \mathbf{C}_T is a covariance matrix that expresses uncertainties attributed to the theoretical relation $\Gamma(\cdot)$. Similarly, for the distribution of the measurement data we can write:

$$\pi(\mathbf{d}) \propto \exp\left(-\frac{1}{2}(\mathbf{d} - \bar{\mathbf{d}})^T \mathbf{C}_D^{-1}(\mathbf{d} - \bar{\mathbf{d}})\right), \quad (4.18)$$

where \mathbf{C}_D and $\bar{\mathbf{d}}$ is the covariance matrix and mean of the measurement data, respectively.

If we assume that \mathfrak{D} is a linear space, the homogeneous density function for the measurement data is $\nu(\mathbf{d}) = \text{const}$. Acknowledging that the covariance matrices are symmetric and positive-definite, it can be shown that combining (4.17) and (4.18) with (4.16) yields [80]:

$$L(\mathbf{m}) \propto \exp\left(-\frac{1}{2}(\Gamma(\mathbf{m}) - \bar{\mathbf{d}})^T \mathbf{C}_L^{-1}(\Gamma(\mathbf{m}) - \bar{\mathbf{d}})\right), \quad (4.19)$$

where:

$$\mathbf{C}_L = \mathbf{C}_D + \mathbf{C}_T. \quad (4.20)$$

Equations (4.19) and (4.20) show that theoretical and measurement uncertainties, if Gaussian, combine by addition of their covariance matrices into one Gaussian uncertainty with the covariance matrix \mathbf{C}_L .

4.2.3 Random and systematic uncertainties

Although our knowledge about the measurement data is described by a single probability density function $\pi(\mathbf{d})$ in the theory of stochastic inverse problems, we have to discuss briefly errors arising in the measurement process and their effect on our knowledge of the measurand. This will be very important for interpretation of the results of the proposed inversion procedure in Section 4.5 and for the discussion on the electronic instrumentation requirements in Chapter 6. Also, this discussion will serve us as a basis for generation of the synthetic data and for setting the numerical experiments conducted in order to illustrate the inversion procedure.

Imperfections in a measurement are caused by what is traditionally recognised as random and systematic effects [85]. By definition, random variations in the result of the measurement can be described using a probability density function with zero expected value. A part of the measurement uncertainty caused by the random effects is a random uncertainty.

A recognised effect of an influence quantity on a measurement result is a systematic effect. It can be quantified and compensated for using a correction procedure. It is generally assumed that the measurement result has been corrected for all recognised significant systematic effects. However, correction values are not perfectly known either. This introduces additional uncertainty in the corrected measurement result known as a systematic uncertainty [86]. All we know about a certain systematic effect is that it shifts the measurement result within a certain interval. Since the systematic effect are assumed constant during one measurement or experiment, we cannot say anything about the density function of the systematic uncertainty connected with a single systematic effect. The most pessimistic view is to assume uniform probability density function in the given interval. However, according to the central limit theorem we will have an asymptotic convergence to the normal distribution as the number of independent systematic effects is increased.

Thus, in a complex measurement setting, it is arguable that there is a number of independent systematic effects whose total contribution to the measurement is normally distributed. Using that assumption, the result of the correction procedure is a normally distributed random variable with the mean value equal to the corrected measurement result and the variance estimated to the best of one's knowledge [86]. If the correction procedure is good and the variance is determined correctly, the true value of the measurand will fall within some small interval around the corrected measurement result. What is precisely the error of the measurement cannot be known, since the true value

of the measurand is unknown. Both, random and systematic uncertainties can be determined using Type A and Type B evaluation according to [85]. The sum of two independent normally distributed random variables is normal, with the mean value equal to the sum of the two means, and the variance equal to the sum of the two variances.

From the above discussion and for the purpose of this thesis, we will assume that the measurand is a normally distributed random variable with the mean value equal to the measurement result corrected for the systematic effects and the variance equal to the sum of the variances of the random and systematic uncertainties. The distribution in question is $\pi(\mathbf{d})$. The true value of the measurand cannot be determined from the repeated measurements because the systematic uncertainties take on the same value each time, unless the setting and environment of the experiment is changed [86]. In the theory of the inverse problems, the summation of the random and systematic uncertainties can also be viewed in light of the summation of the Gaussian theoretical and measurement uncertainties in 4.2.2. The theoretical and systematic uncertainties are compatible notions since the correction procedure can be recognised either as a part of the model or processing of the raw measurement data.

4.3 Monte Carlo Markov chain methods

The posterior probability density function can be obtained by extensive exploration of the model space only in case of a very small number of dimensions and computationally very simple forward problems [80]. Monte Carlo methods are much more efficient since they result in samples of the posterior distribution from which all usual characteristics, like mean or standard deviation, can be determined [87, 88]. Monte Carlo methods such as importance sampling or rejection sampling require that we can sample from distributions that are similar to the targeted distribution and they are practical only for one-dimensional spaces [87]. Another possibility is a dependence sampling where next sample is drawn from a proposal distribution depending exclusively on the previous sample. Because of the dependence on the previous sample only, this random walk is a Markov chain. Dependence sampling methods based on the Markov process are called Monte Carlo Markov chain methods (MCMC) [89]. A distinguished example of MCMC methods is the Metropolis-Hastings algorithm, which is generalisation of the Gibbs and Metropolis sampling methods and a starting point for a number of other MCMC methods [90–93]. In the rest of this section we will explain the basic Metropolis-Hastings algorithm and its application to inverse problems.

4.3.1 Metropolis-Hastings algorithm

For the sake of a simpler notation, we will not use bold font to denote vectors in the description of the Metropolis-Hastings algorithm, although we should

bear in mind that multidimensionality is implied. Our objective is to generate samples from the absolutely continuous probability density $p(x) = kf(x)$ where $x \in \mathbb{R}^n$, $f(x)$ is unnormalised density and k is the normalising constant that can be unknown as we will see shortly. A proposal x' for the next sample $x^{(t)}$ is generated from a proposal density $q(x'; x^{(t-1)})$, e.g. $X' \sim N(x^{(t-1)}, \Sigma)$. The probability of accepting x' as the next sample is equal to:

$$\alpha(x'; x^{(t-1)}) = \min \left\{ \frac{f(x') q(x^{(t-1)}; x')}{f(x^{(t-1)}) q(x'; x^{(t-1)})}, 1 \right\}. \quad (4.21)$$

In practice, this is achieved by taking a realisation u of the uniformly distributed random variable in the interval $[0, 1]$. If $u \leq \alpha(x'; x^{(t-1)})$, the proposal is accepted, i.e. $x^{(t)} = x'$. Otherwise, the proposal is discarded and the next sample is the same as the previous one, $x^{(t)} = x^{(t-1)}$.

The result of N iterations of the Metropolis-Hastings algorithm is the Markov chain $\{x^{(1)}, x^{(1)}, \dots, x^{(N)}\}$ with the transition probability density equal to $q(x^{(t)}; x^{(t-1)}) \alpha(x^{(t)}; x^{(t-1)})$. Such a choice of the transition probability density and the acceptance rule (4.21) results in the stationary distribution of the Markov chain equal to the targeted distribution $p(x)$ [90]. Since the acceptance rule depends only on the ratio $p(x')/p(x^{(t-1)})$, the normalising constant k is not required.

The application of Metropolis-Hastings algorithm to the solution of an inverse problem is straight-forward. The posterior distribution, which we want to take samples from, is given by (4.15) and repeated here because of its importance:

$$\pi'(\mathbf{m}) = k\pi(\mathbf{m})L(\mathbf{m}). \quad (4.15)$$

The acceptance probability (4.21) in this case is:

$$\alpha(\mathbf{m}'; \mathbf{m}^{(t-1)}) = \min \left\{ \frac{\pi(\mathbf{m}')L(\mathbf{m}')q(\mathbf{m}^{(t-1)}; \mathbf{m}')}{\pi(\mathbf{m}^{(t-1)})L(\mathbf{m}^{(t-1)})q(\mathbf{m}'; \mathbf{m}^{(t-1)})}, 1 \right\}. \quad (4.22)$$

If the prior probability density function $\pi(\mathbf{m}')$ is uniform and $q(\mathbf{m}^{(t-1)}; \mathbf{m}') = q(\mathbf{m}'; \mathbf{m}^{(t-1)})$, we get the acceptance probability as in [80]:

$$\alpha(\mathbf{m}'; \mathbf{m}^{(t-1)}) = \min \left\{ \frac{L(\mathbf{m}')}{L(\mathbf{m}^{(t-1)})}, 1 \right\}.$$

In case of a non-uniform prior probability density function one can first obtain its sample by applying:

$$\alpha_1(\mathbf{m}'; \mathbf{m}^{(t-1)}) = \min \left\{ \frac{\pi(\mathbf{m}')q(\mathbf{m}^{(t-1)}; \mathbf{m}')}{\pi(\mathbf{m}^{(t-1)})q(\mathbf{m}'; \mathbf{m}^{(t-1)})}, 1 \right\},$$

and then accept it as a sample of the posterior distribution with probability:

$$\alpha_2(\mathbf{m}'; \mathbf{m}^{(t-1)}) = \min \left\{ \frac{L(\mathbf{m}')}{L(\mathbf{m}^{(t-1)})}, 1 \right\}.$$

This is the cascaded version of the algorithm that is, by induction, applicable to the product of any number of densities $\pi(\mathbf{m}) = k\pi_1(\mathbf{m})\pi_2(\mathbf{m})\dots\pi_n(\mathbf{m})$ [80].

4.3.2 MCMC output analysis

The elements of the resultant Markov chain are samples of the posterior distribution after the chain reaches the equilibrium. The elements in the burn-in phase before the chain reached the equilibrium are discarded. The formal analysis of duration of the burn-in phase does not seem necessary in practice in which the burn-in phase is determined visually followed by the routine discarding of at least 1% or 2% of a run [94, 95].

The acceptance ratio, i.e. the ratio of the accepted proposals and the total number of samples is a crucial indication of the quality of the sampler. A very high acceptance ratio can indicate that the proposal distribution generates samples only within a small region of the parameter space and that we don't explore the space fast enough. A very low acceptance ratio can indicate that we waste computational resources to test the samples with the low likelihood. The acceptance ratio depends directly on the width of the proposal distribution (smaller steps — higher acceptance ratio). The rule of thumb says that the acceptance ratio should be about 20% to 50%. For the normal posterior and proposal densities the acceptance ratio should be about 45% for a one-dimensional case and around 25% for as low as six dimensions, whereas the limit for infinite number of dimensions is around 23% [92, 96]. However, it will be sometimes necessary to design the sampler with as low as 10% acceptance ratio in order to achieve lower autocorrelations, as discussed below [88].

The law of large numbers holds for any ergodic Markov chain [89]. This means that for the ergodic Markov chain $\{X_1, \dots, X_N\}$ with a stationary distribution $p(x)$ and for a statistic $f(\cdot)$ we can estimate the expectation $E_p(f(X))$ by averaging the Markov chain [89]:

$$\lim_{N \rightarrow \infty} \bar{f}_N = \lim_{N \rightarrow \infty} \frac{1}{N} \sum_{k=1}^N f(X_k) = E_p(f(X)). \quad (4.23)$$

In practice, (4.23) is usually used for estimation of the mean and variance of $X \sim p(x)$.

Average \bar{f}_N is a random variable (because we will always get different set of N realisations of X), which, according to the central limit theorem weakly converges to a normal distribution with zero mean and variance σ_f^2 [89, 94, 95]:

$$\sqrt{N}(\bar{f}_N - E_p(f(X))) \xrightarrow[N \rightarrow \infty]{\mathcal{D}} \mathcal{N}(0, \sigma_f^2).$$

If the realisations of X are independent, variance of the estimator \bar{f}_N is:

$$\sigma_f^2 = \frac{\text{var}(f(X))}{N}.$$

For dependent realisations of X , such as the Markov chain $\{X_1, \dots, X_N\}$, variance of the estimator \bar{f}_N is larger for τ_f [94]:

$$\sigma_f^2 = \frac{\tau_f \text{var}(f(X))}{N},$$

where τ_f is called the integrated autocorrelation time (IACT) in physics literature or autocovariance time in statistics literature [97]. It can be shown that:

$$\tau_f = 1 + 2 \sum_{s=1}^{\infty} \rho_{ff}(s), \quad (4.24)$$

where $\rho_{ff}(s)$ is the normalised autocovariance function:

$$\rho_{ff}(s) = \frac{C_{ff}(s)}{C_{ff}(0)} = \frac{\text{cov}(f(X_n), f(X_{n+s}))}{\text{cov}(f(X_n), f(X_n))}.$$

The autocovariance function of a stationary stochastic process does not depend on the position n and for finite-length sequences it can be approximated using:

$$C_{ff}(s) = \frac{1}{N} \sum_{n=1}^N f(x^{(n)}) f(x^{(n+s)}) - \frac{1}{N^2} \left[\sum_{n=1}^N f(x^{(n)}) \right]^2. \quad (4.25)$$

In practice, the normalised autocovariance ρ_{ff} is calculated using the finite-length approximation (4.25). Since $\lim_{s \rightarrow \infty} \rho_{ff}(s) = 0$, we can let $\rho_{ff}(s) = 0, \forall s \geq M$, which avoids effects of numerical summation errors in the calculation of τ_f [97]. Thus, the autocovariance time is usually determined using:

$$\tau_f = 1 + 2 \sum_{s=1}^M \rho_{ff}(s). \quad (4.26)$$

There are several methods for evaluation of M , but a good and simple approximation is to use lag s at which ρ_{ff} reaches the abscissa [94, 95, 97].

If the elements of the ergodic Markov chain are N_d -dimensional vectors $\{\mathbf{X}^{(i)}\}_{i=1}^N, \mathbf{X}^{(i)} \in \Omega \subset \mathbb{R}^{N_d}$, they are distributed according to the stationary distribution $\mathbf{X}^{(i)} \sim p(\mathbf{x})$ in the equilibrium. The chain's ergodicity allows us very simple calculation of the marginal distribution of each component of $\mathbf{X}^{(i)}$ without numerical integration of the joint distribution $p(\mathbf{x})$ [95]. Elements of the chain taken separately for each of the components $\{x_j^{(i)}\}_{i=1}^N, j = 1, \dots, N_d$ are samples of the corresponding marginal distributions $p_j(x_j), j = 1, \dots, N_d$, that is to say:

$$X_j \sim p_j(x_j), \quad j = 1, \dots, N_d,$$

where:

$$p_j(x_j) = \int_{\Omega_1} \dots \int_{\Omega_{N_d}} p(\mathbf{x}) dx_1 \dots dx_{j-1} dx_{j+1} \dots dx_{N_d}.$$

From the above theoretical considerations, we are now in position to summarise the apparatus we will use in the analysis of the output of the MCMC simulations in section 4.5:

1. Burn-in phase is determined visually and we routinely discard at least 5% of a run.
2. The acceptance ratio is targeted between 10% and 25% because of the multidimensionality and in order to achieve lower autocovariance times.
3. Samples of the marginal distribution of a component of the resulting Markov chain can be obtained discarding the remaining components of the chain because of its ergodicity.
4. Stationarity and ergodicity of the resulting Markov chain allows us to estimate the expectation of a statistic by the simple averaging of the chain.
5. The variance of the estimators is calculated using the central limit theorem for Markov chains, namely the autocovariance time.
6. The efficiency of the sampling process is determined by observing the normalised autocovariance and the autocovariance time. We want rapidly decreasing autocovariance and low values of the autocovariance time.
7. We will use histograms in visualisation of the marginal distributions. All elements of the chain are countable because of the chain's ergodicity and stationarity.

4.4 Formulation of the inverse problem

In this section, we will adapt the theoretical foundations developed in the previous sections of this chapter to the inverse problem of determination of the casing properties and conductivity of the surrounding formation. First, we will parameterise the model space \mathfrak{M} and the data space \mathfrak{D} . Coordinates in the model space are casing's relative magnetic permeability μ_r , electrical conductivity σ_t , wall thickness c and conductivity of the homogeneous surrounding formation σ_f . The vector of the model parameters is:

$$\mathbf{m} = \begin{bmatrix} \mu_r \\ \sigma_t \\ c \\ \sigma_f \end{bmatrix}.$$

Coordinates in the data space are the measured real and imaginary parts of the magnetic field at several distances from a single transmitter coil. The vector

of distance is $\mathbf{z} = [z_1 \ z_2 \ \dots \ z_n]^T$ and the vector of the measured data is:

$$\mathbf{d} = \begin{bmatrix} B_{re}(z_1) \\ B_{im}(z_1) \\ B_{re}(z_2) \\ B_{im}(z_2) \\ \vdots \\ B_{re}(z_n) \\ B_{im}(z_n) \end{bmatrix}, \quad (4.27)$$

where indices *re* and *im* denote real and imaginary parts, respectively.

4.4.1 A priori information

We will assume that we have quite elementary information on the model parameters in form of their minimum and maximum values. Although from theoretical analysis in section 3.2.3 we can introduce some correlations between the casing properties through the casing factor and permeability-to-conductivity ratio, we chose not do so. Introduction of such a knowledge would most likely require some first, rough analysis of the measurement data and that would violate our assumption of independency between *a priori* information on model parameters and observations, see section 4.2.1 and [80].

Electrical conductivity and resistivity are a Jeffreys pair, meaning that we have to treat them symmetrically [80]. This is satisfied by the logarithmic distance between two samples of a casing or formation defined as $|\log(\sigma_2/\sigma_1)|$ or equivalently $|\log(\rho_2/\rho_1)|$. Thus, the homogeneous probability density function for electrical conductivity is uniform for $\log(\sigma)$, i.e. proportional to $1/\sigma$. This fits well with the levelsets — casing factor and permeability-to-conductivity ratio, whose logarithmic values depend linearly on the logarithmic values of the casing properties. We will use logarithmic distance and log-uniform homogeneous probability density function for relative magnetic permeability because it is also a Jeffreys quantity logarithmically connected with the casing conductivity through PCR. Since the expected values of the wall thickness c are only a small fraction of the casing's radii we choose the uniform homogeneous density for c .

We can finally state the chosen prior probability density of the parameters. Let M_0 be the set defined by the specified minimum and maximum values:

$$M_0 = \{\mathbf{m} \mid (\mu_{r,min} \leq \mu_r \leq \mu_{r,max}) \wedge (\sigma_{t,min} \leq \sigma_t \leq \sigma_{t,max}) \wedge (c_{min} \leq c \leq c_{max}) \wedge (\sigma_{f,min} \leq \sigma_f \leq \sigma_{f,max})\}.$$

The joint prior probability density of the model parameters is the product of the corresponding marginal probability densities:

$$\pi(\mathbf{m}) = \begin{cases} \frac{k}{\mu_r \sigma_t \sigma_f} & \text{if } \mathbf{m} \in M_0, \\ 0 & \text{otherwise,} \end{cases}$$

where k is the normalisation constant.

Typical values of the properties of the oil-well casings are standardised and tabulated [13]. We assume that information available from the oil-well casing completion plans is reliable enough to allow us formulation of the *a priori* intervals based on the casing standards [14]. These intervals can be further narrowed by other inspection methods.

4.4.2 Measurement data

We will assume that the measurement data \mathbf{d} given by (4.27) have Gaussian uncertainties defined by the covariance matrix \mathbf{C}_L . According to the discussion in sections 4.2.2 and 4.2.3, these uncertainties include both random and systematic (theoretical) uncertainties. In the situation of a perfect knowledge, without random and theoretical uncertainties, the modelling result would be equal to the measurement result. We will denote this value with \mathbf{d}_0 . In a realistic situation under Gaussian assumption, the measurement result is given as $\mathbf{d} \sim \mathcal{N}(\bar{\mathbf{d}}, \mathbf{C}_L)$, what results in the likelihood $L(\mathbf{m})$ given by (4.19).

4.4.3 Transition probability distribution

Correlation of the casing properties through the strong dependance of the magnetic field on the permeability-to-conductivity ratio and casing factor must be reflected in our choice of the proposal density function $q(\mathbf{m}'; \mathbf{m}^{(t-1)})$ if we want to construct the effective Metropolis-Hastings sampler. Simple choice of the mutually independent random walks for the four dimensions of the parameter space result in a very low acceptance ratio or high autocovariance of the resultant Markov chain.

Instead of using the chosen parametrisation of \mathfrak{M} for construction of the random walk, we will propose new samples \mathbf{m}' by making a move in \mathfrak{M} parameterised by:

$$\mathbf{m}^* = \begin{bmatrix} \log C_f \\ \log \text{PCR} \\ \log c \\ \log \sigma_f \end{bmatrix},$$

from which we easily calculate \mathbf{m} . The random walk can be defined using the normal distribution with mean \mathbf{m}^* and covariance matrix \mathbf{K} :

$$\mathbf{m}^{*'} \sim \mathcal{N}(\mathbf{m}^*, \mathbf{K}).$$

The covariance matrix \mathbf{K} is diagonal:

$$\mathbf{K} = \begin{bmatrix} k_{cf}^2 & 0 & 0 & 0 \\ 0 & k_{pcr}^2 & 0 & 0 \\ 0 & 0 & k_c^2 & 0 \\ 0 & 0 & 0 & k_{form}^2 \end{bmatrix}.$$

For easier notation, we define $\mathbf{k} = [k_{cf} \ k_{pcr} \ k_c \ k_{form}]^T$.

Because the logarithmic values of C_f and PCR are linearly related to the logarithmic values of μ_r , σ_t and c , the proposal distribution can be written as:

$$\mathbf{m}'_L \sim \mathcal{N}(\mathbf{m}_L, \mathbf{H}\mathbf{K}\mathbf{H}^T),$$

where $\mathbf{m}_L = [\log \mu_r \ \log \sigma_t \ \log c \ \log \sigma_f]^T$ and:

$$\mathbf{H} = \begin{bmatrix} 1 & 1/2 & -1 & 0 \\ 1 & -1/2 & -1 & 0 \\ 0 & 0 & 1 & 0 \\ 0 & 0 & 0 & 1 \end{bmatrix}.$$

Matrix \mathbf{H} satisfies $\mathbf{m}_L = \mathbf{H}\mathbf{m}^*$.

The proposal probability density function is not symmetric for the parametrisation \mathbf{m} , i.e. $q(\mathbf{m}'; \mathbf{m}^{(t-1)}) \neq q(\mathbf{m}^{(t-1)}; \mathbf{m}')$. Because the distribution is log-normal, following holds:

$$\frac{q(\mathbf{m}^{(t-1)}; \mathbf{m}')}{q(\mathbf{m}'; \mathbf{m}^{(t-1)})} = \frac{\mu'_r \sigma'_t c' \sigma'_f}{\mu_r^{(t-1)} \sigma_t^{(t-1)} c^{(t-1)} \sigma_f^{(t-1)}}. \quad (4.28)$$

4.4.4 Metropolis-Hastings algorithm

We will use the cascaded version of the Metropolis-Hastings algorithm. In the first step we need to determine whether a proposal comes from the prior distribution. For the prior density, we have $\pi(\mathbf{m}) \propto 1/(\mu_r \sigma_t \sigma_f)$, $\forall \mathbf{m} \in M_0$. Taking this and (4.28) into account, the acceptance probability for the prior distribution is:

$$\begin{aligned} \alpha_1(\mathbf{m}'; \mathbf{m}^{(t-1)}) &= \min \left\{ \frac{\pi(\mathbf{m}') q(\mathbf{m}^{(t-1)}; \mathbf{m}')}{\pi(\mathbf{m}^{(t-1)}) q(\mathbf{m}'; \mathbf{m}^{(t-1)})}, 1 \right\} = \\ &= \min \left\{ \frac{c'}{c^{(t-1)}}, 1 \right\}. \end{aligned} \quad (4.29)$$

Equation (4.29) is valid for $\mathbf{m}' \in M_0$, whereas for $\mathbf{m}' \notin M_0$ the acceptance probability is $\alpha_1(\mathbf{m}'; \mathbf{m}^{(t-1)}) = 0$. In the second step, the proposal is accepted as a sample of the posterior distribution with probability:

$$\alpha_2(\mathbf{m}'; \mathbf{m}^{(t-1)}) = \min \left\{ \frac{L(\mathbf{m}')}{L(\mathbf{m}^{(t-1)})}, 1 \right\}, \quad (4.30)$$

where $L(\mathbf{m})$ is calculated from (4.20). Pseudocode of the inversion procedure is shown in Algorithm 3.

Algorithm 3 Monte Carlo Markov chain inversion procedure for determination of the casing properties and conductivity of the surrounding formation

Require: $\bar{\mathbf{d}}, \mathbf{C}_L, \mathbf{z}, \mathbf{m}^{(1)}, M_0, N$, for additional requirements see Algorithms 1 and 2.

Ensure: Markov chain $\{\mathbf{m}^{(1)}, \mathbf{m}^{(2)}, \dots, \mathbf{m}^{(N)}\}$ with the stationary distribution $\pi'(\mathbf{m})$

```

1: for  $t = 2$  to  $N$  do
2:   Generate proposal  $\mathbf{m}'$  from  $\mathcal{N}(\mathbf{m}_L^{(t-1)}, \mathbf{H}\mathbf{K}\mathbf{H}^T)$ 
3:   if  $\mathbf{m}' \in M_0$  then
4:     Calculate  $\alpha_1(\mathbf{m}'; \mathbf{m}^{(t-1)})$  using (4.29)
5:   else
6:      $\alpha_1 = 0$ 
7:   end if
8:   Draw  $u \sim \mathcal{U}(0, 1)$ 
9:   if  $u > \alpha_1$  then
10:    Reject the proposal
11:    Copy the previous sample,  $\mathbf{m}^{(t)} \leftarrow \mathbf{m}^{(t-1)}$ 
12:   else
13:    Calculate the forward problem for  $\mathbf{m}'$  // The most time-consuming section! See Algorithms 1 and 2.
14:    Calculate the likelihood  $L(\mathbf{m}')$  using (4.19)
15:    Calculate  $\alpha_2(\mathbf{m}'; \mathbf{m}^{(t-1)})$  using (4.30)
16:    Draw  $u \sim \mathcal{U}(0, 1)$ 
17:    if  $u > \alpha_2$  then
18:      Reject the proposal
19:      Copy the previous sample,  $\mathbf{m}^{(t)} \leftarrow \mathbf{m}^{(t-1)}$ 
20:    else
21:      Accept the proposal as a sample of the posterior distribution,
       $\mathbf{m}^{(t)} \leftarrow \mathbf{m}'$ 
22:      Increase the number of accepted samples,  $a \leftarrow a + 1$ 
23:    end if
24:   end if
25: end for
26: Calculate the acceptance ratio,  $a/N$ 

```

4.5 Solution of the inverse problem

In this section we will apply the presented stochastic formulation of the inverse problem for the synthetic data generated using the forward model. Detailed output analysis will be made for introductory example in section 4.5.1. In sections 4.5.2 and 4.5.3 we answer the two very important questions:

1. What is the maximal uncertainty of the magnetic field measurement that satisfies given criteria of useful inference about the formation conductivity?
2. How big is the effect of the systematic (theoretic) uncertainties?

Although we will use only one casing in the following analysis, this does not weaken the generality of the conclusions because of the two reasons. Firstly, the effects of the casing and the surrounding formation are separable for a large interval of the casing properties as shown in section 3.3. Secondly, the permeability-to-conductivity ratio and casing factor are stable forms of the levelset for the direct and remote zone, respectively, which are in turn scalable with the casing's inner radius and relatively insensitive to other casing's properties, see section 3.2.3 and references therein.

The casing used in the following sections is $C(100 \text{ mm}, 10 \text{ mm}, 4.6 \text{ MS/m}, 100)$. Radius of the transmitter and the receiver coils is 80 mm. The three receivers are positioned at distances $\mathbf{z} = [0.15 \text{ m } 0.9 \text{ m } 5 \text{ m}]^T$. Excitation frequency is 60 Hz. The measurement covariance matrix is:

$$\mathbf{C}_{\mathbf{L}} = p_B^2 \begin{bmatrix} |B_1|^2 & 0 & 0 & 0 & 0 & 0 \\ 0 & |B_1|^2 & 0 & 0 & 0 & 0 \\ 0 & 0 & |B_2|^2 & 0 & 0 & 0 \\ 0 & 0 & 0 & |B_2|^2 & 0 & 0 \\ 0 & 0 & 0 & 0 & |B_3|^2 & 0 \\ 0 & 0 & 0 & 0 & 0 & |B_3|^2 \end{bmatrix},$$

where p_B is the relative measurement uncertainty.

The form of $\mathbf{C}_{\mathbf{L}}$ is such that the variances of the real and imaginary parts of the magnetic field are proportional to the absolute value of the magnetic field. This stems from the fact that both measurements for a receiver are made by comparing a record of the receiver signal with the orthogonal reference signals using the digital lock-in technique, see Chapter 6. Strictly speaking, this introduces covariances between measurements of the real and imaginary parts. However, it makes a little difference in the final results because of the similar levelsets for real and imaginary parts of the magnetic field, see Figs. 3.20 and 3.21 in section 3.2.3. For the sake of simplicity, we assumed independent measurements and the same relative measurement uncertainty p_B for all receivers. Matrix $\mathbf{C}_{\mathbf{L}}$ is calculated for the true values of the casing properties.

The boundaries that define our prior knowledge are:

$$M_0 = \{\mathbf{m} \mid (20 \leq \mu_r \leq 300) \wedge (1 \text{ MS/m} \leq \sigma_t \leq 7 \text{ MS/m}) \wedge (1 \text{ mm} \leq c \leq 20 \text{ mm}) \wedge (10^{-3} \text{ S/m} \leq \sigma_f \leq 10 \text{ S/m})\}.$$

The boundaries of the casing properties can be corroborated by the available literature [13, 14, 48, 68]. Furthermore, the chosen prior intervals are much wider than the posterior intervals obtained from the measurements with the expected uncertainties—consequently, the prior intervals have the minimal effect on the posterior knowledge. The conductivity of the formations of interest may range from 10^{-3} S/m (e.g. “tight” limestone, oil sand) to 2 S/m (e.g. clay, shale, saltwater sand), see section 3.3 in [1]. Our choice of the prior interval for formation conductivity acknowledge the range for typical formations from [1] as well as no available additional information of the formation in question.

4.5.1 Introductory example

In this section we show detailed output analysis for the case of the total measurement uncertainty $p_B = 10^{-3}$ and formation conductivity $\sigma_f = 1$ S/m. The parameters of the proposal distribution are given in Table 4.1. These parameters are obtained experimentally by observing the acceptance ratio of a number of short MCMC runs ($N < 10000$). The final acceptance ratio is about 17%. The large value of coefficient k_{form} , which controls the variance of the formation-conductivity component of the proposal distribution, reflects our expectation of the large statistical dispersion of the posterior distribution of the formation conductivity. In order to achieve faster convergence of the simulation, k_{form} can be adaptively changed under the condition that one keeps only the elements of the chain corresponding to the last value of k_{form} [98].

The four components of the Markov chain obtained in MCMC run 1 ($N = 250000$) are depicted in Fig. 4.3. The burn-in phase lasts for approximately 20000 iterations, but we discarded the first 50000 iterations prior to the further analysis. Fig. 4.4 shows the random walk in the space of the casing parameters μ_r , σ_t and c .

The autocovariance functions are shown in Fig. 4.5. The zero-crossings for all four parameters are around 550, what indicates the length of the sum in (4.26) for calculation of the autocovariance time shown in Fig. 4.6. The exact values for autocovariance zero-crossings and IACT are given in Table 4.2. The largest value of the autocovariance time $\tau_f = 295$ indicates that it is enough

Table 4.1: Parameters of the proposal distribution for the introductory example.

Run	$p_B/10^{-3}$	σ_f/Sm^{-1}	k_{cf}	k_{pcr}	k_c	k_{form}
1	1	1	$2.5 \cdot 10^{-4}$	$3 \cdot 10^{-3}$	$1 \cdot 10^{-2}$	0.6

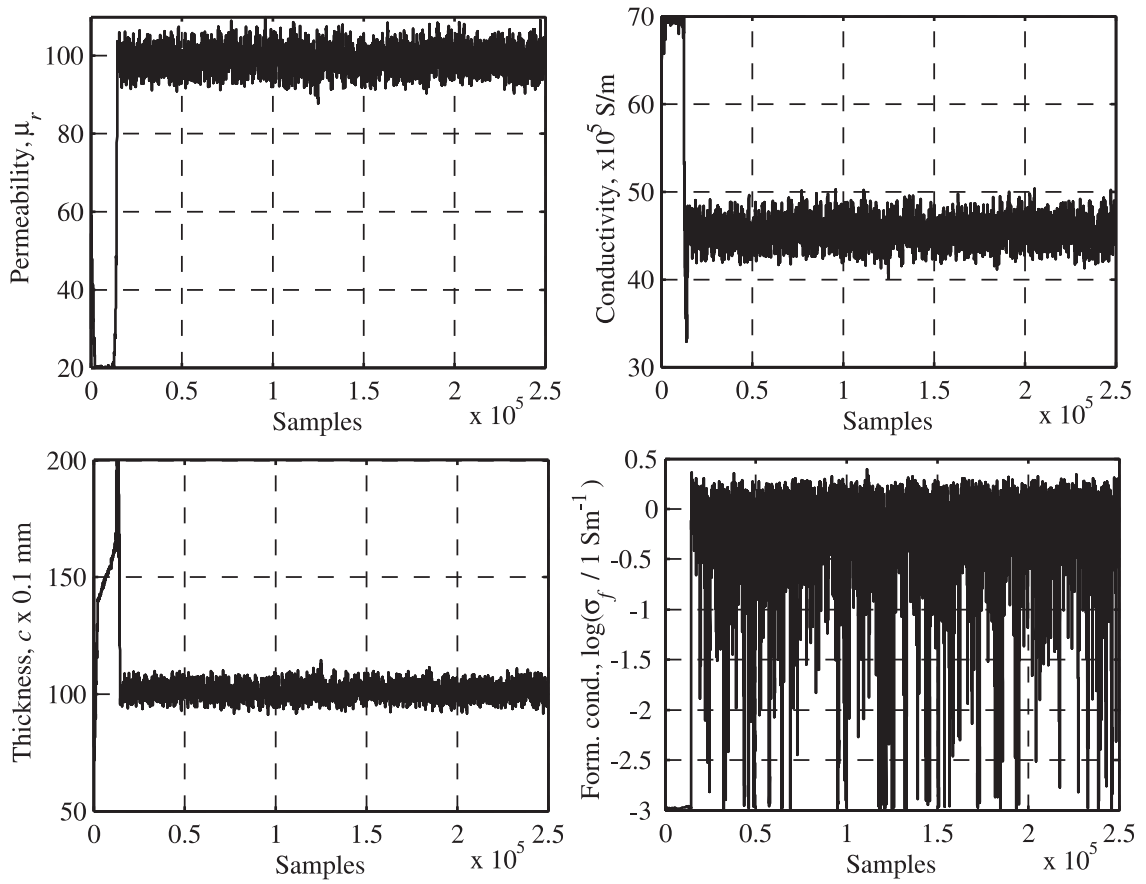


Figure 4.3: MCMC run 1 with the burn-in phase shown. Starting point is $C_0(100 \text{ mm}, 15 \text{ mm}, 3 \text{ MS/m}, 30)$ and $\sigma_f = 10^{-3} \text{ S/m}$.

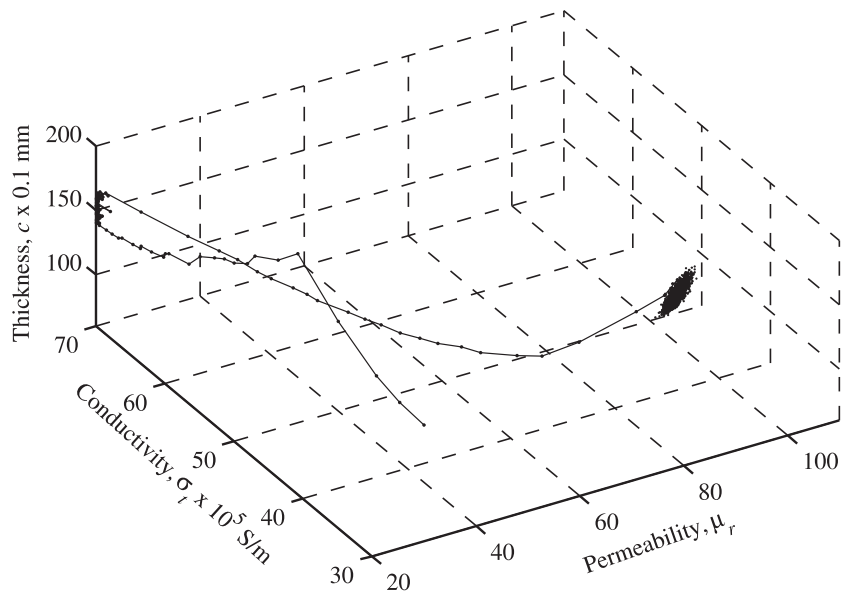


Figure 4.4: Random walk in the space of parameters μ_r , σ_t and c , see Fig. 4.3.

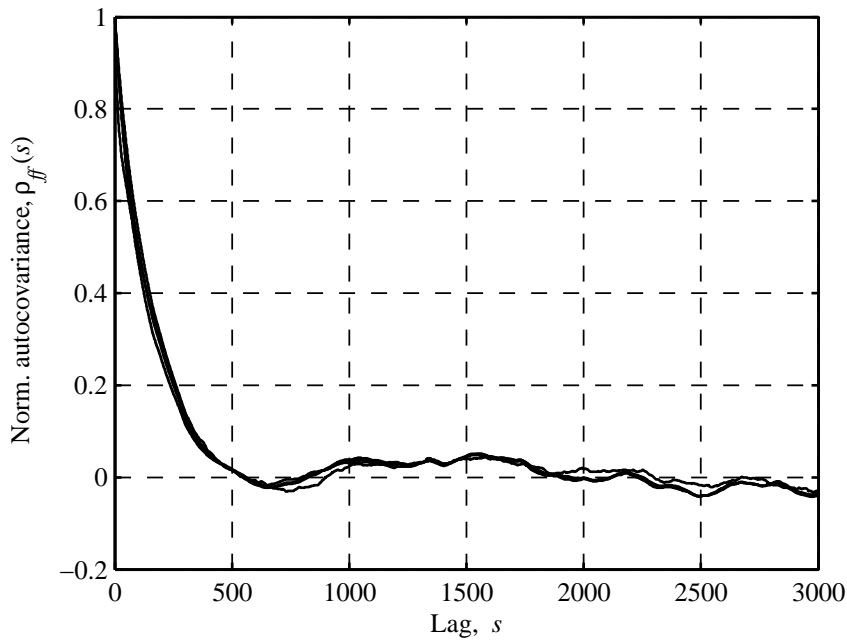


Figure 4.5: Autocovariance functions for the chains in Fig. 4.3, Table 4.2.

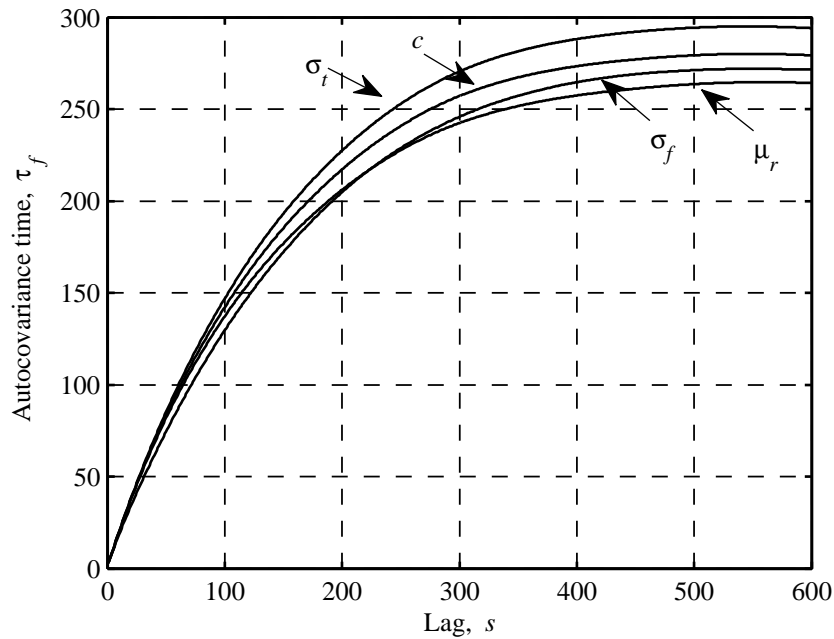


Figure 4.6: Autocovariance time for the chains in Fig. 4.3, Table 4.2.

to take every 300-th element of the Markov chain in order to get independent samples of the posterior distribution.

The normalised histograms of the marginal posterior distributions of the model parameters are shown in Fig. 4.7. Normality hypothesis for the posterior distributions of $\log \mu_r$, $\log \sigma_f$ and c cannot be rejected by the Kolmogorov-Smirnov test at 5% significance level. The posterior distribution of the for-

Table 4.2: Introductory example. Sampling efficiency: acceptance ratio, autocovariance zero-crossing and autocovariance time.

Run	$p_B/10^{-3}$	σ_f/Sm^{-1}	a_r	ρ_{ZC}				IACT			
				μ_r	σ_t	c	σ_f	μ_r	σ_t	c	σ_f
1	1	1	17%	562	546	552	550	265	295	280	272

mation conductivity shows the heavy tail in the direction of decreasing conductivities due to the chosen prior distribution proportional to $1/\sigma_f$, as well as relatively high measurement uncertainty, see section 4.5.2. Because of the normality of posterior distributions for the casing parameters, we will use the mean and standard deviation as measures of the central tendency and dispersion. In case of the formation conductivity, we will use mode, if it can be determined, and different quantiles, e.g 10% or 90% of all samples.

Table 4.3 shows the central tendency and dispersion measures of the posterior marginal distributions of the model parameters. The relative error of the mean values of the casing parameters compared to the true values is less

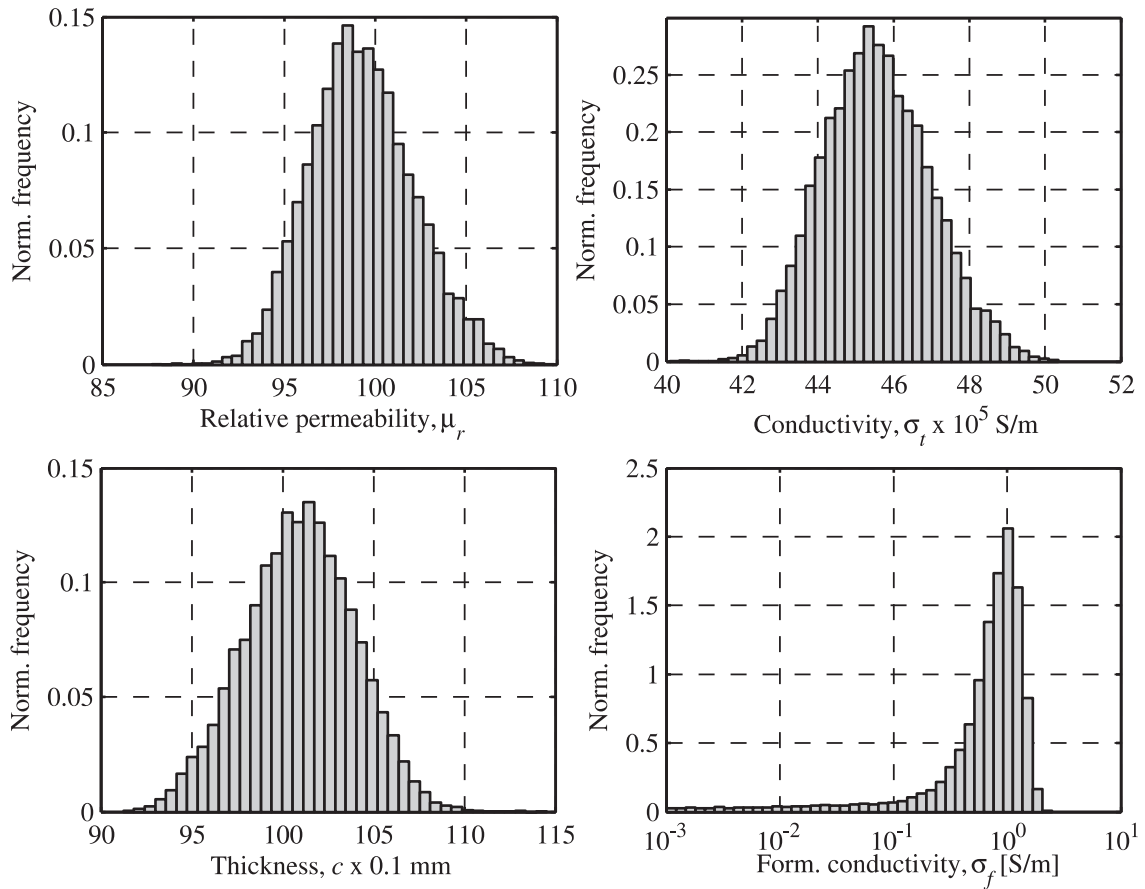


Figure 4.7: Normalised histograms of the marginal posterior distributions of the model parameters.

4.5 Solution of the inverse problem

Table 4.3: Introductory example. Properties of the marginal posterior distributions. Multipliers: casing conductivity – 10^5 S/m, casing thickness – 0.1 mm, formation conductivity – 1 S/m, casing factor – $1 \sqrt{\text{Sm}}$, PCR – $1 \mu\Omega\text{m}$.

Run	1
Mean	
$\bar{\mu}_r$	99.3
$\bar{\sigma}_t$	45.57
\bar{c}	100.9
\bar{C}_f	214.513
$\overline{\text{PCR}}$	21.795
Standard deviation	
s_{μ_r}	2.8
s_{σ_t}	1.41
s_c	3.0
s_{C_f}	0.088
s_{PCR}	0.170
St. dev. of mean	
$s_{\bar{\mu}_r}$	0.1
$s_{\bar{\sigma}_t}$	0.05
$s_{\bar{c}}$	0.1
$s_{\bar{C}_f}$	0.003
$s_{\overline{\text{PCR}}}$	0.006
Mode of $\pi'(\sigma_f)$	1.005
Quantiles of $\pi'(\sigma_f)$	
10%	0.174
25%	0.506
50%	0.814
75%	1.094
90%	1.338

than 1%. Standard deviations of the casing properties is around 3% relatively to the true values. However, a complete picture about the effect of the measurement uncertainty on the uncertainty of the casing properties will be obtained in section 4.5.2 with introduction of the measurement error — difference between the corrected value and the true value of the measurand, see section 4.2.2. Standard deviation of the mean estimator for μ_r and c is around 0.1, indicating that the number of samples and achieved autocovariance times are appropriate for the mean estimation up to the first decimal place. The

mode of the posterior density function for the formation conductivity is close to the true value of 1 S/m. More than 80% of the samples of the posterior distribution is between 0.5 S/m to 1.5 S/m or 0.5 decades out of four decades of the prior interval (1 mS/m – 10 S/m). The relative standard deviation for the casing factor is only 0.04% and 0.7% for PCR, what confirms that the procedure for determination of the casing's lump parameters is well-conditioned, see section 4.1.

4.5.2 Maximal measurement uncertainty

A very important question for the discussion of the practical realisability of the formation conductivity evaluation is about the maximal uncertainty of the magnetic field measurement that satisfies some given criteria of useful inference about the formation conductivity. As a criterium, we take the difference between the posterior marginal distributions of the formation conductivity for two true values of the formation conductivity, 0.1 S/m and 1 S/m. An acceptable level of the measurement uncertainty is one for which we can differentiate between the two formations.

We investigate the uncertainty levels of 10^{-4} , 10^{-3} , $2 \cdot 10^{-3}$, and $5 \cdot 10^{-3}$ (8 runs). Details on the simulations and the corresponding proposal distributions are given in Table 4.4. The autocovariance zero-crossings and IACT are given in Table 4.5.

Table 4.4: MCMC simulations for the analysis of max. measurement uncertainty. Parameters of the proposal distribution.

Run	$p_B/10^{-3}$	σ_f/Sm^{-1}	k_{cf}	k_{pcr}	k_c	k_{form}
2	0.1	0.1	$3 \cdot 10^{-5}$	$5 \cdot 10^{-4}$	$1.5 \cdot 10^{-3}$	0.3
3	0.1	1	$3 \cdot 10^{-5}$	$5 \cdot 10^{-4}$	$1.5 \cdot 10^{-3}$	0.05
4	1	0.1	$2.5 \cdot 10^{-4}$	$3 \cdot 10^{-3}$	10^{-2}	0.5
5	1	1	$2.5 \cdot 10^{-4}$	$3 \cdot 10^{-3}$	10^{-2}	0.5
6	2	0.1	$5 \cdot 10^{-4}$	$6 \cdot 10^{-3}$	$2 \cdot 10^{-2}$	0.75
7	2	1	$5 \cdot 10^{-4}$	$6 \cdot 10^{-3}$	$2 \cdot 10^{-2}$	0.75
8	5	0.1	$1.25 \cdot 10^{-3}$	$1.5 \cdot 10^{-2}$	$5 \cdot 10^{-2}$	1
9	5	1	$1.25 \cdot 10^{-3}$	$1.5 \cdot 10^{-2}$	$5 \cdot 10^{-2}$	1

Figs. 4.8–4.11 depict the normalised histograms of the marginal posterior distributions $\pi'(\sigma_f)$ for the four values of the measurement uncertainty. From the figures, one can immediately observe that the maximal measurement uncertainty in the sense of the above criterium is between $2 \cdot 10^{-3}$ and $5 \cdot 10^{-3}$, Figs. 4.10 and 4.11. With increase in the measurement uncertainty, the posterior density functions of the formation conductivity transform from the gaussian to uniform shape. The posterior distribution for 0.1 S/m has no distin-

4.5 Solution of the inverse problem

guished mode already at $p_B = 10^{-3}$, Fig. 4.9. Using two-sample Kolmogorov-Smirnov test to compare the posterior distributions for 0.1 S/m and 1 S/m, one can reject the hypothesis that the distributions are the same at 5% significance level. However, the p-value of the test for the case of $p_B = 6 \cdot 10^{-3}$ (not shown here) is 0.022 indicating that $p_B = 5 \cdot 10^{-3}$ is the largest uncertainty at which we can at least hope to establish differences between 0.1 S/m and 1 S/m.

Table 4.5: MCMC simulations for the analysis of max. measurement uncertainty. Sampling efficiency: acceptance ratio, autocovariance zero-crossing and autocovariance time.

Run	p_B $\times 10^{-3}$	σ_f [S/m]	a_r	ρ_{ZC}				IACT			
				μ_r	σ_t	c	σ_f	μ_r	σ_t	c	σ_f
2	0.1	0.1	17%	710	790	781	1700	207	263	241	360
3	0.1	1	12%	456	453	453	497	149	171	162	141
4	1	0.1	27%	297	311	300	568	99	104	101	185
5	1	1	19%	1554	1630	1570	1800	331	385	365	360
6	2	0.1	26%	359	352	352	524	103	107	104	111
7	2	1	24%	485	499	492	621	166	199	179	234
8	5	0.1	25%	256	245	252	176	92	87	87	69
9	5	1	25%	251	321	321	451	103	107	101	113

Table 4.6 contains properties of the marginal posterior distributions. Only at $p_B = 10^{-4}$ is the mode of the posterior distribution well-defined for both conductivities 0.1 S/m and 1 S/m. The insensitivity to low values of the formation conductivity is apparent in Figs. 4.8–4.11. Besides the histogram and depending on the measurement uncertainty, the result of the inversion procedure for the formation conductivity can be described using a quantile range or as the interval bounded from above by a quantile. For $p_B = 10^{-3}$, 90% of the samples are below 0.257 S/m for the true value of 0.1 S/m, or below 1.291 S/m for the true value of 1 S/m. As it can be seen from Table 4.6, such a description of the marginal posterior distribution of the formation conductivity is applicable for $p_B < 2 \cdot 10^{-3}$. For higher uncertainties, the resolution of the formation conductivity is unacceptably low. The relative standard deviations of μ_r , σ_t and c increase linearly with the measurement uncertainty by a factor of approximately 22. The casing factor and PCR are given in Table 4.7.

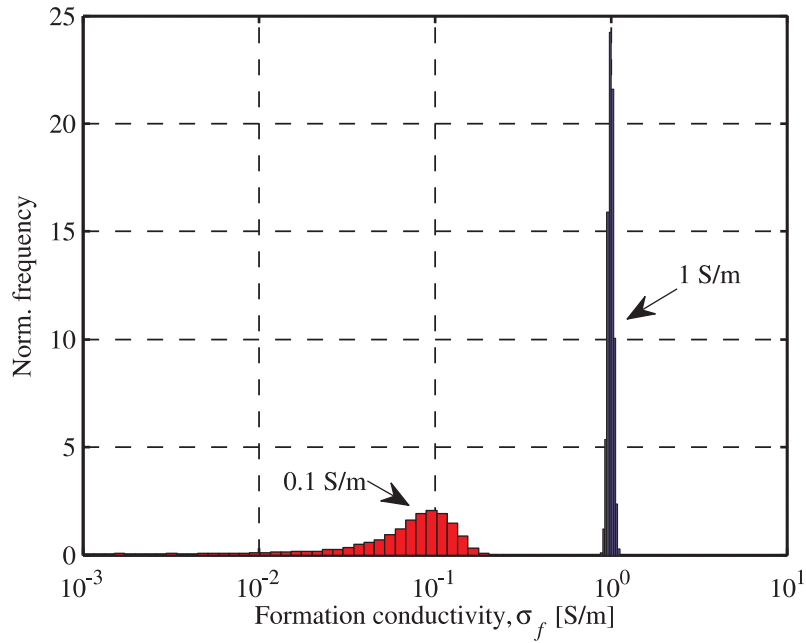


Figure 4.8: Normalised histogram of the posterior distribution $\pi'(\sigma_f)$ for MCMC runs 2 and 3. The relative measurement uncertainty is $p_B = 10^{-4}$.

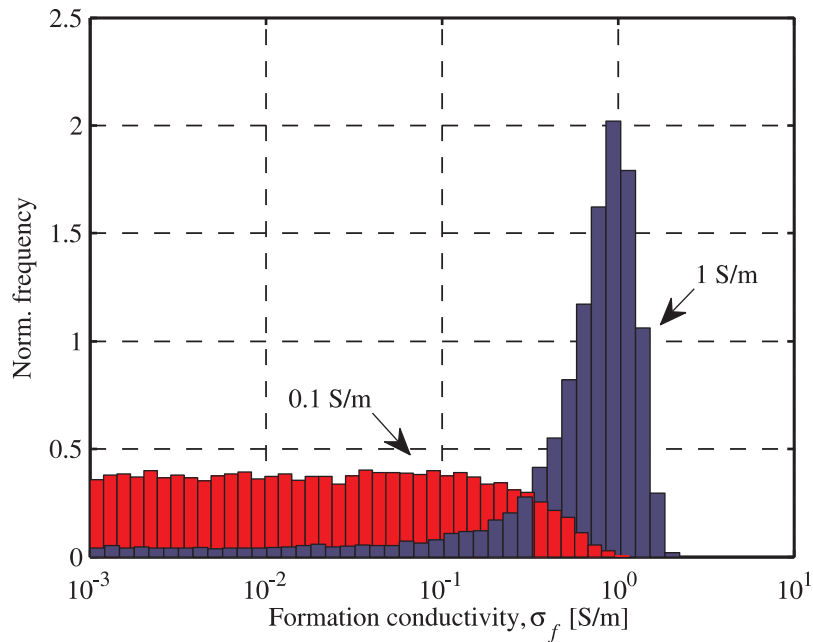


Figure 4.9: Normalised histogram of the posterior distribution $\pi'(\sigma_f)$ for MCMC run 4 and 5. The relative measurement uncertainty is $p_B = 10^{-3}$.

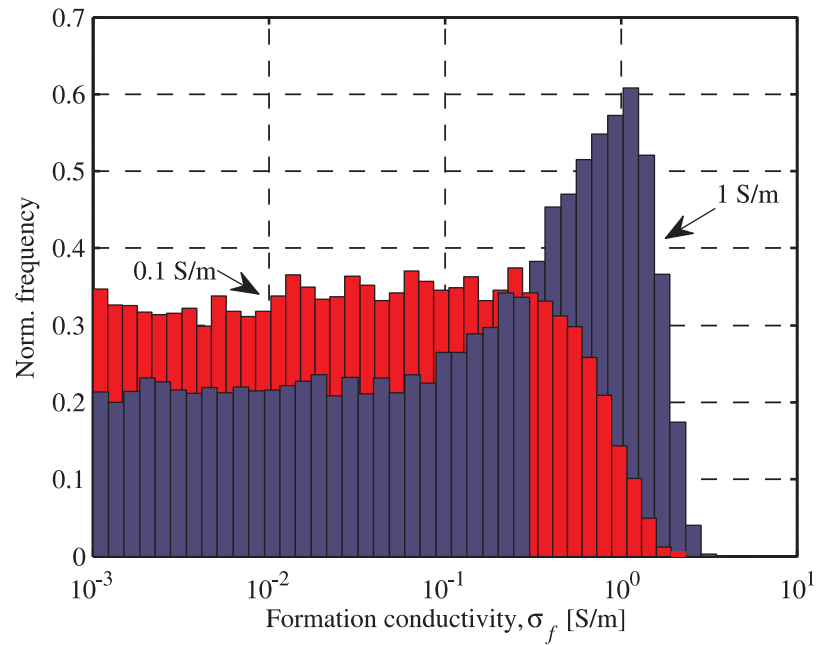


Figure 4.10: Normalised histogram of the posterior distribution $\pi'(\sigma_f)$ for MCMC run 6 and 7. The relative measurement uncertainty is $p_B = 2 \cdot 10^{-3}$.

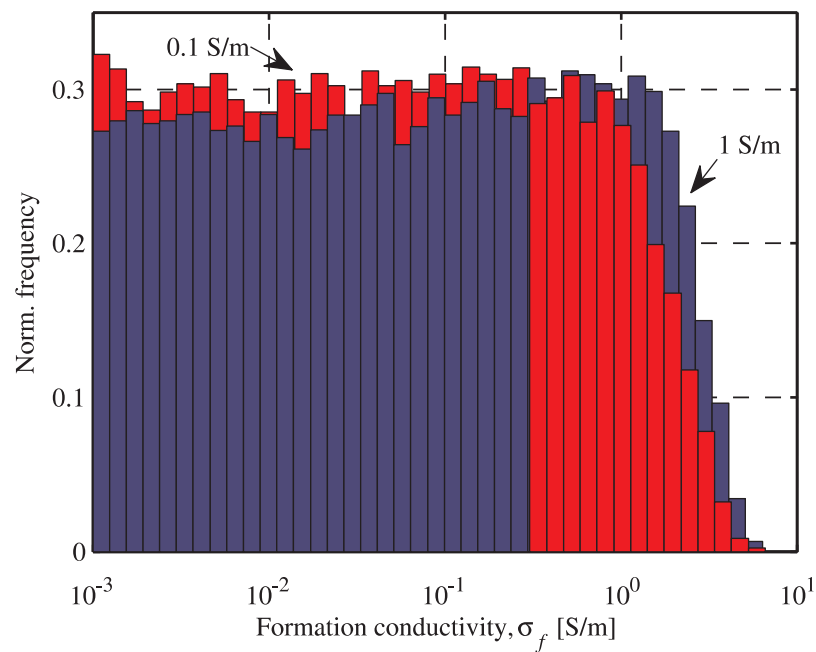


Figure 4.11: Normalised histogram of the posterior distribution $\pi'(\sigma_f)$ for MCMC run 8 and 9. The relative measurement uncertainty is $p_B = 5 \cdot 10^{-3}$.

Table 4.6: MCMC simulations for the analysis of max. measurement uncertainty. Properties of the marginal posterior distributions. Multipliers: casing conductivity – 10^5 S/m, casing thickness – 0.1 mm, formation conductivity – 1 S/m.

Run	Mean			Standard deviation			St. dev. of mean			Mode of $\pi'(\sigma_f)$	Quantiles of $\pi'(\sigma_f)$				
	$\bar{\mu}_r$	$\bar{\sigma}_t$	\bar{c}	s_{μ_r}	s_{σ_t}	s_c	$s_{\bar{\mu}_r}$	$s_{\bar{\sigma}_t}$	$s_{\bar{c}}$		10%	25%	50%	75%	90%
2	99.90	45.94	100.12	0.28	0.14	0.29	0.01	0.01	0.01	0.100	0.019	0.049	0.079	0.106	0.129
3	99.99	46.00	100.01	0.26	0.13	0.27	0.01	0.01	0.01	0.993	0.954	0.974	0.999	1.023	1.044
4	99.98	45.97	100.09	2.31	1.00	2.22	0.05	0.02	0.05	-	0.002	0.005	0.022	0.099	0.257
5	99.12	45.44	101.16	2.79	1.37	2.96	0.12	0.06	0.13	0.999	0.106	0.459	0.783	1.058	1.291
6	100.42	46.20	99.75	4.45	1.94	4.25	0.11	0.05	0.10	-	0.002	0.006	0.033	0.168	0.464
7	97.92	44.71	102.80	4.83	2.22	5.00	0.15	0.07	0.16	1.165	0.003	0.014	0.163	0.688	1.253
8	102.41	47.15	98.76	11.76	5.11	10.62	0.27	0.11	0.23	-	0.002	0.007	0.047	0.301	0.976
9	98.45	44.90	103.28	11.20	4.87	11.05	0.27	0.12	0.26	-	0.002	0.008	0.063	0.453	1.407

69

Table 4.7: MCMC simulations for the analysis of max. measurement uncertainty. Properties of the marginal posterior distributions. Multipliers: casing factor – 1 $\sqrt{\text{S/m}}$, PCR – 1 $\mu\Omega\text{m}$

Run	Mean		Standard deviation		St. dev. of mean	
	\bar{C}_f	$\overline{\text{PCR}}$	$s_{\bar{C}_f}$	s_{PCR}	$s_{\bar{C}_f}$	$s_{\overline{\text{PCR}}}$
2	214.4803	21.7451	0.0084	0.0168	0.0004	0.0005
3	214.4763	21.7392	0.0077	0.0166	0.0002	0.0005
4	214.480	21.747	0.050	0.144	0.001	0.004
5	214.522	21.813	0.086	0.170	0.004	0.006
6	214.468	21.734	0.096	0.274	0.002	0.006
7	214.583	21.902	0.128	0.302	0.005	0.008
8	214.439	21.713	0.236	0.687	0.005	0.016
9	214.592	21.922	0.252	0.713	0.006	0.017

4.5.3 Repeated experiments and systematic uncertainty

One of the “inverse crimes” as described by Kaipio and Somersalo in their book is to use numerically simulated data produced by the same model that is employed in the inversion of the data [82]. This fits well with our discussion about the random and systematic uncertainties in section 4.2.3. In order to evaluate the effect of the total measurement uncertainty and to observe the inversion procedure in a realistic measurement situation (and, thus, avoid the “inverse crime”), we will conduct the MCMC simulations using the procedure below.

Firstly, we calculate the error-free data $\mathbf{d}_0 = \Gamma(\mathbf{m}_0)$ using the true values of the casing and formation parameters \mathbf{m}_0 . Secondly, the measurement data are randomly drawn as $\bar{\mathbf{d}} \sim \mathcal{N}(\mathbf{d}_0, \mathbf{C}_L)$. Finally, the MCMC simulation is run with the normally distributed measurement data with mean $\bar{\mathbf{d}}$ and covariance matrix \mathbf{C}_L . Thus, we enter the inversion procedure with the mean value of the measurement data that is different from the error-free value. The error-free value is unknown for the procedure, but it is with probability of 68.2% somewhere in the region whose width is determined by the covariance matrix \mathbf{C}_L , which includes random and systematic uncertainties. Difference between \mathbf{d}_0 and $\bar{\mathbf{d}}$ can be viewed as due to the systematic effects.

For fixed \mathbf{m}_0 and a chosen measurement uncertainty, the described procedure was carried out six times in order to simulate repeated experiments with different systematic effects and, consequently, different $\bar{\mathbf{d}}$. The posterior distributions obtained from such repeated experiments are equivalent in sense that each of them is a solution of the inverse problem conditioned on the accuracy of the procedure for the compensation of the systematic effects. We take that six experiments are a good trade-off between the required computational burden and our need to estimate the average quality of the inversion procedure at a chosen level of the measurement uncertainty.

From the analysis of the maximal measurement uncertainty in section 4.5.2, it is evident that only for $p_B < 2 \cdot 10^{-3}$ one can expect to obtain acceptably well differentiation between 0.1 S/m and 1 S/m. Thus, in this section, we pay more attention to uncertainties $p_B = 10^{-4}$ and $p_B = 10^{-3}$. We conducted simulations for the formation conductivities of 0.01 S/m, 0.05 S/m, 0.1 S/m, 0.5 S/m, 1 S/m, and 5 S/m, at each of the two uncertainty levels. For each choice of the conductivity and uncertainty, we made 7 MCMC runs; the first one with error-free measurement data $\bar{\mathbf{d}} = \mathbf{d}_0$, and other six simulations with measurement data drawn from $\mathcal{N}(\mathbf{d}_0, \mathbf{C}_L)$.

Because of the large number of simulations, parameters of the proposal distributions and analysis of sampling efficiency are not given in detail. However, one can obtain a good insight into the quality of the MCMC simulations by knowing that the resulting acceptance ratios were between 12% and 25%, whereas autocovariance times were mostly between 50 and 250, and have never exceeded 450. We used 200000 iterations with the properties of the proposal distribution similar to ones in the previous sections.

Table 4.8 contains the parameters of the marginal posterior distribution of the casing properties for $p_B = 10^{-4}$. The posterior distributions of the casing properties resemble the normal distribution, so mean and standard deviation are appropriate descriptors. The actual value of the formation conductivity has negligible effect on the posteriors of the casing properties, so all 42 simulations in Table 4.8 can be viewed as repeated measurements of the same true situation. The runs marked with number 0 are made using the error-free data. The number of iterations and the autocovariance time below 450 for all cases ensure that the number of significant decimal places in an estimated mean value is at least for one place larger than the first non-zero decimal place of the corresponding standard deviation. Relative standard deviations (with respect to the true values) for permeability, conductivity and wall thickness are in all cases around $3 \cdot 10^{-3}$. This is by itself a small number, but it is 30 times larger than the measurement uncertainty, what indicates an ill-conditioned procedure, as already discussed in section 4.1. Relative errors of the mean values of permeability, conductivity and thickness with respect to their true values reach $6 \cdot 10^{-3}$, but for the most of the cases the errors are below $3 \cdot 10^{-3}$. Casing factor has a relative standard deviation smaller than $5 \cdot 10^{-5}$, what is only a half of the measurement uncertainty. For PCR, the boundary is at $8.3 \cdot 10^{-4}$, or about 8 times higher than p_B . Relative errors of the mean values are below $9 \cdot 10^{-5}$ for C_f , and below $1.7 \cdot 10^{-3}$ for PCR.

Table 4.9 contains the parameters of the posteriors of the formation conductivity for $p_B = 10^{-4}$. The histograms of the distributions for runs 1–6 for all six true values of the formation conductivity are shown in Figs. 4.12–4.17. Two lowest true values of the formation conductivities, 0.01 S/m and 0.05 S/m can not be measured at this level of the measurement uncertainty, Figs. 4.12 and 4.13. The main feature of these two sets of the posteriors is that they kept the shape of the prior assumption of logarithmic uniform distribution of the formation conductivity up to 0.1 S/m, as seen in Figs. 4.12(a)–(d), 4.13(a) and (c). The situation is somewhat better in Fig. 4.14 for 0.1 S/m, where one notices the presence of a heavy tail caused by the prior assumption, but also the presence of a distinct mode mostly in the range of 0.07 S/m–0.11 S/m. However, there are distributions that could be placed in either of the three groups, Figs. 4.12(e), (f); 4.13(b), (e), (f); and 4.14(b) (or runs 5 and 6 for 0.01 S/m; 2, 5 and 6 for 0.05 S/m; and 2 for 0.1 S/m from Table 4.9). The results of the simulations for 0.5 S/m, 1 S/m and 5 S/m are more accurate, Figs. 4.15–4.17. The distributions are bell-shaped without heavy tails. Both the median (50% quantile) and the mode are very close and typically within 5% from the true value. Also, 70% of the samples of a distribution are within the interval shorter than 0.09 S/m. From these results, we corroborate that, assuming the uncertainty of $p_B = 10^{-4}$, the formation conductivity can be measured if it is higher than 0.1 S/m. For lower conductivities, one may be forced to come up with the weaker, but still quantitative conclusion that the result is with certainty lower than 0.1 S/m.

The summary of the simulations for the measurement uncertainty $p_B =$

10^{-3} is given in Tables 4.10 and 4.11, whereas the histograms of the formation conductivity posteriors are depicted in Figs. 4.18–4.23. Relative standard deviations of the permeability, conductivity and wall thickness are around $3 \cdot 10^{-2}$, and relative errors of the mean values are below $7 \cdot 10^{-3}$. Casing factor has relative standard deviation around $4 \cdot 10^{-4}$, whereas for PCR the value is $8.3 \cdot 10^{-3}$. Relative errors of the mean values are below $8.6 \cdot 10^{-4}$ for C_f and $2.7 \cdot 10^{-2}$ for PCR. Ten times higher measurement uncertainty resulted in an almost tenfold increase in the relative standard deviations and errors of the casing parameters. There is no significant difference between the distributions for 0.01 S/m–0.5 S/m, Figs. 4.18–4.21. Although the distributions for 1 S/m as depicted in Fig. 4.22 show the heavy tail on the left with 70% of the samples within 0.9 S/m range on average, Table 4.11, there is a significant difference in comparison to the lower conductivities. Distributions for 5 S/m have their mode within ± 0.5 S/m around the true value, and 70% of the samples within 0.77 S/m range. Assuming the uncertainty of $p_B = 10^{-3}$, the lowest measurable formation conductivity is about 1 S/m. For a lower conductivity, a posterior distribution is no more informative than the statement that the conductivity is with certainty lower than 1 S/m.

From this analysis it follows that the properties of the distributions are scalable with the measurement uncertainty with roughly the same coefficient (10 in this case). We have to bear in mind that the results obtained in this section are made with homogeneous prior distributions. Any additional information as well as combination of the results from the repeated experiments would certainly improve our posterior knowledge of the formation conductivity and the casing properties.

Table 4.8: MCMC simulations of repeated experiments for $p_B = 10^{-4}$. Properties of the marginal posterior distributions of the casing parameters. Multipliers: conductivity – 10^5 S/m, thickness – 0.1 mm, casing factor – $1 \sqrt{\text{S/m}}$, PCR – $1 \mu\Omega\text{m}$, relative errors – 10^{-6} .

True σ_f	Run	Permeability, μ_r			Conductivity, σ_t			Thickness, c			Casing factor, C_f			PCR		
		$\bar{\mu}_r$	s_{μ_r}	p_{μ_r}	$\bar{\sigma}_t$	s_{σ_t}	p_{σ_t}	\bar{c}	s_c	p_c	\bar{C}_f	s_{C_f}	p_{C_f}	$\overline{\text{PCR}}$	s_{PCR}	p_{PCR}
0.01 S/m	0	100.02	0.23	200	46.01	0.10	261	99.98	0.22	200	214.4755	0.0051	3	21.739	0.014	6
	1	100.34	0.22	3400	46.12	0.10	2696	99.70	0.22	3000	214.4790	0.0049	13	21.754	0.014	684
	2	100.08	0.24	800	46.05	0.11	1087	99.90	0.23	1000	214.4742	0.0055	9	21.734	0.014	236
	3	99.53	0.23	4700	45.80	0.10	4261	100.45	0.22	4500	214.4811	0.0048	23	21.729	0.014	466
	4	99.90	0.22	1000	46.01	0.10	174	100.04	0.21	400	214.4718	0.0049	20	21.714	0.014	1156
	5	99.85	0.25	1500	45.98	0.12	435	100.09	0.26	900	214.4708	0.0069	25	21.715	0.015	1110
6	99.98	0.25	200	46.00	0.12	0	100.01	0.25	100	214.4742	0.0067	9	21.734	0.015	236	
0.05 S/m	0	99.91	0.25	900	45.95	0.12	1087	100.10	0.25	1000	214.4799	0.0067	18	21.745	0.015	270
	1	100.19	0.24	1900	46.04	0.11	870	99.87	0.24	1300	214.4848	0.0059	41	21.762	0.015	1052
	2	100.00	0.26	0	46.00	0.12	0	100.00	0.27	0	214.4775	0.0073	7	21.738	0.016	52
	3	99.38	0.23	6200	45.72	0.11	6087	100.63	0.23	6300	214.4869	0.0057	50	21.737	0.014	98
	4	99.77	0.24	2300	45.93	0.11	1522	100.19	0.24	1900	214.4770	0.0061	4	21.721	0.015	834
	5	99.87	0.28	1300	46.00	0.14	0	100.07	0.29	700	214.4700	0.0082	28	21.713	0.017	1202
6	99.99	0.29	100	46.01	0.14	217	100.00	0.30	0	214.4738	0.0084	11	21.734	0.017	236	
0.1 S/m	0	99.91	0.28	900	45.95	0.14	1087	100.10	0.29	1000	214.4799	0.0085	18	21.745	0.017	270
	1	100.05	0.28	500	45.95	0.14	1087	100.04	0.29	400	214.4888	0.0084	59	21.773	0.017	1558
	2	99.69	0.25	3100	45.84	0.11	3478	100.34	0.25	3400	214.4876	0.0065	54	21.750	0.015	500
	3	99.62	0.27	3800	45.77	0.13	5000	100.46	0.28	4600	214.4926	0.0080	77	21.766	0.017	1236
	4	100.04	0.29	400	46.02	0.14	435	99.95	0.30	500	214.4753	0.0086	4	21.737	0.017	98
	5	100.31	0.29	3100	46.07	0.14	1522	99.77	0.30	2300	214.4835	0.0084	34	21.773	0.017	1558
6	99.84	0.27	1600	45.91	0.13	1957	100.18	0.28	1800	214.4810	0.0078	23	21.749	0.017	454	

continued on next page

continued from previous page

True σ_f	Run	Permeability, μ_r			Conductivity, σ_t			Thickness, c			Casing factor, C_f			PCR		
		$\bar{\mu}_r$	s_{μ_r}	p_{μ_r}	$\bar{\sigma}_t$	s_{σ_t}	p_{σ_r}	\bar{c}	s_c	p_c	\bar{C}_f	s_{C_f}	p_{C_f}	$\overline{\text{PCR}}$	s_{PCR}	p_{PCR}
0.5 S/m	0	99.99	0.26	100	46.00	0.13	0	100.01	0.27	100	214.4764	0.0076	1	21.740	0.016	40
	1	99.98	0.27	200	45.99	0.13	217	100.02	0.27	200	214.4763	0.0077	1	21.739	0.016	6
	2	100.41	0.27	4100	46.18	0.13	3913	99.60	0.27	4000	214.4745	0.0077	7	21.743	0.016	178
	3	99.81	0.26	1900	45.86	0.13	3043	100.26	0.27	2600	214.4874	0.0078	53	21.765	0.017	1190
	4	99.89	0.26	1100	45.98	0.13	435	100.08	0.27	800	214.4710	0.0076	24	21.726	0.016	604
	5	99.87	0.27	1300	45.96	0.13	870	100.12	0.27	1200	214.4767	0.0077	3	21.730	0.016	420
6	99.70	0.26	3000	45.90	0.13	2174	100.26	0.27	2600	214.4714	0.0075	22	21.722	0.016	788	
1 S/m	0	100.00	0.26	0	46.00	0.13	0	100.00	0.27	0	214.4762	0.0077	0	21.739	0.016	6
	1	100.17	0.27	1700	46.11	0.13	2391	99.80	0.27	2000	214.4693	0.0078	32	21.725	0.017	650
	2	100.25	0.27	2500	46.11	0.13	2391	99.75	0.27	2500	214.4734	0.0076	13	21.741	0.017	86
	3	100.23	0.27	2300	46.19	0.13	4130	99.68	0.27	3200	214.4573	0.0078	88	21.701	0.016	1754
	4	99.97	0.26	300	45.95	0.13	1087	100.07	0.27	700	214.4814	0.0076	25	21.755	0.016	730
	5	100.11	0.26	1100	46.03	0.13	652	99.91	0.27	900	214.4770	0.0076	4	21.748	0.016	408
6	99.91	0.26	900	45.95	0.12	1087	100.10	0.26	1000	214.4781	0.0076	9	21.742	0.016	132	
5 S/m	0	100.01	0.24	100	46.00	0.12	0	99.99	0.25	100	214.4759	0.0074	1	21.739	0.016	6
	1	100.18	0.24	1800	46.10	0.11	2174	99.8	0.24	2000	214.4690	0.0073	33	21.731	0.016	374
	2	99.97	0.25	300	45.94	0.12	1304	100.08	0.25	800	214.4833	0.0075	34	21.760	0.017	960
	3	100.14	0.24	1400	46.06	0.12	1304	99.86	0.25	1400	214.4750	0.0075	5	21.741	0.017	86
	4	99.95	0.24	500	45.94	0.11	1304	100.09	0.24	900	214.4819	0.0073	27	21.755	0.016	730
	5	99.61	0.24	3900	45.87	0.11	2826	100.33	0.24	3300	214.4730	0.0075	14	21.715	0.017	1110
6	100.06	0.25	600	45.95	0.12	1087	100.03	0.25	300	214.4875	0.0075	53	21.773	0.016	1558	

Table 4.9: MCMC simulations of repeated experiments for $p_B = 10^{-4}$. Properties of the marginal posterior distributions of the formation conductivity. Multiplier is 1 S/m.

Run	True	Quantiles			Mode	True	Quantiles			Mode
	σ_f	15%	50%	85%			σ_f	15%	50%	
0	0.01 S/m	0.00	0.01	0.03	-	0.5 S/m	0.46	0.50	0.53	0.51
1		0.00	0.01	0.02	-		0.47	0.51	0.54	0.51
2		0.00	0.01	0.04	-		0.47	0.51	0.54	0.52
3		0.00	0.00	0.02	-		0.41	0.45	0.48	0.45
4		0.00	0.01	0.02	-		0.46	0.49	0.53	0.49
5		0.00	0.02	0.06	0.05		0.44	0.48	0.51	0.47
6		0.00	0.02	0.06	0.06		0.47	0.50	0.54	0.51
0	0.05 S/m	0.00	0.02	0.06	0.04	1 S/m	0.96	1.00	1.04	1.00
1		0.00	0.01	0.04	0.03		0.99	1.03	1.07	1.03
2		0.00	0.03	0.08	0.07		0.96	0.99	1.03	0.99
3		0.00	0.01	0.04	0.03		1.03	1.07	1.11	1.06
4		0.00	0.01	0.05	0.03		0.94	0.97	1.01	0.97
5		0.03	0.08	0.12	0.09		0.96	0.99	1.03	1.00
6		0.03	0.07	0.11	0.10		0.98	1.01	1.05	1.01
0	0.1 S/m	0.03	0.08	0.12	0.09	5 S/m	4.96	5.00	5.04	5.00
1		0.02	0.06	0.11	0.09		4.99	5.03	5.07	5.03
2		0.00	0.02	0.06	0.04		4.96	5.00	5.04	4.99
3		0.01	0.05	0.09	0.07		4.98	5.02	5.05	5.02
4		0.05	0.10	0.14	0.11		4.94	4.98	5.02	4.98
5		0.06	0.10	0.14	0.10		4.95	4.99	5.03	4.98
6		0.01	0.04	0.08	0.07		4.89	4.93	4.97	4.94

4.5 Solution of the inverse problem

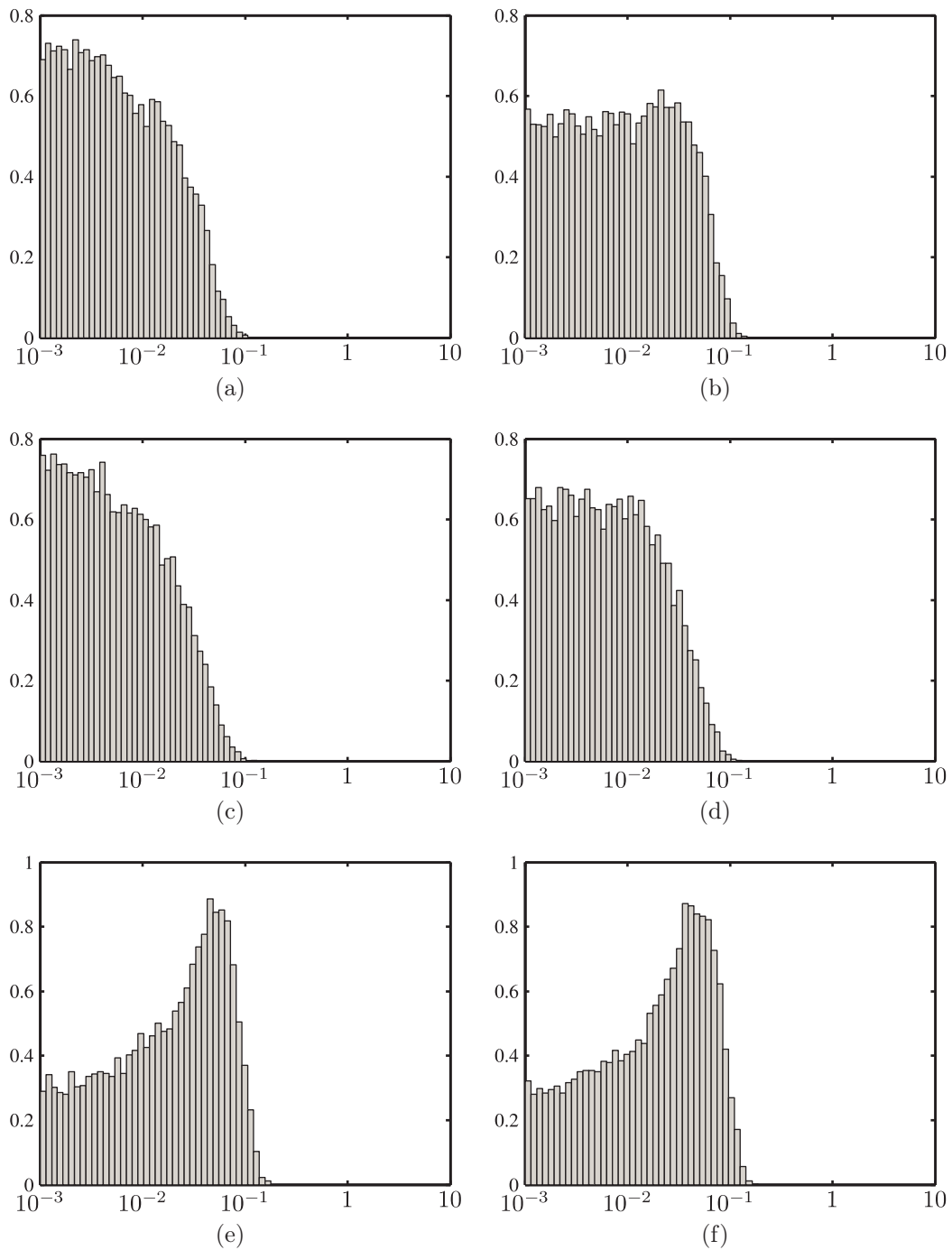


Figure 4.12: Normalised histograms of posterior distributions of the formation conductivity for different measurement data, measurement uncertainty $p_B = 10^{-4}$ and true value $\sigma_f = 0.01$ S/m.

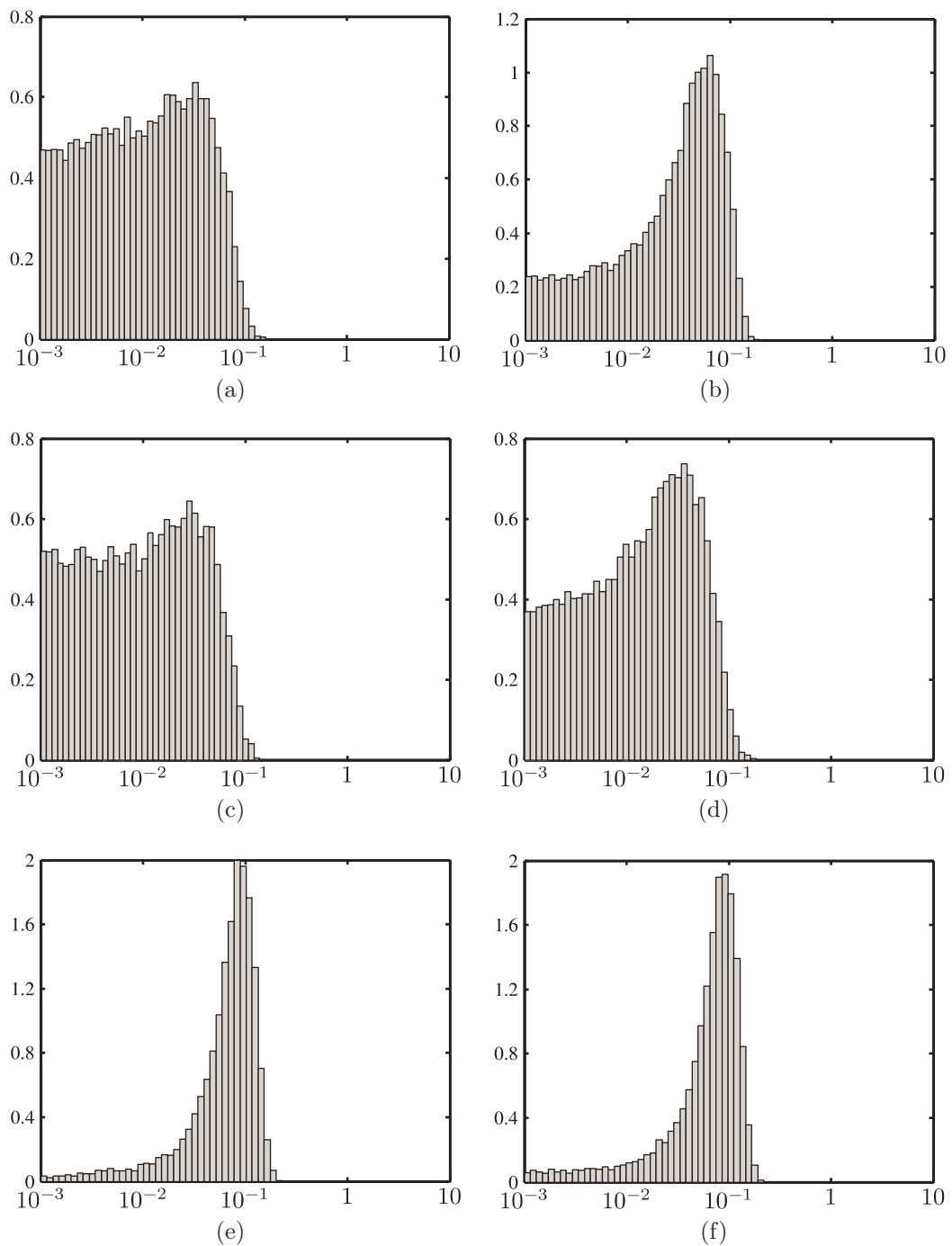


Figure 4.13: Normalised histograms of posterior distributions of the formation conductivity for different measurement data, measurement uncertainty $p_B = 10^{-4}$ and true value $\sigma_f = 0.05$ S/m.

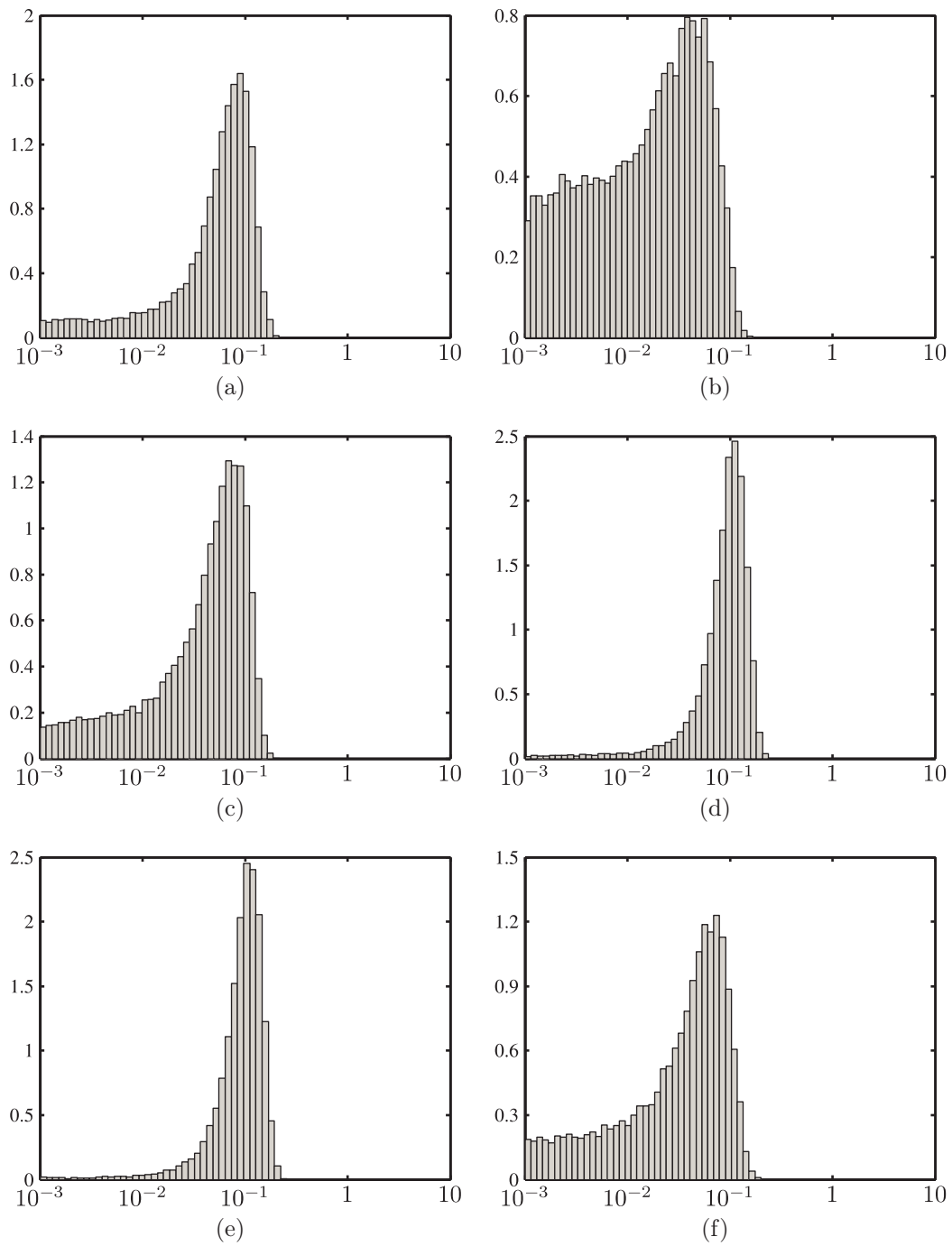


Figure 4.14: Normalised histograms of posterior distributions of the formation conductivity for different measurement data, measurement uncertainty $p_B = 10^{-4}$ and true value $\sigma_f = 0.1$ S/m.

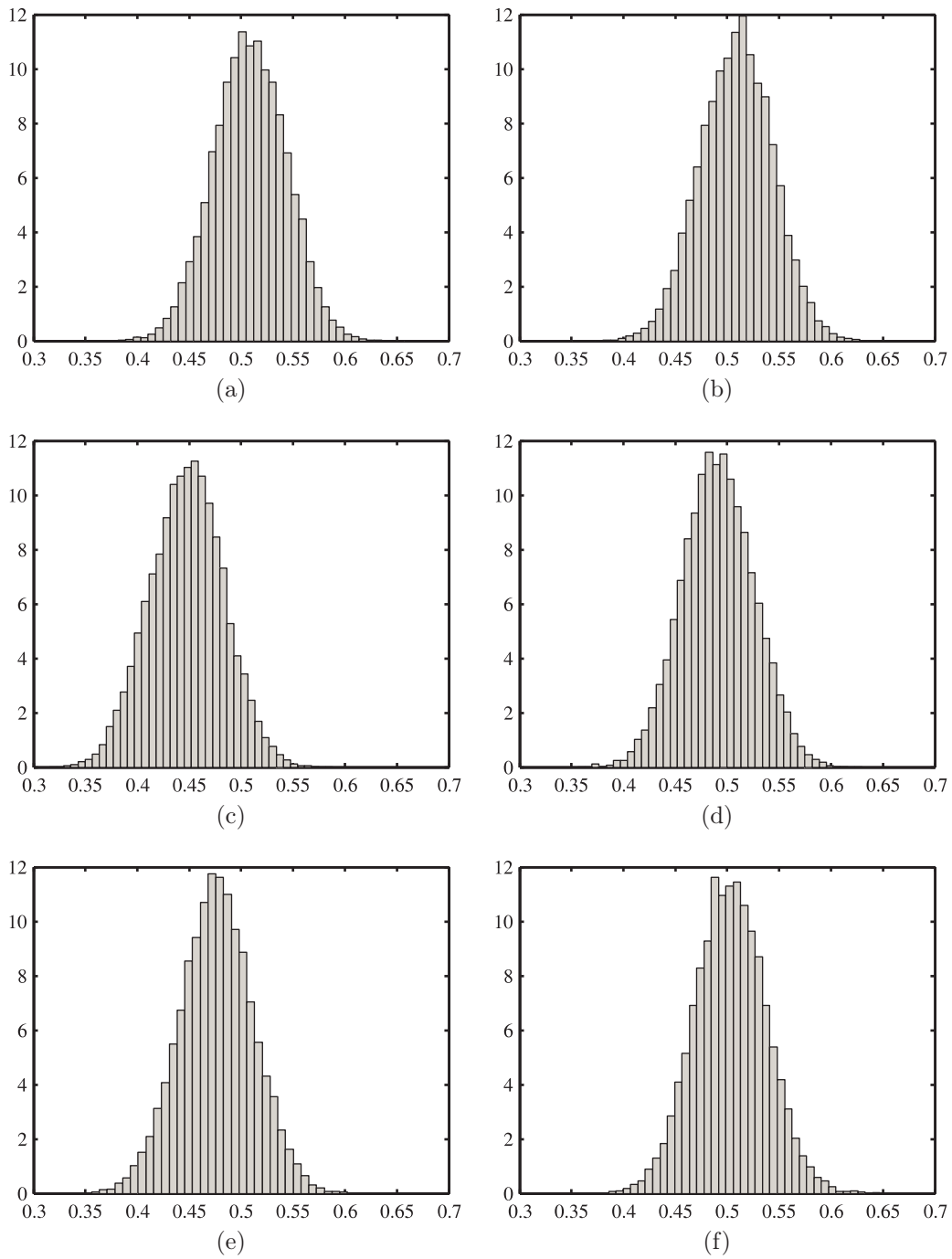


Figure 4.15: Normalised histograms of posterior distributions of the formation conductivity for different measurement data, measurement uncertainty $p_B = 10^{-4}$ and true value $\sigma_f = 0.5$ S/m.

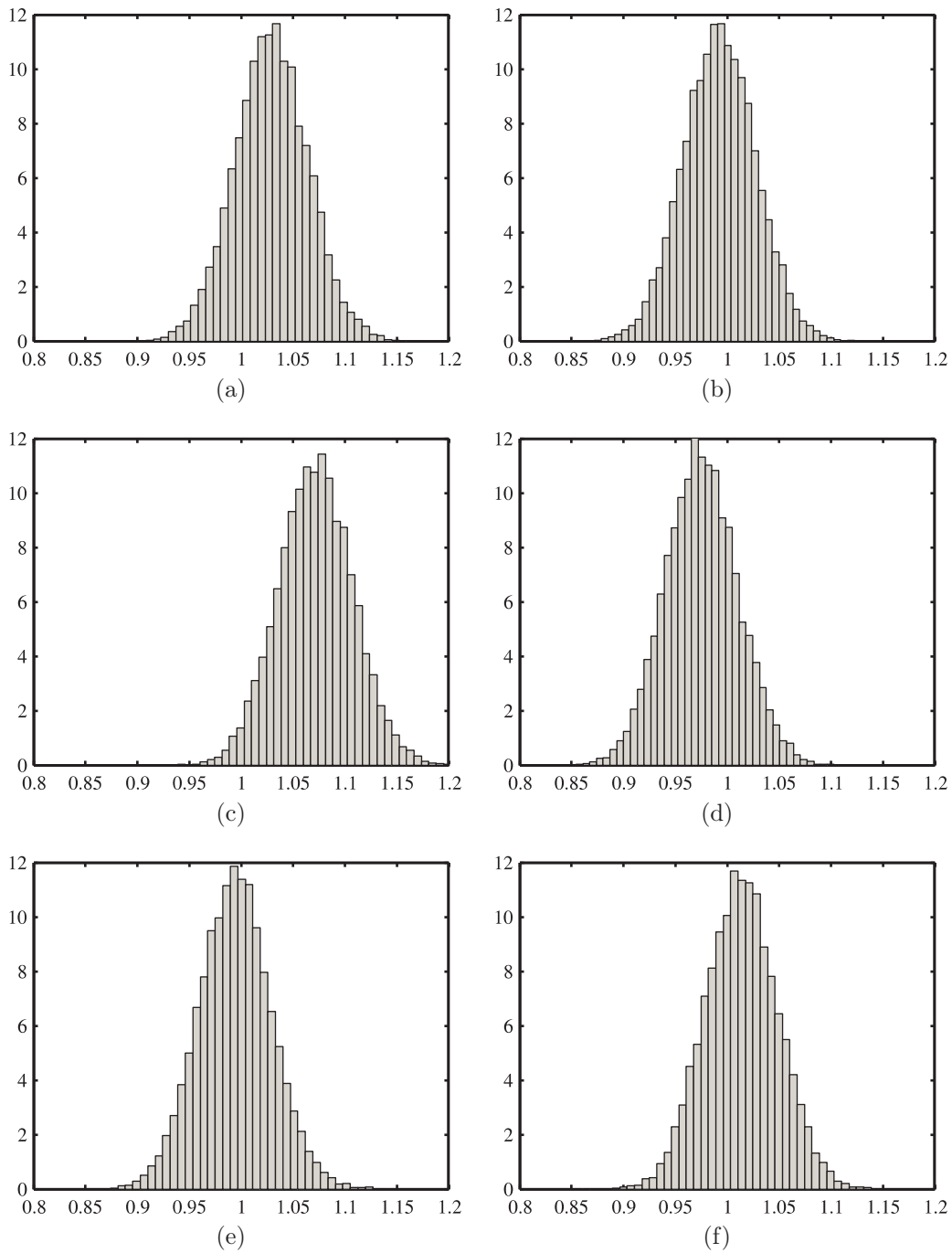


Figure 4.16: Normalised histograms of posterior distributions of the formation conductivity for different measurement data, measurement uncertainty $p_B = 10^{-4}$ and true value $\sigma_f = 1$ S/m.

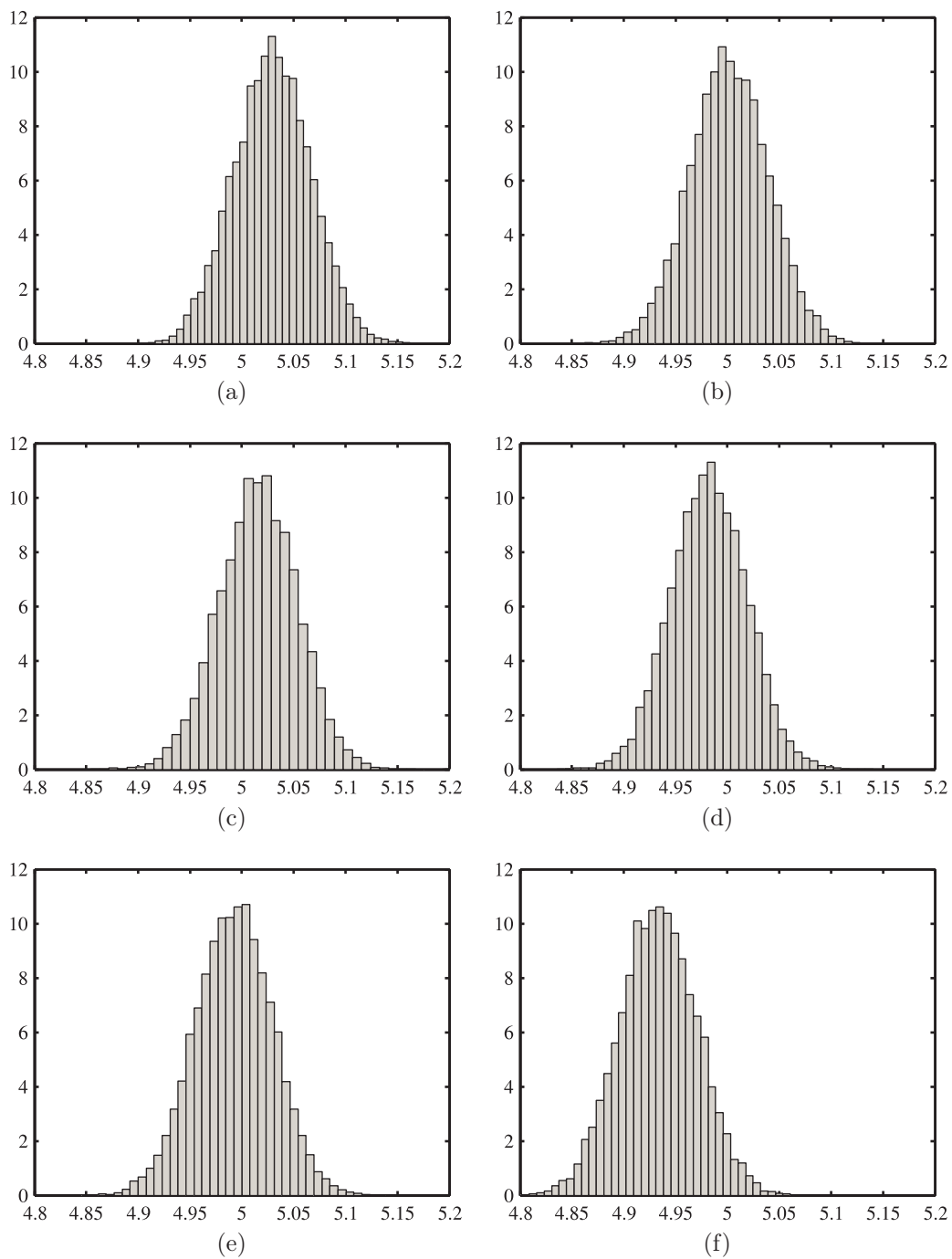


Figure 4.17: Normalised histograms of posterior distributions of the formation conductivity for different measurement data, measurement uncertainty $p_B = 10^{-4}$ and true value $\sigma_f = 5$ S/m.

Table 4.10: MCMC simulations of repeated experiments for $p_B = 10^{-3}$. Properties of the marginal posterior distributions of the casing parameters. Multipliers: conductivity – 10^5 S/m, thickness – 0.1 mm, casing factor – $1 \sqrt{\text{S/m}}$, PCR – $1 \mu\Omega\text{m}$, relative errors – 10^{-3} .

True σ_f	Run	Permeability, μ_r			Conductivity, σ_t			Thickness, c			Casing factor, C_f			PCR		
		$\bar{\mu}_r$	s_{μ_r}	p_{μ_r}	$\bar{\sigma}_t$	s_{σ_t}	p_{σ_t}	\bar{c}	s_c	p_c	\bar{C}_f	s_{C_f}	p_{C_f}	$\overline{\text{PCR}}$	s_{PCR}	p_{PCR}
0.01 S/m	0	100.4	2.3	4	46.2	1.0	4	99.6	2.2	4	214.463	0.049	0.06	21.72	0.14	1
	1	103.7	2.3	37	47.4	1.0	30	96.8	2.1	32	214.499	0.046	0.11	21.88	0.14	6
	2	100.9	2.3	9	46.5	1.0	11	99.0	2.2	10	214.455	0.051	0.10	21.69	0.14	2
	3	95.7	2.0	43	44.2	0.9	39	104.3	2.1	43	214.518	0.045	0.20	21.63	0.14	5
	4	99.2	2.2	8	46.2	1.0	3	100.3	2.1	3	214.429	0.046	0.22	21.49	0.13	11
	5	98.4	2.3	16	45.8	1.1	4	101.1	2.4	11	214.429	0.062	0.22	21.50	0.15	11
	6	99.7	2.4	3	46.0	1.1	0	100.3	2.4	3	214.461	0.063	0.07	21.70	0.15	2
0.05 S/m	0	100.2	2.2	2	46.1	1.0	2	99.9	2.2	1	214.471	0.049	0.02	21.73	0.14	0
	1	103.5	2.4	35	47.3	1.0	28	97.0	2.1	30	214.506	0.047	0.14	21.89	0.14	7
	2	100.8	2.3	8	46.4	1.0	9	99.2	2.2	8	214.461	0.051	0.07	21.69	0.14	2
	3	95.5	2.0	45	44.1	0.9	40	104.5	2.1	45	214.524	0.045	0.22	21.64	0.14	5
	4	99.1	2.2	9	46.1	1.0	2	100.4	2.1	4	214.433	0.046	0.20	21.49	0.13	11
	5	98.4	2.4	16	45.7	1.1	7	101.2	2.5	12	214.431	0.064	0.21	21.51	0.15	11
	6	99.6	2.4	4	45.9	1.1	2	100.3	2.4	3	214.465	0.064	0.05	21.70	0.15	2
0.1 S/m	0	100.0	2.3	0	46.0	1.0	0	100.0	2.2	0	214.479	0.050	0.01	21.75	0.14	1
	1	103.3	2.4	33	47.2	1.0	26	97.2	2.1	28	214.513	0.048	0.17	21.90	0.14	7
	2	100.6	2.4	6	46.4	1.1	9	99.4	2.3	6	214.469	0.053	0.03	21.71	0.14	1
	3	95.3	2.0	47	44.0	0.9	43	104.8	2.1	48	214.532	0.046	0.26	21.65	0.14	4
	4	98.8	2.2	12	45.9	0.9	1	100.7	2.1	7	214.443	0.047	0.15	21.50	0.14	11
	5	98.3	2.5	17	45.7	1.2	7	101.2	2.6	12	214.434	0.068	0.20	21.51	0.15	11
	6	99.5	2.4	5	45.8	1.1	4	100.5	2.5	5	214.468	0.066	0.04	21.71	0.15	1

continued on next page

continued from previous page

True σ_f	Run	Permeability, μ_r			Conductivity, σ_t			Thickness, c			Casing factor, C_f			PCR		
		$\bar{\mu}_r$	s_{μ_r}	p_{μ_r}	$\bar{\sigma}_t$	s_{σ_t}	p_{σ_r}	\bar{c}	s_c	p_c	\bar{C}_f	s_{C_f}	p_{C_f}	$\overline{\text{PCR}}$	s_{PCR}	p_{PCR}
0.5 S/m	0	98.9	2.5	11	45.3	1.1	15	101.4	2.5	14	214.527	0.066	0.24	21.81	0.15	3
	1	99.1	2.5	9	45.7	1.2	7	100.8	2.6	8	214.492	0.069	0.07	21.68	0.16	3
	2	100.6	2.3	6	45.8	1.0	5	100.0	2.2	0	214.563	0.048	0.41	21.99	0.14	12
	3	100.5	2.6	5	46.3	1.3	7	99.5	2.7	5	214.468	0.075	0.04	21.72	0.16	1
	4	102.8	3.1	28	47.7	1.5	37	96.9	3.0	31	214.378	0.089	0.46	21.54	0.17	9
	5	100.6	2.2	6	45.4	0.9	13	100.4	2.1	4	214.621	0.045	0.68	22.16	0.14	19
	6	96.5	2.3	35	44.6	1.0	30	103.4	2.4	34	214.496	0.062	0.09	21.65	0.15	4
1 S/m	0	99.1	2.9	9	45.5	1.4	11	101.1	3.1	11	214.519	0.092	0.20	21.80	0.18	3
	1	101.4	2.8	14	46.1	1.3	2	99.4	2.8	6	214.593	0.082	0.55	22.01	0.17	12
	2	100.3	2.7	3	46.2	1.4	4	99.8	2.9	2	214.483	0.086	0.03	21.72	0.17	1
	3	93.5	2.4	65	43.0	1.2	65	107.1	2.9	71	214.616	0.082	0.65	21.77	0.17	1
	4	97.4	2.6	26	45.1	1.3	20	102.5	2.8	25	214.507	0.082	0.14	21.59	0.16	7
	5	99.1	2.6	9	46.1	1.3	2	100.3	2.7	3	214.401	0.078	0.35	21.47	0.16	12
	6	100.1	2.7	1	46.2	1.3	4	99.8	2.8	2	214.440	0.082	0.17	21.67	0.17	3
5 S/m	0	100.0	2.4	0	46.0	1.2	0	100.1	2.5	1	214.480	0.075	0.02	21.75	0.16	1
	1	99.7	2.4	3	46.4	1.2	9	99.7	2.5	3	214.369	0.074	0.50	21.48	0.16	12
	2	99.2	2.4	8	45.1	1.1	20	101.5	2.5	15	214.578	0.074	0.48	22.00	0.17	12
	3	97.9	2.3	21	45.3	1.1	15	101.9	2.4	19	214.507	0.073	0.14	21.61	0.17	6
	4	96.5	2.3	35	44.8	1.1	26	103.2	2.5	32	214.463	0.075	0.06	21.54	0.17	9
	5	101.5	2.5	15	46.9	1.2	20	98.3	2.4	17	214.411	0.073	0.30	21.64	0.16	5
	6	102.1	2.5	21	45.7	1.2	7	99.4	2.5	6	214.660	0.073	0.86	22.33	0.17	27

4.5 Solution of the inverse problem

Table 4.11: MCMC simulations of repeated experiments for $p_B = 10^{-3}$. Properties of the marginal posterior distributions of the formation conductivity. Multiplier is 1 S/m.

Run	True	Quantiles			Mode	True	Quantiles			Mode
	σ_f	15%	50%	85%			σ_f	15%	50%	
0	0.01 S/m	0.00	0.02	0.17	-	0.5 S/m	0.00	0.09	0.53	0.51
1		0.00	0.02	0.12	-		0.00	0.10	0.59	0.51
2		0.00	0.02	0.21	-		0.00	0.02	0.17	-
3		0.00	0.01	0.11	-		0.01	0.23	0.73	0.52
4		0.00	0.01	0.11	-		0.09	0.65	1.10	0.91
5		0.00	0.07	0.46	0.45		0.00	0.01	0.10	-
6		0.00	0.07	0.45	0.43		0.00	0.08	0.47	0.44
0	0.05 S/m	0.00	0.02	0.17	-	1 S/m	0.22	0.80	1.23	0.97
1		0.00	0.01	0.12	-		0.05	0.52	0.97	0.84
2		0.00	0.02	0.23	-		0.51	0.96	1.35	1.09
3		0.00	0.02	0.12	-		0.03	0.48	0.94	0.82
4		0.00	0.02	0.14	-		0.12	0.61	1.03	0.86
5		0.00	0.10	0.51	0.45		0.95	1.34	1.72	1.47
6		0.00	0.09	0.49	0.46		0.92	1.32	1.70	1.48
0	0.1 S/m	0.00	0.02	0.19	-	5 S/m	4.59	4.98	5.36	5.03
1		0.00	0.02	0.14	-		5.16	5.54	5.93	5.64
2		0.00	0.03	0.25	-		4.13	4.50	4.88	4.49
3		0.00	0.02	0.13	-		4.42	4.80	5.18	4.81
4		0.00	0.02	0.13	-		4.59	4.98	5.36	4.90
5		0.00	0.13	0.58	0.51		5.13	5.52	5.89	5.55
6		0.01	0.12	0.56	0.62		3.72	4.09	4.46	4.14

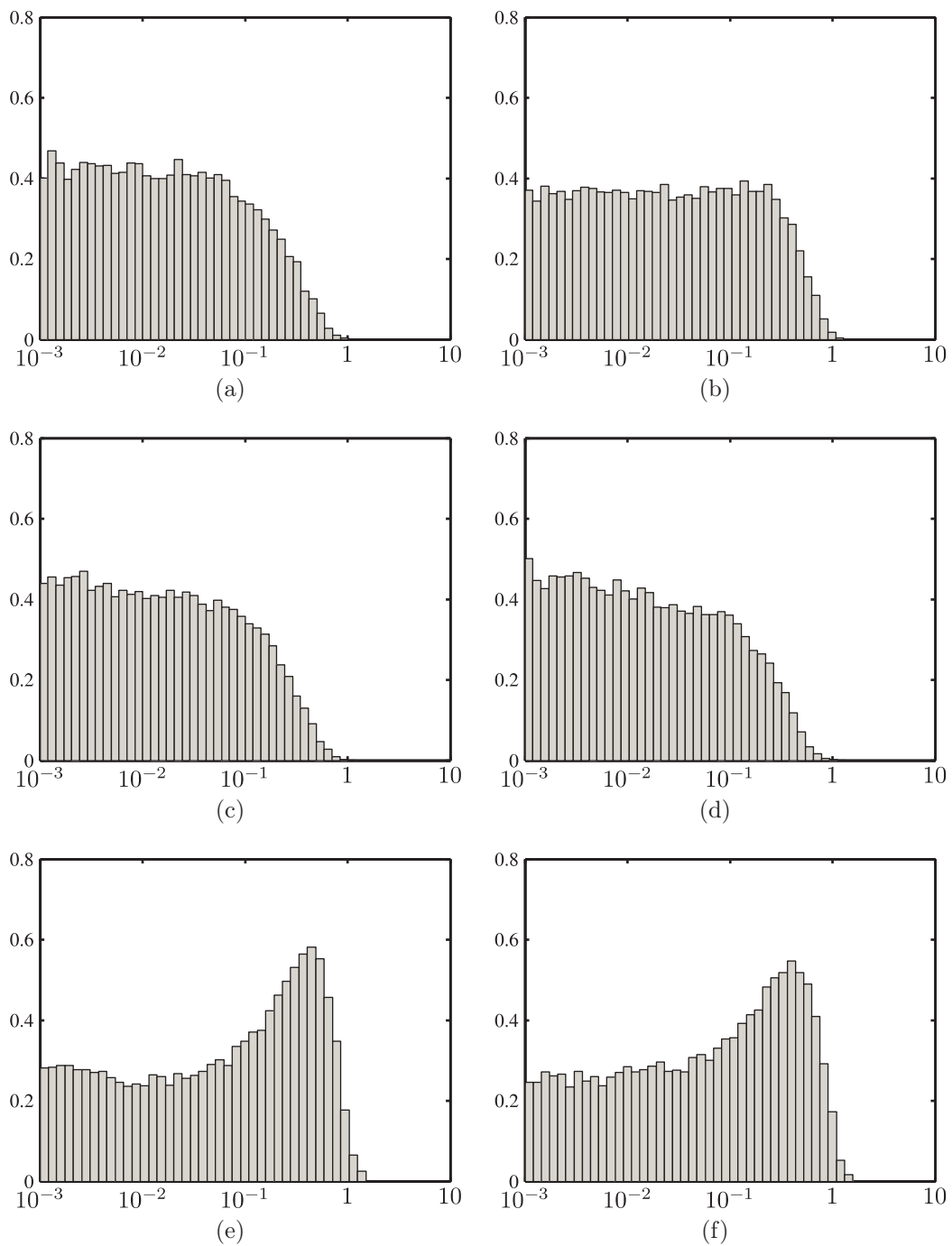


Figure 4.18: Normalised histograms of posterior distributions of the formation conductivity for different measurement data, measurement uncertainty $p_B = 10^{-3}$ and true value $\sigma_f = 0.01$ S/m.

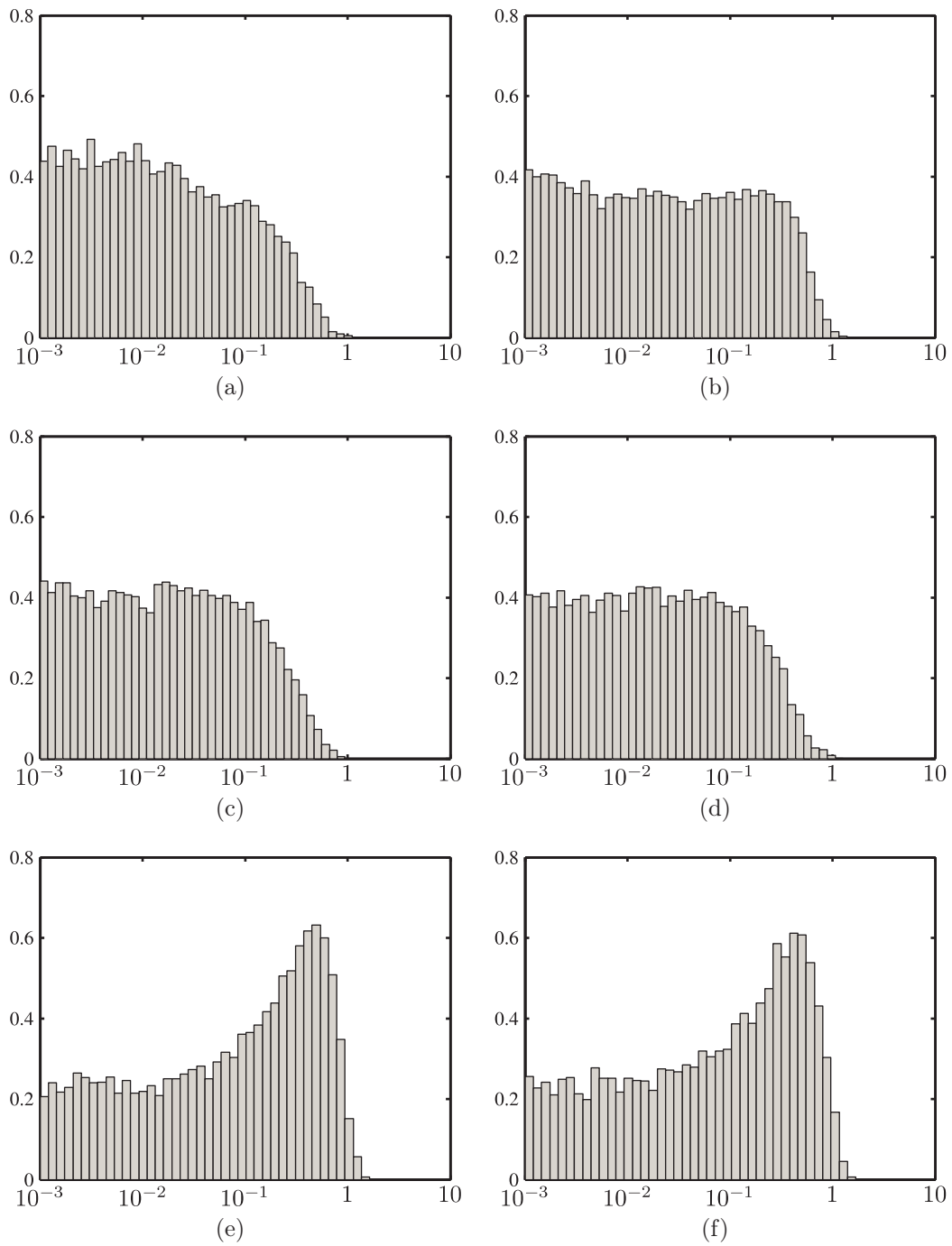


Figure 4.19: Normalised histograms of posterior distributions of the formation conductivity for different measurement data, measurement uncertainty $p_B = 10^{-3}$ and true value $\sigma_f = 0.05$ S/m.

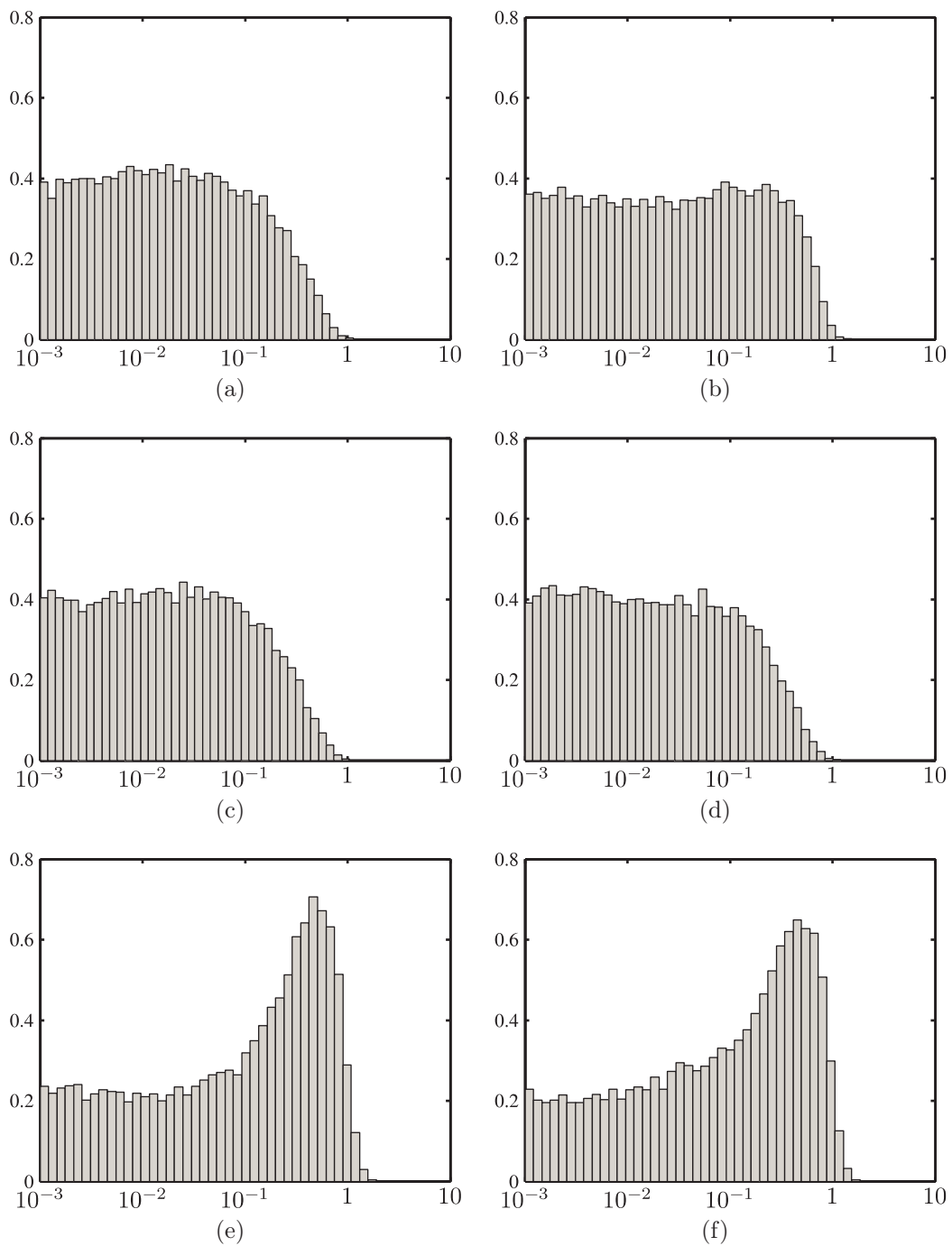


Figure 4.20: Normalised histograms of posterior distributions of the formation conductivity for different measurement data, measurement uncertainty $p_B = 10^{-3}$ and true value $\sigma_f = 0.1$ S/m.

4.5 Solution of the inverse problem

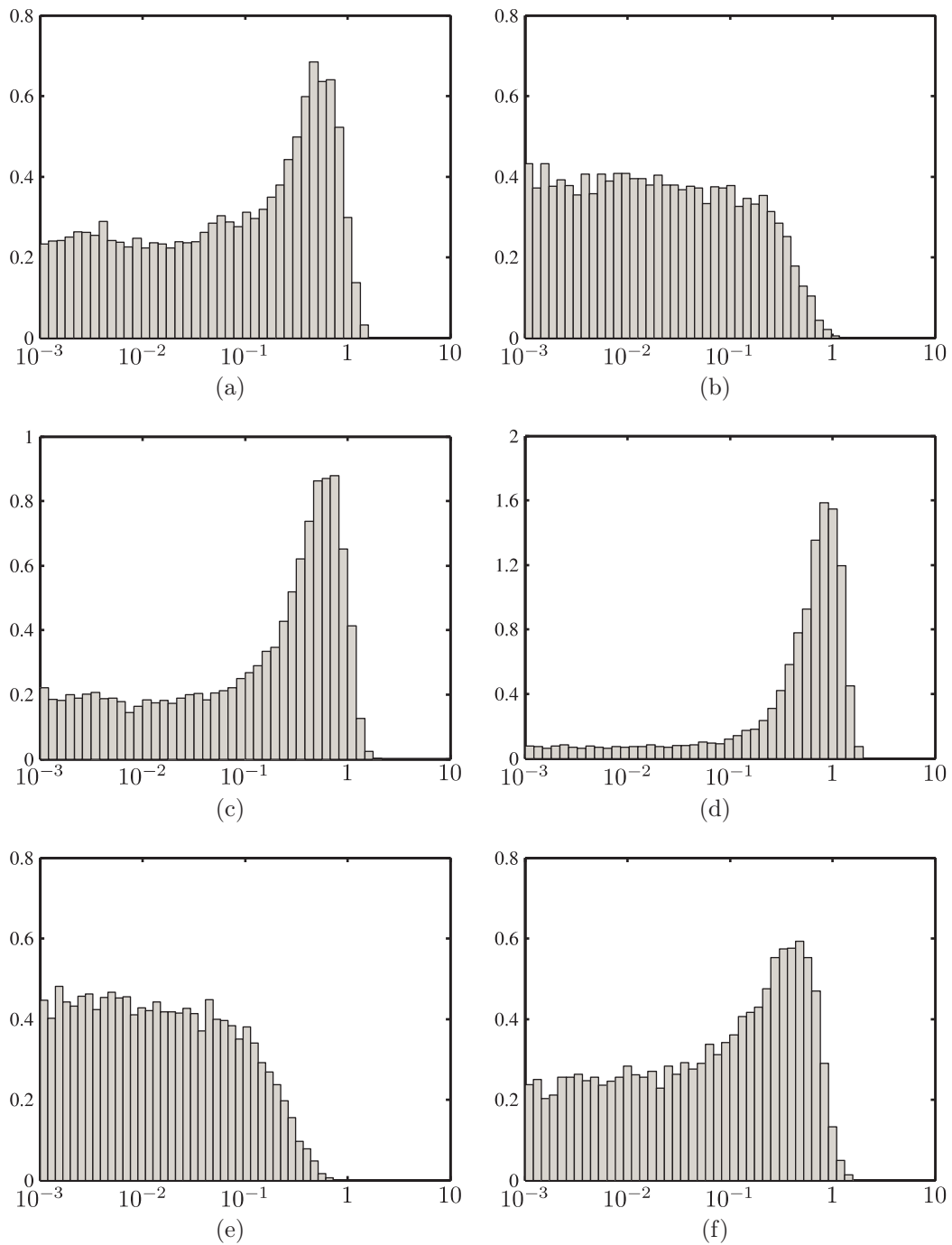


Figure 4.21: Normalised histograms of posterior distributions of the formation conductivity for different measurement data, measurement uncertainty $p_B = 10^{-3}$ and true value $\sigma_f = 0.5$ S/m.

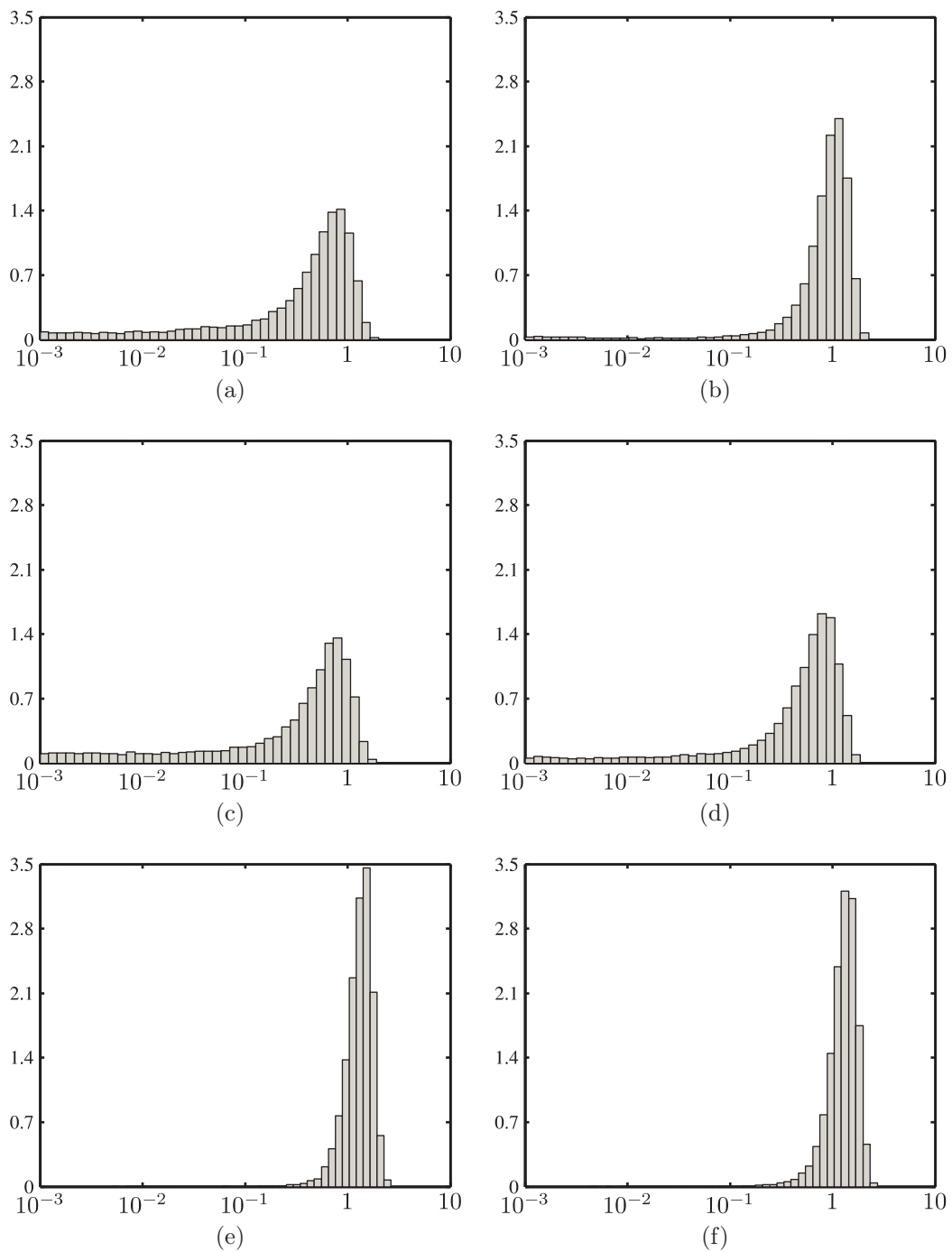


Figure 4.22: Normalised histograms of posterior distributions of the formation conductivity for different measurement data, measurement uncertainty $p_B = 10^{-3}$ and true value $\sigma_f = 1$ S/m.

4.5 Solution of the inverse problem

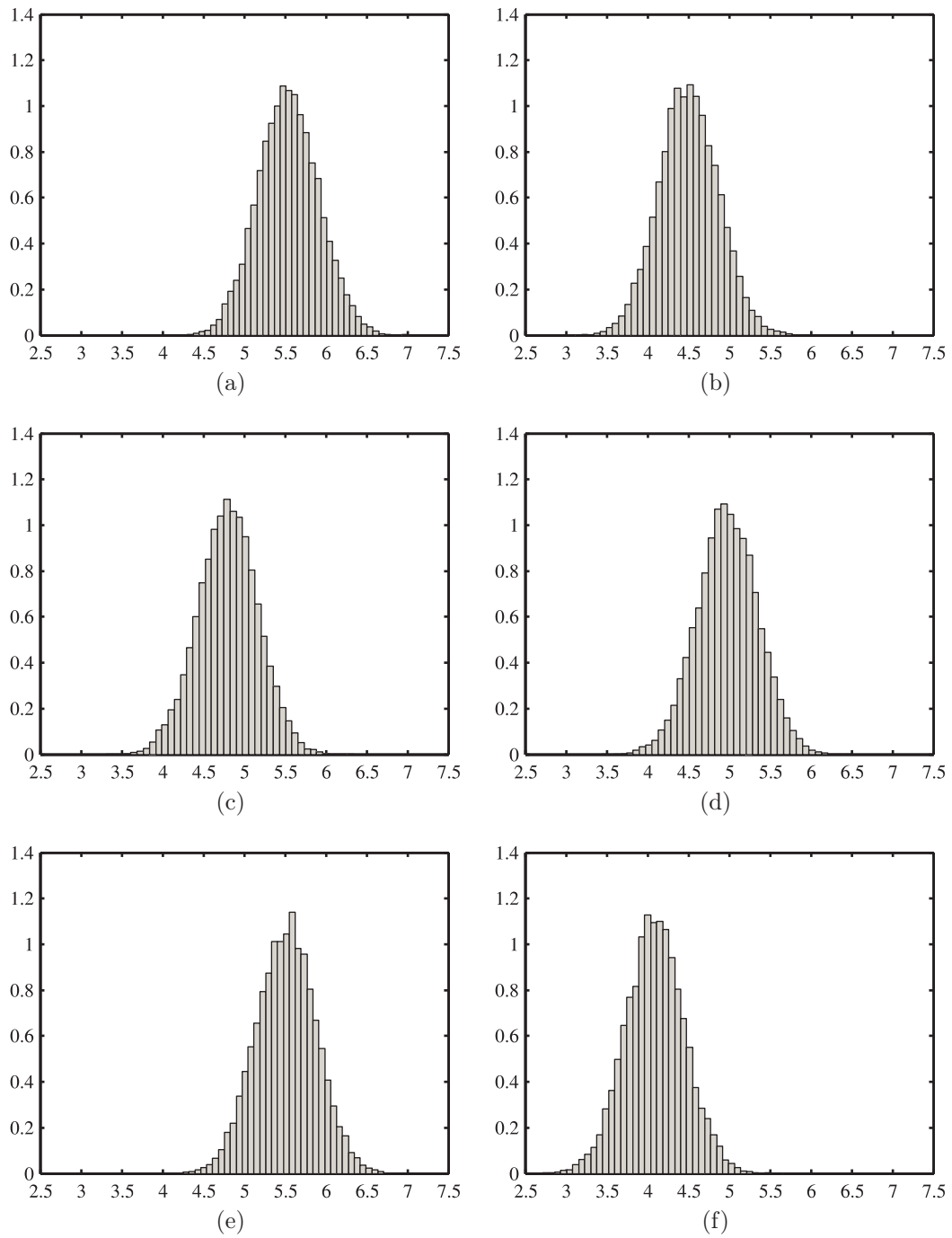


Figure 4.23: Normalised histograms of posterior distributions of the formation conductivity for different measurement data, measurement uncertainty $p_B = 10^{-3}$ and true value $\sigma_f = 5$ S/m.

Chapter 5

Experimental results

If your experiment needs statistics, you ought to have done a better experiment.

Ernest Rutherford (1871–1937)

Langworthy Professor of physics at
University of Manchester
Norman T. J. Bailey, “The Mathematical
Approach to Biology and Medicine,” 1967

Physical scale modelling is an important technique for obtaining the electromagnetic response of a large systems that would be otherwise impossible to realise in a laboratory [99–101]. We will use this technique in order to develop a laboratory model of a cased well surrounded with a low-conductive medium. The results of the experiments made with the scaled model and the characteristics of the employed electronic instrumentation will indicate the feasibility of such a measurement in a real situation as well as the sensor interface requirements. At the end of the chapter, we will discuss the single-coil method and the remote-field technique, both used for the casing inspection.

5.1 Scaled model

5.1.1 Scaling relations

In what follows, these definitions will be useful: a field system or model is an actual, target measurement situation with realistic dimensions; a scaled model of a field system has all dimensions scaled, as well as the frequency or time range, the electromagnetic properties of the medium, and the intensity of the electromagnetic field [100]. The field system must be made only of materials with linear electromagnetic properties. The scaling factors of dimensions, electromagnetic properties and the fields are interdependent.

Using k_l for the length scale factor, the coordinates in the field system are related to the coordinates in the scaled model by the transformations:

$$x = k_l x', \quad y = k_l y', \quad z = k_l z', \quad (5.1)$$

where primed quantities belong to the scaled system. In order to keep the Maxwell's equations invariant under transformation (5.1), it is necessary to scale fields \mathbf{E} , \mathbf{H} and time t or frequency f [100]:

$$\mathbf{E}(x, y, z, t) = k_e \mathbf{E}'(x', y', z', t'), \quad (5.2)$$

$$\mathbf{H}(x, y, z, t) = k_h \mathbf{H}'(x', y', z', t'), \quad (5.3)$$

$$t = k_t t', \quad (5.4)$$

$$f = \frac{1}{k_t} f', \quad (5.5)$$

where k_e , k_h , and k_t are the scale factors for electric field, magnetic field, and time, respectively. These transformations result in the following relationships between the properties of the media in the scaled model and the field system:

$$\sigma' = \frac{k_l k_e}{k_h} \sigma, \quad (5.6)$$

$$\varepsilon' = \frac{k_l k_e}{k_h k_t} \varepsilon, \quad (5.7)$$

$$\mu' = \frac{k_l k_h}{k_e k_t} \mu. \quad (5.8)$$

Scaling relations for voltage, current and impedance can be derived from Faraday's and Ohm's laws:

$$U' = \frac{1}{k_e k_l} U, \quad (5.9)$$

$$I' = \frac{1}{k_e k_t} I, \quad (5.10)$$

$$Z' = \frac{k_t}{k_l} Z. \quad (5.11)$$

According to Sinclair, models in which (5.6)–(5.8) are obeyed and in which k_e and k_h are established separately are called “absolute” models. For such models all quantities (including power levels and the fields) can be used to calculate corresponding full-scale quantities [99]. The other class of models are “geometrical” models where only the ratio of k_e and k_h is known (equal to 1 if $\mu' = \mu$ and $\varepsilon' = \varepsilon$). As a consequence, in geometrical models one can establish relations only between few scaled and full-scale quantities such as resistance, inductance or capacitance but cannot do so in case of e.g. power levels or field magnitudes [99].

It is difficult to find the suitable materials that would satisfy equations (5.6)–(5.8). The problem can be ameliorated if we assume that $\mu' = \mu$ and $\varepsilon' = \varepsilon$ and if we ignore displacement currents. In that case, the following relations need to be satisfied:

$$\frac{k_e}{k_h} = \frac{k_l}{k_t}, \quad (5.12)$$

$$\sigma' = \frac{k_l^2}{k_t} \sigma. \quad (5.13)$$

We can now establish the basic criteria and relations valid for our scaled model that we will present in more details in section 5.1.2. We will assume that all materials in the field and scaled systems have the same electromagnetic properties. This significantly simplifies the construction of the laboratory model. Equation (5.12) guarantees that $\mu' = \mu$ and $\varepsilon' = \varepsilon$, and if $\sigma' = \sigma$, from (5.13) it follows that:

$$k_t = k_l^2.$$

In order for our model to be absolute, we must fix the values of k_e and k_h . We will make it so by choosing equal transmitter currents in the full-scale and scaled case. From (5.10) and $I' = I$ we get $k_e k_t = 1$, what in combination with (5.12) results in $k_h k_l = 1$.

To summarise, for our scaled model following scaling relations hold:

$$k_l, \text{ arbitrary}, \quad (5.14)$$

$$k_t = k_l^2, \quad (5.15)$$

$$k_e = \frac{1}{k_t} = \frac{1}{k_l^2}, \quad (5.16)$$

$$k_h = \frac{1}{k_l}. \quad (5.17)$$

Electromagnetic properties and transmitter currents are the same in the field and scaled systems, whereas magnetic field in the field system is weaker k_l times compared to the field in the scaled model.

5.1.2 Cased borehole model

The laboratory scaled model of a cased borehole is schematically depicted in Fig. 5.1. The metal tube can be easily inserted into a plastic tube coaxially fixed within the plastic tank filled with a saline solution, which could be drained using the valve at the bottom of the tank. The solution represents low-conductive rocks (formation) surrounding the casing. The transmitter and receiver coils are placed inside the metal tube in the vertically symmetrical position with respect to the solution. The thermocouple inside the tube is used to monitor the temperature of the coils. The transmitter and receiver coils are connected to their respective interfaces, section 5.1.3.

Based on the typical dimensions of the field system and available materials, we decided to use the time scale factor $k_t = 200$, or the length scale factor $k_l = \sqrt{200}$ according to (5.15). Dimensions of the scaled model and the field system are given in Table 5.1. The resulting field system is similar to the cases examined in Chapters 3 and 4. The material properties are unaffected by the scaling as discussed in section 5.1.1. The radius of the tank is less than one half of the coil separation and corresponding radius of investigation, according to section 3.1.4. Since the response of the inductive sonde depends on both volume and conductivity of the surrounding formation, see [11], we will use solution that is more conductive than its real-world counterpart for a factor of about 5, which stems from the ratio of the coil separation and tank radius.

5.1 Scaled model

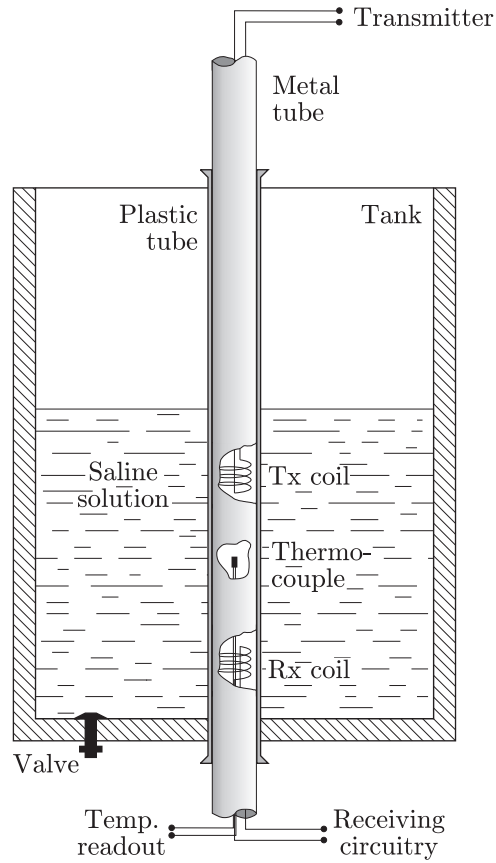


Figure 5.1: Schematic representation of the scaled model of the cased borehole.

Table 5.1: Properties of the scaled model and the field system for the time scale factor $k_t = 200$.

Quantity	Scaled model	Field system
Metal tube		
Outer radius	11 mm	155.6 mm
Wall thickness	1 mm	14.14 mm
Length	1.9 m	27 m
Tank (formation)		
Radius	15 cm	2.12 m
Height	0.48 m	6.8 m
Coils		
Height	40 mm	560 mm
Mean radius	4.1 mm	58 mm
Mean separation	34 cm	4.8 m
Frequency	12 kHz	60 Hz
Materials	Identical	

5.1.3 Signal generation, acquisition and processing

The coils were wound on the cylindrical formers made of the MACOR machineable glass-ceramic with length of 40 mm and radius of 3.5 mm. The transmitter coil had 266 turns of 0.4 mm wire in 3 layers. The receiver coil had approximately 1000 turns of 0.25 mm wire in 8 layers. At 12 kHz the transmitter coil had inductivity of 104 μH and serial resistance of 1.08 Ω (impedance of 7.92 Ω), whereas the receiver coil had 1.51 mH and 10.59 Ω .

The transmitter coil was fed from an amplifier built around LM3875T audio power amplifier driven by a function generator (Agilent HP3245A). The excitation current, around 1.55 A_{pp} , was monitored with a current probe (Tektronix TM502A). The temperature of the coil was monitored by Fluke 80TK thermocouple connected to Fluke 45 multimeter.

The receiver coil was connected to a proprietary differential amplifier, originally aimed for EEG applications [102]. The amplifier has a guard shield, input impedance of around 130 M Ω , CMRR of 120 dB at frequencies below 200 Hz, differential gain 2000, cut-off frequency of 29 kHz, and equivalent input voltage noise of 4.18 nV/ $\sqrt{\text{Hz}}$ [102].

The outputs of the current probe, the receiver amplifier and the multimeter were digitised using a 16-bit USB digital acquisition module (National Instruments, NI USB-6211) connected to a battery powered laptop. The software for monitoring, processing and logging of the measurement data was implemented in the NI LabVIEW platform, Fig. 5.2.

The main task of the monitoring application was the implementation of a digital phase-sensitive amplifier (lock-in) for the measurement of the phase difference between the excitation current signal and the voltage induced in the receiver [103–106]. The two signals in ± 200 mV range were simultaneously sampled with 125 kHz each. Number of samples multiplied by the 12 kHz digital reference signal and its $\pi/2$ shifted replica was 30000. The in-phase and quadrature components of the input signals were determined by averaging the multiplication results. The final result, the phase difference between the input signals, was determined by averaging the results of 30 iterations. The phase difference was measured every 10 seconds, what can be easily estimated from the sampling frequency, and the number of samples and iterations.

5.1.4 Interference reduction

The sources of interference in this experimental set-up were thermal variations, electrical mains coupling, and capacitive coupling of the transmitter and receiver coils. The latter is by far the most conspicuous, because we measured very small inductive coupling of the transmitter and receiver through the saline solution (i.e. formation). The thermal variations were handled by a careful design of the experimental procedure, section 5.1.5, whereas the electrical mains coupling were taken care of in the process of minimising the capacitive coupling of the coils, and by the phase sensitive detection.

5.1 Scaled model

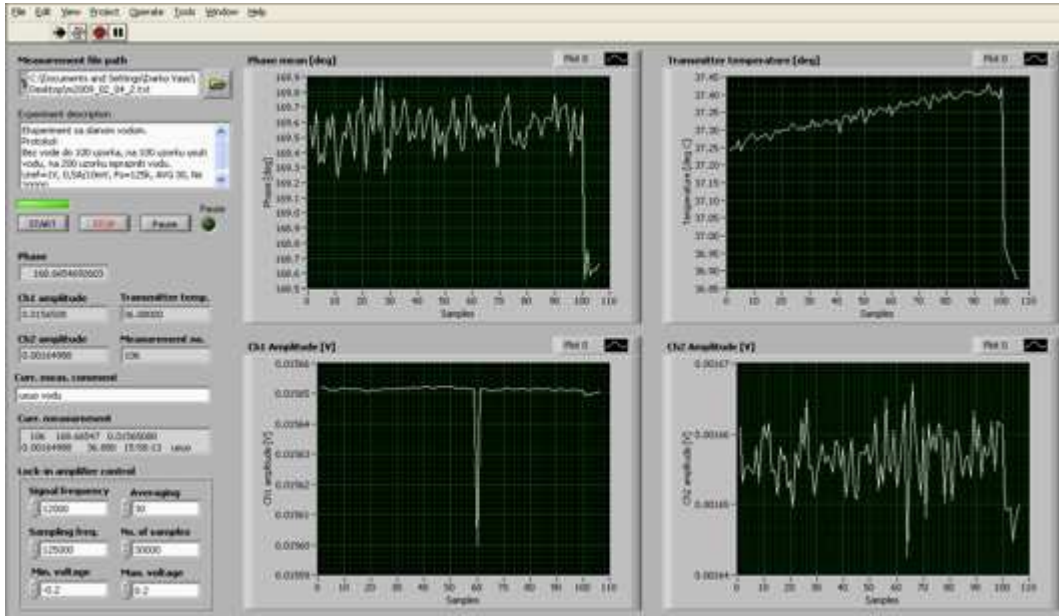


Figure 5.2: Screenshot of the monitoring application developed in the NI LabVIEW package. Controls of the acquisition and digital lock-in amplifier are on the left. The graphs on the right shows time logs of phase difference, coil temperature, excitation current and induced voltage.

The capacitive coupling was reduced below the level of the inductive effects by shielding the coils, guarding the receiver's shield and connecting the transmitter coil and the metal tube to the common point. The coil shields were made of thin, parallel, isolated wires of the ribbon cable short-circuited at one end, Fig. 5.3. Such a construction minimises the eddy current effect; the impedances of the coils with and without the shield remained unchanged for frequencies below 100 kHz. The shielded receiver coil was connected through a screened twisted pair to the receiver amplifier. The cable and coil shields were guarded with the common-mode voltage, Fig. 5.4 [108, 109]. The transmitter coil was connected to the power amplifier through double-shielded cable,

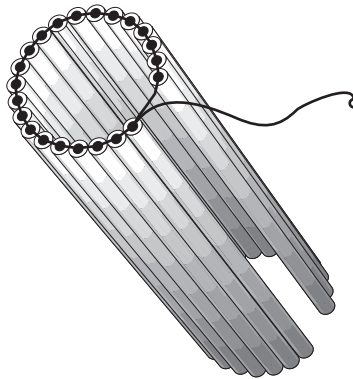


Figure 5.3: Coil shield made from a ribbon cable short-circuited at one end.

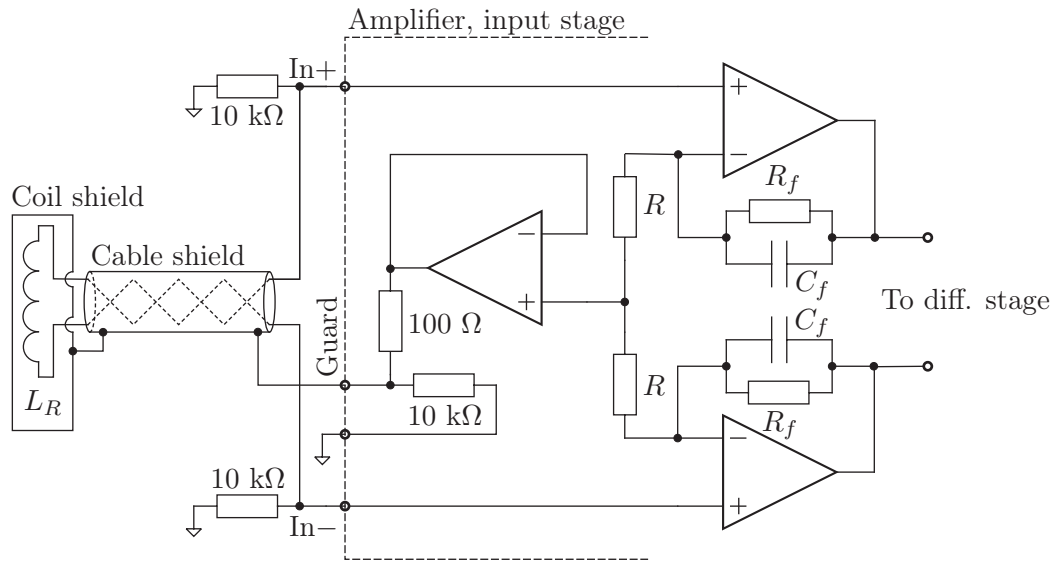


Figure 5.4: Connection of the shielded receiver coil and cable with the amplifier using guarding with the common-mode voltage, according to [102, 107, 108].

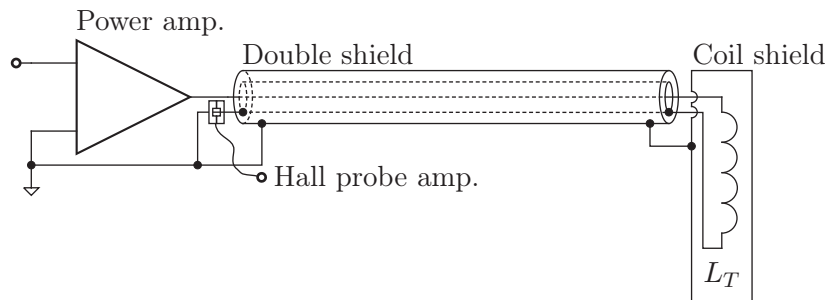


Figure 5.5: Connection of the transmitter coil and power amplifier through double-shielded cable.

Fig. 5.5. The inner shield serves as a return path for the excitation coil, what cancels the excitation current's field [109]. The outer shield drains the leakage current flowing through the coil-shield capacitance into the amplifier common. Position of the Hall's probe ensures that one measures only the current flowing out of the coil.

Fig. 5.6 depicts the equivalent circuit of the measurement with the coils inside the casing. We assume that the remnants of the electrical mains coupling are negligible because of the phase sensitive detection at 12 kHz. The impedance of the transmitter and receiver coils are Z_T and Z_R , respectively. There are lump impedances Z_{TS} between the transmitter coil and its shield, and Z_{SC} between the shield and the casing. Similarly on the receiver side, we have Z_{RS} and Z_{SC} . Let $Z_1 = Z_{TS} + Z_{SC}$ and $Z_2 = Z_{RS} + Z_{SC}$. Let $X_M = j\omega M(\omega)$ be the mutual inductance between the transmitter and re-

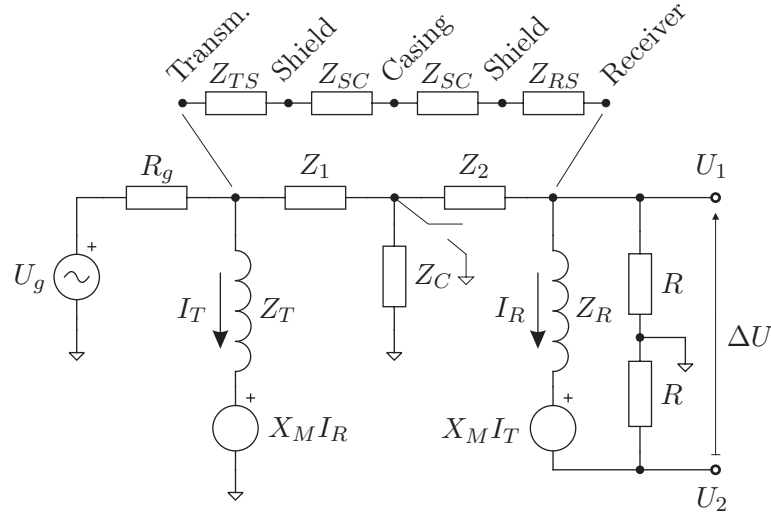


Figure 5.6: Equivalent circuit of the inductive measurement.

ceiver including contributions of the casing and surrounding formation. The impedance between the casing and the earth is Z_C . The power amplifier is depicted as a voltage generator U_g with the output resistance R_g . The transmitter current is I_T , and the receiver current is I_R . The components of the receiver current are due to the mutual inductance and the current that leaked across the current divider Z_C, Z_2 .

We are interested in the transfer function H between the induced voltage $\Delta U = U_1 - U_2$ and the transmitter current I_T . After somewhat demanding algebraic manipulations, we obtain:

$$\begin{aligned}
 H &= \frac{\Delta U}{I_T} = \\
 &= \left(RX_M (-X_M Z_C + 2Z_2 Z_C + R(Z_1 + Z_C) + 2Z_1(Z_2 + Z_C)) + RZ_C Z_R Z_T \right) / \\
 &\quad \left(RZ_1(R + 2Z_2) + RZ_C(R - X_M + 2(Z_1 + Z_2)) + \right. \\
 &\quad \left. + Z_R(Z_1(R + Z_2) + Z_C(R + Z_1 + Z_2)) \right). \quad (5.18)
 \end{aligned}$$

In the idealised situation, there is no capacitive coupling between the coils and casing, i.e. $Z_1 \rightarrow \infty, Z_2 \rightarrow \infty$, and:

$$H_{ideal} = \frac{2RX_M}{2R + Z_R}. \quad (5.19)$$

Since $R \gg Z_R$, it follows from (5.19) that $H \approx X_M$, i.e. the transfer function is proportional to the mutual inductance as predicted by the equations in Chapter 2. In reality we must ground the shields and the casing in order for the model to approximate the measured transfer function. Grounding the casings results in $Z_C = 0$ and the transfer function is:

$$H_{gnd} = \frac{X_M}{1 + \frac{Z_R}{R} \frac{R + Z_2}{R + 2Z_2}}. \quad (5.20)$$

It is interesting to note that, according to (5.20), the transfer function in case of the grounded casing does not depend on the capacitances between the transmitter, its shield and the casing. Impedance Z_2 is reduced by grounding the receiver shield (Z_{SC} is short-circuited). Finally, because of $R \gg Z_R$, we have $H \approx X_M$. From this discussion follows single most important measure of reducing the unwanted capacitive coupling — connection of the casing to the reference point of the electronic circuitry.

5.1.5 Results

We have conducted a number of experiments in order to rule out the possibility of the capacitive coupling between the coils. Experiments included variation of the casing's environment and its capacitance, such as a person touching the casing, introduction of metallic objects (grounded or not) near the casing, etc. In all measurement situations variations in the receiver's output were significant if the casing and shields were not grounded, and nonexistent if the casing was grounded. For the sake of shortness and clarity, these experiments are omitted here.

The objective of the experiments explained herein was to establish if there was a detectable phase difference between the cases when the tank was empty, full of tap water, or full of the NaCl solution. A single experiment consisted of three steps. Firstly, we measured the phase difference with the empty tank. Then the tank was filled with the water or the saline solution, while we continued to measure the phase. Finally, the tank was drained and we obtained another set of the measurement results with the empty tank. Thus, each recorded phase difference log has three segments; first with the empty, second with the full, and third with the empty tank again. The electrical conductivity of the tap water is negligible. The electrical conductivity of the NaCl solution was 15.5 S/m, which we measured with Mettler-Toledo S47 conductivity meter. This conductivity is achieved by adding approximately 8 kg of salt into 50 L of the tap water. Both containers with the liquids were held for days in the laboratory and the liquids achieved stable temperature of $(26.3 \pm 0.3)^\circ\text{C}$ in all experiments.

The phase difference logs for the two experiments made with the copper casing are shown in Fig. 5.7. There is a distinctive change in the phase difference when the saline solution is poured into the tank. Such difference is not visible for the case with the tap water in the tank. Furthermore, the phase differences in both experiments for the empty tank are equal. This is seen clearly in Figs. 5.8 and 5.9 that show the phase difference histograms of the logs from Fig. 5.7 for each of the segments. The significant difference exists only in the case of the saline solution in the tank.

Logs of the transmitter current are depicted in Fig. 5.10. The current was around 0.748 A, and its variations during experiments were less than 0.0008 A. The receiver voltage, shown in Fig. 5.11, was around 1600 μV with variations less than 25 μV . It is interesting to note that there is no visible difference in the induced voltage when the content of the tank is changed. This confirms our conclusions from Chapter 3 that the changes in the formation conductivity are not observable in the amplitude of the induced voltage.

The transmitter temperature logs are depicted in Fig. 5.12. All experiments started only after the temperature of the transmitter was stabilised. It took about 1 h for the temperature to stabilise within ± 0.1 $^{\circ}\text{C}$. Although the effect of adding a cooler liquid into the tank is clearly visible in the temperature logs, the temperature changes are similar for the saline solution and tap water, so they can be ruled out as a reason for the observed changes in the phase difference.

Considering all of the above, we can conclude that the observed change of the phase difference is exclusively due to inductive coupling with the conductive saline solution.

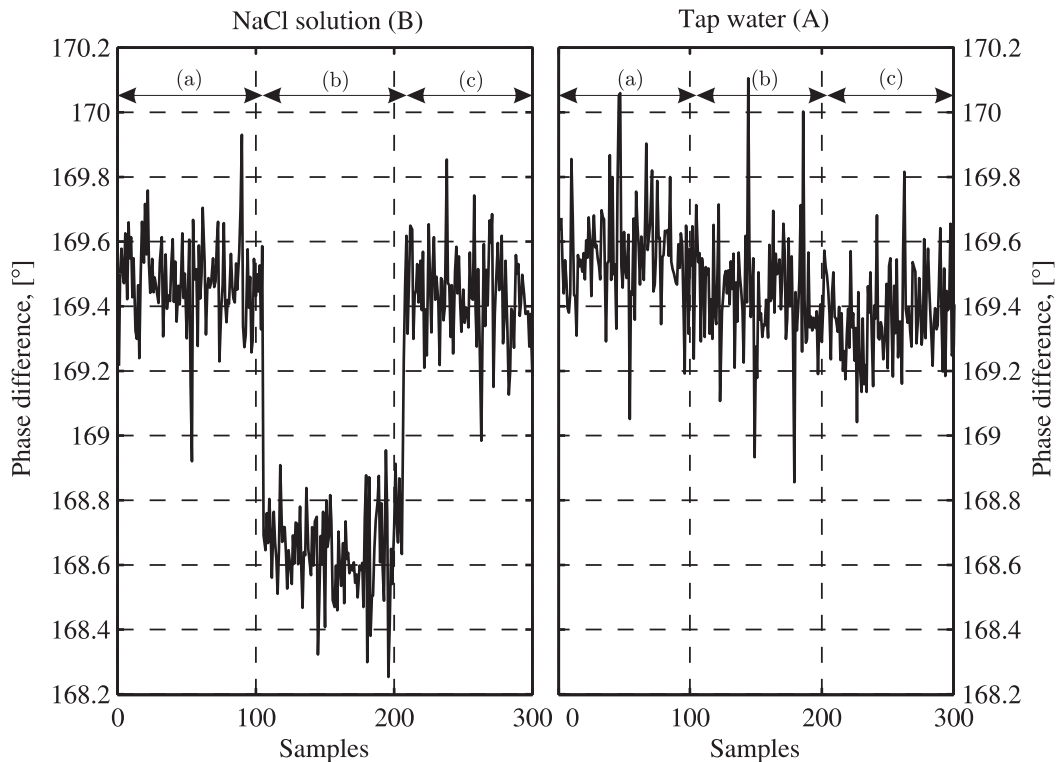


Figure 5.7: Phase difference logs for the copper casing in the experiments with NaCl solution (B) and tap water (A). The segments are approximately between indices 1–100, 101–200, and 201–300; respectively: a) before the solution was poured in the tank, b) while the tank was filled with NaCl solution or tap water, and c) after the tank was drained. The segments' histograms are shown in Figs. 5.8 and 5.9

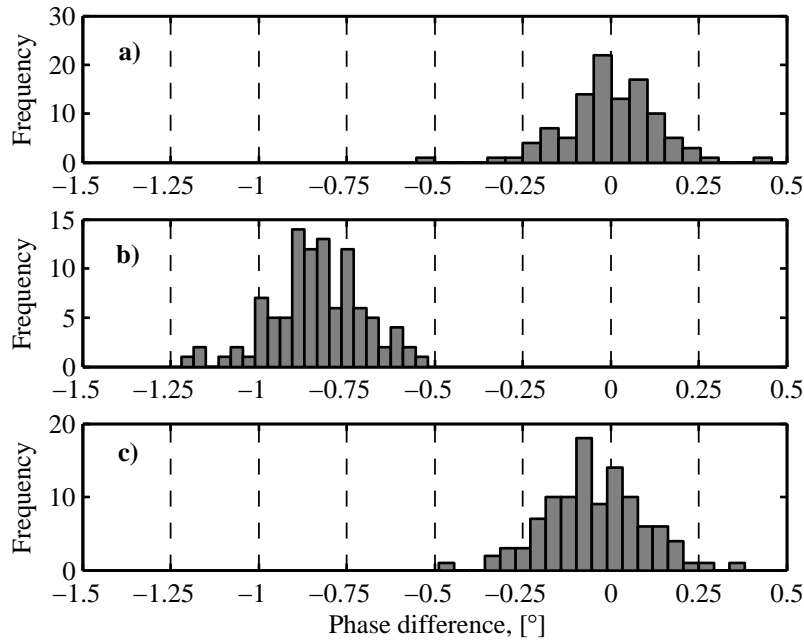


Figure 5.8: Histograms of the three segments of the phase difference log from Fig. 5.7 for NaCl solution. See Fig. 5.7 for explanation of the segments. The mean value of the first segment was reduced from all three segments.

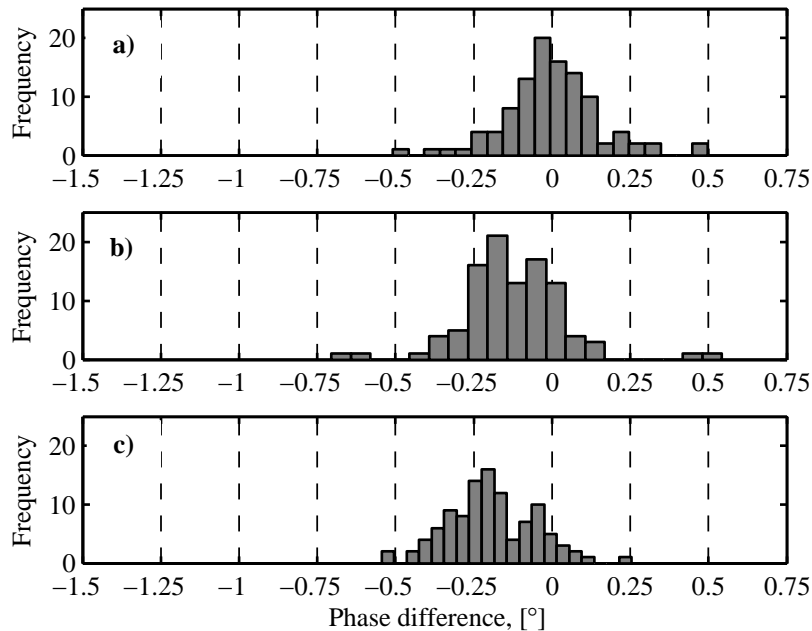


Figure 5.9: Histograms of the three segments of the phase difference log from Fig. 5.7 for tap water. See Fig. 5.7 for explanation of the segments. The mean value of the first segment was reduced from all three segments.

5.1 Scaled model

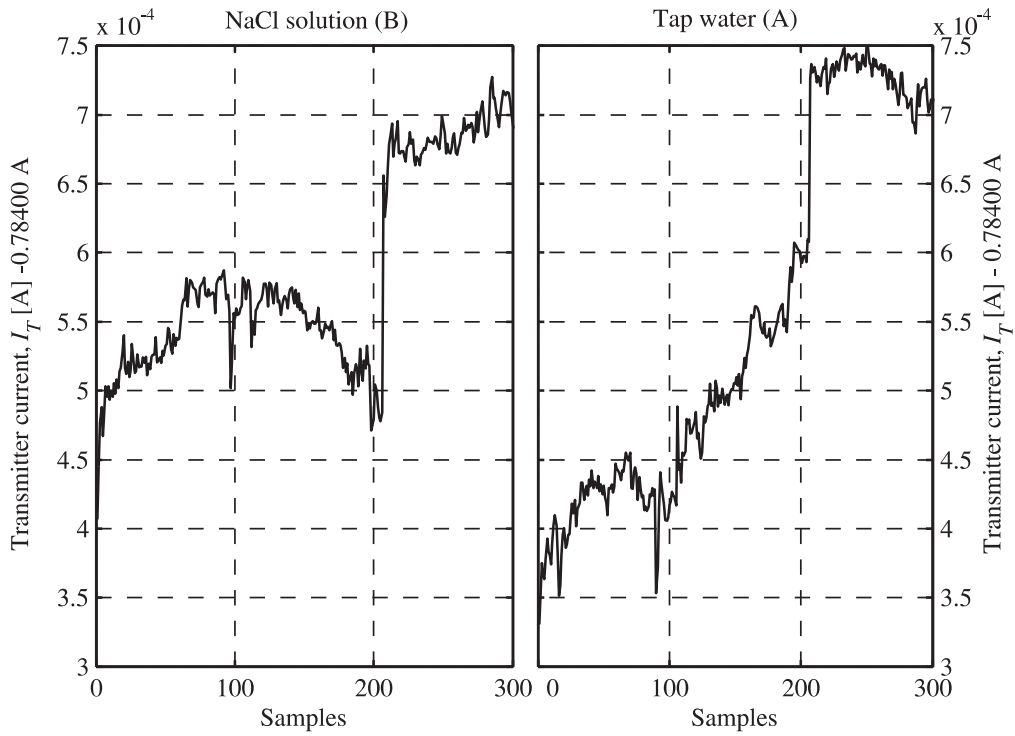


Figure 5.10: Variations of the transmitter current around the baseline of 0.78400 A for the copper casing in the experiments with NaCl solution (B) and tap water (A).

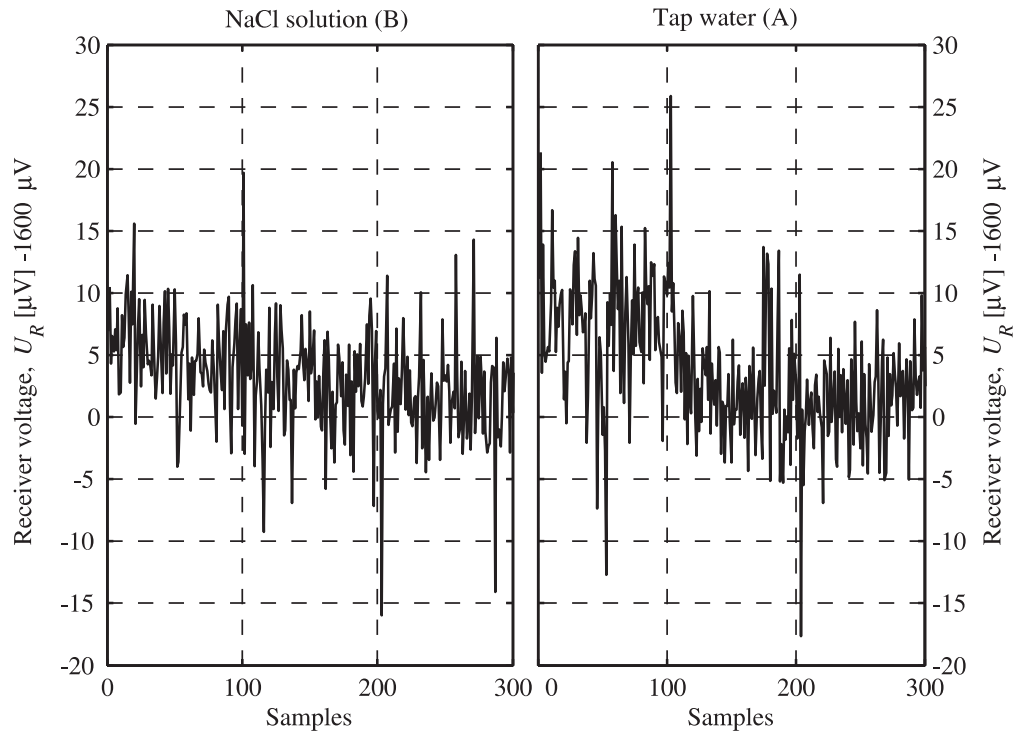


Figure 5.11: Variations of the receiver voltage around the baseline of 1600 μ V for the copper casing in the experiments with NaCl solution (B) and tap water (A).

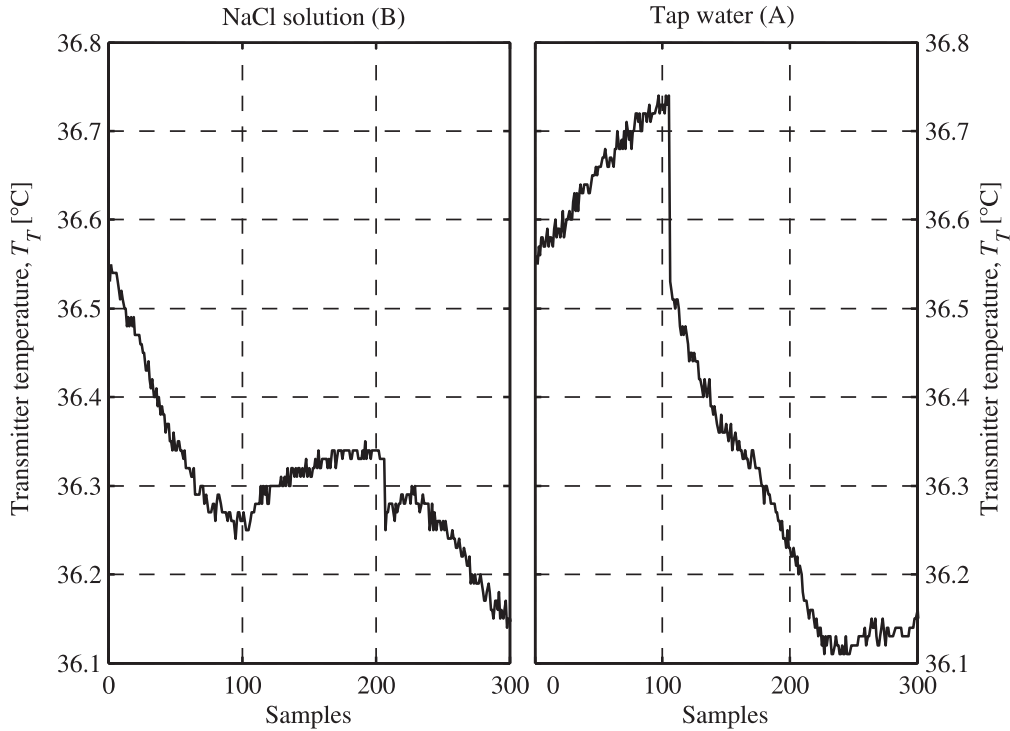


Figure 5.12: Transmitter temperature for the copper casing in the experiments with NaCl solution (B) and tap water (A).

5.1.6 Comparison with the analytical model

We calculated the expected phase difference using the analytical model from Chapter 2. The casing had properties given in Table 5.1, $C(10 \text{ mm}, 1 \text{ mm}, 56 \text{ MS/m}, 1)$. The surrounding medium was $M(42 \text{ cm}, 15.5 \text{ S/m}, 0 \text{ S/m})$. The phase difference was obtained by subtracting the phases of the magnetic fields for $r_3 = 2 \text{ cm}$ and $r_3 = 15 \text{ cm}$. The phase difference, calculated in such a way, does not contain effects of the casing and the formation beyond 15 cm. The latter acknowledges the fact that the radius of the tank was only 15 cm. We assumed that the interaction of the induced currents in the parts of the formation is negligible, see section 3.3 and [11].

From the measurement results for the copper casing in Fig. 5.7, we obtained the phase difference of $(-0.81 \pm 0.19)^\circ$ for the saline solution, whereas the model prediction for the single-turn transmitter and receiver is -0.75° . The model prediction and measurement result are alike considering the fact that the experimental set-up was not calibrated in terms of the amplifier gain, inter-turn coil capacitances, number of coil turns, etc. The measured induced voltage was around $(1600 \pm 20) \mu\text{V}$ at the output of the amplifier. The model prediction of the induced voltage, obtained using single-turn coils and corrected for the magnetic moments of the real coils, is between $700 \mu\text{V}$ and $1200 \mu\text{V}$ for 10% variations in the casing properties. Besides large sensitivity to the

casing properties and aforementioned calibration of the experimental setup, the discrepancy can be attributed mainly to the much longer tube in the modelling.

5.2 Single-coil method for inner radius

Measurement of the inner radius has been discussed in this author's master's thesis entitled "Single-coil method for simultaneous measurement of multiple parameters of a metal tube" [49, 71]. The measurement is based on minimisation of the Euclidian distance between the prediction of an impedance model and the actually measured impedance of a single coil at a single frequency. Here, we give a summary of the most important findings.

The coil impedance model, based on the work of Dodd and Deeds, was implemented in Matlab [41]. We analysed the errors of the numerical implementation of the model and concluded that the accuracy of the calculated coil impedance is at least 4 significant decimal digits.

The effect of finite tube wall thickness on the coil impedance is made negligible by a choice of higher excitation frequency. From the analysis of the impedance sensitivity to the wall thickness, it follows that the excitation frequency should be at least 10 kHz for the minimal wall thickness of 1 mm over the expected ranges of permeability and conductivity. If these conditions are met, inner radius, magnetic permeability and electrical conductivity remain the only tube properties that the model needs to account for. Thus, the search space for the optimisation procedure is 3-dimensional.

Coil resistance and inductance are between 10 Ω and 1 k Ω for coils that fit typical tubing and casing. The sensitivity of the impedance to the inner radius is between 1 Ω /mm and 10 Ω /mm. The optimisation procedure is ill-conditioned with respect to permeability and conductivity, i.e. small errors in impedance measurement (e.g. ± 0.01 Ω in (10–1000) Ω range) will result in poor accuracy of permeability and conductivity (between 10% and 50%). On the other hand, permeability-to-conductivity ratio can be determined with accuracy better than 5% if the excitation frequency is higher than 20 kHz and the impedance measurement accuracy is better than 0.5 Ω . Separation of permeability and conductivity would require very high impedance accuracy of the order of ± 0.001 Ω . In practice, only the inner radius and permeability-to-conductivity ratio can be determined using the single-coil method.

From the Monte Carlo analysis it follows that inner radius and PCR will be normally distributed for normally distributed errors in the impedance measurement. Relative standard deviation of the inner radius is approximately 2.5 times smaller and deviation of PCR is 3 times greater than relative standard deviation of the impedance.

An appropriate choice of the coil can significantly improve the quality (accuracy and precision) of the measurement results. The radius of the coil should be as close as possible to the radius of the inspected tube, i.e. fill-factor should be close to 1. If the fill-factor decreases by 25%, sensitivities to inner radius

and PCR are halved. Higher turn density and longer coil also improve the sensitivities. However, a longer coil implies lower axial resolution.

Coil decentralisation, material non-idealities and environmental temperature can influence the result of the single-coil method. We have assumed practical realisability of the centralisation (using centralisers), relying on the fact that the accuracies of other methods for testing tubular products depend on centralisation too. Another possibility is to use vibrations, so called “road noise,” of the probe while it travels along the tube — minimal coil resistance corresponds to the perfectly centred coil [110]. The single-coil method results in tube properties that are actually averaged circumferential distribution of the inner radius and PCR (e.g. only a part of the tube circumference has internal corrosion or material inhomogeneity). Because of the small magnitude of the coil excitation current, nonlinearity of ferromagnetic tube materials is not considered to be a problem. The temperature at which the measurement is carried out must be measured, and the impedance of the coil must be corrected for its temperature variations.

We measured the inner radius and PCR of several tubes using the single-coil method. The reported experimental results validated the proposed procedure within the range of 10 kHz to 100 kHz for both nonmagnetic and ferromagnetic tube materials. The results obtained at any two frequencies from the interval differed less than 0.5% for the inner radius and 2% for PCR. Error of the inner radius was of the order of 1% relatively to the nominal inner radius, specified by the tube manufacturer. Error of PCR was between 1% and 10%, estimated using the sensitivity analysis.

Coil parasitic capacities (interwinding and winding-to-tube) was identified as having a significant effect on accuracy of measured inner radius and PCR. Proposed procedure for correction of parasitic capacities uses a single lump impedance to represent the effect of interwinding capacities only. Accuracy of the method can be improved by the employment of a more realistic equivalent circuit for the coil.

5.3 Remote-field technique

The theoretical background of the remote-field technique (RFT) or remote-field eddy-current technique (RFEC), both names being somewhat of a misnomer, was given in section 3.2. Instead of rewriting a number of experimental studies on the casing inductive inspection we published so far, we will list only the most important experimental results that goes hand in hand with the theoretical findings of section 3.2.

1. Measured induced voltage spectrum shows distinctive low and high frequency bands that correspond to the remote and direct zones, respectively [48].
2. The direct zone is sensitive to the changes of the inner radius, whereas

the remote zone exhibits much greater sensitivity to the wall thickness than to the inner radius [48].

3. A response to a pulsed excitation calculated from the measured transfer function fits well to the measured pulsed response [111].
4. The measurement system can be treated as a linear, time-invariant system allowing applications of the system identification procedures [111].
5. Pulsed excitation and linearity of the system allows simultaneous measurement of the inner radius and wall thickness using the zero-crossing time and voltage peak value as respective signal features [48].
6. All of the measured results corroborate the analytical model based on the Dodd-Deeds approach [63].
7. An instrument for casing inspection based on the transient inductive technique suitable for operation in harsh oil-well environment was successfully prototyped [112].

Chapter 6

Electronic instrumentation

They couldn't hit an elephant at this distance.

General John Sedgwick (1813–1864)

His last words few minutes before he was hit by sniper fire at the battle of Spotsylvania on 9 May, 1864

In this chapter, we will discuss the main factors that influence the electronic instrumentation design and accuracy of the inductive measurement. Furthermore, we will describe the key system components (transmitter, receiver and acquisition circuitry) and analyse the expected measurement uncertainty and high-temperature operation.

6.1 Influential factors

The influential factors that restrain the overall measurement accuracy and impose additional requirements on the system design are the presence of noise, coil decentralisation, parasitic capacitances, nonlinearity of the casing material and environmental temperature. We will pay due attention to the noise effect in section 6.3, while in this section we discuss the remaining factors.

6.1.1 Coil decentralisation

Coil decentralisation or misalignment of the coils' axes and the casing's axis are caused by the uncontrolled motion (wobble, "road noise") of the coils inside the casing during the measurement. The effect of the decentralisation weakens with the distance between the receiver and transmitter coils. The remote field technique at low frequencies is practically insensitive to the eccentricity [113]. Well-logging tools are usually equipped with the bow-spring centralisers in order to reduce the wobble. If that is not enough, a model-based approach can be tried, although it is analytically and computationally demanding [114, 115].

The single-coil method for measurement of the inner radius is very susceptible to the coil decentralisation [49]. In [116], we used an impedance model based on the second-order vector potential for correction of the wobble effect [115]. Another possibility, examined in [110], is to use the wobble and the fact that the resistive part of the coil impedance is minimal when the coil is perfectly centred. The minimal impedance is determined from a series of measurements affected by the wobble.

6.1.2 Parasitic capacitances

Parasitic capacitances between the casing and coils are reduced using the coil shields and proper grounding as described in section 5.1.4. However, there remain distributed parasitic capacitances of each coil: turn-to-turn capacitances between turns in one layer, turn-to-turn capacitances between adjacent layers, turn-to-core, and turn-to-shield capacitances, as discussed in [117].

All inductive methods require correction for non-ideal transfer function of the employed coils [71, 118, 119]. Since the coil-to-casing capacitance is made negligible by shielding and grounding, an equivalent lump capacitance for the remaining coil parasitic capacitances can be experimentally obtained measuring the coil's frequency characteristic in the air. These results can be combined with the analytical approach of [117] or [120], if one requires an equivalent circuit more complicated than a simple parallel of an inductor and a capacitor.

6.1.3 Nonlinearity of casing material

The fact that casings are usually made of ferromagnetic steel is rarely discussed in the literature on the electromagnetic casing inspection beyond the observation that the relative permeability is on the order of 100 [69]. The prevailing assumption of linearity of the ferromagnetic material, adopted in this thesis too, holds for weak magnetic fields up to 100 A/m (small signal regime). The proportionality constant between the magnetic field strength and induction under the assumption of weak AC magnetic field is the incremental permeability or, in limit when the field amplitude reaches zero, the reversible permeability [121]. The reversible permeability depends on many factors: magnetic history of the material, biasing magnetic field, imposed stress, temperature, frequency, etc.

The frequency dependence of the permeability is a critical issue in the multifrequency induction tools for the casing inspection, as noticed in [49]. Unfortunately, it seems that this is scarcely discussed in the available literature on the casing inspection topic—the notable exception is [69]. Sometimes, the issue is neglected completely [119]. We deem necessary for any multifrequency system to count for the frequency dependence of the permeability. A complex, frequency-dependent permeability due to a magnetic relaxation can be described in terms of a Cole-Cole model [122]. Experimental results in

e.g. [122, 123] show that the complex nature of the permeability cannot be neglected even at frequencies as low as 10 Hz for various grades of steel. This however does not violate the assumptions made in the modelling in Chapter 2 as long as the system operates in the small signal regime. The frequency dependence of the permeability is the main reason we used only one excitation frequency in this thesis. This guaranties that we can freely combine measurements at different distances from the transmitter coil without a model of frequency dependent permeability.

The mechanical properties of steel (strength, grade, hardness, etc.) are interrelated with its magnetic properties (permeability, saturation magnetization, etc.). Permeability measurement is potentially applicable to tube grade identification and stress evaluation [124, 125]. The Jiles-Atherton model of ferromagnetic hysteresis was proposed in their papers appearing between 1983 and 1986 [126–129]. Since then, the original model has been extended and generalized to include numerous experimentally observed features of ferromagnetic behavior (effect of stress, asymmetric and minor loops, anisotropy, etc.) and to improve the model’s computational effectiveness [130]. The Jiles-Atherton model is now considered to be a classic model of ferromagnetic hysteresis (beside the Stoner-Wolhfarth model, the Globus model and the Preisach model) [131]. At present, the model includes the effects of stress only in the elastic region. Existing theoretical models are unable to accommodate inelastic deformation and the full stress-strain history of the sample [124, 132, 133]. However, attempts within the framework of the original work of Jiles and Atherton have recently been made to include the effect of plastic deformation [134].

In the case of inhomogeneous casing material, it is expected that the measurement would result in an effective permeability that is an average measure of the electromagnetic property over all locations inside the inspected part of the casing wall. Anisotropy of the electromagnetic properties in the radial and axial direction can be taken into account within the scope of the modelling methods in Chapter 2.

6.1.4 Environmental temperature

The temperature in a well at full depth reaches 175 °C and its variations affect the impedance of the coils, electromagnetic properties of the casing material and operation characteristics of the electronic circuitry [1]. In order to compensate for the thermally induced variations in the tool response, it is essential to measure the temperature at critical points in the system.

Temperature dependence of the casing conductivity and permeability is discussed in [69] and [121]. Compensation of this dependence is important if one wants to infer the state of the casing and examine potential stress induced changes in the casing material using the electromagnetic methods [49, 69]. The coil properties can be corrected for the temperature variations using a look-up table.

Downhole electronic instrumentation must retain its functionality and per-

formance in the whole temperature range [135]. High-temperature design of the instrumentation is based on an approach that combines the application of high-temperature rated parts and components specified for commercial or military temperature ranges. The latter are usually the critical components such as voltage references, oscillators, analog-to-digital converters and microcontrollers. Using a component outside the manufacturer’s specified temperature range is possible through a process known as uprating, which is a collection of procedures for assessing “the capability of a part to meet the functional and performance requirements” in the high temperature range [136]. One often finds that commercial parts can be uprated [136, 137]. We reference to the possible choices of high-temperature rated components in section 6.2

A measurement method embodied by the electronic instrumentation must be suited for the harsh environment as well. It is beneficial to reduce the number of analog components in order to minimise measurement errors arising due to deterioration of their performances at high temperatures (e.g. increase in leakage currents and noise, decrease in open-loop gain). For the inductive methods of casing inspection and formation evaluation, digital phase sensitive (lock-in) detection of the voltages induced in the receivers conforms to these requirements.

6.2 Key system components

The key components of the system, proposed in this thesis, for measurement of the casing properties and the formation conductivity are one transmitter and three receiver coils (shielded), transmitter circuitry and digital lock-in (phase sensitive) amplifier built around an analog-to-digital converter and microcontroller, Fig. 6.1. Additional components, not shown in Fig 6.1, are clock generator, downhole-surface communication circuitry, power supply, etc. These are present in almost any well logging tool and are not of primary interest to this discussion.

6.2.1 Transmitter coil

The main design requirements for the transmitter coil are connected with the operating frequency, power, dimensions and weight. The transmitter coil should operate at low frequencies (< 100 Hz) and provide the magnetic field strong enough to be detected several metres away by the receiver coils, while remaining in the small signal-regime for the material’s ferromagnetic characteristic. The magnetic field is proportional to the magnetic moment of the coil given approximately as:

$$m_T = \pi \bar{r}_T^2 N_T I_T k_e,$$

where \bar{r}_T is the transmitter’s mean radius, N_T is number of turns, I_T is the excitation current, and k_e is the moment enhancement due to the magnetic core.

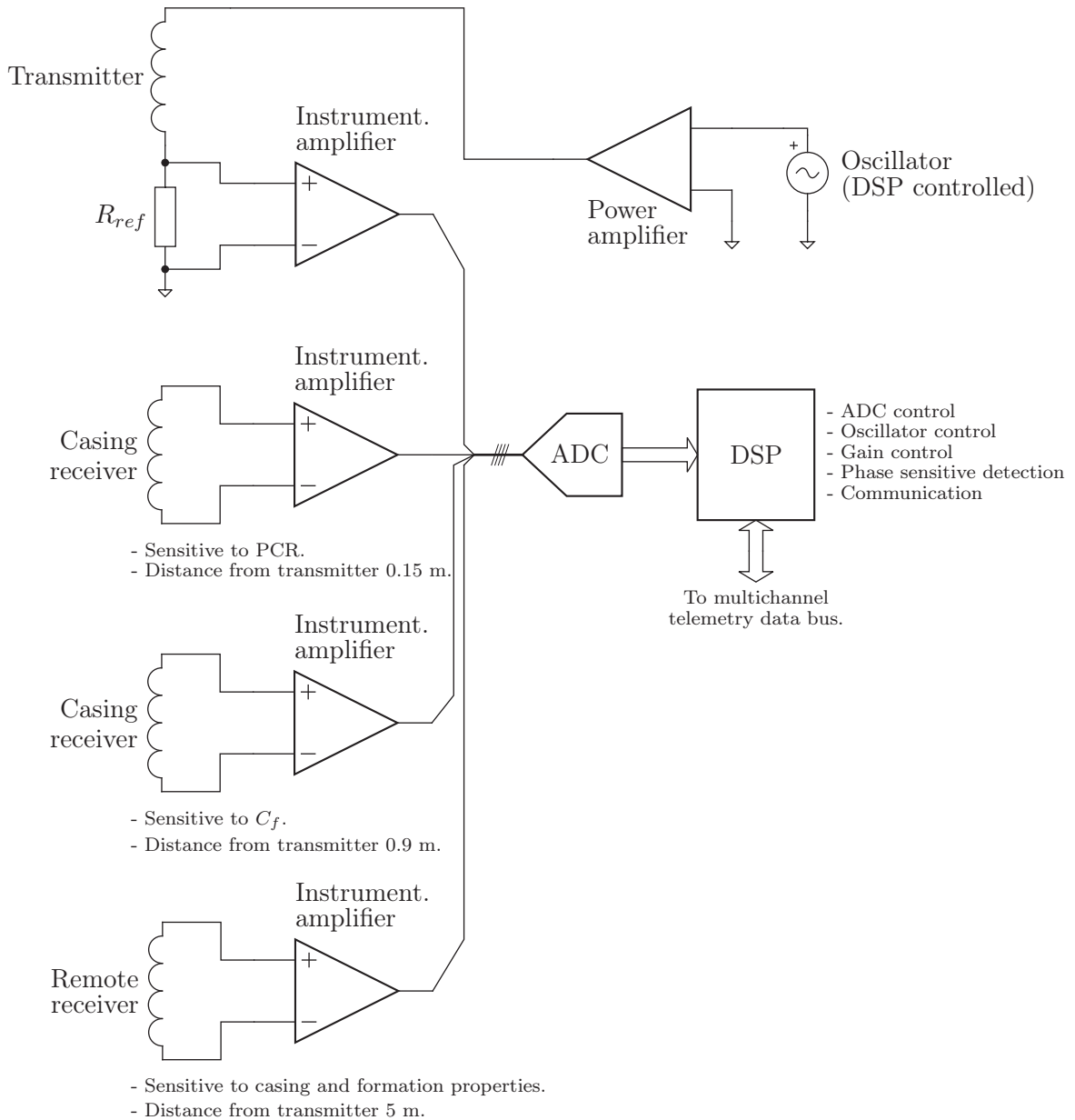


Figure 6.1: Key components of the four-coil system for the measurement of the casing and formation properties.

The choice of the number of turns, mean radius, maximum excitation current and the wire diameter is not an easy one. The transmitter coil should closely fit inside the casing in order to achieve higher magnetic moment. The product of the number of turns and the current should be high, but this is limited by the output characteristics of the transmitter's power supply circuitry. The power supply is characterised with the maximum power P_{max} , maximum output voltage U_{max} , and maximum current I_{max} . We will assume that the transmitter coil is tuned to the serial resonance with a capacitor [138]. Because of $N \propto R_T$, where R_T is the wire resistance of the transmitter coil, the

6.2 Key system components

requirement $(N_T I_T)_{\max}$ is identical to the requirement $U_{\max} = R_T I_T$. Hence, the operating point of the power supply is $(U_{\max}, I_T = P_{\max}/U_{\max})$, whereas the coil should have the number of turns N_T such that $R_T = U_{\max}^2/P_{\max}$. The wire diameter must be chosen according to the specified current and self-heating limitations. Downhole power supplies can routinely provide maximum power of 150 W, at maximum voltage of 35 V and frequencies below 20 kHz [138].

Following this discussion, we calculated data for four transmitter coils intended to span the range of the casing inner radius from 50 mm to 120 mm, what covers typical surface casings, and all of the intermediate and production casings, and liners [13, 14], Table 6.1. These coils are given here only to gain insight into typical design parameters and their quantitative estimates. The magnetic moment can be enhanced using the magnetic rod made of mu-metal (a nickel-iron alloy) at frequencies below 1 kHz, or ferrite below 1 MHz [138, 139].

Table 6.1: Transmitter coils for casing inner radius 50 mm–120 mm

Parameter	K1	K2	K3	K4
Outer radius, r_{T2} [mm]	45	60	75	90
Inner radius, r_{T1} [mm]	20	35	50	70
Mean radius, \bar{r}_T [mm]	32.5	47.5	62.5	80
Length, l_T [mm]	300	300	300	300
Wire diameter, d_w [mm]	1.6	1.6	1.6	1.6
Turns, N_T	2344	2344	2344	1875
Current, I_T [A]	5.30	4.87	4.24	4.20
$N_T I_T$, [At]	12423	11415	9939	7866
Wire resistance, R_T [Ω]	5.6	6.3	8.3	8.5
Magnetic moment, m_T [Am^2]	41	81	122	158
Magnetic field in air*, $ B_z $ [nT]	65.6	129.6	195.2	252.8
Magnetic field in casing*, $ B_z $ [nT]	0.25	0.5	0.78	1

*Magnetic field calculated at $z = 5$ m and 60 Hz. Casing is $C(120$ mm, 10 mm, 4.6 MS/m, 100)

6.2.2 Receiver coil

Small diameter casings represent the worst case for the design of a receiver coil. The available space limits the magnetic moment of the transmitter and the winding number of the receiver. As an example of the receiver design we will take a coil that can fit into a casing with 50 mm inner radius. According to Table 6.1 the minimum magnetic field at 5 m and 60 Hz is 250 pT. We will evaluate the receiver parameters for the more severe casing attenuation resulting in the magnetic field of 50 pT.

Let the receiver have the same radii and length as transmitter K1 from Table 6.1. If we choose 0.4 mm wire and coil packing factor of 0.75, the coil will have number of turns $N_R = 35156$ and wire resistance $R_R = 1040 \Omega$. The inductance of the coil is around 11.4 H, calculated using the formula for long multilayer solenoidal air-cored coils given in [140]. From (6.4) it follows that receiver sensitivity at 60 Hz is $S_B = 44 \mu\text{V/nT}$. The induced voltage is $U_R = 2.2 \mu\text{V}$ for $|B_z| = 50 \text{ pT}$.

The coil has to be wound with a special care in order to minimise its self-capacitance [140]. One usually divides the coil into sections, each wound separately using e.g. the deep narrow winding [140, 141]. Stray capacitances up to 40 pF have been reported for the coils of similar dimensions as the aforementioned receiver and number of turns up to 48000 [141, 142]. Under the realistic assumption that the coil can be produced with the stray capacitance less than 1000 pF, its self-resonance frequency is 1490 Hz, what is quite acceptable for measurements below 100 Hz. There is no need for flux-feedback preamplifier to flatten the coil's characteristic, because of the narrow band-pass nature of the measurement [143].

Voltage spectral density of the coil noise is $4.93 \text{ nV}/\sqrt{\text{Hz}}$ at the temperature of $150 \text{ }^\circ\text{C}$, or equivalently $112 \text{ fT}/\sqrt{\text{Hz}}$, see section 6.3.1. The noise power and signal-to-noise ratio depend on the frequency bandwidth, which in turn depends on the coil's stray capacitance and the input impedance of the receiver amplifier. Since the coil's resonance frequency is above 1 kHz, we will assume that the bandwidth is limited by the receiver amplifier with the first-order low-pass transfer function with cut-off frequency at 200 Hz. In that case, we obtain $\text{SNR} = 25 \text{ dB}$ at 50 pT. This number does not include the amplifier's contribution to the noise.

The sensitivity of the coil can be significantly increased using a magnetic core [139]. The main disadvantages of using the core are additional magnetic noise (Barkhausen noise) and nonlinearity. A core made of amorphous cobalt-based alloy Metglas 2714A was reported to have low noise performance and very high permeability of tens of thousands (continuous service temperature of $90 \text{ }^\circ\text{C}$ and Curie temperature of $225 \text{ }^\circ\text{C}$) [144, 145]. Using this material, the coil in [145] approaches the theoretical noise limit at the room temperature. If the permeability of the core's material is high, the resultant permeability and the sensitivity enhancement depend mostly on the geometry of the coil and its core—the core should be long and of small diameter. For the receiver described herein, the increase in sensitivity is estimated to be 30 times, or $S_B \approx 1300 \mu\text{V/nT}$ and $U_R = 65 \mu\text{V}$ for $|B_z| = 50 \text{ pT}$.

6.2.3 Receiver amplifier

We can specify the requirements on the receiver amplifier following the discussion about the receiver's properties in section 6.2.2. It is clear that the right choice for the amplifier's topology is the one of instrumentation amplifier because of its high input impedance, common-mode rejection ratio and low

offset, drift and noise.

In order to amplify the induced voltage of the receiver from the lowest range of $\sim 10 \mu\text{V}$ to $\sim 10 \text{mV}$, the amplifier should have the differential gain on the order of 1000. The input impedance should be high enough not to interfere with the receiver's frequency characteristic; the input resistance should be on the order of $10 \text{M}\Omega$ and capacitance below 100pF . The equivalent input noise of the amplifier should not be considerably larger than the coil noise ($\sim 5 \text{nV}/\sqrt{\text{Hz}}$) in order to keep the noise factor close to 1. The amplifier we used in the experiment in Chapter 5 satisfies these criteria: input impedance of around $130 \text{M}\Omega$, CMRR of 120dB at frequencies below 200Hz , differential gain 2000, cut-off frequency of 29kHz , and equivalent input voltage noise of $4.18 \text{nV}/\sqrt{\text{Hz}}$ [102]. Additional requirement is high-temperature operation.

High-temperature rated instrumentation amplifiers are commercially available. Amplifier INA129-HT (Texas Instruments) is rated for operation up to $210 \text{ }^\circ\text{C}$. The amplifier has differential impedance $10^{10} \Omega$ and 2pF , typical CMRR of 130dB and 95dB at $210 \text{ }^\circ\text{C}$, gain up to 10000, noise below $20 \text{nV}/\sqrt{\text{Hz}}$ and $1 \text{pA}/\sqrt{\text{Hz}}$ at 100Hz , and bandwidth of 7.5kHz for 1000 gain and $210 \text{ }^\circ\text{C}$ [146]. The same vendor offers also a range of high-temperature operational amplifiers [147]. Another example of a high-temperature instrumentation amplifier is Micropac's 52301, capable for operation up to $180 \text{ }^\circ\text{C}$ [148].

6.2.4 Mixed-signal and digital circuitry

After the instrumentation amplifier, next in the measurement chain are mixed-signal and digital circuitry, namely an analog-to-digital converter (ADC), and microcontroller or digital signal processor. High-temperature digital signal processors are available from Texas Instruments, see e.g. [149].

While there is a lot of high-speed and high-resolution analog-to-digital converters available, those capable for high-temperature operation are still extremely rare. We will summarise characteristics of a state-of-the-art high temperature ADC understanding that converters for the lower temperature range can easily match or surpass its performance. The converter in question is ADS1278-HT (Texas Instruments) [150]. The converter is a 24-bit, delta-sigma ($\Delta\Sigma$) ADC capable for 128kHz simultaneous sampling of eight channels and operation up to $210 \text{ }^\circ\text{C}$. Specified maximal integral nonlinearity is $\pm 14 \text{ppm}$ of the full scale range, and maximal noise in the high-resolution mode is $13 \mu\text{V}_{\text{rms}}$. The offset error is 2mV and gain error is 0.5% of the full scale. Total harmonic distortion is lower than -96dB and spurious-free dynamic range is typically 109dB .

6.2.5 Digital phase-sensitive detection

We have already mentioned that the method of choice for the measurement of the parameters of a sine wave in conditions of poor SNR and harsh environment

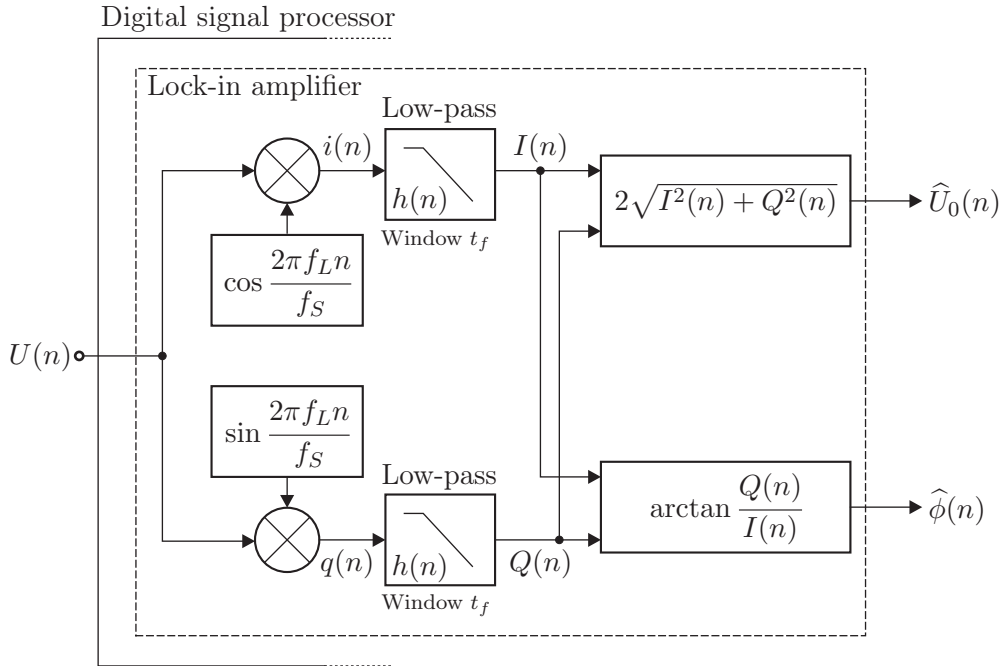


Figure 6.2: Block scheme of the digital lock-in (phase sensitive) amplifier implemented in a digital signal processor. The lock-in frequency is f_L and the sampling frequency is f_S .

should be based on a digital phase sensitive (lock-in) amplifier [103–106]. The basic principle of the lock-in detection is shown in Fig. 6.2. Quantised signal $U(n)$, containing noise, various harmonics and a spectral component of known frequency f_L , whose amplitude and phase we want to measure, is multiplied by digital versions of the sine and cosine reference signals of the same frequency f_L . The multiplication with the cosine and sine references results in $i(n)$ and $q(n)$, respectively. So-called in-phase and quadrature components, $I(n)$ and $Q(n)$, obtained after the digital low-pass filtering correspond to the mean values of $i(n)$ and $q(n)$; they are still time-dependent because of the finitely low cut-off frequency of the filters with impulse response $h(n)$. The mean values are related to the amplitude and phase of the measured harmonic as:

$$I(n) = (h * i)(n) \approx \frac{1}{2}U_0 \cos \phi,$$

$$Q(n) = (h * q)(n) \approx \frac{1}{2}U_0 \sin \phi.$$

Estimates of the amplitude and phase, $\hat{U}_0(n)$ and $\hat{\phi}(n)$ are readily obtained as shown in Fig. 6.2. There is a trade-off between the requirements for low cut-off frequency of the digital low-pass filter, corresponding to the accuracy of $\hat{U}_0(n)$ and $\hat{\phi}(n)$, and response time of the lock-in amplifier.

6.3 Effects of noise and interferences

6.3.1 Scaled model vs. field system

We will concentrate here on thermal noise of the receiver coil since this is the only noise source that depends upon the physical scaling. Noise sources of the laboratory interface circuitry remain invariant under scaling and can be considered as a good indication of requirements on the noise characteristics of actual field instrumentation.

We will assume that the receiver is a cylindrical air coil with inner radius r_{R1} , outer radius r_{R2} , length l_R and N_R turns of wire with diameter d_w . Also, let \bar{r}_R denote coil's mean radius, $\bar{r}_R = (r_{R1} + r_{R2})/2$. Since the receiver is placed far from the transmitter, we can assume that the magnetic field inside the tube at the receiver's location is uniform over the cross-section parallel to $z = 0$ plane and that it decays slowly along the length of the receiver. Bearing that in mind, we will introduce a mean uniform magnetic field $\bar{\mathbf{B}}$ which induces the same voltage in the receiver coil as the magnetic field of the transmitter. For the harmonic excitation, the voltage induced in the receiver coil is:

$$U_R = N \frac{d\Phi}{dt} = N \bar{B}_z \bar{S} \omega = 2\pi^2 f N \bar{r}_R^2 \bar{B}_z, \quad (6.1)$$

where Φ is total magnetic flux, \bar{S} mean cross-section and \bar{B}_z is a component of the mean magnetic field in z direction. If we define the coil packing factor k_p as the ratio of the cross-section area taken by the coil winding and total coil area, we can write for number of turns:

$$N = k_p \frac{(r_{R2} - r_{R1}) l_R}{d_w^2}. \quad (6.2)$$

Inserting (6.2) into (6.1) we get:

$$U_R = 2\pi^2 k_p f \frac{\bar{r}_R^2 (r_{R2} - r_{R1}) l_R}{d_w^2} \bar{B}_z. \quad (6.3)$$

Thus, the sensitivity of the receiver coil $S_B = U/B_z$ can be calculated as [139]:

$$S_B = 2\pi^2 k_p f \frac{\bar{r}_R^2 (r_{R2} - r_{R1}) l_R}{d_w^2}. \quad (6.4)$$

The noise source of a coil is associated with DC resistance of the wire [139, 142]. Power spectral density of the coil noise is:

$$\bar{u}_N^2 = 4k_B T R_{dc},$$

where the Boltzmann constant $k_B = 1.3806504(24) \cdot 10^{-23} \text{ JK}^{-1}$, T is absolute temperature (in kelvins) and R_{dc} is DC resistance of the coil. The total length of the wire used in winding the coil is:

$$l_w = 2\pi N \bar{r}_R = 2\pi k_p \frac{\bar{r}_R (r_{R2} - r_{R1}) l_R}{d_w^2},$$

and its resistance is:

$$R_{dc} = \frac{1}{\sigma_w} \frac{l_w}{S_w} = 8 \frac{k_p \bar{r}_R (r_{R2} - r_{R1}) l_R}{\sigma_w d_w^4},$$

where σ_w is conductivity of the wire and S_w its cross-section area. The noise power U_N^2 for a given frequency bandwidth f_{bw} is:

$$U_N^2 = 32k_B T \frac{k_p \bar{r}_R (r_{R2} - r_{R1}) l_R}{\sigma_w d_w^4} f_{bw}. \quad (6.5)$$

Signal-to-noise ratio SNR of the receiver coil is

$$\text{SNR} = \frac{U_R^2}{2U_N^2} = \frac{\pi^4 k_p}{16k_B T} \frac{f^2}{f_{bw}} \sigma_w \bar{r}_R^3 (r_{R2} - r_{R1}) l_R \bar{B}_z^2, \quad (6.6)$$

where we divided U_R with $\sqrt{2}$ to obtain RMS value of the induced voltage. It is interesting to observe that, according to (6.6), SNR of the receiver does not depend on the wire diameter and that the best way of increasing the ratio is to increase the coil mean radius [139].

We can now compare signal-to-noise ratios of the field system SNR and scale model SNR':

$$\frac{\text{SNR}}{\text{SNR}'} = \frac{f^2 \bar{r}_R^3 (r_{R2} - r_{R1}) l_R \bar{B}_z^2 f'_{bw}}{f'^2 \bar{r}'_R^3 (r'_{R2} - r'_{R1}) l'_R \bar{B}'_z{}^2 f_{bw}},$$

where primed quantities belong to the scaled model. Using the scaling relations (5.1)–(5.5) and (5.14)–(5.17) we get:

$$\frac{\text{SNR}}{\text{SNR}'} = \frac{1}{k_l} \frac{f'_{bw}}{f_{bw}}. \quad (6.7)$$

Signal-to-noise ratio of the field system is reduced for the length scaling factor k_l . This scaling effect is compensated in some degree by the fact that one can expect narrower frequency bandwidth f_{bw} for the field system. If we assume the relation $f'_{bw}/f_{bw} > k_l$, then

$$\frac{\text{SNR}}{\text{SNR}'} > 1,$$

what shifts the comparison of the signal-to-noise ratios in favor of the field system.

6.3.2 Measurement channel

The noise and interferences in the received signal collected through the measurement channel shown in Fig. 6.3 result in the errors of the lock-in detection. As we have already discussed, the receiver coil introduces noise of its resistance and magnetic core. The instrumentation amplifier and the anti-aliasing filter

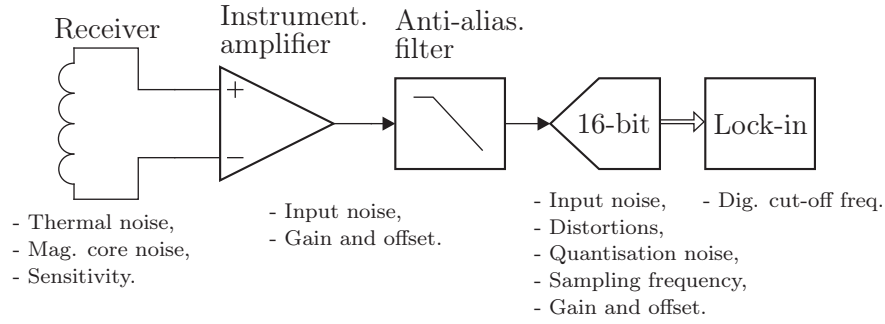


Figure 6.3: Block scheme of the receiver interface with digital lock-in amplifier and main error sources.

result in the $1/f$ and white noise, whereas the analog-to-digital converter introduces its input noise, quantisation noise and distortions. Other error sources, such as changes in the receiver's sensitivity, as well as gains and offsets of the amplifier, anti-aliasing filter and ADC, require calibration. In order to investigate the applicability of the digital lock-in detection and suitability of the system electronic components discussed in the previous sections, we will simulate the effects of the noise and interferences on the phase and amplitude measurement in the AC coupled measurement channel. We will assume that the channel is calibrated, i.e. its total gain is known.

The noise of the analog circuitry $U_{n,an}$, the input noise of the analog-to-digital converter $U_{n,adc}$, quantisation noise $U_{n,q}$ and distortions U_{dist} can be lumped into the joint noise source $U_{n,lump}$, band limited by the anti-aliasing filter at f_C . The root mean square (RMS) value of the lump noise source is:

$$U_{n,lump}^2 = U_{n,an}^2 + U_{n,adc}^2 + U_{n,q}^2 + U_{dist}^2, \quad (6.8)$$

where U_{dist} includes all harmonics arisen due to the nonlinear effects of the transfer functions of the ADC or the analog circuitry. If we divide the RMS value of the signal with the lump noise, we obtain signal-to-noise-and-distortion ratio:

$$\text{SINAD} = 20 \log \frac{U_0}{\sqrt{2}U_{n,lump}},$$

which is usually used for an analog-to-digital converter as a good indication of its overall dynamic performance as a function of input frequency [151]. Since we have broadened the definition of SINAD to include the noise and distortions before the ADC, it became a measure of the overall quality of the receiver measurement channel.

Let the measured spectral component have the frequency $f_L = 60$ Hz and amplitude $U_0 = 10$ mV or $U_0 = 100$ mV. This is a voltage amplified by the instrumentation amplifier with gain 1000 and it corresponds to the induced voltage of the receiver on the order of $10 \mu\text{V}$ or $100 \mu\text{V}$. According to our previous analysis, the lowest voltage amplitude in the receiver coil is on the order of $10 \mu\text{V}$ at distance $z = 5$ m from the transmitter and 60 Hz. The

anti-aliasing filter has cut-off frequency $f_C = 200$ Hz, what determines the noise bandwidth for the analog part of the receiver interface circuitry. We will assume that the signal is sampled by a 16-bit ADC at sampling rate of 32768 Hz. Using the Matlab, we produced the signal $U(n) = U_0 \sin(2\pi f_L n / f_s + \phi)$ in the 16-bit precision with the input range of the quantiser ± 2 V and added the Gaussian lump noise band limited to 200 Hz with the total power depending on SINAD and U_0 . Then, we estimated U_0 and ϕ using the lock-in method implemented in the 32-bit floating point arithmetic. We tested two digital low-pass filters based on the simple averaging of $N = 100000$ or $N = 500000$ samples corresponding to the filter times of $t_f = 3$ s and $t_f = 15$ s, respectively. This procedure is repeated for the phase range 10° – 170° with 1° steps at each SINAD level, and for $U_0 = 10$ mV and $U_0 = 100$ mV.

Fig. 6.4 depicts the phase error defined as:

$$p_\phi = |\phi - \hat{\phi}(N)|,$$

and Fig. 6.5 depicts the amplitude error defined as:

$$p_U = \left| \frac{U_0 - \hat{U}_0(N)}{U_0} \right|.$$

Both figures show the minimal (dashed lines) and maximal errors (full lines) in the range of investigated signal phases. The errors depend on SINAD level and not on the signal amplitudes. That is why we didn't explicitly joined the amplitude data to the curves on the figures. Three times longer averaging time reduces the errors for 2 to 3 times. There is a significant difference between the minimal and maximal errors—for two or, even, three orders of magnitude. The phase error is less than 0.1° for $\text{SINAD} > 25$ dB and $t_f = 15$ s, or less than 0.04° for $\text{SINAD} > 30$ dB. The amplitude errors are less than 10^{-3} for $\text{SINAD} > 30$ dB and $t_f = 15$ s. These worst-case error boundaries are within the uncertainties analysed in Chapter 4.

SINAD level of 30 dB means that the RMS value of the lump noise is about 0.224 mV for $U_0 = 10$ mV, or 2.24 mV for $U_0 = 100$ mV. In the terms of noise spectral density, this is $15.8 \mu\text{V}/\sqrt{\text{Hz}}$ for $U_0 = 10$ mV, or $158 \mu\text{V}/\sqrt{\text{Hz}}$ for $U_0 = 100$ mV at $f_C = 200$ Hz. Table 6.2 lists conservative estimates of the individual contributions of the error sources referred to the ADC input. In the case of $U_0 = 10$ mV, the RMS value of the noise is estimated to 295 μV and SINAD to 27.6 dB for the situation without the magnetic core, which is more likely considering the low amplitude of the signal. For $U_0 = 100$ mV and the magnetic core, the noise is about 652 μV resulting in SINAD of 40.7 dB. From these results we can corroborate that the digital lock-in amplifier, satisfying the accuracy requirements in Chapter 4, can be implemented using the commercially available components, rated for high-temperature operation.

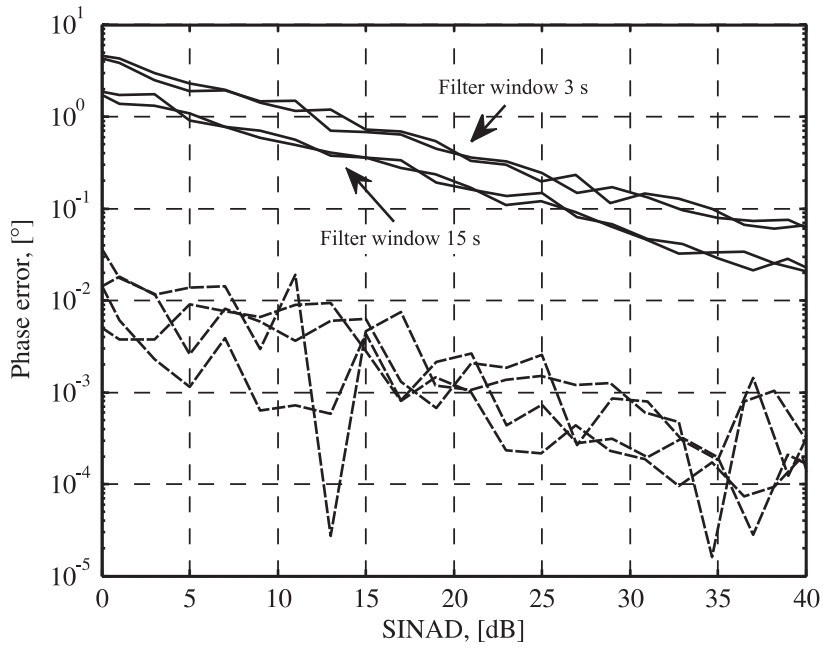


Figure 6.4: Maximal (full lines) and minimal (dashed lines) phase errors of the lock-in amplifier vs. SINAD for the filtering times 3 s and 15 s (denoted for full lines only), and the sine waves of 60 Hz and amplitudes 10 mV and 100 mV (not denoted). The noise bandwidth is 200 Hz.

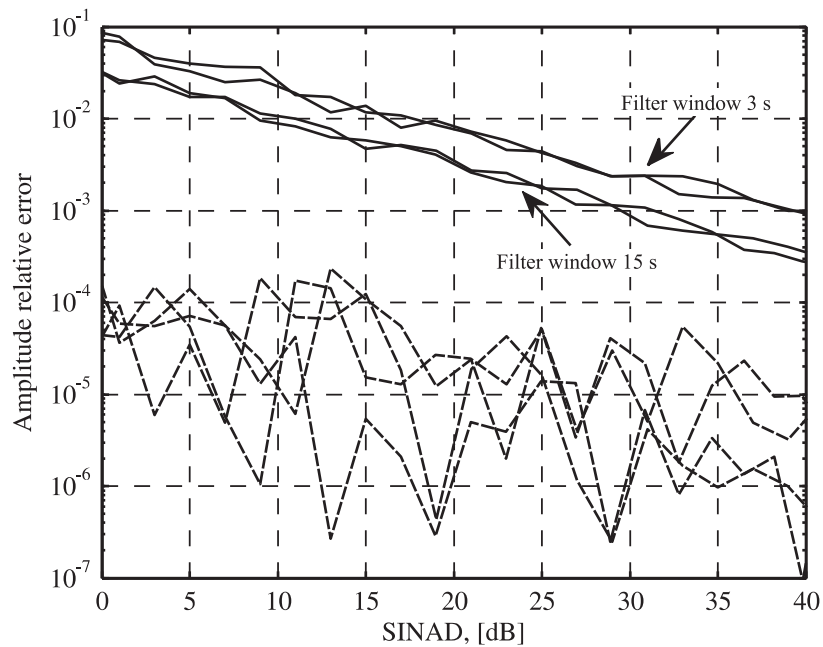


Figure 6.5: Maximal (full lines) and minimal (dashed lines) amplitude errors of the lock-in amplifier vs. SINAD, see Fig. 6.4.

Table 6.2: Contributions of the individual error sources referred to the ADC input.

Source	Conditions ⁽¹⁾	$U_0 = 10 \text{ mV}$ ⁽²⁾	$U_0 = 100 \text{ mV}$ ⁽²⁾
Receiver coil			
Thermal noise	$5 \text{ nV}/\sqrt{\text{Hz}}$		$71 \text{ }\mu\text{V}$
Mag. core noise	$30 \text{ nV}/\sqrt{\text{Hz}}$ ⁽³⁾		$424 \text{ }\mu\text{V}$
Instrum. amp. ⁽⁴⁾			
Total noise	$20 \text{ nV}/\sqrt{\text{Hz}}$		$283 \text{ }\mu\text{V}$
Low-pass filter			
Total noise	$100 \text{ nV}/\sqrt{\text{Hz}}$		$1.4 \text{ }\mu\text{V}$
ADC, 16-bit ⁽⁵⁾			
Input noise			$13 \text{ }\mu\text{V}$
Quantisation noise	$\text{SNR}_Q = 96.2 \text{ dB}$	$0.1 \text{ }\mu\text{V}$	$1 \text{ }\mu\text{V}$
Distortions			
All harmonics	$\text{THD} = 50 \text{ dB}$ ^{(3),(6)}	$40 \text{ }\mu\text{V}$	$400 \text{ }\mu\text{V}$
Total			
noise	With the core	$516 \text{ }\mu\text{V}$	$652 \text{ }\mu\text{V}$
	Without the core	$295 \text{ }\mu\text{V}$	$495 \text{ }\mu\text{V}$
SINAD			
	With the core	22.7 dB	40.7 dB
	Without the core	27.6 dB	43.1 dB

(1) Gain of the instrumentation amplifier is 1000, the filter cut-off frequency is 200 Hz, AC coupled measurement channel.

(2) At the ADC input.

(3) Estimated.

(4) INA129-HT.

(5) ADS1278-HT, 23-bit, the last 7 bits neglected.

(6) Includes nonlinearity of the analog circuitry and ADC.

Chapter 7

Conclusions

I almost wish I hadn't gone down that rabbit-hole—and yet—and yet—it's rather curious, you know, this sort of life!

Alice

Lewis Carroll, "Alice's Adventures in Wonderland," Ch. 4, 1865

Resistivity (conductivity) measurement is an all-important method in the formation evaluation. In the open-hole logging, the conductivity measurement, either of electrode or inductive kind, distinguishes between the hydrocarbon bearing formation (low conductivity) and formation containing brine (high conductivity). Radiation methods can be applied to the same purpose through the measurement of the water saturation, but they are beset by a number of environmental effects and small radius of investigation. Still, the radiation methods were the only ones applicable in a cased well before recent introduction of the electrode trough-casing resistivity device. This tool measures the formation conductivity lower than 1 S/m at a few hertz. Its main disadvantage is the strong force required to establish a good contact between a casing and the electrodes that can damage or rupture the casing. Another tool, commercialised in 2009, is based on a cross-well inductive principle. It employs a high power transmitter coil in one well, and an array of receiver coils in the second well. The receiver well can be cased with steel only if the transmitter well is open. The result of such a measurement is a tomographic resistivity image of the interwell space. The through casing inductive resistivity measurement from within a single steel-cased well would be applicable for evaluation of formations with the conductivity higher than 1 S/m without the danger of damaging the casing or need for two wells. The objective of this thesis was to prove the concept of such a measurement. This was achieved in five steps.

First, we derived the analytical model of the magnetic field distribution of a transmitter coil positioned inside the casing surrounded with the low-conductive medium representing the formation. The medium is cylindrically layered with one horizontal boundary. The model is based on the quasi-static

approximation of the Maxwell's equations and the truncated region method with the eigenvalue expansion of the vector potential. Truncation of the problem domain in z direction leads to the discrete eigenvalues. This allows easier numerical implementation (the set of eigenvalues is determined by the domain's height) and convergence control (on term-by-term basis in summation of the solution sequence).

A special difficulty of this modelling approach arises due to the fact that the eigenvalues are given as solutions of transcendental equations in complex domain. We solved this problem using the argument principle based on the Cauchy's theorem. However, this can be time consuming if there are more horizontal boundaries and there is a need to repeatedly change their positions or conductivities of the neighboring regions. Faster numerical based models may be required for the field application if one expects the surrounding formation of several layers with the total height commensurable with the tool's length.

High contrast in conductivities of the casing and formation causes large dynamics of arguments of the Bessel functions. Thus, we took special care in rearranging the final expressions of the model into the ratio of Bessel functions in order to obtain stable numerical implementation of the model in double precision floating point arithmetic. The model proved to strike a good balance between its analytical complexity and primary application to assess the proposed measurement concept.

Second, using the model, we investigated the space-frequency dependence of the measurement sensitivity to the casing and formation properties. Unlike the amplitude of the induced voltage, its phase difference with respect to the transmitter's current is sensitive to the conductivity of the surrounding formation. The sensitivity increases with the frequency and transmitter-to-receiver separation. The lowest detectable voltage for a given transmitter and receiver coils determines the highest applicable frequency and the largest separation. For the excitation frequency of 60 Hz and coil separation of 5 m, one can expect phase difference on the order of 1° for 1 S/m formation and voltage on the order of $10 \mu\text{V}$ depending on the casing. The vertical resolution is better for shorter coil separations; this is the weakest spot of this method since it requires several times larger transmitter-receiver separation than the first generation of the open-hole induction logging tool (about 1 m). On the other hand, large separation between the coils improves the radius of investigation. The parts of the formation with radius larger than two coil separations contribute less than 20% of the total phase difference. This is a handy rule of thumb for estimation of the radius of investigation (10 m for separation of 5 m).

We defined the levelset of the induced voltage as a surface in the space of casing parameters (μ_r, σ_t, c) for which the induced voltage is constant for given coil separation and frequency. Space-frequency analysis of the sensitivity to the casing properties showed that the levelset transforms with separation from the surface of constant permeability-to-conductivity ratio, $\text{PCR} = \mu_r/\sigma_r$, to the surface of constant casing factor, $C_f = c\sqrt{\mu_r\sigma_t}$. By placing two receiver coils in the corresponding positions, we restricted the solution of the inverse

problem to the trajectory determined by the intersection of the two surfaces.

The effects of the casing and formation are separable. The measured phase difference is a sum of two mutually independent terms: the formation contribution and the casing contribution. The latter can be compensated if the casing properties are known, and we demonstrated this on a number of different casings. As already stated, the casing effect can be quantified by placing two additional receivers near the transmitter. We proposed positioning of the first receiver coil at 0.15 m to measure the casing's permeability-to-conductivity ratio, the second receiver at 0.9 m to measure the casing factor, and the third receiver coil at 5 m to measure the casing and formation effects. The proposed excitation frequency is 60 Hz. We proposed the use of single-frequency excitation in order to avoid the problems arising with the frequency dependence of the reversible permeability of the casing steel.

Third, we employed the stochastic approach to the inverse problem of determination of the casing and formation properties using the proposed minimal configuration of the coils. The stochastic inversion is based on the representation of the measurement quantities, a priori knowledge of the sought properties and their theoretical relationships in form of probability distributions. Posterior information on the properties of interest is obtained applying the Bayes theorem. The posterior distributions are sampled using the Monte Carlo Markov chain method based on the Metropolis-Hastings algorithm. The stochastic formulation gave us a relatively easy but detailed insight into the quality of the inverse-problem solution obtainable using the proposed configuration of the coils. We ran a number of Monte Carlo simulations in order to examine the effects of accuracy and precision of the magnetic field measurement on the posterior uncertainty of the formation conductivity. The finite accuracy of the measurement stems from limitations of the calibration procedure, whereas the finite precision is due to the inherent noise of the overall measurement system.

Based on the results of the Monte Carlo simulations, we concluded that the relative uncertainty of the magnetic field measurement must be between 10^{-4} and 10^{-3} in order to achieve the lowest measurable formation conductivity between 0.1 S/m and 1 S/m. For even lower formation conductivities and with these uncertainty levels, it is only possible to state that the formation conductivity is with the certainty lower than the specified minimal value. Measurement results for true values of the formation conductivity around 5 S/m are typically off by 5% or 10% from the true value. Uncertainty of the casing properties (thickness, conductivity and permeability) are about 30 times larger than the uncertainty of the magnetic field, what indicates the ill-conditioned procedure. However, resulting uncertainty of the casing factor is only one half of the measurement uncertainty, and 8 times larger for permeability-to-conductivity ratio.

Fourth, we produced the laboratory scaled model of the cased borehole in order to corroborate the proposed measurement technique. We used the scaling relations that preserve the same material properties in the field and scaled

systems. The dimensions were scaled for the factor of $\sqrt{200}$ and frequency was increased 200 times, from 60 Hz in the field system to 12 kHz in the scaled system. The instrumentation was built around the 16-bit digital phase sensitive (lock-in) amplifier. Special care was taken of the shielding and grounding in order to remove all capacitive coupling. The basic experiment affirmatively answered the question of whether or not the system distinguishes the saline solution from very low-conductive tap water or air through the highly conductive metal tube. The phase difference due to the presence of the saline solution was off by 0.06° or 8% from the model prediction of 0.75° . The experiment proved the feasibility of such a measurement using the proprietary wound air-cored coils, differential amplifier and 16-bit analog-to-digital converter.

Fifth, we analysed the requirements on the electronic instrumentation and its realisability using the commercially available components. The influential factors that restrain the achievable measurement accuracy are noise, coil decentralisation, parasitic capacitances, nonlinearity of the casing material, and environmental temperature. These influences must be accounted for when one designs the electronic instrumentation (centralisers, shielding, grounding, single excitation frequency, small signal regime, high-temperature rated components) or in the data processing (calibration and filtering).

The key system components are transmitter and receiver coils, transmitter circuitry and digital lock-in amplifier built around an analog-to-digital converter and a digital signal processor. The transmitter coil should be designed to match the output characteristic of the transmitter circuitry. We proposed several transmitter coils covering the entire range of the production casing diameters. The achieved magnetic moments or the power consumption can be improved using the magnetic cores. We showed that it is possible to design the receiver coil that fits into the casing and has required sensitivity of $\sim 50 \mu\text{V/nT}$ without the magnetic core or $\sim 1300 \mu\text{V/nT}$ with the core. The specifications of commercially available components (instrumentation amplifier, analog-to-digital converter and digital signal processor) capable for operation up to 210° match those of the instrumentation we used in the experiment. Their only recent availability will certainly improve and expedite development of high-precision well logging instrumentation capable for operation in the harsh environment of a well, as required by the proposed application. We analysed the total noise and distortions of the complete receiver channel and concluded that the worst case signal-to-noise-and-distortion ratio (SINAD) is around 30 dB, what results in the phase error of 0.04° and relative amplitude error less than 10^{-3} using the 16-bit single floating precision lock-in amplifier and the averaging window of 15 s. This estimation puts the total errors of the measurement channel within the uncertainty bounds obtained using the Monte Carlo simulations.

The future work should proceed in several directions: investigation of new transmitter-receiver patterns, prototyping of an actual field system, characterisation of ferromagnetic materials in small-signal regime, and modelling of more complex geometries. We will present few ideas for extending the current

research along these lines.

In the thesis, for solving the inverse problem, we assumed that we had only the results of the stationary measurement at our disposal, i.e. three complex-valued voltages induced in the three receiver coils. However, the voltages would be measured at several closely spaced positions in reality, so one can expect to have several times larger measurement set for the same length of the casing. Under the assumption, first mentioned in [52], that the spatial frequency of changes in the casing properties is larger than that of the formation conductivity, one can filter out the casing effect to some degree.

By designing the coils in such a way that they can switch their role and act either as transmitters or receivers, one can in principle achieve a better evaluation of the casing properties and, consequently, more accurate measurement of the formation conductivity. Throughout the thesis, we stressed the importance of the interdependent selections of coil separations and excitation frequencies in order to achieve satisfactory sensitivity to the formation conductivity and casing properties. Since the coil separations are fixed by the design, the variable frequency would allow the system to adapt itself to changing conditions inside the well, such as different casing grades, radii or thickness. Furthermore, by continuous monitoring of the received signal strength and SNR, the system could operate at the highest possible frequency to increase the sensitivity to the formation conductivity. An appealing fact in the tool prototyping is a possibility to modify and use the components of existing tools for casing inspection and open-hole inductive tools in order to speed up the development process and to cut down its costs.

In order to use the multi-frequency excitation, models of the ferromagnetic behavior should be incorporated into the existing models, more specifically frequency dependence of the reversible permeability. Development of fast numerical codes for forward simulation of the inhomogeneous casing and multi-layered formation would allow computationally efficient inversion procedures as a support for off-line geophysical interpretation.

The single-well trough-casing inductive resistivity tool is feasible using commercially available electronic components. The tool is applicable for measurement of the formation conductivity larger than 1 S/m. The proposed method with its inherent Bayes formalism should be viewed as a support to the long term process of knowledge building about the well and surrounding formation through time-lapse measurements.

Bibliography

- [1] D. S. Ellis and J. M. Singer, *Well logging for earth scientists*, 2nd ed. Dordrecht, The Netherlands: Springer, 2007.
- [2] B. I. Anderson, “Modeling and inversion methods for the interpretation of resistivity logging tool response,” Ph.D. dissertation, Delft University of Technology, Delft, The Netherlands, 2001.
- [3] M. Perić, *Englesko-hrvatski enciklopedijski rječnik istraživanja i proizvodnje nafte i plina*, M. Ivurek, Ed. Zagreb, Croatia: INA Industrija nafte, 2007.
- [4] M. R. Taherian, T. M. Habashy, R. J. Schroeder, D. R. Mariani, and M.-Y. Chen, “Laboratory study of the spontaneous potential—experimental and modeling results,” *The Log Analyst*, vol. 36, no. 5, pp. 34–48, 1995.
- [5] J. Tittman and J. S. Wahl, “The physical foundations of formation density logging (gamma-gamma),” *Geophysics*, vol. 30, no. 2, pp. 284–294, Apr. 1965.
- [6] C. W. Tittle, “Theory of neutron logging I,” *Geophysics*, vol. 26, no. 1, pp. 27–39, Feb. 1961.
- [7] G. D. Myers, “A review of nuclear logging,” *The Log Analyst*, vol. 33, no. 3, May-June 1992.
- [8] X.-M. Tang and A. Cheng, *Quantitative borehole acoustic methods*, S. Treitel and K. Helbig, Eds. Amsterdam, The Netherlands: Elsevier Ltd., 2004.
- [9] G. R. Coates, L. Xiao, and M. G. Prammer, *NMR logging: Principles and applications*. Houston, Texas: Gulf Professional Publishing, 2001.
- [10] G. E. Archie, “The electrical resistivity log as an aid in determining some reservoir characteristics,” *Petroleum Transactions, AIME*, vol. 146, pp. 54–62, 1942.
- [11] A. A. Kaufman and Y. A. Dashevsky, *Principles of induction logging*, 1st ed., ser. Methods in Geochemistry and Geophysics. Elsevier Science B.V., 2003.

BIBLIOGRAPHY

- [12] H. G. Doll, "Introduction to induction logging and application to logging of wells drilled with oil base mud," *Journal of Petroleum Technology*, vol. 1, pp. 148–162, June 1949.
- [13] S. S. Rahman and G. V. Chilingarian, *Casing design — theory and practice*, ser. Developments in Petroleum Science, 42. Amsterdam: Elsevier Science B.V., 1995.
- [14] *Specification for casing and tubing*, International Organization for Standardization & American Petroleum Institute Std. ISO 11 960:2004 / API 5CT, 8. ed., July 2005.
- [15] (2010, Mar.) ABC analysis behind casing. Schlumberger Ltd. [Online]. Available: www.slb.com
- [16] Z. Bassiouni and J. Velić, "Prospecting for bypassed oil and gas," *Geologia Croatica*, vol. 49, no. 2, pp. 197–202, Dec. 1996.
- [17] K. Lang, "Locating bypassed oil in existing wells," *Excerpts in PTTC Network News*, vol. 6, no. 3, pp. 7–9, Sept. 2000. [Online]. Available: www.pttc.org
- [18] M. A. Gutierrez, J. Dvorkin, and A. Nur, "Theoretical rock physics for bypassed oil detection behind the casing: La Cira-Infantas oil field," *The Leading Edge*, vol. 20, no. 2, pp. 192–197, Feb. 2001.
- [19] M. Wilt, J. Little, P. Zhang, and J. Chen, "Using crosswell em to track waterflooding at the lost hills oil field," *SEG Technical Program Expanded Abstracts*, vol. 24, no. 1, pp. 1269–1271, 2005. [Online]. Available: <http://link.aip.org/link/?SGA/24/1269/1>
- [20] *Cased hole log interpretation: Principles/Applications*, 4th ed. Houston, Texas: Schlumberger Wireline & Testing, Mar. 1989. [Online]. Available: www.slb.com
- [21] J. J. Smolen, *Cased hole and production log evaluation*. South Sheridan, USA: PennWell Publishing Company, 1996.
- [22] W. B. Vail, "Electronic measurement apparatus movable in a cased borehole and compensating for casing resistance differences," U.S. Patent 5 075 626, Dec. 24, 1991.
- [23] —, "Calibrating and compensating influence of casing thickness variations on measurement of low frequency A.C. magnetic fields within cased boreholes to determine properties of geological formations," U.S. Patent 5 260 661, Nov. 9, 1993.
- [24] A. A. Kaufman, A. D. Karinsky, and W. E. Wightman, "Influence of inductive effect on measurements of resistivity through casing," *Geophysics*, vol. 61, no. 1, pp. 34–42, Jan.–Feb. 1996.

BIBLIOGRAPHY

- [25] W. B. Vail and S. T. Momii, “Proof of concept of moving through casing resistivity apparatus — Final report,” US Department of Energy, Tech. Rep. DOE/BC/14617–T12, Mar. 1997.
- [26] W. B. Vail, “Methods and apparatus for measurement of low frequency AC magnetic fields within cased boreholes to determine properties of geological formations,” U.S. Patent 4901 023, Feb. 13, 1990.
- [27] K. Aulia, B. Poernomo, W. C. Richmond, A. H. Wicaksono, P. Béguin, D. Benimeli, *et al.*, “Resistivity behind casing,” *Oilfield Review*, vol. Spring, pp. 2–25, 2001.
- [28] M. Novak, personal communication, 2009.
- [29] A. M. Augustin, W. D. Kennedy, H. F. Morrison, and K. H. Lee, “A theoretical study of surface-to-borehole electromagnetic logging in cased holes,” *Geophysics*, vol. 54, no. 1, pp. 90–99, 1989.
- [30] M. Wilt, K. H. Lee, A. Becker, B. Spies, and S. Wang, “Crosshole EM in steel-cased boreholes,” *SEG Technical Program Expanded Abstracts*, vol. 15, no. 1, pp. 230–233, 1996. [Online]. Available: <http://link.aip.org/link/?SGA/15/230/1>
- [31] A. Becker, B. Wang, K. H. Lee, and M. Wilt, “Subsurface electromagnetic measurement through steel casing,” Ernest Orlando Lawrence Berkeley National Laboratory, Tech. Rep. LBNL-42375, Nov. 1998.
- [32] M. J. Wilt, D. L. Alumbaugh, H. F. Morrison, A. Becker, K. H. Lee, and M. Deszcz-Pan, “Croswell electromagnetic tomography: System design considerations and field results,” *Geophysics*, vol. 60, no. 3, pp. 871–885, 1995.
- [33] E. Nichols, “Electromagnetic induction method and apparatus for the measurement of the electrical resistivity of geologic formations surrounding boreholes cased with a conductive liner,” U.S. Patent 6 294 917 B1, Sept. 25, 2001.
- [34] E. Haber and P. Zhang, “Determination of borehole geometry inside cased wells with croswell electromagnetics,” U.S. Patent 7 095 232B2, Aug. 22, 2006.
- [35] U. Conti, “System, apparatus, and method for conducting electromagnetic surveys,” U.S. Patent 7 030 617B2, Apr. 18, 2006.
- [36] “DeepLook-EM—Enhanced croswell reservoir monitoring system,” Brochure, 2009. [Online]. Available: www.slb.com/deeplook

- [37] G. Gao, D. Alumbaugh, P. Zhang, H. Zhang, C. Levesque, R. Rosthal, J. Liu, A. Abubakar, and T. Habashy, “Practical implications of nonlinear inversion for cross-well electromagnetic data collected in cased-wells,” *SEG Technical Program Expanded Abstracts*, vol. 27, pp. 299–303, 2008.
- [38] (2010, Mar.) DeepLook-EM—services & product site. Schlumberger, Ltd. [Online]. Available: www.slb.com/deeplook
- [39] J. R. Wait and D. A. Hill, “Electromagnetic shielding of sources within a metal-cased bore hole,” *IEEE Transactions on Geoscience Electronics*, vol. GE-15, no. 2, pp. 108–112, Apr. 1977.
- [40] J. R. Wait, “Analysis for the electromagnetic fields of a dipole located within a metal-cased borehole,” *Journal of Applied Physics*, vol. 48, no. 3, pp. 1009–1012, Mar. 1977.
- [41] C. V. Dodd and W. E. Deeds, “Analytical solutions to eddy-current probe-coil problems,” *Journal of Applied Physics*, vol. 39, no. 6, pp. 2829–2838, 1968.
- [42] C. V. Dodd, C. C. Cheng, and W. E. Deeds, “Induction coils coaxial with an arbitrary number of cylindrical conductors,” *Journal of Applied Physics*, vol. 45, no. 2, pp. 638–647, Feb. 1974.
- [43] X. Wu and T. M. Habashy, “Influence of steel casings on electromagnetic signals,” *Geophysics*, vol. 59, no. 3, pp. 378–390, 1994.
- [44] G. S. Smith, “Electromagnetic inspection tool for ferromagnetic casings,” U.S. Patent 4 292 588, Sept. 29, 1981.
- [45] (2004, Aug.) Mett, Multifrequency Electromagnetic Thickness Tool. Datasheet. Schlumberger, Ltd. [Online]. Available: www.slb.com
- [46] K. H. Lee, H. J. Kim, and Y. Song, “Electromagnetic method for analyzing the property of steel casing,” Ernest Orlando Lawrence Berkeley National Laboratory, Tech. Rep. LBNL-41525, Feb. 1998.
- [47] K. H. Lee, H. J. Kim, and T. Uchida, “Electromagnetic fields in a steel-cased borehole,” *Geophysical Prospecting*, vol. 53, pp. 13–21, 2005.
- [48] D. Vasić, V. Bilas, and D. Ambruš, “Pulsed eddy-current nondestructive testing of ferromagnetic tubes,” *IEEE Transactions on Instrumentation and Measurement*, vol. 53, no. 4, pp. 1289–1294, Aug. 2004.
- [49] D. Vasić, “Single-coil method for simultaneous measurement of multiple parameters of a metal tube,” Master’s thesis, University of Zagreb, Faculty of Electrical Engineering and Computing, Nov. 2005.
- [50] M. I. Epov and G. M. Morozova, “TEM soundings in magnetic media,” *Russian Geology and Geophysics*, vol. 51, pp. 204–208, Jan. 2010.

- [51] W. Yang, C. Torres-Verdin, H. Junsheng, and Z. I. Zhang, "1D subsurface electromagnetic fields excited by energized steel casing," *Geophysics*, vol. 74, no. 4, pp. E159–E180, July 2009.
- [52] H. J. Kim and K. H. Lee, "Electromagnetic fields in a non-uniform steel-cased borehole," *Geophysical Prospecting*, vol. 54, pp. 433–439, 2006.
- [53] T. P. Theodoulidis and J. R. Bowler, "The truncated region eigenfunction expansion method for the solution of boundary value problems in eddy current nondestructive evaluation," *Review of Quantitative Nondestructive Evaluation*, vol. 24, pp. 403–408, 2005.
- [54] H. Sun, J. R. Bowler, and T. P. Theodoulidis, "Eddy currents induced in a finite length layered rod by a coaxial coil," *IEEE Transactions on Magnetics*, vol. 41, no. 9, pp. 2455–2461, Sept. 2005.
- [55] (2007) Wolfram Mathematica ver. 6. Wolfram Research, Inc. [Online]. Available: www.wolfram.com
- [56] W. Rudin, *Real and complex analysis*, 3rd ed. New York: McGraw-Hill, 1987.
- [57] P. Henrici, *Applied and computational complex analysis*. New York, USA: John Wiley & Sons, 1974, vol. 1.
- [58] K. Weigelt, "Solution of complex eigenvalue equations as used in the analytical solution of eddy-current problems of coupled regions," *Journal of Magnetism and Magnetic Materials*, vol. 83, pp. 501–505, 1990.
- [59] T. P. Theodoulidis and J. R. Bowler, "Eddy-current interaction of a long coil with a slot in a conductive plate," *IEEE Transactions on Magnetics*, vol. 41, no. 4, pp. 1238–1247, Apr. 2005.
- [60] L. M. Delves and J. N. Lyness, "A numerical method for locating the zeros of an analytic function," *Mathematics of Computation*, vol. 21, no. 100, pp. 543–560, oct 1967.
- [61] L. F. Abd-Elall, L. M. Delves, and J. K. Reid, "A numerical method for locating the zeros and poles of a meromorphic function," in *Numerical methods for nonlinear algebraic equations*, 2nd ed., P. Rabinowitz, Ed. Gordon and Breach Science Publisher, Jun 1988, ch. 3, pp. 47–59.
- [62] E. Anemogiannis, E. N. Glytsis, and T. K. Gaylord, "Efficient solution of eigenvalue equations of optical waveguiding structures," *Journal of Lightwave Technology*, vol. 12, no. 12, pp. 2080–2084, Dec. 1994.
- [63] D. Vasić, V. Bilas, and B. Šnajder, "Analytical modelling in low-frequency electromagnetic measurements of steel casing properties," *NDT&E International*, vol. 40, no. 2, pp. 103–111, Mar. 2007.

BIBLIOGRAPHY

- [64] (2007, Aug.) Matlab R2007b. The MathWorks, Inc. [Online]. Available: www.mathworks.com
- [65] J. H. Moran and K. S. Kunz, “Basic theory of induction logging and application to study of two-coil sondes,” *Geophysics*, vol. 27, no. 6, pp. 829–858, Dec. 1962.
- [66] (2009, Aug.) Schlumberger Oilfield Glossary. Schlumberger Ltd. [Online]. Available: www.glossary.oilfield.slb.com
- [67] T. R. Schmidt, “The remote field eddy current inspection technique,” *Materials Evaluation*, vol. 42, pp. 225–230, Feb. 1984.
- [68] G. N. Minerbo and G. A. Hazen, “Apparatus for measuring the inside diameter of a metallic pipe in a well,” U.S. Patent 4 546 315, Oct. 8, 1985.
- [69] M. I. Epov, G. M. Morozova, E. Y. Antonov, and I. G. Kuzin, “Method of nondestructive testing for technical state of casing strings in oil and gas wells basing on the transient electromagnetic method,” *Journal of Mining Science*, vol. 39, no. 3, pp. 216–224, 2003.
- [70] V. V. Dyakin, V. A. Sandovskii, and M. S. Dudarev, “Eddy-current inspection of tubes in a nonuniform field,” *Russian Journal of Nondestructive Testing*, vol. 40, no. 8, pp. 38–49, 2004.
- [71] D. Vasić, V. Bilas, and D. Ambruš, “Validation of a coil impedance model for simultaneous measurement of electromagnetic properties and inner diameter of a conductive tube,” *IEEE Transactions on Instrumentation and Measurement*, vol. 55, no. 1, pp. 337–342, 2006.
- [72] I. N. Bronshtein, K. A. Semendyayev, G. Musiol, and H. Muehlig, *Handbook of mathematics*, 4th ed. Berlin, Germany: Springer-Verlag, 2004.
- [73] K. H. Lee, G. Liu, and H. F. Morrison, “A new approach to modeling the electromagnetic response of conductive media,” *Geophysics*, vol. 54, no. 9, pp. 1180–1192, Sep 1989.
- [74] Y. Song and K. H. Lee, “Electromagnetic fields due to a loop current in a cased borehole surrounded by uniform whole space,” Ernest Orlando Lawrence Berkeley National Laboratory, Tech. Rep. LBNL-42371, Jan. 1998.
- [75] C. D. Meyer, *Matrix analysis and applied linear algebra*. Philadelphia, USA: SIAM, 2000.
- [76] J. O. Berger, *Statistical decision theory and Bayesian analysis*, 2nd ed. Springer-Verlag, New York, 1985.

- [77] C. P. Robert, *The Bayesian choice — From decision-theoretic foundations to computational implementation*, 2nd ed. New York: Springer, 2007.
- [78] R. E. Kass and L. Wasserman, “The selection of prior distributions by formal rules,” *Journal of the American Statistical Association*, vol. 91, no. 435, pp. 1343–1370, Sept. 1996.
- [79] R. E. Kass, “The geometry of asymptotic inference,” *Statistical Science*, vol. 4, no. 3, pp. 188–234, 1989.
- [80] A. Tarantola, *Inverse problem theory and methods for model parameter estimation*. Philadelphia, USA: SIAM, 2005.
- [81] A. Tarantola and B. Valette, “Inverse problems = Quest for information,” *Journal of Geophysics*, vol. 50, pp. 159–170, 1982.
- [82] J. Kaipio and E. Somersalo, *Statistical and computational inverse problems*, ser. Applied Mathematical Sciences, S. S. Antman, J. E. Marsden, and L. Sirovich, Eds. New York, USA: Springer-Verlag, 2004, vol. 160.
- [83] E. T. Jaynes, *Probability theory — The logic of science*, G. L. Bretthorst, Ed. Cambridge: Cambridge University Press, 2003.
- [84] K. Mosegaard and A. Tarantola, “Probabilistic approach to inverse problems,” in *International handbook of earthquake & engineering seismology (part A)*. Academic Press, 2002, pp. 237–265.
- [85] *Evaluation of measurement data—Guide to the expression of uncertainty in measurement*, Working Group 1, Joint Committee for Guides in Metrology Std., Rev. JCGM 100:2008—GUM 1995 with minor corrections, 2008.
- [86] C. F. Dietrich, *Uncertainty, calibration and probability: The statistics of scientific and industrial measurement*, 2nd ed. Boca Raton: Taylor & Francis Group, 1991.
- [87] D. J. C. MacKay, “Introduction to Monte Carlo methods,” in *Learning in graphical models*, ser. NATO Science Series, J. M. I., Ed. Kluwer Academic Press, 1998, pp. 175–204. [Online]. Available: <http://www.inference.phy.cam.ac.uk/mackay/erice.pdf>
- [88] C. J. Geyer. (2005, Nov.) Markov chain Monte Carlo lecture notes. [Online]. Available: <http://www.stat.umn.edu/geyer/f05/8931/n1998.pdf>
- [89] L. Tierney, “Markov chains for exploring posterior distributions,” *The Annals of Statistics*, vol. 22, no. 4, pp. 1701–1728, 1994.
- [90] W. K. Hastings, “Monte Carlo sampling methods using Markov chains and their applications,” *Biometrika*, vol. 57, no. 1, pp. 97–109, Apr. 1970.

BIBLIOGRAPHY

- [91] R. M. Neal, “Probabilistic inference using Markov chain Monte Carlo methods,” University of Toronto, Department of Computer Science, Tech. Rep. CRG-TR-93-1, Sept. 1993.
- [92] S. Chib and E. Greenberg, “Understanding the Metropolis-Hastings algorithm,” *The American Statistician*, vol. 49, no. 4, pp. 327–335, Nov. 1995.
- [93] J. S. Liu, F. Liang, and W. H. Wong, “The multiple-try method and local optimization in Metropolis sampling,” *Journal of the American Statistical Association*, vol. 95, no. 449, pp. 121–134, Mar. 2000.
- [94] C. J. Geyer, “Practical Markov chain Monte Carlo,” *Statistical Science*, vol. 7, no. 4, pp. 473–511, 1992.
- [95] H. Džapo, “Model-based measurement with application to grounding system testing,” Ph.D. dissertation, University of Zagreb, Faculty of Electrical Engineering and Computing, 2007, in Croatian.
- [96] G. O. Roberts, A. Gelman, and W. R. Gilks, “Weak convergence and optimal scaling of random walk Metropolis algorithms,” *The Annals of Applied Probability*, vol. 7, no. 1, pp. 110–120, 1997.
- [97] S. M. Tan, C. Fox, and G. K. Nicholls, *Inverse problems—course materials*. The University of Auckland, 2009. [Online]. Available: <http://home.comcast.net/~szemengtan/>
- [98] W. R. Gilks, G. O. Roberts, and S. K. Sahu, “Adaptive Markov chain Monte Carlo through regeneration,” *Journal of the American Statistical Association*, vol. 93, no. 443, pp. 1045–1054, Sept. 1998.
- [99] G. Sinclair, “Theory of models of electromagnetic systems,” *Proceedings of the I.R.E.*, vol. 36, no. 11, pp. 1364–1370, Nov. 1948.
- [100] F. C. Frischknecht, “Electromagnetic physical scale modeling,” in *Electromagnetic methods in applied geophysics*, M. N. Nabighian, Ed., 1988, pp. 365–441.
- [101] F. Gao and D. P. Shattuck, “A scale model of the through-casing resistivity measurement,” in *Proc. of Fourth International Conference on Signal Processing, ICSP*, vol. 2, 1998, pp. 1589–1592.
- [102] I. Krois, “Measurement system for neurophysiological functions monitoring,” Ph.D. dissertation, University of Zagreb, Faculty of Electrical Engineering and Computing, 2001, in Croatian.
- [103] P.-A. Probst and B. Collet, “Low-frequency digital lock-in amplifier,” *Review of Scientific Instruments*, vol. 56, no. 3, pp. 466–470, Mar. 1985.

BIBLIOGRAPHY

- [104] P.-A. Probst and A. Jaquier, “Multiple-channel digital lock-in amplifier with PPM resolution,” *Review of Scientific Instruments*, vol. 65, no. 3, pp. 747–750, Mar. 1994.
- [105] L. A. Barragan, J. I. Artigas, R. Alonso, and F. Villuendas, “A modular, low-cost, digital signal processor-based lock-in card for measuring optical attenuation,” *Review of Scientific Instruments*, vol. 72, no. 1, pp. 247–251, Jan. 2001.
- [106] J. M. Masciotti, J. M. Lasker, and A. H. Hielscher, “Digital lock-in detection for discriminating multiple modulation frequencies with high accuracy and computational efficiency,” *IEEE Transactions on Instrumentation and Measurement*, vol. 57, no. 1, pp. 182–189, Jan. 2008.
- [107] I. Krois, personal communication, Jan. 2009.
- [108] A. C. Metting van Rijn, A. Peper, and C. A. Grimbergen, “High-quality recording of bioelectric events — Part 1: Interference reduction, theory and practice,” *Medical & Biological Engineering & Computing*, vol. 28, pp. 389–397, Sept. 1990.
- [109] H. W. Otto, *Noise reduction techniques in electronic systems*, 2nd ed. New York: John Wiley & Sons, 1988.
- [110] D. Vasić, S. Perković, and V. Bilas, “Electromagnetic gauge of tube inner radius compensated for material properties and coil radial offset,” in *Proc. of the XIX IMEKO World Congress*, P. S. Girao, Ed., Lisbon, Portugal, Sept. 2009, pp. 638–642.
- [111] M. Dadić, D. Vasić, and V. Bilas, “A system identification approach to the modelling of pulsed eddy-current systems,” *NDT&E International*, vol. 38, pp. 107–111, 2005.
- [112] D. Ambruš, D. Vasić, and V. Bilas, “A low-power automated measurement system for pulsed eddy-current based inspection of oil-well casing,” in *Proc. of the 13th International Symposium on Measurements for Research and Industry Applications, IMEKO TC-4*, E. Kayafas and V. Loumos, Eds., vol. 2, Athens, Greece, Sept. 2004, pp. 401–404.
- [113] D. L. Atherton, T. R. Schmidt, T. Svendsen, and E. von Rosen, “Effects of remote field exciter coil tilt and eccentricity in a steel pipe,” *Materials Evaluation*, vol. 50, no. 1, pp. 44–50, Jan. 1992.
- [114] J. R. Lovell and W. C. Chew, “Effect of tool eccentricity on some electrical well-logging tools,” *IEEE Transactions on Geoscience and Remote Sensing*, vol. 28, no. 1, pp. 127–136, Jan. 1990.

- [115] T. P. Theodoulidis, "Analytical modeling of wobble in eddy current tube testing with bobbin coils," *Research in Nondestructive Evaluation*, vol. 14, no. 2, pp. 111–126, Feb 2002.
- [116] D. Vasić, V. Bilas, and D. Ambruš, "Compensation of coil radial offset in single-coil measurement of metal tube properties," in *Proc. of the 24th IEEE Instrum. and Meas. Tech. Conference, IMTC*, T. Wolinski, Ed., Warsaw, Poland, May 2007.
- [117] A. Massarini and M. K. Kazimierczuk, "Self-capacitance of inductors," *IEEE Transactions on Power Electronics*, vol. 12, no. 4, pp. 671–676, July 1997.
- [118] D. J. Harrison, L. D. Jones, and K. Burke, "Benchmark problems for defect size and shape determination in eddy-current nondestructive evaluation," *Journal of Nondestructive Evaluation*, vol. 15, no. 1, pp. 21–34, 1996.
- [119] J. C. Moulder, C.-C. Tai, B. F. Larson, and J. H. Rose, "Inductance of a coil on a thick ferromagnetic metal plate," *IEEE Transactions on Magnetics*, vol. 34, no. 2, pp. 505–514, Mar. 1998.
- [120] G. Grandi and M. K. Kazimierczuk, "Stray capacitances of single-layer solenoid air-core inductors," *IEEE Transactions on Industry Applications*, vol. 35, no. 5, p. 5, Sept.–Oct. 1999.
- [121] R. M. Bozorth, *Ferromagnetism*, 7th ed. Princeton, New Jersey: D. Van Nostrand Company, Inc., 1963.
- [122] N. Bowler, "Frequency-dependence of relative permeability in steel," *Review of Quantitative Nondestructive Evaluation*, vol. 25, pp. 1269–1276, 2006.
- [123] G. Buttino, A. Cecchetti, and A. Drigo, "Reversible permeability enhanced by Barkhausen jumps in ferromagnetic samples exhibiting a strong magnetic aftereffect," *IEEE Transactions on Magnetics*, vol. 4, no. 3, pp. 544–547, Sept. 1968.
- [124] K. J. Stevens, "Stress dependence of ferromagnetic hysteresis loops for two grades of steel," *NDT&E International*, vol. 33, pp. 111–121, 2000.
- [125] D. Stegemann, W. Reimche, B. Heutling, A. Krysz, J. Kroos, M. Stolzenberg, G. Westkämper, and R. Angerer, "Characterisation of steel grades by magnetoinductive method," in *Proc. of the 15th World Conference on Nondestructive Testing*, Rome, Italy, Oct. 2000.
- [126] D. C. Jiles and D. L. Atherton, "Ferromagnetic hysteresis," *IEEE Transactions on Magnetics*, vol. 19, no. 5, pp. 2183–2185, Sept. 1983.

BIBLIOGRAPHY

- [127] —, “Theory of the magnetisation process in ferromagnets and its application to the magnetomechanical effect,” *Journal of Physics D: Applied Physics*, vol. 17, pp. 1265–1281, 1984.
- [128] —, “Theory of ferromagnetic hysteresis,” *Journal of Magnetism and Magnetic Material*, vol. 61, pp. 48–60, 1986.
- [129] D. Jiles, *Introduction to magnetism and magnetic materials*, 2nd ed. London: Chapman & Hall, 1998.
- [130] M. J. Sablik, G. L. Burkhardt, and H. Kwun, “A model for the effect of stress on the low-frequency harmonic content of the magnetic induction in ferromagnetic materials,” *Journal of Applied Physics*, vol. 63, no. 8, pp. 3930–3932, Apr. 1988.
- [131] F. Liorzou, B. Phelps, and D. L. Atherton, “Macroscopic models of magnetization,” *IEEE Transactions on Magnetics*, vol. 36, no. 2, pp. 418–428, Mar. 2000.
- [132] D. C. Jiles, “Theory of magnetomechanical effect,” *Journal of Physics D: Applied Physics*, vol. 28, pp. 1573–1546, 1995.
- [133] D. P. Bulte and R. A. Langman, “Origins of the magnetomechanical effect,” *Journal of Magnetism and Magnetic Materials*, vol. 251, pp. 229–243, 2002.
- [134] M. J. Sablik, T. Yonamine, and F. J. G. Landgraf, “Modeling plastic deformation effects in steel on hysteresis loops with the same maximum flux density,” *IEEE Transactions on Magnetics*, vol. 40, no. 5, pp. 3219–3226, Sept. 2004.
- [135] D. Ambruš, V. Bilas, and D. Vasić, “Inspection tool for harsh environment operation utilizing pulsed remote field technique,” in *Proc. of the IEEE Instrum. and Meas. Tech. Conference, IMTC*, V. Groza, Ed., Ottawa, Canada, May 2005, pp. 1297–1300.
- [136] M. G. Pecht and D. Humphrey, “Addressing obsolescence—The uprating option,” *IEEE Transactions on Components and Packaging Technologies*, vol. 31, no. 3, pp. 741–745, Sept. 2008.
- [137] O. Krkač, V. Bilas, and D. Ambruš, “Thermal uprating of a mixed signal microcontroller,” in *Proc. of the IEEE Int. Symp. Ind. Electron., ISIE*, N. Perić, I. Petrović, and v. Butković, Eds., vol. 3, Dubrovnik, Croatia, June 2005, pp. 1111–1116.
- [138] G. Holladay and M. J. Wilt, “Borehole induction coil transmitter,” U.S. Patent 6 489 772 B1, Dec. 3, 2002.

BIBLIOGRAPHY

- [139] S. Tumanski, “Induction coil sensors — a review,” *Measurement Science and Technology*, vol. 18, pp. R31–R46, Jan. 2007.
- [140] F. E. Terman, *Radio engineers’ handbook*, 1st ed. New York: McGraw-Hill Company, Inc., 1943.
- [141] H. C. Serán and P. Fergeau, “An optimized low-frequency three-axis search coil magnetometer for space research,” *Review of Scientific Instruments*, vol. 76, pp. 044 502(1–10), Apr. 2005.
- [142] W. D. Stanley and R. D. Tinkler, “A practical, low-noise coil system for magnetotellurics,” United States Department of the Interior Geological Survey, Tech. Rep. Open-file report No. 83-85, 1983.
- [143] E. Nichols, U. Conti, and D. Omeragic, “Sensor for detecting the magnetic field in the area of downhole casing,” U.S. Patent 6 597 178 B1, July 22, 2003.
- [144] (2010, Mar.) Metglas magnetic alloy 2714A (cobalt-based). Metglas, Inc. Conway, SC, USA. [Online]. Available: www.metglas.com
- [145] R. J. Prance, T. D. Clark, and H. Prance, “Ultra low noise induction magnetometer for variable temperature operation,” *Sensors and Actuators. A: Physical*, vol. 85, pp. 361–364, 2000.
- [146] (2010, Jan.) Instrumentation amplifier INA129-HT. Datasheet. Texas Instruments, Inc. Dallas, TX, USA. [Online]. Available: www.ti.com
- [147] (2010, Mar.) Texas Instruments, Harsh Environments. Texas Instruments, Inc. Dallas, TX, USA. [Online]. Available: www.ti.com/he
- [148] (2010, Mar.) Instrumentation amplifier 52301. Datasheet. Micropac Industries, Inc. Garland, TX, USA. [Online]. Available: www.micropac.com
- [149] (2009, June) Digital signal processor SM320F2812-HT. Datasheet. Texas Instruments, Inc. Dallas, TX, USA. [Online]. Available: www.ti.com
- [150] (2010, Mar.) Analog-to-digital-converter ADS1278-HT. Datasheet. Texas Instruments, Inc. Dallas, TX, USA. [Online]. Available: www.ti.com
- [151] The technical staff of Analog Devices, *The data conversion handbook*, W. Kester, Ed. Oxford, UK: Newnes is an imprint of Elsevier, 2005.

Summary

Rock conductivity measurement is a pivotal method in the open-hole well logging for evaluation of hydrocarbon reservoirs. The conductivity measurement is also required in cased wells as an addition to the radiation methods. Only a contact conductivity tool is available for the cased well application. This thesis proposes an inductive method for simultaneous measurement of the rock conductivity and the casing properties (thickness, conductivity, and permeability) from within single steel-cased well. The analytical electromagnetic model was derived for a transmitter coil inside a steel casing surrounded by a cylindrically and horizontally layered low-conductive medium. Using the space-frequency analysis of the sensitivity on the casing and formation properties, the measurement configuration consisting of one transmitter and three receiver coils was proposed. The investigation radius, vertical resolution, and separability of the casing and formation contributions were discussed. The inverse problem of determination of the casing and formation properties was based on the Bayesian approach. The method was corroborated on the scaled laboratory model of the cased well. The requirements were established for the electronic instrumentation that would embody the proposed method. The single-well through-casing inductive tool is found to be feasible for operation in the high-temperature environment using commercially available electronic components. The method is applicable for the rock conductivity larger than 1 S/m with the investigation radius of 10 m.

Keywords: cased well, rock resistivity, casing inspection, inductive measurement, analytical electromagnetic modelling, inverse problems, Monte Carlo Markov chains, scaled modelling, electronic instrumentation, high temperature environment.

About the author

Darko Vasić was born in Zenica, Bosnia and Herzegovina, on February 19, 1978, where he completed his primary education in 1992. During his secondary education in Zagreb, Croatia, he participated in student physics and chemistry competitions at the country level. He was a member of Croatian representation at the 27th International Physics Olympiad in Sudbury, Canada in 1997. He enrolled at the University of Zagreb, Faculty of Electrical Engineering and Computing in 1997, where he received the Dipl.-Eng. degree in electrical engineering (industrial electronics) in 2002. The degree thesis is entitled “Pulsed Eddy-Current Nondestructive Evaluation.” As a student, he received three “Josip Lončar” awards for an exemplary success at the second, third and fourth year of the study. In 2001, he received the Award of Rector of the University of Zagreb for his student work entitled “Pulsed Eddy-Current Thickness Measurement of Metal Plates.” He enrolled in the postgraduate study of electronics at the Faculty of Electrical Engineering and Computing in 2002. He has been a research assistant with the Department of Electronic Systems and Information Processing at the same Faculty since 2002. In November 2005, he received the M.Sc. degree in electronics under the supervision of Prof. Vedran Bilas for the thesis entitled “Single-Coil Method for Simultaneous Measurement of Multiple Parameters of a Metal Tube,” written and defended in English. He was awarded the silver “Josip Lončar” plaque in 2006 for the results of the thesis. He received a fellowship for four-months research stay at the University of Manchester in 2008. He was awarded with the young scientist award “Vera Johanides” of the Croatian Academy of Engineering in 2008. His current professional and research interests include analysis and development of electromagnetic methods for nondestructive/noninvasive evaluation focused on the application of signal processing and inverse techniques, and development of electronic instrumentation suitable for operation in high-temperature environments. He is a co-author of six journal papers and more than twenty papers published at international conferences. He serves as a reviewer for IEEE Transactions on Instrumentation and Measurement. He is a member of following professional societies: Institute of Electrical and Electronic Engineers (IEEE), Croatian Medical and Biological Engineering Society (CROMBES), International Federation for Medical and Biological Engineering (IFMBE), and Society of Exploration Geophysicist (SEG). He speaks English and some German.

Sažetak

Mjerenje otpornosti stijena induktivnom metodom u zacijevljenoj bušotini

Mjerenje vodljivosti stijena je ključna metoda u geofizičkom ispitivanju ležišta ugljikovodika iz nezacijevljenih bušotina. Mjerenje vodljivosti je potrebno i u zacijevljenim bušotinama kao dodatak radioaktivnim metodama. Za primjenu u zacijevljenim bušotinama raspoloživo je samo kontaktno mjerenje vodljivosti. U ovome radu je predložena induktivna metoda za istodobno mjerenje vodljivosti stijena i značajki zaštitne cijevi (debljina stijenke, vodljivost i permeabilnost) u zacijevljenoj bušotini. Izveden je analitički elektromagnetski model odašiljačke zavojnice unutar čelične zaštitne cijevi okružene cilindrično i horizontalno slojevitim slabo vodljivim medijem. Na temelju prostorno-frekvencijske analize osjetljivosti na značajke zaštitne cijevi i okolnih stijena, predložen je mjerni sustav od jedne odašiljačke i tri prijamne zavojnice. Istraženi su polumjer ispitivanja, vertikalna razlučivost te odvojivost doprinosa zaštitne cijevi i stijena. Inverzni je problem određivanja značajki cijevi i stijena temeljen na Bayesovom pristupu. Metoda je potvrđena na skaliranom laboratorijskom modelu zacijevljene bušotine. Utvrđeni su zahtjevi na izvedbu elektroničke instrumentacije kojom bi se realizirala mjerna metoda. Potvrđeno je da komercijalno dobavljive elektroničke komponente dopuštaju izvedivost induktivnog uređaja za mjerenje u zacijevljenoj bušotini u okolišu s visokom temperaturom. Mjerna metoda je primjenjiva za vodljivosti stijena veće od 1 S/m s polumjerom ispitivanja od 10 m.

Ključne riječi: zacijevljena bušotina, otpornost stijena, ispitivanje zaštitne cijevi, induktivno mjerenje, analitičko elektromagnetsko modeliranje, inverzni problemi, Monte Carlo Markovljevi lanci, skalirano modeliranje, elektronička instrumentacija, visokotemperaturno okruženje.

Životopis

Darko Vasić je rođen 19. veljače 1978. godine u Zenici, Bosna i Hercegovina, gdje je 1992. godine završio osnovnu školu. Tijekom srednjoškolskog obrazovanja u Zagrebu sudjelovao je na natjecanjima iz fizike i kemije na državnoj razini. Bio je član hrvatske reprezentacije na 27. Međunarodnoj olimpijadi iz fizike 1997. godine u Sudburyju, Kanada. Fakultet elektrotehnike i računarstva Sveučilišta u Zagrebu upisao je 1997. godine, a diplomu diplomiranog inženjera elektrotehnike (smjer industrijska elektronika) je stekao 2002. godine. Naslov diplomskog rada s naglaskom na znanstveno-istraživačkom radu je “Nerazorno ispitivanje primjenom skokovitim pobudom izazvanih vrtložnih struja”. Tijekom studija je dobio tri priznanja “Josip Lončar” za primjeren uspjeh na drugoj, trećoj i četvrtoj godini studija. Godine 2001. dobio je Rektorovu nagradu Sveučilišta u Zagrebu za rad “Mjerenje debljine metalnog sloja primjenom skokovitim pobudom izazvanih vrtložnih struja”. Poslijediplomski studij elektronike na Fakultetu elektrotehnike i računarstva upisao je 2002. godine. Iste godine se zaposlio kao znanstveni novak na Zavodu za elektroničke sustave i obradbu informacija. U studenom 2005. godine je stekao stupanj magistra znanosti pod mentorstvom prof. dr. sc. Vedrana Bilasa. Naziv magistarskog rada kojeg je napisao i obranio na engleskom jeziku je “*Single-Coil Method for Simultaneous Measurement of Multiple Parameters of a Metal Tube*” (“Istodobno mjerenje više parametara metalne cijevi metodom jedne zavojnice”). Za rezultate magistarskog rada nagrađen je 2006. godine srebrnom plaketom “Josip Lončar”. U sklopu doktorskog studija, 2008. godine proveo je četiri mjeseca na Sveučilištu u Manchesteru (*University of Manchester*) u Velikoj Britaniji radi znanstvenog usavršavanja. Godine 2008. dobio je nagradu za mladog znanstvenika “Vera Johanides” Hrvatske akademije tehničkih znanosti. Njegovi profesionalni i znanstveni interesi uključuju elektromagnetske metode za nerazorna i neinvazivna ispitivanja s naglaskom na primjenu obradbe signala i metoda rješavanja inverznih problema te razvoj elektroničke instrumentacije za rad u uvjetima visokih temperatura. Koautor je šest članaka u znanstvenim časopisima referiranim u svjetskim bazama, te dvadesetak članaka objavljenih na konferencijama s međunarodnom recenzijom. Stalni je recenzent za časopis *IEEE Transactions on Instrumentation and Measurement*. Član je sljedećih društava: *Institute of Electrical and Electronic Engineers (IEEE)*, Hrvatsko društvo za medicinsku i biološku tehniku (HDMBT), *International Federation for Medical and Biological Engineering (IFMBE)* i *Society of Exploration Geophysicists (SEG)*. Aktivno govori engleski, a služi se i njemačkim jezikom.